Advances in Materials Science and Engineering

Advances in Modeling of Heat and Mass Transfer in Porous Materials

Special Issue Editor in Chief: Giorgio Pia
Guest Editors: Jianchao Cai, Zhien Zhang, and Shimin Liu

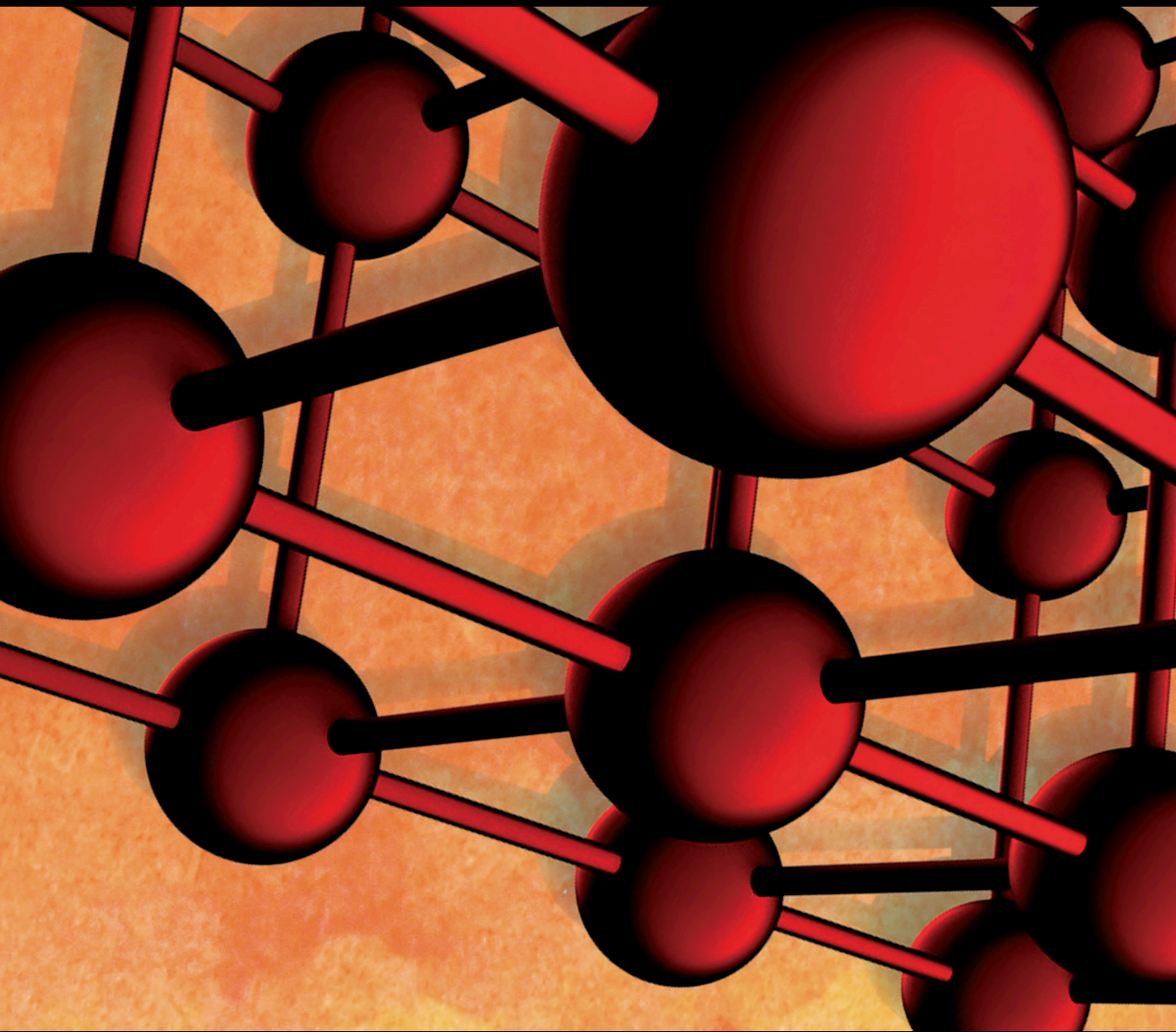

Advances in Modeling of Heat and Mass Transfer in Porous Materials

Advances in Materials Science and Engineering

Advances in Modeling of Heat and Mass Transfer in Porous Materials

Special Issue Editor in Chief: Giorgio Pia
Guest Editors: Jianchao Cai, Zhien Zhang, and Shimin Liu

Contents

Hindawi
Advances in Materials Science and Engineering
Volume 2019, Article ID 7089718, 2 pages
https://doi.org/10.1155/2019/7089718

Editorial

Advances in Modelling of Heat and Mass Transfer in Porous Materials

Giorgio Pia,[1] **Jianchao Cai**,[2] **Zhien Zhang**,[3] **and Shimin Liu**[4]

[1]*Dipartimento di Ingegneria Meccanica, Chimica e dei Materiali, Università degli Studi di Cagliari, via Marengo 2, 09123 Cagliari, Italy*
[2]*China University of Geosciences, Wuhan, China*
[3]*The Ohio State University, Columbus, OH 43210, USA*
[4]*Center for Geomechanics, Geofluids and Geohazards, Penn State University, State College, USA*

Correspondence should be addressed to Giorgio Pia; giorgio.pia@dimcm.unica.it

Received 2 September 2019; Accepted 5 September 2019; Published 31 December 2019

Porous materials are used across a huge array of applied sciences and engineering disciplines.

From biology to geoscience, chemistry to materials science and civil engineering to environmental engineering, the research of porous media represents a remarkable issue. The understanding of the relationships between structures and properties symbolise an ultimate step for traditional and advanced applications as in chemical, food, petroleum, gas, and nuclear industries.

Thanks to their significance and prevalence, the investigation of transport phenomena in porous materials has emerged as a distinct field of study. Transport phenomena, comprehended from the microscopic scale upward, encompass the general theories behind flow and transport in porous media and form the basis of deterministic and stochastic models that describe them. Research in the area generally evaluates the role of porous media in single and multiphase fluid flow, solid particle motions, heat conduction and convection, and electrical and acoustical transport along with their biomolecular and chemical composition.

This special issue has been dealt in seven high quality papers that focused on theory and simulation in an endeavour to advance the understanding of heat and mass transfer in porous materials, especially as a function of their structure and properties.

The paper proposed by H. Singh and R. S. Myong, titled "Critical Review of Fluid Flow Physics at Micro- to Nano-Scale Porous Media Applications in the Energy Sector," pronounces the gas and liquid flow at micro- and nano-scale and identified critical gaps to improve fluid flow modelling in four diverse applications related to the energy sector. The review for gas flow is primarily focused on gas flow at rarefied conditions, the velocity slip and temperature jump conditions. The review for liquid flow bestows fundamental flow regimes of liquid flow and liquid slip models as a function of key modelling parameters.

M. O. Dominguez et al., in the paper entitled "Modeling of the Growth Kinetics of Boride Layers in Powder-Pack Borided ASTM A36 Steel Based on Two Different Approaches" made use of two mathematical approaches for determining the value of activation energy in the Fe_2B layers on ASTM A36 steel during the iron powder-pack boriding in the temperature range of 1123–1273 K (treatments times between 2 and 8 h). The first approach was based on the mass balance equation at the interface (Fe_2B/substrate) and the solution of Fick's second law under steady state (devoid of time-dependent). The second approach was based on the same mathematical principles as the first approach for one-dimensional analysis under non–steady state condition. The measurements of the thickness (Fe_2B), for different temperatures of boriding, were used for the calculations. Consequently, the boron activation energy for the ASTM A36 steel was estimated to be 161 $kJ{\cdot}mol^{-1}$. This value of energy was compared for both models and other literature data. Experimental tests for characterising the Fe_2B layers grown on ASTM A36 are carried out by X-ray diffraction (XRD), scanning electron microscopy (SEM), and energy

dispersive X-ray spectroscopy (EDS). Finally, the experimental value of the Fe_2B layer's thickness obtained at 1123 K with exposure times of 2.5 h was compared with the predicted thicknesses by using these two approaches. A good agreement between the experimental data and the simulated results has been noted.

Y. Luo et al., in the work titled "Longitudinal Reservoir Evaluation Technique for Tight Oil Reservoirs," studied pore structure at microscopic scale, fluid occurrence conditions, start-up pressure gradient, and the content of clay minerals in the longitudinal direction of tight reservoirs. Each parameter signified a physical property of the reservoir. These parameters were independent of each other and did not affect each other, so the assessment results obtained in this way were objective. The longitudinal evaluation method for tight reservoirs was proposed, and the optimal development mode was selected in accordance with the reservoir assessment results.

The paper titled "Molding of Polymeric Composite Reinforced with Glass Fiber and Ceramic Inserts: Mathematical Modeling and Simulation" by T. R. N. Porto et al. carried out a numerical study of a polymer composite manufactured by using liquid composite material moulding. Simulation, by using the Ansys FLUENT®, of resin flow into a porous media constituted by fibre perform (reinforcement) inserted in a mould with pre-allocated ceramic inserts has been done. Results of resin volumetric fraction, stream lines, and pressure distribution inside the mould and mass flow rate (inlet and outlet gates) of the resin, as a function of filling time, have been presented and deliberated. Results indicate that the number of inserts affects the filling time, whereas the distance between them has no influence on the process.

X. Zhu et al. proposed a paper titled "Entire Process Simulation of Corrosion due to the Ingress of Chloride Ions and CO_2 in Concrete" and studied a comprehensive mathematical model capable of simulating the entire corrosion process of reinforcement in concrete. The mutual effect of carbonation and chloride ingress has also been deliberated in the mass transport module. Nonuniform corrosion distribution has been employed for studying the mechanical damage in concrete. The association of ABAQUS with MATLAB has been adopted for the numerical implementation of the developed model. The numerical results of an illustrative example designate that the depassivation time of reinforcement, corrosion rate and expansion displacement, and cracking pattern of concrete can be precisely predicted.

The paper entitled "Effect of Seepage Velocity on Formation of Shaft Frozen Wall in Loose Aquifer" by J. Lin et al. addressed the difficult closure of a frozen wall in a coal mine shaft owing to excessive seepage velocity in an aquifer when the aquifer is penetrated via artificial freezing method. Based on hydrothermal coupling theory and bearing in mind the effect of diminished absolute porosity on seepage during the freezing process, a mathematical model of hydrothermal full parameter coupling with a phase change is created. A shaft is used as a prototype and COMSOL multi-physics finite element software is used to perform a numerical simulation of the shaft freezing process at numerous stratum seepage velocities. The numerical simulation results are substantiated via a comparison with field measurement data. Based on the numerical simulation results, the impact of various underground water seepage velocities on the artificial frozen wall formation process with the seepage temperature field coupling effect is investigated. Based on the analysis results, the recommended principles of the optimization design for a freezing plan are described as follows. Firstly, the downstream area is closed to enable the water insulation effect. Secondly, the closure of the upstream area is accelerated to diminish the total closure time of a frozen wall.

B. Wang et al. proposed a work titled "Study on the Formation Law of the Freezing Temperature Field of Freezing Shaft Sinking under the Action of Large-Flow-Rate Groundwater." It testified a numerical model of hydrothermal coupling using laws of conservation of energy and mass. The model is substantiated by the results of large-scale laboratory tests. By applying the numerical calculation model to the formation of artificial shaft freezing temperature fields under the action of large flow groundwater, we conclude that groundwater with flow rates of less than 5 m/d will not have a substantial impact on the artificial freezing temperature field. The maximum flow rates that can be handled by single-row freezing pipes and double-row freezing pipes are 10 m/d and 20 m/d, respectively, during the process of freezing shaft sinking. By analysing the variation of groundwater flow rate during freezing process, we found that the groundwater flow velocity can reach 5–7 times the initial flow velocity near the closure moment of the frozen wall. Finally, in the light of the action characteristics of groundwater on the freezing temperature field, we made recommendations for optimal pipe and row spacing in freezing pipe arrangement.

Conflicts of Interest

The editors declare that there are no conflicts of interest regarding the publication of the special issue.

Acknowledgments

The guest editorial team would like to express gratitude to all the authors for their interest in selecting this special issue as a venue for disseminating their scholarly work. The editors also wish to thank the anonymous reviewers for their careful reading of the manuscripts submitted to this special issue collection and their several insightful comments and suggestions.

Giorgio Pia
Jianchao Cai
Zhien Zhang
Shimin Liu

Hindawi
Advances in Materials Science and Engineering
Volume 2019, Article ID 5985617, 12 pages
https://doi.org/10.1155/2019/5985617

Research Article

Modeling of the Growth Kinetics of Boride Layers in Powder-Pack Borided ASTM A36 Steel Based on Two Different Approaches

M. Ortiz-Domínguez,[1] **O. A. Gómez-Vargas**,[2] **G. Ares de Parga**,[3] **G. Torres-Santiago**,[2] **R. Velázquez-Mancilla**,[2] **V. A. Castellanos-Escamilla**,[2] **J. Mendoza-Camargo**,[2] **and R. Trujillo-Sánchez**[2]

[1]*Universidad Autónoma del Estado de Hidalgo, Escuela Superior de Ciudad Sahagún-Ingeniería Mecánica, Carretera Cd. Sahagún-Otumba s/n, CP. 43990, Hidalgo, Mexico*
[2]*Instituto Tecnológico de Tlalnepantla-ITTLA. Av., Instituto Tecnológico, S/N. Col. La Comunidad, Tlalnepantla de Baz, CP. 54070, Estado de Mexico, Mexico*
[3]*Instituto Politécnico Nacional-ESFM, U.P. Adolfo López Mateos, Zacatenco, CP. 07738. Cd, De Mexico, Mexico*

Correspondence should be addressed to M. Ortiz-Domínguez; martin_ortiz@uaeh.edu.mx

Received 11 October 2018; Accepted 7 July 2019; Published 7 October 2019

Academic Editor: Giorgio Pia

An indispensable tool to choose the suitable process parameters for obtaining boride layer of an adequate thickness is the modeling of the bording kinetics. In this work, two mathematical approaches were used in order to determine the value of activation energy in the Fe_2B layers on ASTM A36 steel during the iron powder-pack boriding in the temperature range of 1123–1273 K for treatment times between 2 and 8 h. The first approach was based on the mass balance equation at the interface (Fe_2B/substrate) and the solution of Fick's second law under steady state (without time dependent). The second approach was based on the same mathematical principles as the first approach for one-dimensional analysis under non-steady-state condition. The measurements of the thickness (Fe_2B), for different temperatures of boriding, were used for calculations. As a result, the boron activation energy for the ASTM A36 steel was estimated as 161 kJ·mol^{-1}. This value of energy was compared between both models and with other literature data. The Fe_2B layers grown on ASTM A36 steel were characterized by use of the following experimental techniques: X-ray diffraction (XRD), scanning electron microscopy (SEM), and energy dispersive X-ray Spectroscopy (EDS). Finally, the experimental value of Fe_2B layer's thickness obtained at 1123 K with an exposure time of 2.5 h was compared with the predicted thicknesses by using these two approaches. A good concordance was achieved between the experimental data and the simulated results.

1. Introduction

Nowadays and due to the increasing technological development, it is necessary to have metallic materials with specific features that must be maintained in critical service conditions: for example, the metal dies are used in the different hot and cold working metallurgical processes, which given the working conditions require high toughness and high surface hardness. The thermochemical treatments applied to steel are those in which the composition of the surface of the workpiece is altered by the addition of carbon, nitrogen, sulphur, boron, aluminium, zinc, chromium, or other elements. The most common treatments in the industry are carburization, nitriding, carbonitriding, and boriding. Boriding is a thermochemical treatment controlled by the diffusion of boron atoms, which modifies the properties of the material generating hard surfaces. Likewise, the boriding process has a positive effect on the tribological applications: abrasive, adhesive, fatigue, and corrosion wear in acid and alkaline media. The process involves heating a ferrous or nonferrous alloy for a temperature range of 700°C to 1000°C with a treatment time of 1 to 12 hours for powder-

pack methods. When boron diffuses in a substrate, a monolayer (Fe_2B) or a double layer (FeB–Fe_2B) can be formed, depending on the chemical composition of the substrate and the chemical potential of boron. These phases consist of orthorhombic and tetragonal lattices (body-centred), respectively. One basic advantage of boride layers is that they can reach high hardness values (between 1800 and 2000 HV), kept at high temperatures [1–4]. Abrasion and adhesion wear are forms of wear by contact between a particle and solid material, being the characteristic result of almost all types of mechanical stress. Borided steels are resistant to abrasion because of their extreme hardness on the surface; this characteristic makes them suitable to be applied in pneumatic conveying systems; dies for stamping; components of plastic processing machines, such as extrusion screws; bearings for oil extraction pumps; ball valves; plungers for use in manufacturing glass; and components in textile machinery. In practice, there are many techniques of surface modification by boriding, such as powder-pack boriding [5], paste boriding [6], gaseous boriding [7], plasma boriding [8], plasma paste boriding [9], and laser boriding [10]. However, the most frequently used method in industry is the powder-pack boriding, which demands a low investment cost of equipment and an easy handling. From a kinetic point of view, several approaches [3, 5–7, 11–33] were developed in the objective of optimizing the thicknesses of borided layers in order to meet the functional requirements during industrial use of borided steels. Some of these models that estimate the thickness of the monolayer (Fe_2B) or a double layer (FeB–Fe_2B) are based on the solution of Fick's second law without time dependent ($\nabla^2 C_{Fe_2B}(x) = 0 \longrightarrow$ steady state) [3, 6, 7, 16–18, 20–22, 24–26, 30] and some others on the solution of Fick's second law with time dependent ($\partial C_{Fe_2B}(x,t)/\partial t = D_{Fe_2B}\partial^2 C_{Fe_2B}(x,t)/\partial x^2 \longrightarrow$ non-steady state) [5, 24, 27, 28, 31, 33].

The ASTM A36 steel has a good machinability with an acceptable wear resistance. ASTM A36 steel has the following applications:

(i) It is used in bolted, riveted, or welded construction of bridges, buildings, and oil rigs

(ii) It is used in forming tanks, bins, bearing plates, fixtures, rings, templates, jigs, sprockets, cams, gears, base plates, forgings, ornamental works, stakes, brackets, automotive and agricultural equipment, frames, and machinery parts

(iii) It is used for various parts obtained by flame cutting such as in parking garages, walkways, boat landing ramps, and trenches

In the present work, two different models were suggested for simulating the growth kinetics of monolayer (Fe_2B) on ASTM A36 steel in the range of boriding temperature 1123–1273 K. The parabolic growth constants of Fe_2B were determined. The boron diffusion coefficient in the boride layers was estimated from these two approaches based on the conditions of the boriding process in the Fe-B system. X-ray diffraction (XRD), scanning electron microscopy (SEM), and energy dispersive X-ray spectroscopy (EDS) were conducted on material borided to characterize the presence of the Fe_2B layer and the distribution of heavy elements in the surface of the ASTM A36 steel. Finally, the experimental value of Fe_2B layer's thickness obtained at 1123 K with an exposure time of 2.5 h was compared with the predicted result from these two approaches.

2. Mathematical Approaches

One basic parameter that characterizes the Fe_2B layers is the thickness, since the properties of the coating depend on it, such as resistance to wear, fatigue, hardness, and dynamic loads, as well as to a large extent determining the grip with the substrate. Having an expression that allows estimating the layer thickness during the boriding process facilitates the appropriate selection of the technological parameters in order to guarantee the desired properties. The layer thickness exhibits a time dependent such that

$$\text{Layer thickness v} \approx t^{1/2}. \tag{1}$$

2.1. Derivation of the Parabolic Growth Law. In diffusion in solid, parabolic kinetics occurs when the mass gain on a sample is proportional to the square root of time. In general, parabolic kinetics indicates that diffusion of reactants (such as boron) through a growing layer is rate-determining. If the diffusion of B atoms is rate-determining, the layer rate is proportional to the flux through the substrate:

$$\frac{dx}{dt} \approx J_{Fe_2B}(x,t). \tag{2}$$

El flux, $J_{Fe_2B}(x,t)$, can be written as

$$J_{Fe_2B}(x,t) = C_{Fe_2B}(x,t)\left(\frac{dx}{dt}\right), \tag{3}$$

where $C_{Fe_2B}(x,t)$ is the boron concentration profile in mol/m^3 and dx/dt is the velocity of Fe_2B layer in m/s, and $J_{Fe_2B}(x,t)$ giving units of mol/m^2·s. The velocity of a particle is proportional to the force, F, on the particle:

$$\frac{dx}{dt} = B_{Fe_2B}F, \tag{4}$$

where B_{Fe_2B} is the mobility of the boron atoms. Writing the chemical potential as μ_{Fe_2B}, this force is written as

$$F = \frac{-\partial \mu_{Fe_2B}}{\partial x}, \tag{5}$$

for a Fe_2B layer with thickness x. If combining equations (4) and (5), then equation (3) can be written as

$$J_{Fe_2B}(x,t) = \frac{-C_{Fe_2B}(x,t)B_{Fe_2B}\partial \mu_{Fe_2B}}{\partial x}. \tag{6}$$

From the relationship,

$$\mu_{Fe_2B} = \mu^o_{Fe_2B} + k_B T \ln a_{Fe_2B}, \tag{7}$$

where k_B is the Boltzmann's constant, we can write

$$\frac{\partial \mu_{Fe_2B}}{\partial x} = \frac{\partial\left(\mu^{o}_{Fe_2B} + k_B T \ln a_{Fe_2B}\right)}{\partial x} = k_B T \frac{\partial \ln a_{Fe_2B}}{\partial x}. \quad (8)$$

In an ideal system, the concentration, $C_{Fe_2B}(x,t)$, is equivalent to activity, $a\ (x,t)$. Substituting equations (8) into (6), we get

$$J_{Fe_2B}(x,t) = -C_{Fe_2B}(x,t) B_{Fe_2B} k_B T \frac{\partial \ln C_{Fe_2B}(x,t)}{\partial x} = -B_{Fe_2B} k_B T \frac{\partial C_{Fe_2B}(x,t)}{\partial x}. \quad (9)$$

As shown in equation (2),

$$\frac{dx}{dt} = (\text{constant}) J_{Fe_2B}(x,t), \quad (10)$$

so that a combination of equations (2) and (9) gives

$$\frac{dx}{dt} = -(\text{constant}) B_{Fe_2B} k_B T \frac{\partial C_{Fe_2B}(x,t)}{\partial x}. \quad (11)$$

If we assume that the potential is fixed at each boundary of the Fe_2B layer, we can replace $\partial C_{Fe_2B}(x,t)/\partial x$ in equation (11) with the slope $(=\Delta C_{Fe_2B}/x)$. We then introduce the parabolic growth constant k_{Fe_2B}, and set

$$k_{Fe_2B} = -(\text{constant}) B_{Fe_2B} k_B T \Delta C_{Fe_2B}. \quad (12)$$

Combining equations (11) and (12) gives

$$\frac{dx}{dt} = \frac{k_{Fe_2B}}{x}. \quad (13)$$

Equation (13) can be rewritten as

$$x dx = k_{Fe_2B} dt. \quad (14)$$

Upon integration of equation (14),

$$\int_{x=v_0}^{x=v} x dx = k_{Fe_2B} \int_{t=t_0^{Fe_2B}}^{t=t} dt. \quad (15)$$

We arrive at the parabolic growth law (with $v_0 \approx 0$):

$$v^2 = 2k_{Fe_2B}\left(t - t_0^{Fe_2B}\right) = 2k_{Fe_2B} t_v, \quad (16)$$

where v represents the Fe_2B layer thickness.

2.2. First Approach: Steady-State Diffusion Model. The first approach is based on the diffusion model proposed by Flores-Rentería et al. [3], where a mathematical model has been applied based on the mass balance equation at the (Fe_2B/substrate) interface $((C_{up}^{Fe_2B} + C_{low}^{Fe_2B} - 2C_0/2)dx/dt_v|_{x=v} = -D_{Fe_2B} dC_{Fe_2B}(x)/dx|_{x=v})$ by assuming a linear boron concentration profile through the Fe_2B layer $(C_{Fe_2B}(x) = (C_{low}^{Fe_2B} - C_{up}^{Fe_2B})x/v + C_{up}^{Fe_2B} \longrightarrow$ steady state). This approach was used to simulate the kinetics of formation of Fe_2B layer on ASTM A36 steel with the presence of boride incubation time. Steady state means that there will not be any change in the composition profile with time. $C_{up}^{Fe_2B} = 60 \times 10^3\ \text{mol}\cdot\text{m}^{-3}$ and $C_{low}^{Fe_2B} = 59.8 \times 10^3\ \text{mol}\cdot\text{m}^{-3}$ denote the upper and lower boron concentrations in the Fe_2B phase [3, 34, 35]. C_0 represents the boron solubility in the matrix and can be neglected [3, 34, 35]. The assumptions made during the mathematical formulation of the diffusion model are given in the reference work [3].

The mass balance equation [3], describing the evolution of displacement of growing interface with respect to the time, is given by

$$\left(C_{up}^{Fe_2B} + C_{low}^{Fe_2B} - \frac{2C_0}{2}\right)\left.\frac{dx}{dt_v}\right|_{x=v} = -D_{Fe_2B}\left.\frac{dC_{Fe_2B}(x)}{dx}\right|_{x=v}. \quad (17)$$

The linear boron concentration profile [3], through the Fe_2B layer, is given by the solution of Fick's second law without time dependent $(\nabla^2 C_{Fe_2B}(x) = 0 \longrightarrow$ steady state $(\nabla^2 = d^2/dx^2$ (is called the Laplace operator or Laplacian in one dimension)) and is rewritten as

$$C_{Fe_2B}(x) = \frac{\left(C_{low}^{Fe_2B} - C_{up}^{Fe_2B}\right)}{v} x + C_{up}^{Fe_2B}. \quad (18)$$

By substituting equations (18) and (16) into equation (17),

$$D_{Fe_2B} = \frac{1}{2}\left(\frac{C_{up}^{Fe_2B} + C_{low}^{Fe_2B} - 2C_0}{C_{up}^{Fe_2B} - C_{low}^{Fe_2B}}\right) k_{Fe_2B}. \quad (19)$$

2.3. Second Approach: Non-Steady-State Diffusion Model in One Dimension. The second approach [5] was applied to analyze the kinetics of formation of the monolayer (Fe_2B) generated at the surface of pack-borided AISI 1045 steel. In the present work, this mathematical model was adopted for studying the boriding kinetics of ASTM A36 steel. Likewise, the mass balance equation [5], describing the evolution of displacement of growing interface with respect to the time, is given by

$$\left(C_{up}^{Fe_2B} + C_{low}^{Fe_2B} - \frac{2C_0}{2}\right)\left.\frac{dx}{dt_v}\right|_{x=v} = -D_{Fe_2B}\left.\frac{\partial C_{Fe_2B}(x,t_v)}{\partial x}\right|_{x=v}. \quad (20)$$

The linear boron concentration profile [5], through the Fe_2B layer, is given by the solution of Fick's second law with time dependent $(\partial C_{Fe_2B}(x,t_v)/\partial t_v = D_{Fe_2B}\partial^2 C_{Fe_2B}(x,t_v)/\partial x^2 \longrightarrow$ non-steady state) and is deduced as follows:

$$C_{Fe_2B}(x,t_v) = C_{up}^{Fe_2B} + \frac{\left(C_{low}^{Fe_2B} - C_{up}^{Fe_2B}\right)}{\text{erf}\left(v/2\sqrt{D_{Fe_2B} t_v}\right)} \text{erf}\left(\frac{x}{2\sqrt{D_{Fe_2B} t_v}}\right). \quad (21)$$

By substituting equations (21) into (20), the following equation is obtained:

$$\left(\frac{C_{up}^{Fe_2B}+C_{low}^{Fe_2B}-2C_0}{2}\right)\frac{dv}{dt_v}=\sqrt{\frac{D_{Fe_2B}}{\pi t_v}}\;\frac{C_{up}^{Fe_2B}-C_{low}^{Fe_2B}}{\operatorname{erf}\left(v/2\sqrt{D_{Fe_2B}t_v}\right)}\cdot\exp\left(-\frac{v^2}{4D_{Fe_2B}t_v}\right),\tag{22}$$

Substituting the expression of the parabolic growth law obtained from equation (16) ($v=(2k_{Fe_2B}t_v)^{1/2}$) into equation (22), we have

$$\left(\frac{C_{up}^{Fe_2B}+C_{low}^{Fe_2B}-2C_0}{4}\right)\left(2k_{Fe_2B}\right)^{1/2}=\sqrt{\frac{D_{Fe_2B}}{\pi}}\cdot\frac{C_{up}^{Fe_2B}-C_{low}^{Fe_2B}}{\operatorname{erf}\left(\sqrt{k_{Fe_2B}/2D_{Fe_2B}}\right)}\exp\left(-\frac{k_{Fe_2B}}{2D_{Fe_2B}}\right).\tag{23}$$

The diffusion coefficient (D_{Fe_2B}) can be estimated numerically from equation (23) by the Newton–Raphson method. An illustrative representation of the parabolic growth law of Fe_2B layer thickness ($v^2=2k_{Fe_2B}t=2k_{Fe_2B}(t_v+t_0^{Fe_2B})$) is represented in Figure 1. In addition, $t_v(=t-t_0^{Fe_2B})$ is the effective growth time of the Fe_2B layer and t is the boriding time [3, 5].

3. Materials and Methods

3.1. Powder-Pack Boriding Process. ASTM A36 steel was used for investigation. It had a nominal chemical composition of 0.25–0.29% C, 0.20–0.28% Si, 0.85–1.35% Mn, 0.15–0.20% Cu, 0.035–0.040% P, and 0.050% S. The steel samples were sectioned into small cubes with the following dimensions: 10 mm × 10 mm × 10 mm. Prior to the boriding process, the steel samples were grinded with SiC abrasive paper up to grit 2500 and cleaned using a multistage ultrasonic bath with n-heptane and ethanol for 20 min. The mean hardness of the substrate was 170 HV. The ASTM A36 steel samples were immersed in a closed cylindrical case made of AISI 316L steel as shown in Figure 2, using Ekabor 2 as a boron-rich mixture.

The thermochemical process was carried out in a conventional furnace model Nabertherm N 250/85 HA (this type of furnace is gas-tight; it is equipped with direct heating depending on the temperature. It is excellent for maintaining an atmosphere defined by an inert gas), maintaining a pure argon atmosphere, to eliminate the oxidation of the boron released in the chemical reaction of the boriding medium [1]. The thermochemical treatment was carried out at boriding temperatures of 1123, 1173, 1223, and 1273 K for a variable time (2, 4, 6, and 8 h). The treatment temperatures were selected according to the Fe-B phase diagram.

3.2. Microscopical Observations of Boride Layers. The hardened samples were sectioned and prepared metallographically (the samples were polished using a diamond suspension with a particle size of 6 μm, finishing with a particle size of 3 μm), using a GX51 Olympus equipment. Likewise, the borided samples were analyzed through scanning electron microscope. The equipment used was the Quanta 3D FEG-FEI JSM7800-JOEL. Figure 3 shows the cross sections of Fe_2B layers formed on the surfaces of ASTM A36 steel at different exposure times (2, 4, 6, and 8 h) and for 1173 K of boriding temperature. The mechanical properties of borided alloys depend on the composition and structure of the boride layer. The images obtained from the scanning electron microscope (Figure 3) present a sawtooth morphology; this characteristic is typical of ARMCO pure iron, and low and medium carbon steels [24, 36].

When the alloying elements and/or the carbon content of the steel increases, the layer thickness tends to favor the formation of iron borides with flat growth fronts. The alloying elements have obvious effects on the formation of the layer thickness, restricted diffusion of the boron atoms, thus forming a diffusion barrier. Because of the diffusion of boron atoms, there is a segregation of the alloying elements from the surface to the (Fe_2B/substrate) interface. Some alloying elements tend to form compounds with the boron atoms and others cannot interact with them. Boron has some weird and wonderful chemistry. The alloying elements cannot form compounds and tend to concentrate at the tips of boride columns, decreasing the layer thickness [36].

Figure 3 shows that the boride layer thickness increases with respect to the boriding time for a predetermined temperature. For simulating the growth kinetics of the Fe_2B layer grown on ASTM A36 steel, an average measurement of the boride layer thickness was made, where the longest tips of the sawtooth morphology were taken into account (see Figure 4), and the software used was MSQ Materials Analysis. Fifty measurements were collected from the boride surface to the longest tips of boride columns of the borided ASTM A36 steel, as plotted in Figure 4 [3, 5]. The identification of phases formed on the surface of the borided sample was conducted through the X-ray diffraction technique (XRD). The equipment used for the study was an INEL EQUINOX 2000 X-ray diffractometer, using CoK_α radiation of 0.179 nm wavelength, operated at 30 mA and 20 kV.

Likewise, Match version 3.3 was the software for phase identification. In addition, the elemental distribution of the transition elements within the cross section of boride layer was determined by using scanning electron microscopy-energy dispersive X-ray spectroscopy (SEM-EDS). The equipment used for the study was a Quanta™ 3D FEG scanning electron microscope, with an accelerating voltage of 200 V–30 kV and a magnification of 30 X–1280 kX in "quad" mode.

4. Results and Discussion

4.1. SEM Observations and EDS Analysis. The metallography of coating/substrate formed in ASTM A36 borided steel at different exposure times (2, 4, 6, and 8 h) and for 1123 K of boriding temperature is shown in Figure 5.

The EDS analysis obtained by SEM is shown in Figures 5(a) and 5(b). The results show in Figure 5(a) that the manganese (Mn) negatively affects the boride layer thickness

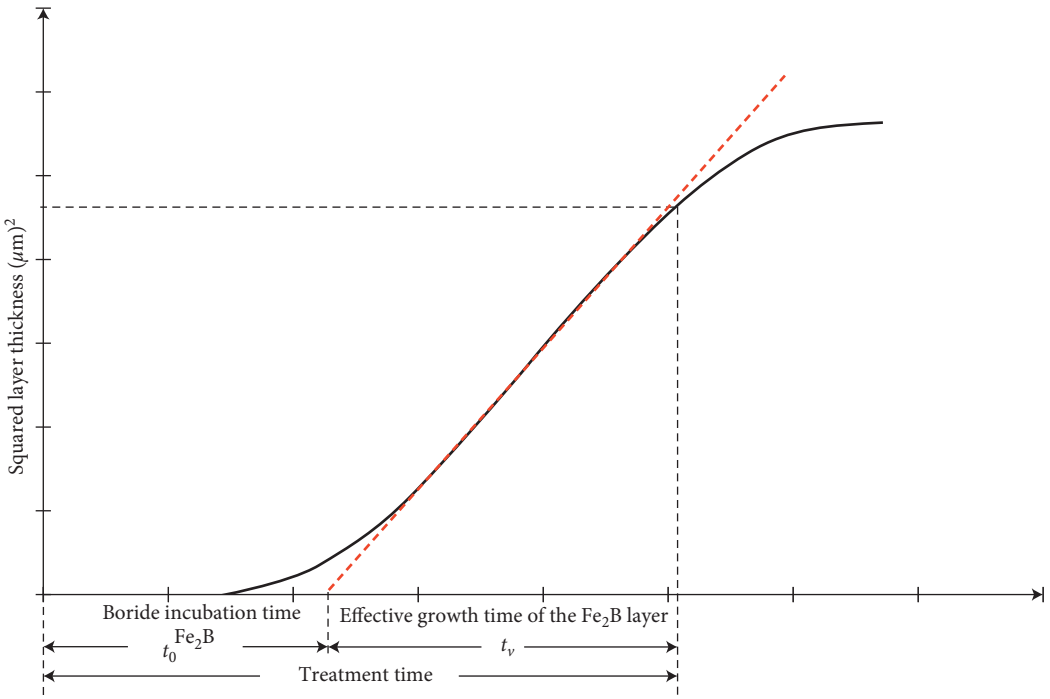

Figure 1: A schematic diagram of the parabolic growth law of Fe_2B layer thickness against boriding time [3, 5].

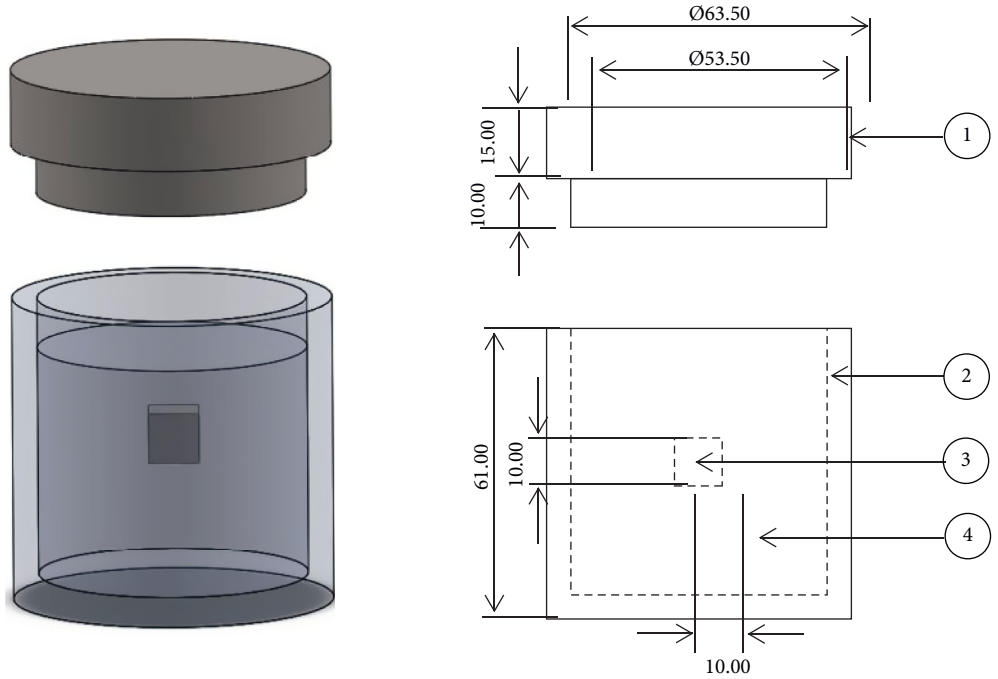

Figure 2: Schematic view of the stainless steel AISI 316L container for the pack-powder boriding treatment (1: lid; 2: powder boriding medium ($B_4C + KBF_4 + SiC$); 3: sample; 4: container) (millimeter scale) [29, 32].

and morphology. Likewise, as can be seen in Figure 5(b), carbon (C) and silicon (Si) do not dissolve and diffusive through the boride layer. During the boriding process, carbon is transmitted from the boride surface to the matrix and forms, together with boron, borocementite $Fe_3(B, C)$ (or, more appropriately, $Fe_3(B_{0.67}C_{0.33})$) [21, 32]. In addition to carbon, silicon is also not soluble in the boride layer. This element is expelled from the surface by boron atoms to the growth interface (Fe_2B/substrate), forming iron-silicoborates ($FeSi_{0.4}B_{0.6}$ and Fe_5SiB_2) [37].

4.2. X-Ray Diffraction Analysis. Figure 6 shows the diffractogram recorded on the surface of the borided ASTM

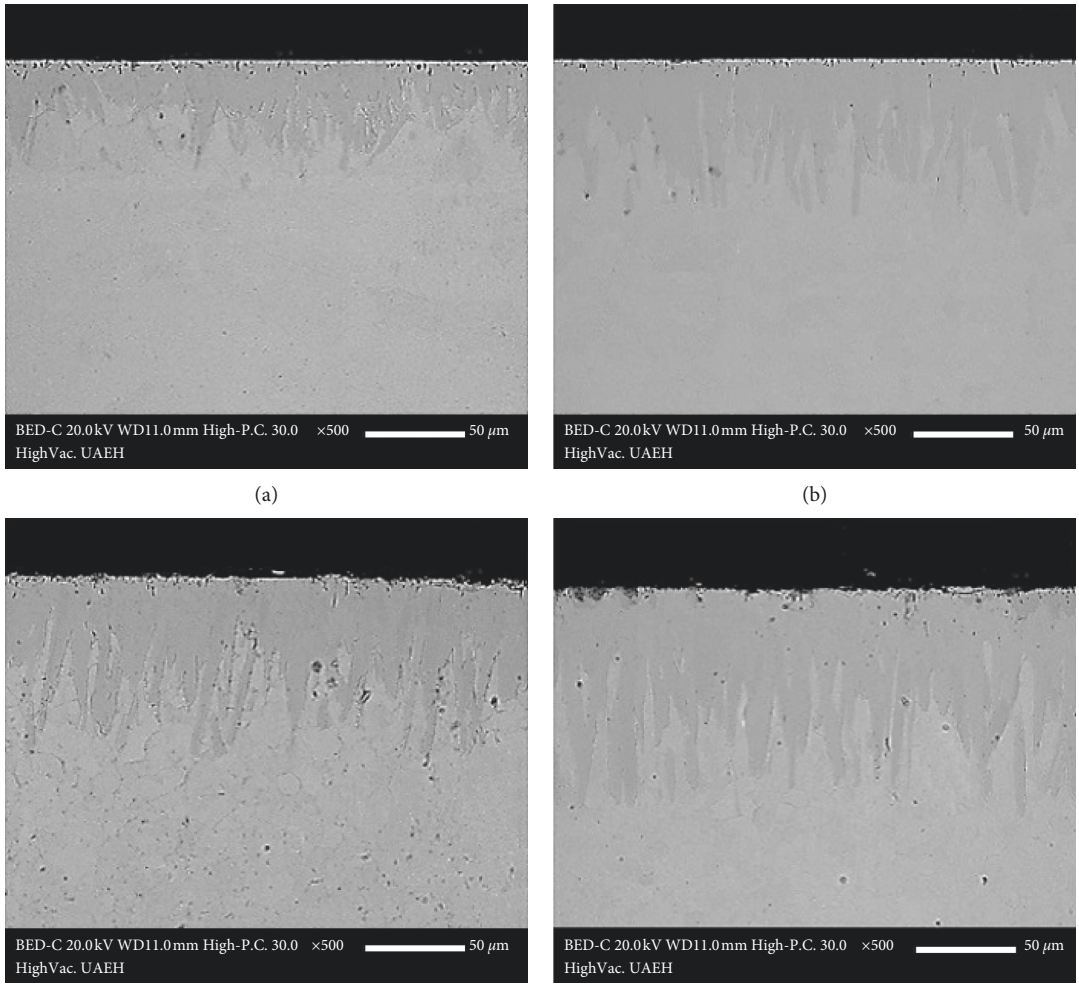

Figure 3: SEM micrographs of the cross sections of ASTM A36 steel samples borided at 1123 K during different exposure times: (a) 2 h, (b) 4 h, (c) 6 h, and (d) 8 h.

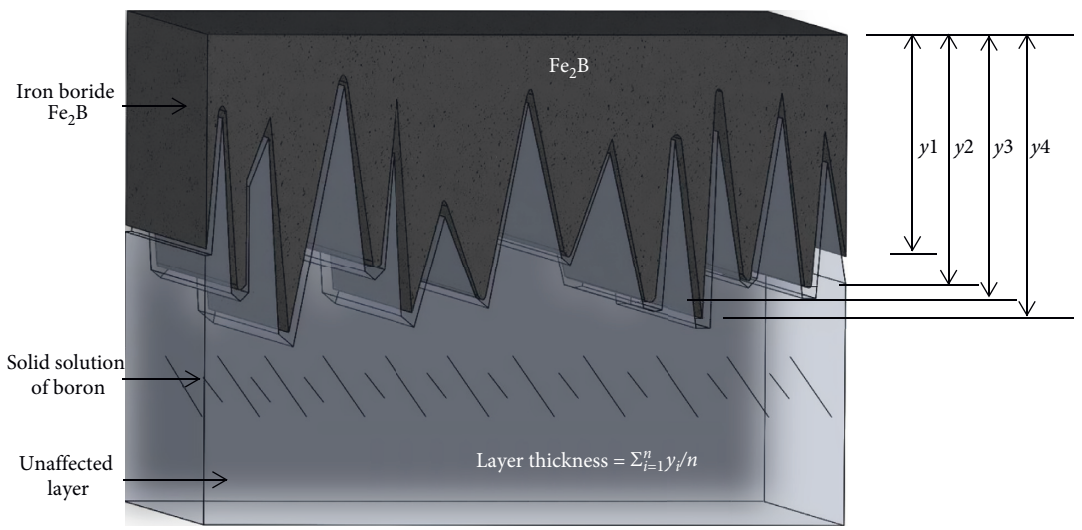

Figure 4: A schematic diagram illustrating the procedure for estimation of boride layer thickness in ASTM A36 steel [3, 5].

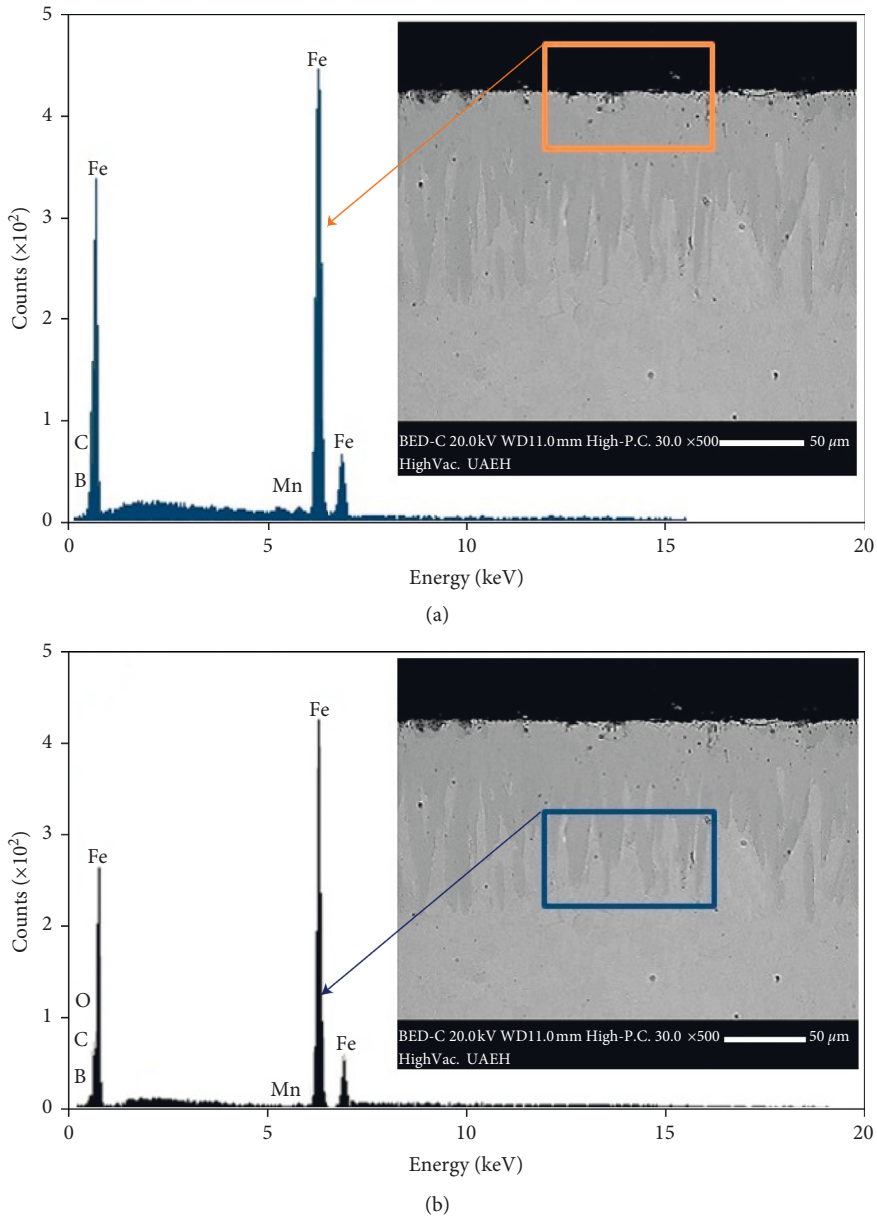

Figure 5: SEM micrograph of the cross sections of the borided ASTM A36 steel micrograph image of microstructure of the ASTM A36 boride layer obtained at 1123 K with exposure time of 8 h (a) and (b) EDS analysis on cross section of the borided sample.

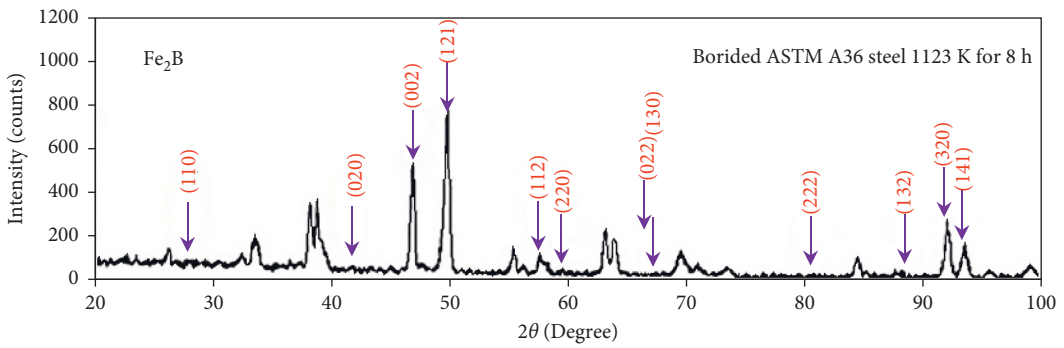

Figure 6: XRD patterns obtained at the surface of the borided ASTM A36. The boriding temperature of 1123 K for 8 h of treatment.

A36 steel at a temperature of 1123 K for a treatment time of 8 h. The X-ray diffraction patters (see Figure 6) show the intensity of X-rays scattered at different angles by a borided sample, where the presence of the Fe_2B phase is confirmed.

4.3. First Approach: Estimation of Boron Activation Energy with Steady-State Model. To study the growth kinetic of Fe_2B on ASTM A36 steel, a simple diffusion model inspired from the mass balance equation at the (Fe_2B/substrate) interface and the solution of Fick's second law under steady-state condition for one-dimensional analysis was applied [3, 6, 7, 16–18, 20–22, 24–26, 30]. The Fe_2B layer thickness (v) obeys the parabolic growth law given by equation (16), with the presence of boride incubation time ($t_0^{Fe_2B} \approx 30$ min after transferring the sample to the furnace) associated with the formation of the Fe_2B layer. Figure 7 displays the time dependent of the squared value of Fe_2B layer thickness for different temperatures, the slopes of each of the straight lines supply the values of the parabolic growth constants ($=2k_{Fe_2B}$).

Table 1 summarizes the experimental values of parabolic growth constants at the (Fe_2B/substrate) interface in the temperature range of 1123–1273 K with the associated boride incubation time. Also, the plots presented in Figure 7 demonstrate a diffusion-controlled process (Brackman et al. [21]).

The value of activation energy (is the energy required for a reaction to proceed) for boron diffusion in Fe_2B ($Q_{Fe_2B} = 161.00061\ \text{kJ·mol}^{-1}$) and preexponential factor ($D_0 = 1.361592 \times 10^{-3}\ \text{m}^2/\text{s}$) can be calculated after a linear fitting of these data according to Arrhenius relationship from the slope and interception of the straight line, respectively, shown in coordinate system (see equation (24)): $\ln D_{Fe_2B}$ vs $1/T$, it is displayed in Figure 8:

$$D_{Fe_2B} = 1.361592 \times 10^{-3} \exp\left(\frac{-161.00061\ \text{kJ·mol}^{-1}}{RT}\right) \quad \left[\text{m}^2\text{s}^{-1}\right], \tag{24}$$

with $R = 8.314\ \text{Jmol}^{-1}\text{K}^{-1}$ and T the absolute temperature in Kelvin.

4.4. Second Approach: Estimation of Boron Activation Energy with Non-Steady-State Diffusion Model. The values of the growth constants ($2k_{Fe_2B}$) at each temperature reported in Table 1 are also used in the second approach and in Table 2, the values of the boron diffusion coefficients (D_{Fe_2B}) for Fe_2B are gathered, which were calculated by the Newton–Raphson method using equation (23).

In Figure 9, the $\ln D_{Fe_2B}$ vs $1/T$ is plotted, the values of activation energy and pre exponential factor for boron diffusion in Fe_2B from the second approach were $Q_{Fe_2B} = 160.\ 9922\ \text{kJ·mol}^{-1}$ and $D_0 = 1.35914 \times 10^{-3}\ \text{m}^2/\text{s}$, respectively. Equation (25) was deducted from a fitting of data according to the Arrhenius relationship with the coefficient of determination close to unity.

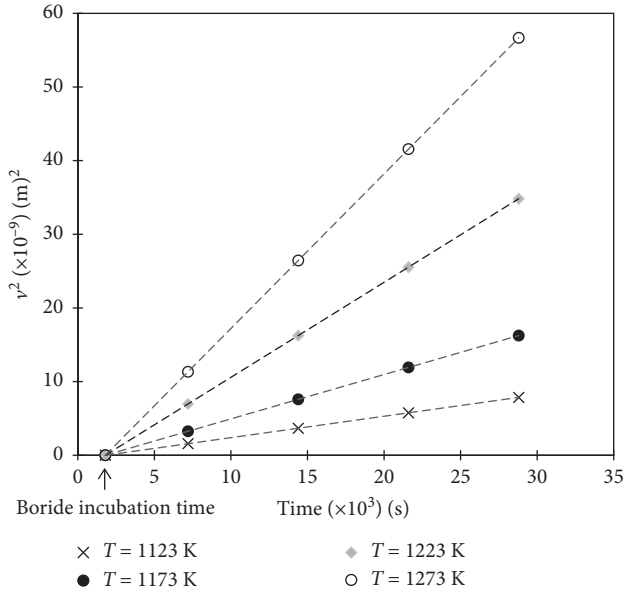

Figure 7: Averaged squares of the boride layers (v^2) vs. boriding time (t) at increasing temperatures.

$$D_{Fe_2B} = 1.35914 \times 10^{-3} \exp\left(\frac{-160.9922\ \text{kJ·mol}^{-1}}{RT}\right) \quad \left[\text{m}^2\text{s}^{-1}\right], \tag{25}$$

with $R = 8.314\ \text{Jmol}^{-1}\text{K}^{-1}$ and T the absolute temperature in Kelvin.

4.5. The Two Diffusion Models. This section describes the differences between the two diffusion models that have been used to compute the growth kinetics of boride layers. It is noticed that the estimated values of boron activation energy ($Q_{Fe_2B} \approx 161\ \text{kJ·mol}^{-1}$) for ASTM A36 steel from the first approach (see equation (24)) and the second approach (see equation (25)) is approximately the same value for both diffusion models. Likewise, in the estimated values of pre exponential factor from the first approach ($D_0 = 1.361592 \times 10^{-3}\ \text{m}^2/\text{s}$) and the second approach ($D_0 = 1.35914 \times 10^{-3}\ \text{m}^2/\text{s}$), there is a small variation. To find out how this similarity is possible in the diffusion coefficients obtained by two different models, we first focus our attention on equation (23). The error function erf ($\sqrt{k_{Fe_2B}/2D_{Fe_2B}}$) is a monotonically increasing function of $\sqrt{k_{Fe_2B}/2D_{Fe_2B}}$. Its Maclaurin series (for small $\sqrt{k_{Fe_2B}/2D_{Fe_2B}}$) is given by [38, 39]:

$$\text{erf}\left(\sqrt{\frac{k_{Fe_2B}}{2D_{Fe_2B}}}\right) = \frac{2}{\sqrt{\pi}}\left(\sqrt{\frac{k_{Fe_2B}}{2D_{Fe_2B}}} - \frac{\left(k_{Fe_2B}/2D_{Fe_2B}\right)^3}{3 \cdot 1!} + \frac{\left(\sqrt{k_{Fe_2B}/2D_{Fe_2B}}\right)^5}{5 \cdot 2!} - \cdots\right). \tag{26}$$

According to the numerical value of the $\sqrt{k_{Fe_2B}/2D_{Fe_2B}}$, equation (26) can be rewritten as

Table 1: Experimental values of parabolic growth constants at the (Fe_2B/substrate) interface in the range of 1123–1273 K and estimated values of boron diffusion coefficients in the Fe_2B layers by using the first approach.

Temperature (K)	Type of layer	Growth constants $2k_{Fe_2B}$ (m^2s^{-1})	$D_{Fe_2B} = (1/2)(C_{up}^{Fe_2B} + C_{low}^{Fe_2B} - 2C_0/C_{up}^{Fe_2B} - C_{low}^{Fe_2B})$ k_{Fe_2B} equation (19) (m^2s^{-1})
1123	Fe_2B	2.810×10^{-1}	4.28×10^{-11}
1173		6.120×10^{-1}	9.32×10^{-11}
1223		12.80×10^{-1}	1.95×10^{-10}
1273		20.89×10^{-1}	3.18×10^{-10}

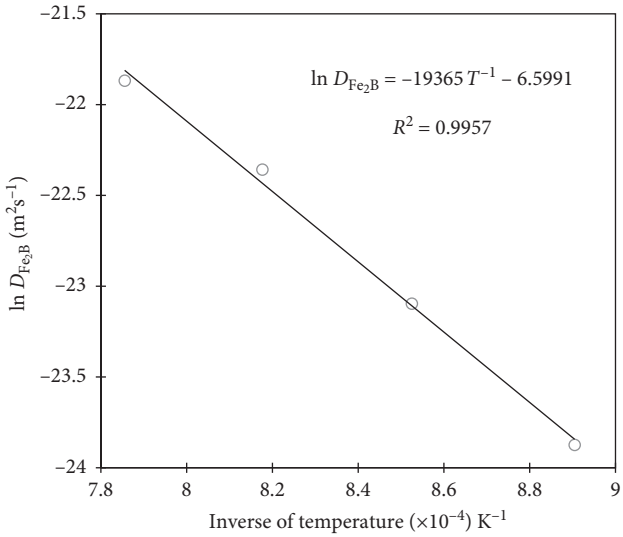

Figure 8: Arrhenius relationship for the boron diffusion coefficient (D_{Fe_2B}) from the first approach in the Fe_2B layer.

Table 2: Estimated values of boron diffusion coefficients in the Fe_2B layer using the second approach (non-steady-state diffusion model).

Temperature (K)	Type of layer	$(C_{up}^{Fe_2B} + C_{low}^{Fe_2B} - 2C_0/4)(2k_{Fe_2B})^{1/2} = \sqrt{D_{Fe_2B}/\pi}\,(C_{up}^{Fe_2B} - C_{low}^{Fe_2B}/\mathrm{erf}(\sqrt{k_{Fe_2B}/2D_{Fe_2B}}))\exp(-k_{Fe_2B}/2D_{Fe_2B})$ equation (23) (m^2s^{-1})
1123	Fe_2B	4.28076×10^{-11}
1173		9.3056×10^{-11}
1223		1.9467×10^{-10}
1273		3.1822×10^{-10}

$$\mathrm{erf}\left(\sqrt{\frac{k_{Fe_2B}}{2D_{Fe_2B}}}\right) = 2\sqrt{\frac{k_{Fe_2B}}{2D_{Fe_2B}}\pi}. \tag{27}$$

Similarly for the real exponential function $\exp(-k_{Fe_2B}/2D_{Fe_2B})$: $\mathbb{R} \longrightarrow \mathbb{R}$ can be characterized in a variety of equivalent ways. Most commonly, it is defined by the following power series [38, 39]:

$$\exp\left(-\frac{k_{Fe_2B}}{2D_{Fe_2B}}\right) = \frac{\left(1 - \left(k_{Fe_2B}/2D_{Fe_2B}\right)\right) + \left(-k_{Fe_2B}/2D_{Fe_2B}\right)^2}{2!} + \frac{\left(-k_{Fe_2B}/2D_{Fe_2B}\right)^3}{3!} + \cdots. \tag{28}$$

Thus, equation (28) can be modified in the following manner:

$$\exp\left(-\frac{k_{Fe_2B}}{2D_{Fe_2B}}\right) = 1. \tag{29}$$

By substituting Equations (27) and (29) into equation (23), we have

$$\left(\frac{C_{up}^{Fe_2B} + C_{low}^{Fe_2B} - 2C_0}{4}\right)\left(2k_{Fe_2B}\right)^{1/2} = \sqrt{\frac{D_{Fe_2B}}{\pi}}\,\frac{C_{up}^{Fe_2B} - C_{low}^{Fe_2B}}{2\sqrt{k_{Fe_2B}/2D_{Fe_2B}\pi}}\,(1), \tag{30}$$

where

$$D_{Fe_2B} = \frac{1}{2}\left(\frac{C_{up}^{Fe_2B} + C_{low}^{Fe_2B} - 2C_0}{C_{up}^{Fe_2B} - C_{low}^{Fe_2B}}\right)k_{Fe_2B}. \tag{31}$$

The result obtained by equation (31) is the same as that obtained in equation (19) estimated by a steady-state

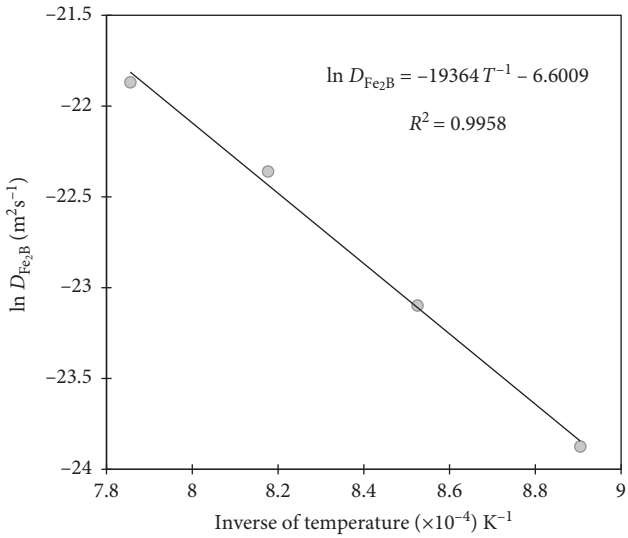

Figure 9: Arrhenius relationship for the boron diffusion coefficient (D_{Fe_2B}) from the second approach in the Fe_2B layer (non-steady-state diffusion model).

Table 3: Reported values of activation energies for boron diffusion in ASTM A36 steel with other borided Armco iron and steels.

Material	Boriding method	Boron activation energy (kJ·mol^{-1})	Temperature range (°C)	Method of calculation	References
Armco iron	Gaseous	73.08 (FeB) 120.65 (Fe_2B)	800–1000	Diffusion model	[7]
Armco iron	Powder	157.5	850–1000	Diffusion model	[27]
AISI M2 steel	Paste	257.5 (FeB) 210.0 (Fe_2B)	920–1000	Diffusion model	[6]
AISI 1018 steel	Electrochemical	172.75 ± 8.6	850–1000	Parabolic growth law	[40]
AISI 1026 steel	Powder	178.4	850–1000	Diffusion model	[3]
AISI 1045 steel	Powder	180.0	850–1000	Diffusion model	[5]
AISI 8620	Plasma paste boriding	124.7–138.5	700–800	Parabolic growth law	[41]
AISI 4340 steel	Salt bath	234.0	800–1000	Parabolic growth law	[42]
AISI D2 steel	Salt bath	170.0	800–1000	Parabolic growth law	[42]
AISI 1018 steel	Powder	159.3 (Fe_2B)	850–1000	Diffusion model	[31]
AISI D2 steel	Powder	201.5 (Fe_2B)	850–1000	Diffusion model	[33]
AISI P20 steel	Powder	200 (FeB + Fe_2B)	800–950	Parabolic growth law	[43]
ASTM A36 steel	Powder	161.00 (Fe_2B)	850–1000	Diffusion models	This work

diffusion model. The result from equation (19) would appear to imply that the non-steady-state diffusion model is superior to the steady-state diffusion model and so should always be used. However, in many interesting cases, the models are equivalent as in this case.

Table 3 presents the values of activation energies for boron diffusion in some different alloys and Armco iron along with the estimated value of boron activation energy in ASTM A36 steel. From Table 3, it is seen that the estimated value of activation energy in ASTM A36 steel is consistent with the literature data [3, 5–7, 27, 31, 33, 40–43].

4.6. Experimental Validation of the Kinetic Models. The suggested models were validated by comparing the experimental value of Fe_2B layers' thickness with the theoretical result. By substituting equation (19) into (16), we have

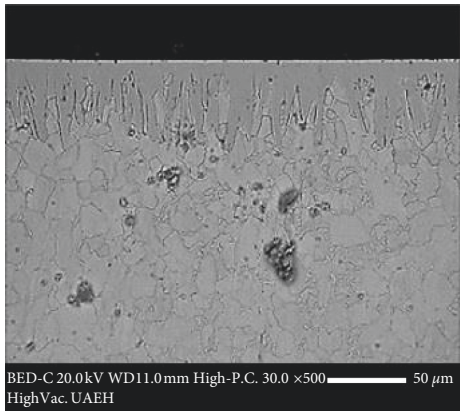

Figure 10: Scanning electron microscopy (SEM) image of the microstructure of boride layer (Fe_2B) formed on the ASTM A36 steel during powder pack at 1123 K with an exposure time of 2.5 h.

Table 4: Estimated value of ASTM A36 boride layer thickness (ν) obtained at the 1123 K of boriding temperature with an exposure time of 2.5 h.

Temperature (K)	Type of layer	Boride layer thicknesses (μm) estimated by equation (32)	Experimental boride layer thickness (μm) for an exposure time of 2.5 h
1123	Fe_2B	Exposure time of 2.5 h $\nu = 46.081\ \mu$m	$\nu = 42.066 \pm 6.9947\ \mu$m

$$\nu = \sqrt{4D_{Fe_2B}\left(\frac{C_{up}^{Fe_2B} - C_{low}^{Fe_2B}}{C_{up}^{Fe_2B} + C_{low}^{Fe_2B} - 2C_0}\right)\left(t - t_0^{Fe_2B}\right)}. \quad (32)$$

Figure 10 shows the SEM micrographs of the cross sections of borided ASTM A36 steels at 1123 K for 2.5 h. Table 4, presents the values of the theoretical result of Fe_2B layers' thickness with the experimental data. A good concordance was the observed value between the experimental result and the simulated value for the given boriding condition.

5. Conclusions

In this work, the ASTM A36 steel was pack-borided in the temperature range of 1123–1273 K for a variable exposure time ranging between 2 and 8 h. The kinetics data on treated ASTM A36 steel by the powder-pack boriding were used to estimate the value of activation energy for boron diffusion in the boride layer (Fe_2B) by means of two different mathematical approaches. In the first approach, the mass balance equation was formulated by assuming a linear boron concentration profile in the boride layer ($C_{Fe_2B}(x) = c_1x + c_2$) for an upper boron content in Fe_2B of 60×10^3 mol·m^{-3}. The second approach was based on the same mathematical principles as the first approach for one-dimensional analysis under non-steady-state condition by assuming the solution of Fick's second law of diffusion when the bulk concentration is greater than the surface concentration ($C_{Fe_2B}(x, t_\nu) = A + B\,\mathrm{erf}\,(x/2(D_{Fe_2B}t_\nu)^{1/2})$), was successfully applied to the boriding kinetics of ASTM A36 steel by considering the effect of boride incubation time. As a main result, the estimated value of activation energy for boron diffusion in the Fe_2B layer by the two approaches was estimated as 161 kJ·mol^{-1}. In a future prospect, these diffusion approaches are in general not identical, both are equivalent models, and this fact can be used as a tool to select optimum values of layers' thicknesses for practical utilization of any borided steels to produce boride layers with sufficient thicknesses that meet the requirements during service life.

Data Availability

The data used to support the findings of this study are available from the corresponding author upon request.

Conflicts of Interest

The authors declare that there is no conflict of interests regarding the publication of this paper.

Acknowledgments

The work described in this paper was supported by a grant of National Council of Science and Technology (CONACyT) and PRODEP México. Also, the authors want to thank Dr. Jorge Zuno Silva, who is a research professor and principal at Escuela Superior de Ciudad Sahagún-UAEH. Likewise, the authors would like to thank Dr. José Solís Romero for his helpful advice on various technical issues examined in this manuscript and Dr. Adrian Leyland for his advice and comments.

References

[1] M. Graf von Matuschka, *Boronizing*, Carl Hanser Verlag, Munich, Germany, 1st edition, 1980.

[2] J. R. Davis, *Surface Hardening of Steels Understanding the Basics*, pp. 213–223, ASM International, Novelty, OH, USA, 2002.

[3] M. A. Flores-Rentería, M. Ortiz-Domínguez, M. Keddam et al., "A simple kinetic model for the growth of Fe_2B layers on AISI 1026 steel during the powder-pack boriding," *High Temperature Materials and Processes*, vol. 34, no. 1, pp. 1–11, 2015.

[4] R. Kara, F. Çolak, and Y. Kayali, "Investigation of wear and adhesion behaviors of borided steels," *Transactions of the Indian Institute of Metals*, vol. 69, no. 6, pp. 1169–1177, 2016.

[5] J. Zuno-Silva, M. Ortiz-Domínguez, M. Keddam et al., "Boriding kinetics of Fe_2B layers formed on AISI 1045 steel," *Journal of Mining and Metallurgy, Section B: Metallurgy*, vol. 50, no. 2, pp. 101–107, 2014.

[6] I. Campos, G. Ramírez, U. Figueroa, J. Martínez, and O. Morales, "Evaluation of boron mobility on the phases FeB, Fe_2B and diffusion zone in AISI 1045 and M2 steels," *Applied Surface Science*, vol. 253, no. 7, pp. 3469–3475, 2007.

[7] M. Keddam, M. Kulka, N. Makuch, A. Pertek, and L. Małdziński, "A kinetic model for estimating the boron activation energies in the FeB and Fe_2B layers during the gas-boriding of Armco iron: effect of boride incubation times," *Applied Surface Science*, vol. 298, pp. 155–163, 2014.

[8] E. R. Cabeo, G. Laudien, S. Biemer, K. T. Rie, and S. Hoppe, "Plasma-assisted boriding of industrial components in a pulsed D. C. glow discharge," *Surface and Coatings Technology*, vol. 116–119, pp. 229–233, 1999.

[9] M. Keddam, R. Chegroune, M. Kulka et al., "Characterization, tribological and mechanical properties of plasma paste borided AISI 316 steel," *Transactions of the Indian Institute of Metals*, vol. 71, no. 1, pp. 79–90, 2018.

[10] M. Kulka, N. Makuch, and A. Pertek, "Microstructure and properties of laser-borided 41Cr4 steel," *Optics & Laser Technology*, vol. 45, pp. 308–318, 2013.

[11] B. Mebarek, M. Keddam, and M. Aboshighiba, "LS-SVM approach for modeling the growthe kinetics of FeB and Fe_2B layers formed on Armco iron," *Ingénierie des Systèmes d'Information*, vol. 23, no. 5, pp. 29–41, 2018.

[12] I. Campos, M. Islas, E. González, P. Ponce, and G. Ramírez, "Use of fuzzy logic for modeling the growth of Fe_2B boride layers during boronizing," *Surface and Coatings Technology*, vol. 201, no. 6, pp. 2717–2723, 2006.

[13] K. Rayane and O. Allaoui, "Application of Artificial Neural Network for prediction of boride layer depth obtained on XC38 steel in molten salts," *Defect and Diffusion Forum*, vol. 365, pp. 194–199, 2015.

[14] I. Campos, M. Islas, G. Ramírez, C. VillaVelázquez, and C. Mota, "Growth kinetics of borided layers: artificial neural network and least square approaches," *Applied Surface Science*, vol. 253, no. 14, pp. 6226–6231, 2007.

[15] R. D. Ramdan, T. Takaki, K. Yashiro, and Y. Tomita, "The effects of structure orientation on the growth of Fe," *Materials Transactions*, vol. 51, no. 1, pp. 62–67, 2010.

[16] M. A. Doñu, N. López-Perrusquia, D. Sánchez-Huerta et al., "Growth kinetics of boride coatings formed at the surface AISI M2 during dehydrated paste pack boriding," *Thin Solid Films*, vol. 596, pp. 147–154, 2015.

[17] M. Keddam and M. Kulka, "A kinetic model for the boriding kinetics of AISI D2 steel during the diffusion annealing process," *Protection of Metals and Physical Chemistry of Surfaces*, vol. 54, no. 2, pp. 282–290, 2018.

[18] M. Keddam and M. Kulka, "Simulation of the growth kinetics of FeB and Fe_2B layers on AISI D2 steel by the integral method," *Physics of Metals and Metallography*, vol. 119, no. 9, pp. 860–869, 2018.

[19] V. I. Dybkov, L. V. Goncharuk, V. G. Khoruzha, K. A. Meleshevich, A. V. Samelyuk, and V. R. Sidorko, "Diffusional growth kinetics of boride layers on iron-chromium alloys," *Solid State Phenomena*, vol. 138, pp. 181–188, 2008.

[20] M. Kulka, N. Makuch, A. Pertek, and L. Maldzinski, "Simulation of the growth kinetics of boride layers formed on Fe during gas boriding in H_2-BCl_3 atmosphere," *Journal of Solid State Chemistry*, vol. 199, pp. 196–203, 2013.

[21] C. M. Brakman, A. W. J. Gommers, and E. J. Mittemeijer, "Boriding Fe and Fe-C, Fe-Cr, and Fe-Ni alloys; Boride-layer growth kinetics," *Journal of Materials Research*, vol. 4, no. 6, pp. 1354–1370, 1989.

[22] L. G. Yu, X. J. Chen, K. A. Khor, and G. Sundararajan, "FeB/Fe_2B phase transformation during SPS pack-boriding: boride layer growth kinetics," *Acta Materialia*, vol. 53, no. 8, pp. 2361–2368, 2005.

[23] I. Campos-Silva, M. Ortiz-Domínguez, N. López-Perrusquia, A. Meneses-Amador, R. Escobar-Galindo, and J. Martínez–Trinidad, "Characterization of AISI 4140 borided steels," *Applied Surface Science*, vol. 256, no. 8, pp. 2372–2379, 2010.

[24] M. Ortiz-Domínguez, *Contribución de la Modelación Matemática en el Tratamiento Termoquímico de Borurización*, Ph.D. thesis, SEPI-ESIME from the Instituto Politécnico Nacional, Mexico, 2013.

[25] I. Campos-Silva, D. Bravo-Bárcenas, A. Meneses-Amador et al., "Growth kinetics and mechanical properties of boride layers formed at surface of the ASTM F–75 biomedical alloy," *Surface and Coatings Technology*, vol. 237, pp. 402–414, 2013.

[26] I. Campos-Silva, M. Ortiz-Domínguez, O. Bravo-Bárcenas et al., "Formation and kinetics of FeB/Fe_2B layers and diffusion zone at the surface of AISI 316 borided steels," *Surface and Coatings Technology*, vol. 205, pp. 403–412, 2010.

[27] M. Elias-Espinosa, M. Ortiz-Domínguez, M. Keddam et al., "Growth kinetics of the Fe_2B layers and adhesion on Armco iron substrate," *Journal of Materials Engineering and Performance*, vol. 23, pp. 2943–2952, 2014.

[28] M. Ortiz-Domínguez, M. Keddam, M. Elias-Espinosa et al., "Investigation of boriding kinetics of AISI D2 steel," *Surface Engineering*, vol. 30, pp. 490–497, 2014.

[29] M. Ortiz-Domínguez, M. A. Flores-Rentería, M. Keddam et al., "Simulation of growth kinetics of Fe_2B layers formed on gray cast iron during the powder-pack boriding," *Materiali in Tehnologije/Materials and Technology*, vol. 48, no. 6, pp. 905–916, 2014.

[30] I. Campos-Silva, M. Ortiz-Domínguez, C. Tapia-Quintero, G. Rodriguez-Castro, M. Y. Jimenez-Reyes, and E. Chavez-Gutierrez, "Kinetics and boron diffusion in the FeB/Fe_2B layers formed at the surface of borided high-alloy steel," *Journal of Materials Engineering and Performance*, vol. 21, no. 8, pp. 1714–1723, 2012.

[31] M. Ortiz-Domínguez, J. Zuno-Silva, M. Keddam, O. Damián-Mejía, and M. Elias-Espinosa, "Diffusion model and characterisation of Fe_2B layers on AISI 1018 steel," *International Journal of Surface Science and Engineering*, vol. 9, no. 4, pp. 281–297, 2015.

[32] E. E. Vera-Cárdenas, R. Lewis, A. I. Martínez-Pérez et al., "Characterization and wear performance of boride phases over tool steel substrates," *Advances in Mechanical Engineering*, vol. 8, no. 2, pp. 1–10, 2016.

[33] M. Ortiz-Domínguez, M. Elias-Espinosa, M. Keddam et al., "Growth kinetics and mechanical properties of Fe_2B layers formed on AISI D2 steel," *Indian Journal of Engineering and Materials Science*, vol. 22, no. 2, pp. 231–243, 2015.

[34] T. B. Massalski, *Binary Alloy Phase Diagrams*, p. 280, ASM International, Materials Park, OH, USA, 1990.

[35] H. Okamoto, "B-Fe (Boron-Iron)," *Journal of Phase Equilibria and Diffusion*, vol. 25, pp. 297-298, 2004.

[36] G. Palombarini and M. Carbucicchio, "Growth of boride coatings on iron," *Journal of Materials Science Letter*, vol. 6, pp. 415-416, 1987.

[37] I. S. Dukarevich, M. V. Mozharov, and A. S. Shigarev, "Redistribution of elements in boride coatings," *Metal Sciencie and Heat Treatment*, vol. 15, no. 2, pp. 64–66, 1973.

[38] G. Ferraro, *The Rise and Development of the Theory of Series up to the Early 1820s*, pp. 147–149, Springer, Denmark, 2008.

[39] W. Rubin, *Real and Complex Analysis*, p. 1, McGraw-Hill, USA, 1987.

[40] G. Kartal, O. Eryilmaz, G. Krumdick, A. Erdemir, and S. Timur, "Kinetics of electrochemical boriding of low carbon steel," *Applied Surface Science*, vol. 257, no. 15, pp. 6928–6934, 2011.

[41] G. Ibrahim, T. Sukru, B. Cuma, Y. Yilmaz, U. Sukru, and K. Yusuf, "Investigation of diffusion kinetics of plasma paste borided AISI 8620 steel using a mixture of B_2O_3 paste and B_4C/SiC," *Sádhaná*, vol. 38, no. 3, pp. 513–526, 2013.

[42] S. Sen, U. Sen, and C. Bindal, "An approach to kinetic study of borided steels," *Surface and Coatings Technology*, vol. 191, no. 2-3, pp. 274–285, 2005.

[43] I. Uslu, H. Comert, M. Ipek, O. Ozdemir, and C. Bindal, "Evaluation of borides formed on AISI P20 steel," *Materials & Design*, vol. 28, no. 1, pp. 55–67, 2007.

Hindawi
Advances in Materials Science and Engineering
Volume 2019, Article ID 1670820, 20 pages
https://doi.org/10.1155/2019/1670820

Research Article

Study on the Formation Law of the Freezing Temperature Field of Freezing Shaft Sinking under the Action of Large-Flow-Rate Groundwater

Bin Wang, Chuan-xin Rong, Jian Lin, Hua Cheng, and Hai-bing Cai

School of Civil Engineering and Architecture, Anhui University of Science and Technology, Huainan, Anhui 232001, China

Correspondence should be addressed to Chuan-xin Rong; chxrong@aust.edu.cn

Received 9 November 2018; Revised 17 December 2018; Accepted 15 January 2019; Published 10 February 2019

Guest Editor: Shimin Liu

Taking into account moisture migration and heat change during the soil freezing process, as well as the influence of absolute porosity reduction on seepage during the freezing process, we construct a numerical model of hydrothermal coupling using laws of conservation of energy and mass. The model is verified by the results of large-scale laboratory tests. By applying the numerical calculation model to the formation of artificial shaft freezing temperature fields under the action of large-flow groundwater, we conclude that groundwater with flow rates of less than 5 m/d will not have a significant impact on the artificial freezing temperature field. The maximum flow rates that can be handled by single-row freezing pipes and double-row freezing pipes are 10 m/d and 20 m/d, respectively, during the process of freezing shaft sinking. By analyzing the variation of groundwater flow rate during freezing process, we find that the groundwater flow velocity can reach 5–7 times the initial flow velocity near the closure moment of the frozen wall. Finally, in light of the action characteristics of groundwater on the freezing temperature field, we make suggestions for optimal pipe and row spacing in freezing pipe arrangement.

1. Introduction

Artificial ground freezing is currently the main method for the construction of shafts in water-rich soft soil layers. This method involves the construction of one or more loops of freezing pipes around a shaft wellbore; through continuous heat exchange between the low-temperature refrigerant in the freezing pipe and the frozen soil, the circulation of fluids results in a frozen wall with a certain strength and good sealing performance, providing a stable environment for the construction of the wellbore [1–4]. However, the increase of the groundwater flow velocity in the soil layer when the traditional freezing pipe arrangement scheme is adopted can lead to increased closure times or even failure to close. This leads to large economic losses when soil excavation and the construction of the wellbore cannot be carried out as scheduled [5–7]. As a result, it is of great interest to study the formation law of the artificial shaft freezing temperature field under the action of groundwater with a large flow rate.

Our work builds on past research. Zhou et al. [8] studied the influence of seepage and pipe spacing on the closure time of saturated sand in the conventional brine freezing process and obtained the development law of temperature field in different regions using the double-pipe freezing orthogonal model test. Huang et al. [9] carried out a model test on a single freezing pipe under seepage conditions and found that the action of water flow resulted in different degrees of reduction in the frozen area upstream and downstream of the freezing pipe compared with nonseepage conditions. Lao et al. [10] obtained a mathematical model of a three-pipe freezing temperature field under the action of groundwater with different flow rates through model testing. Wang et al. [11] studied the effect of groundwater flow rates on the freezing temperature field under liquid nitrogen (−80°C) freezing conditions. The results showed that flowing water with a flow rate of 10 m/d or more had a significant influence on the liquid nitrogen freezing effect. Vitel et al. [12] designed a mathematical model of hydrothermal coupling

that was completely consistent with thermodynamic principles. A three-dimensional freezing test under high-permeability flow conditions provided a key parameter basis for the study of hydrothermal coupling in phase transitions of porous media. Anagnostou et al. [13] summarized previous scholars' models describing the formation of freezing temperature fields under the action of groundwater and designed new experimental devices on the basis of previous solutions to problems of freezing-cold volume loss. Large-scale model tests of artificial ground freezing under seepage conditions with flow rates of 0, 1, 1.5, 2.0, and 2.1 m/d were performed. The test results provide an important basis for the numerical calculation and engineering application of the freezing method.

The large similar model test has limitations. Most notably, it can only partially restore the development law of the freezing temperature field. However, numerical calculation can solve this problem. As a result, the numerical calculation has always been an important technical means to study the hydrothermal coupling problem.

Along these lines, Yang and Pi [14] established a mathematical model for the development of the frozen peak surface of a single frozen pipe under the action of groundwater using the theory of heat transport in porous media and Darcy's law and analyzed variations in the temperature field and groundwater flow field during the freezing process. Gao et al. [15] and Liu et al. [16] used the finite element method to study the evolution of temperature fields in vertical and horizontal tunnel freezing under the action of groundwater. Vitel et al. [12, 17, 18] constructed a hydrothermal numerical model consistent with thermodynamics to simulate the artificial ground freezing of saturated nondeformable porous media under seepage conditions. This numerical model has been well verified by the results of three-dimensional ground freezing experiments under high seepage velocity conditions. Alzoubi et al. [19, 20] conceived and developed a controlled laboratory scale AGF experimental rig and developed a three-dimensional conjugate mathematical and numerical model of the bayonet freeze pipes and porous ground structure using enthalpy-porosity method. The model was further validated against global heat balance and local temperature distributions from experiments at various operating conditions. This study provides an important reference for design and optimization of industrial AGF system. Lin et al. [21] addressed the difficult closure of a frozen wall in a coal Mine shaft due to excessive seepage velocity in an aquifer when the aquifer is penetrated via the artificial freezing method. Huang et al. [22–24] developed a hydrothermal coupling model to simulate the influence of water flow on the freezing process by considering the water/ice phase transition and combined the model with the Nelder–Mead simplex method based on the COMSOL Multiphysics platform. The position of the freezing pipes around the circular tunnel was optimized. Ahmed et al. [25] used the "ant colony algorithm" to optimize the layout of the freezing pipes under the action of low-flow groundwater, thereby shortening the closure time of the frozen wall and making the strength of the frozen wall more uniform. This method led to new ideas for the optimal design of the layout of freezing pipes.

By studying moisture migration and heat changes in the soil during the freezing process and considering the influence of the absolute porosity reduction on seepage during the freezing process, we construct a numerical calculation model for hydrothermal coupling based on the laws of conservation of energy and mass. Then, we verify the model using large-scale laboratory tests. Finally, we calculate and analyze the formation law of the artificial frozen wall temperature field under the action of large-flow groundwater and propose an optimal freezing pipe arrangement.

2. The Coupled Hydrothermal Model

2.1. Temperature Field Equation. In the porous medium, a control body is taken and simultaneously subjected to a seepage field and a temperature field. According to the conservation of energy,

$$Q_{\text{out}} + Q_{\text{in}} = \overline{Q}_{\text{s}} + \overline{Q}_{\text{i}} + \overline{Q}_{\text{l}} + Q_{\text{ph}}, \tag{1}$$

where Q_{out} and Q_{in} are the heat supplied to the control body by an external heat source and the heat generated by the heat source inside the control body, respectively; $\overline{Q}_{\text{s}}$, $\overline{Q}_{\text{i}}$, and $\overline{Q}_{\text{l}}$ are the heat that needs to be consumed to change the temperature of the solid skeleton, ice, and water, respectively; and Q_{ph} is the heat generated during the water-ice phase transition.

The heat from the external heat source flowing into the control unit per unit time is

$$Q_{\text{out}} = \int_{\Omega} -\nabla \vec{\mathbf{q}}\, d\Omega\ , \tag{2}$$

where $\vec{\mathbf{q}}$ is the heat flux density vector, which satisfies the Fourier heat transfer law

$$\vec{\mathbf{q}} = -\lambda_{\text{e}} \nabla T. \tag{3}$$

Regardless of the source influence inside the porous medium,

$$Q_{\text{in}} = 0. \tag{4}$$

The amounts of heat required to change the temperature of the solid skeleton and ice per unit time are expressed as

$$\overline{Q}_{\text{s}} = \int_{\Omega} (1-\phi)\rho_{\text{s}} C_{\text{s}} \frac{\partial T}{\partial t} d\Omega\ , \tag{5}$$

$$\overline{Q}_{\text{i}} = \int_{\Omega} \phi\,(1-w)\rho_{\text{i}} C_{\text{i}} \frac{\partial T}{\partial t}\, d\Omega. \tag{6}$$

Considering the convective heat transfer of water, the amount of heat required to change the temperature of water of per unit time is expressed as

$$\overline{Q}_{\text{l}} = \int_{\Omega} \phi w \rho_{\text{l}} C_{\text{l}} \frac{\partial T}{\partial t} + \rho_{\text{l}} C_{\text{l}} \vec{\mathbf{u}}\, (\nabla T)\, d\Omega, \tag{7}$$

where ϕ is the porosity of the porous media; w is the volumetric content of unfrozen water in the frozen soil; and $\vec{\mathbf{u}}$ is the relative velocity vector of the fluid; ρ and C are density and specific heat, respectively; and subscripts s, i, and l represent solid skeleton, ice, and water, respectively.

During the freezing process, when the temperature of the control body drops to the freezing point, the water in the control body is gradually converted into ice. During this process, the temperature remains just above freezing point, and no significant temperature change occurs. This is the water-ice phase transformation. Water will release latent heat continuously in the stage.

$$Q_{\mathrm{ph}} = \int_{\Omega} \rho_{\mathrm{l}} L \frac{\partial \theta_{\mathrm{l}}}{\partial t}\, d\Omega, \tag{8}$$

where θ_{l} is the content of liquid water and L is the latent heat of the water-ice phase transition.

Substituting equations (2)–(8) in equation (1), we obtain the differential equation of heat conduction for low-temperature porous media:

$$\int_{\Omega} (1-\phi)\rho_{\mathrm{s}} C_{\mathrm{s}} \frac{\partial T}{\partial t} + \phi(1-w)\rho_{\mathrm{i}} C_{\mathrm{i}} \frac{\partial T}{\partial t} + \phi w \rho_{\mathrm{l}} C_{\mathrm{l}} \frac{\partial T}{\partial t} + \rho_{\mathrm{l}} C_{\mathrm{l}} \vec{\mathbf{u}}\,(\nabla T) + \rho_{\mathrm{l}} L \frac{\partial \theta_{\mathrm{l}}}{\partial t}\, d\Omega = \int_{\Omega} \nabla\ \lambda_{\mathrm{e}} \nabla T)\, d\Omega, \tag{9}$$

Since the control body selection is arbitrary, convert equation (1) to

$$C_{\mathrm{ef}} \frac{\partial T}{\partial t} + \rho_{\mathrm{l}} L \frac{\partial \theta_{\mathrm{l}}}{\partial t} + \nabla\left[-\lambda_{\mathrm{e}} \nabla T + \rho_{\mathrm{l}} C_{\mathrm{l}} \vec{\mathbf{u}}\,(T)\right] = 0, \tag{10}$$

where C_{ef} is the equivalent heat capacity.

During the phase-change process, the proportion of water to ice in the control body changes continuously. We assume that the content of unfrozen water is only a function of temperature T. The water-ice phase transformation process only occurs in the interval $[0, -1]^{\circ}\mathrm{C}$. To reasonably describe this process, we introduce the Heaviside function:

$$H\ T - T_{\mathrm{ef}}, \Delta T) = \begin{cases} 0, & T - T_{\mathrm{ef}} < -\Delta T, \\ 1, & T - T_{\mathrm{ef}} > \Delta T, \end{cases} \tag{11}$$

where T is the temperature at a certain location, T_{ef} is the phase transition temperature (and generally $T_{\mathrm{ef}} = 0^{\circ}\mathrm{C}$), and ΔT is the radius of the phase-change interval.

Tests show that when the geotechnical temperature drops below the freezing temperature, a small amount of unfrozen water remains inside [7]. The variation of the unfrozen water content in the space of the control body with temperature can be expressed as

$$w(T) = (1-\psi)H(T) + \psi. \tag{12}$$

The water content of the whole control body Ω can be expressed as

$$\theta_{\mathrm{l}} = \phi w(T) = \phi[(1-\psi)H(T) + \psi]. \tag{13}$$

Furthermore, the ice content of the whole control body Ω can be obtained:

$$\theta_{\mathrm{i}} = \phi[1 - w(T)] = \phi(1-\psi)[(1-\psi)H(T)]. \tag{14}$$

The content of solid particles is as follows:

$$\theta_{\mathrm{s}} = 1 - \phi. \tag{15}$$

The distribution of water, ice, and solid particles in the control body during the freezing process is shown in Figure 1.

According to the volume-averaging method, the equivalent heat capacity of the soil can be obtained as follows:

$$C_{\mathrm{ef}} = (1-\phi)C_{\mathrm{s}} + \phi[(1-\psi)H(T) + \psi]C_{\mathrm{l}} + \phi(1-\psi)[(1-\psi)H(T)]C_{\mathrm{i}}. \tag{16}$$

The thermal conductivity K refers to the heat passing through the unit area soil per unit time under the unit gradient. The thermal conductivity inside the porous media by the volume weighted average method [7, 22, 23] is

$$K_{\mathrm{ef}} = K_{\mathrm{s}}\theta_{\mathrm{s}} + K_{\mathrm{l}}\theta_{\mathrm{l}} + K_{\mathrm{i}}\theta_{\mathrm{i}}. \tag{17}$$

Again, subscripts s, i, and l represent the solid skeleton, ice, and water, respectively.

2.2. Water Flow Field Equation. The surface element dS is taken on the outer surface S of the control body Ω, and the fluid mass passing through the surface of Ω per unit time is expressed as

$$m_{\mathrm{a}} = \iint_{S} \rho \vec{V} \vec{n}\, dS = \int_{\Omega} \nabla(\rho \vec{V})\, d\Omega, \tag{18}$$

where $\vec{V}$ is the flow velocity through the section dS and $\vec{n}$ is the outer normal direction of the section unit dS.

In the control body Ω, for any volume unit $d\Omega$ selected, a change in the ratio of water to ice causes the density of the medium to change with time, causing the mass of the entire control body to change. The process can be described as

$$m_{\mathrm{b}} = \int_{\Omega} \frac{\partial(\rho\phi)}{\partial t} d\Omega = \int_{\Omega} \frac{\partial(\rho w \phi)}{\partial t} + \frac{\partial \rho(1-w)\phi}{\partial t} d\Omega. \tag{19}$$

Regardless of the internal source of the porous medium, using conservation of mass, we can obtain

$$\int_{\Omega} \nabla(\rho \vec{V}) d\Omega + \int_{\Omega} \frac{\partial(\rho w \phi)}{\partial t} + \frac{\partial \rho(1-w)\phi}{\partial t} d\Omega = 0. \tag{20}$$

Water seepage in porous media is assumed to satisfy Darcy's law. And the rate of water seepage $\vec{V}$ in porous media is [21–23]

$$\vec{V} = -\frac{\kappa_{\mathrm{r}}}{\eta} \vec{\kappa}\ \nabla p_{\mathrm{l}} - \rho_{\mathrm{l}} \vec{g}). \tag{21}$$

where $\vec{\kappa} = \begin{bmatrix} \kappa_{\mathrm{s}} & 0 \\ 0 & \kappa_{\mathrm{s}} \end{bmatrix}$ is the intrinsic permeability matrix, in which κ_{s} is the permeability of saturated porous media before freezing; p_{l} is the water pressure; and $\vec{g}$ is the gravity acceleration vector.

η is the viscosity of liquid water which could be expressed as a function of freezing temperature [22, 23]:

$$\eta = 2.1 \times 10^{-6} \exp\left(\frac{1808.5}{273.15 + T}\right), \tag{22}$$

κ_{r} is the relative permeability which could be expressed as a function of water saturation S_{l} [12, 22, 23]:

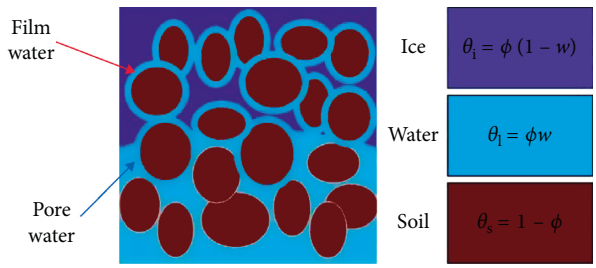

Figure 1: Schematic of a control body of a saturated porous medium.

$$\kappa_r = \sqrt{S_l}\left[1-\left(1-S_l^{1/m}\right)^m\right]^2, \tag{23}$$

where m is the material constant. The water saturation S_l is equal to unfrozen water content $w(T)$ during the freezing process of porous media [12, 22]; then, we can derive the expression of relative permeability combining with equation (12):

$$\kappa_r = \sqrt{w(T)}\left[1-\left(1-w(T)^{1/m}\right)^m\right]^2. \tag{24}$$

When the temperature of the frozen soil drops to the freezing temperature, the liquid water in the soil turns into ice, and the relative porosity of the soil approaches zero; from equation (21) we can find that the seepage velocity becomes zero at this time too. This method that reflected the change mechanism of the seepage velocity in the freezing process by relative permeability is called apparent-heat capacity method. The existing research results are based on the apparent-heat capacity method for mathematical modeling when using Comsol Multiphysics for hydrothermal coupling calculation [12, 15, 17, 21–24]. The main difference between them is the expression of unfrozen water content; however, Vitel et al. discovered through research that the influence of the $w(T)$ function shape is very limited and can be neglected, and reasonable results can be obtained by using the Heaviside function to smoothly approximate the curve of unfrozen water content [17], and this processing method can effectively improve the calculation efficiency. Therefore, we chose this method to express the unfrozen water content in this study, as shown in equation (12).

Substituting equation (21) in equation (20), the continuous equation of the seepage field is obtained:

$$\int_\Omega \frac{\partial\ \rho_l w\phi)}{\partial t} + \frac{\partial \rho_i (1-w)\phi}{\partial t}\, d\Omega + \int_\Omega \nabla\left(-\rho_l \frac{k_r}{\eta}\vec{k}\ \ \nabla p_l - \rho_l \vec{g}\right) d\Omega = 0. \tag{25}$$

It should be noted that when performing hydrothermal coupling numerical calculations, there is another commonly modeling methodology called the enthalpy-porosity method [19, 20], where the water-ice phase-change interface is modeled as a mushy zone. The transformation from water to ice in this zone is considered as a porous medium, where a modified Darcy source term is used to simulate motion in the phase-change region. The main difference between enthalpy-porosity method and apparent-heat capacity method which is used in this paper is the mechanism that is going to force the velocity to a value of zero in the freezing zone. The mechanism of the seepage velocity change of enthalpy-porosity method is described as follows.

The conservation equation of momentum is [19, 20]

$$\frac{1}{\phi}\frac{\partial}{\partial t}\left(\rho_l \vec{V}\right) + \frac{1}{\phi^2}\left[\nabla\left(\rho_l \vec{V}\vec{V}\right)\right] = \frac{1}{\phi}\nabla\left[\mu\left(\nabla\vec{V} + \nabla\vec{V}^T\right)\right] - \nabla P + S_D + S_E + S_B + S_m, \tag{26}$$

where S_D, S_E, S_B, S_m are the Darcy, inertial, buoyancy, and mushy source terms, respectively. They are given as

$$\begin{aligned} S_D &= -\frac{\mu}{K}\vec{V}, \\ S_E &= -\frac{C_E}{K^{1/2}}\rho_l|\overrightarrow{V}|\overrightarrow{V}, \\ S_B &= \rho_l \vec{g}\beta_l\ \ T - T_{ref}), \\ S_m &= -\vec{V}C_m\frac{(1-\gamma)^2}{\gamma^3}. \end{aligned} \tag{27}$$

The Darcy term S_D and inertial term S_E make up the total resistance to the flow. At no-seepage, or low seepage velocity, the inertial term is so low that can be safely neglected [19, 20]. C_E is the Ergun coefficient. The buoyancy source term S_B is used to induce the natural convection within the voids, where $\vec{g}$ is the gravitational acceleration, and β_l is the thermal expansion coefficient. The mushy source term S_m is a modified Darcy source term that is introduced to control the freezing process within the mushy zone [19, 20]. As the temperature of the soil gradually decreases, the liquid fraction γ within the pore fluid gradually reduces to 0, and mushy source term S_m dominates all other terms in the momentum equation (26) and forces the superficial velocity close to zero [19, 20].

In this paper, all numerical calculations are implemented by Comsol Multiphysics, so the apparent-heat capacity method that depends on the relative permeability approach was chosen in mathematical modeling.

2.3. Numerical Implementation. In this study, the hydrothermal coupling numerical calculation model was constructed by the PDE module in COMSOL Multiphysics, and this model was solved by the fully coupled solver. The solution process is shown in Figure 2.

In Figure 2, κ_r is the relative permeability of the frozen soil. Since κ_r changes with the content of unfrozen soil during the freezing process, the change of the relative permeability affects the flow field, so κ_r acts as an intermediate variable to couple the seepage field to the temperature field.

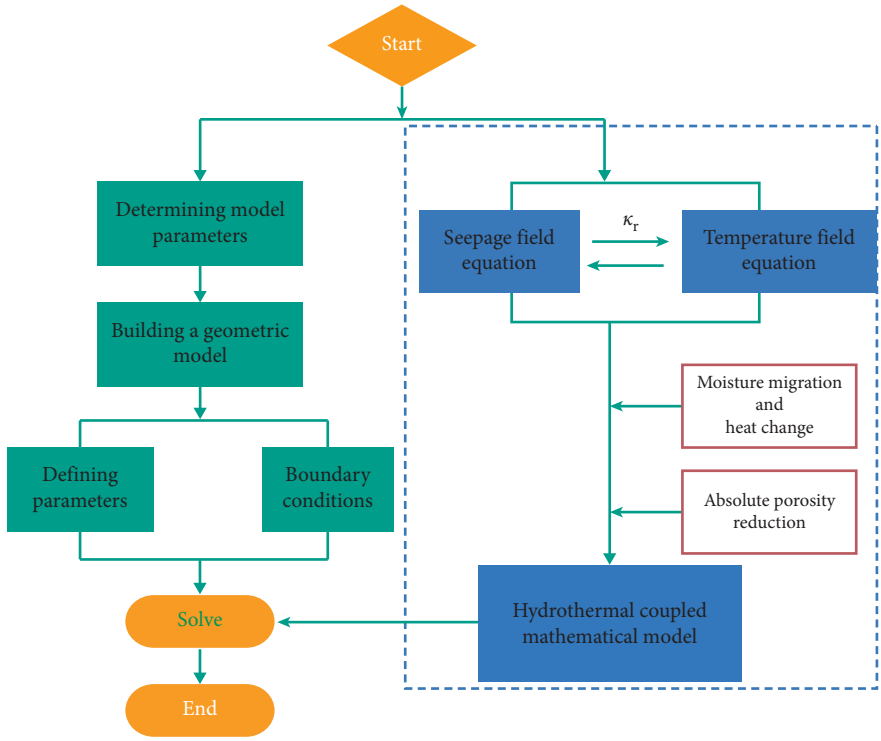

Figure 2: Flow chart of the numeral calculations.

3. Model Validation

3.1. Design of Large Similar Model Test. The test device consists of a test chamber, a freeze simulation system, a groundwater simulation system, and a data test system. The test chamber has a length of 2,400 mm, a width of 1,500 mm, and a height of 800 mm. Among them, the length of the intermediate sand layer test area is 2000 mm. The test device system is shown in Figure 3.

The geometric similarity ratio selected in the experiment is $C_l = 5$. According to the similar model test theory, the main parameters in the test are shown in Table 1.

The arrangements of the freezing pipes and the temperature measuring points are shown in Figure 4. The two pipes on the axis ML2 are used to simulate conventional freezing pipes, and another pipe located on the axis ML1 is used to simulate an auxiliary freezing pipe in an optimized freezing pipe arrangement. This paper mainly studies the development law of the freezing temperature field under the action of groundwater, so only the two freezing pipes located on ML2 are functioning.

Medium-coarse sand (particle size range: 0.25 mm–0.5 mm) was used to simulate the porous medium. The tank was filled with a 50 mm thick sand layer each time, which was vibrated and compacted to ensure uniformity. When the sand layer was filled to an intermediate position of the height of the tank, the temperature measuring points were arranged. To facilitate the accurate positioning of the measuring points and prevent the position of the measuring points from changing due to the flow of water during the test, the thermocouple strings were tied to fine bamboo sticks, and the sand layer of the specified plane was leveled. The thermocouple string was laid out as shown in Figure 5. The minimum distance from the measuring points (nos. 23 and 25) to the boundary of the box reaches 510 mm, which is 4.25 times the distance between the freezing pipe and the measuring points (nos. 23 and 25), and the test is carried out in winter, the indoor temperature being stable at 6~8°C, so the interference of the external environment on the test results can be ignored.

The test system after assembly is shown in Figure 6.

3.2. Establishment of Numerical Calculation Model. The geometric model in the test is three-dimensional. If we neglect freezing pipe deflection during the vertical freezing process, the axially uneven distribution of the freezing pipe wall temperature, and the heterogeneity of the soil, the model becomes two-dimensional. Therefore, the temperature measurement surface is selected for this research.

The transient analysis capabilities of the porous media and subsurface flow module and the hear transfer in porous media module of the COMSOL Multiphysics package are used in this study. The parametric variables are brought into the equation to realize the transient solution of the hydrothermal coupling mathematical model during the freezing process.

The geometric model of the numerical calculation is shown in Figure 7.

We obtain the physical parameters experimentally as follows: the latent heat of the water/ice phase transition is 334 kJ/kg, and the freezing temperature of the sand is −1°C. The relevant physical quantity values involved in the calculation are shown in Table 2.

3.3. Comparison of Numerical Calculation Results and Model Tests. To study the formation law of freezing temperature field under the action of groundwater under different flow

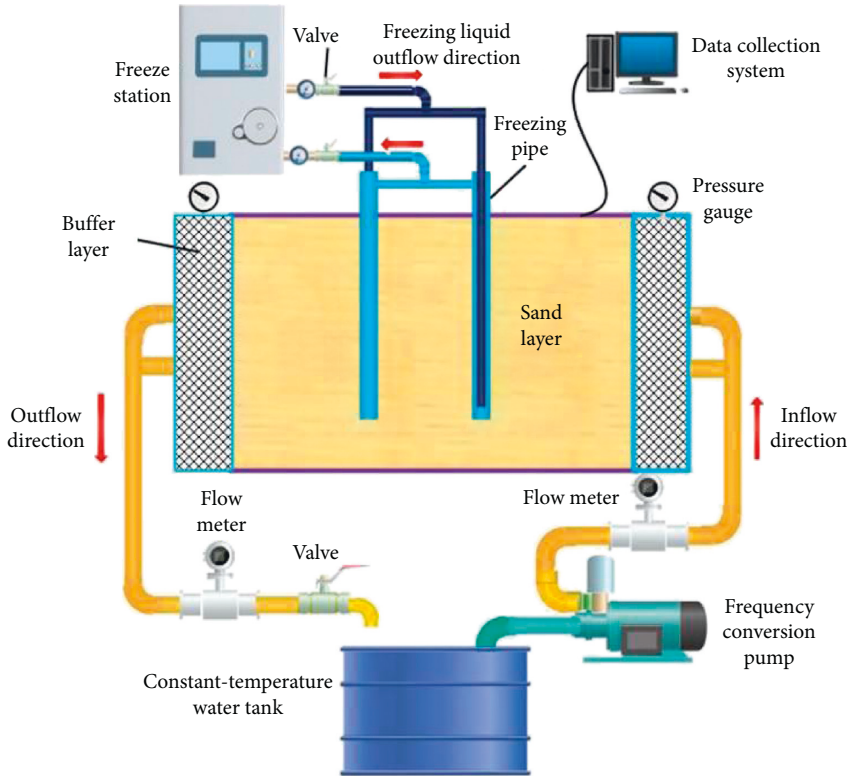

Figure 3: Overall schematic diagram of the test system.

Table 1: Main parameters of the test.

Parameter	In engineering	In test
Size of freezing pipe	110 mm	22 mm
Distance between frozen pipes	1,200 mm	240 mm
Groundwater flow rate	5 m/d	25 m/d
Freeze time	1 d	57.6 min

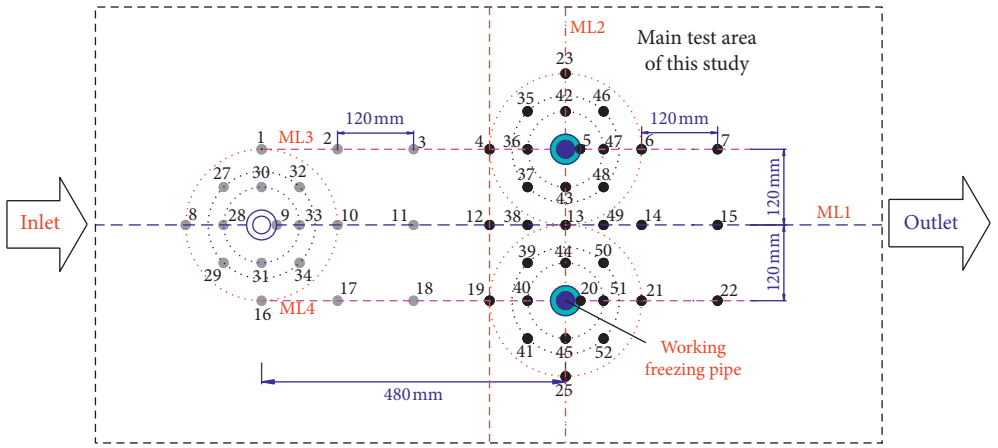

Figure 4: Location of the freezing pipes and measurement points.

rates, the two freezing pipes in the downstream direction are opened in both the test and numerical calculation. The accuracy of the hydrothermal coupling numerical calculation model constructed in this paper is judged by two comparison methods: typical position and frozen range.

3.3.1. Comparison of Typical Position Measurement Data. Measuring point no. 13 is located at the midpoint of the area where the two freezing pipes are located. Changes in the temperature measured at this measuring point with time reflect the formation of the frozen wall formed by the adjacent freezing pipes.

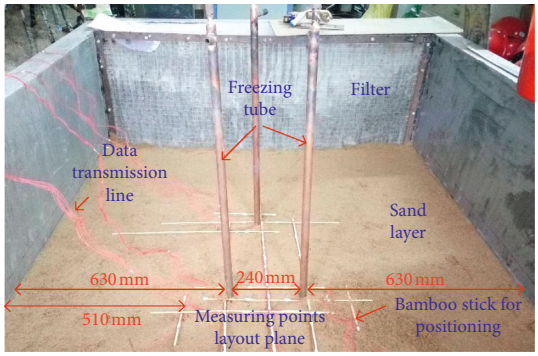

Figure 5: Top view of measuring points layout plane.

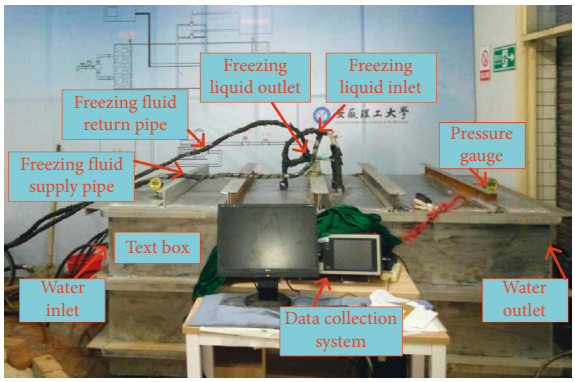

Figure 6: The front view of the test chamber and data collection system.

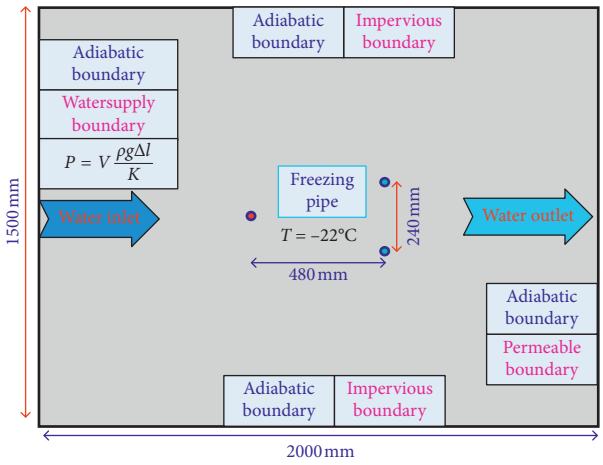

Figure 7: Geometric model and boundary conditions for numerical calculation based on experimental conditions.

It can be seen from Figure 8 that the temperature variations at point no. 13 calculated by the model presented in this paper closely match the experimentally observed variations for a groundwater flow velocity of 0 m/d. More specifically, (1) the temperature changes are consistent—that is, both experience the first rapid temperature drop phase, the phase transition phase, the second rapid temperature drop phase, and the stable freezing phase—and (2) the time corresponding to each stage is basically the same—the first

Table 2: The values of the main calculation parameters.

Material	Density ($kg \cdot m^{-3}$)	Thermal conductivity, $W \cdot (m \cdot K)$	Specific heat capacity, $J \cdot (kg \cdot K)^{-1}$	Porosity
Water	1,000	0.56	4.2	
Ice	918	2.24	2.1	
Sand	1,800	3.22	0.7	0.25

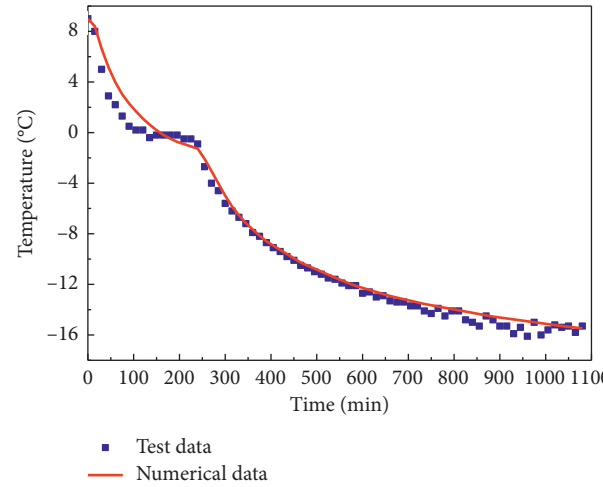

Figure 8: Comparison of simulation and test data for point no. 13 under a flow rate of 0 m/d.

rapid temperature drop phase lasts for about 100 minutes, the closure of the frozen column formed by adjacent frozen pipes occurs at 250 minutes, and the end of the subrapid temperature drop phase occurs at 600 minutes. The test data showed slight fluctuations in the later stage, but the overall change law remained consistent with the simulation results. The comparison between the numerical calculation results and the experimental data of other measuring points is shown in Figure 9. It should be noted that the position of the measuring points around the two freezing pipes is symmetrically distributed along the axis ML1. Therefore, only the data of the measuring points around one of the freezing pipes are analyzed in this part, and the overall distribution law of the freezing temperature field will be presented in the following section by the form of an isotherm. By comparison, it can be found that the numerical calculation results have a high consistency with the overall development law of the test data of most of the measuring points under the condition that the seepage velocity is zero, and only the difference between the numerical calculation result and the experimental result of the no. 15 measuring point is obvious, the reason for the difference may be that the detection data of the measuring point are inaccurate due to some uncertain factors. Since the sand layer is not completely uniform during the test, there are some slight differences in the test data of the measuring points symmetrical on both sides of the axis ML2.

It can be seen from Figure 10 that the overall development trend of the temperature at measuring point no. 13

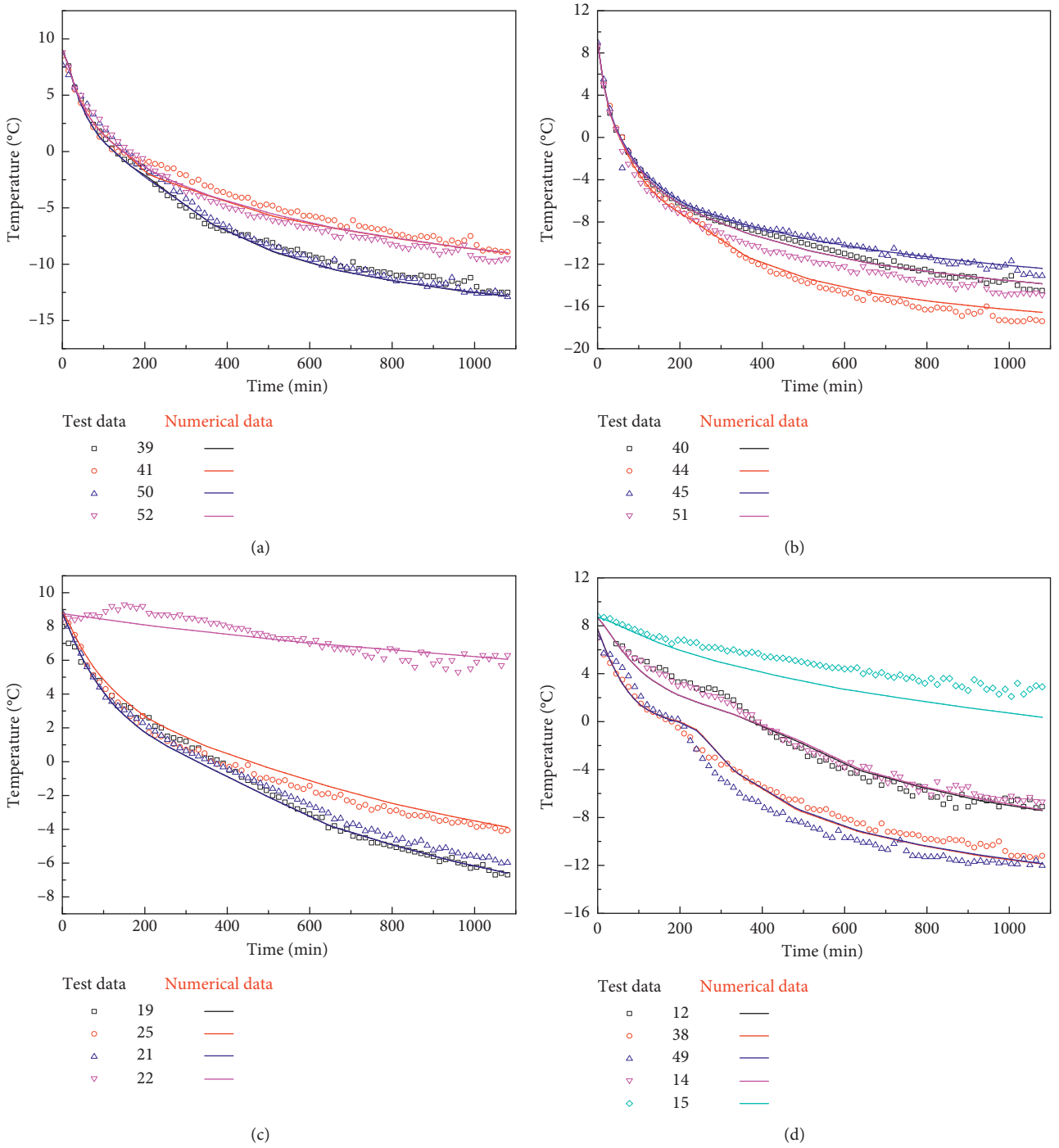

FIGURE 9: Comparison of simulation and test data for measuring point of (a) the inner ring circle, (b) the middle ring circle, (c) the outer ring circle, and (d) the axis ML2 under a flow rate of 0 m/d.

is consistent between the numerical calculation and experimental tests. However, the calculated value is generally slightly higher than the test result, and the calculated end moment of the phase change is delayed by about 20 min. There are several reasons for this. First, in the test, the water flow velocity is controlled by the pressure of the inlet section, and the sand layer is assumed to be uniform in each cross section. However, due to the large size of the test box, the uniformity of the sand layer cannot be guaranteed during the process of sand filling and compaction. Therefore, there is a discrepancy between the actual flow rate of the water flowing between the two adjacent freezing pipes and the rate used in calculations. When the control flow rate is slightly smaller than the design value, the experimentally obtained closure time will be earlier than the numerical calculation result. The comparison between the numerical calculation results and

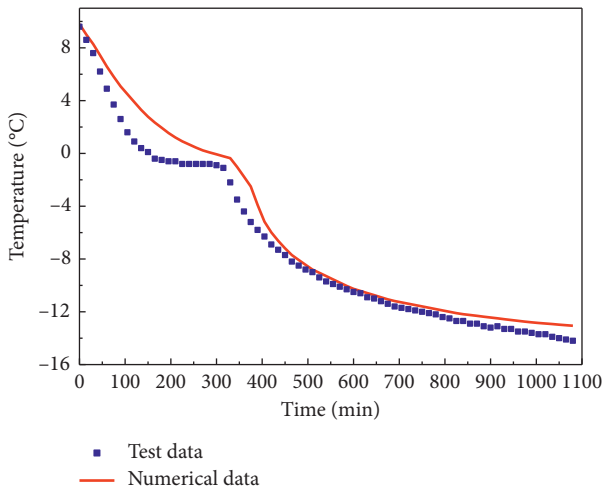

Figure 10: Comparison of simulation and test data for point no. 13 under a flow rate of 5 m/d.

the experimental data of other measuring points is shown in Figure 11. By comparison, it can be found that the numerical calculation results of most measuring points have a high consistency with the overall development law of the test data under the condition that the seepage velocity is 5 m/d except the measuring point no. 15, the reason for the obvious difference between the numerical calculation result and the experimental result of the only one measuring point may be that the detection data of the measuring point are inaccurate due to some uncertain factors. Due to the action of the water flow, the temperature of the measuring point on the right side of the axis ML2 is significantly lower than that of the left side.

3.3.2. Comparison of Frozen Range. Figure 12 shows that the frozen wall formed by the two freezing pipes has been closed when the freezing time reaches 350 min. In addition, the −1°C isotherm at the upstream position has a pronounced concave shape in the middle of the action zone of the two frozen pipes. Due to the action of the water flow, the frozen area on the right side of the axis ML2 is significantly larger than the frozen area on the left side. As the freezing time continues to increase, the frozen area gradually expands. When the freezing time reaches 500 min, the −1°C isotherm at the upstream position is smoother, but the middle of the action zone of the two frozen pipes still has a concave shape along the direction of water flow. After 650 min, the frozen range was further expanded, but the overall shape of the frozen area did not change significantly.

In order to further verify the accuracy of the numerical calculation model, we compare the frozen range obtained by numerical calculation after 350, 500, and 650 minutes under the action of groundwater moving at 5 m/d with the frozen range obtained by the test (Figures 13 and 14).

When the freezing time was 350 min, 500 min, and 650 min, the differences between the frozen range calculated by the numerical calculation and the frozen range obtained by the test were only 2.4%, 4.2%, and 6.2%, respectively, and the shape of the frozen area obtained by the two was more consistent. This shows that the mathematical model and the selected solution method meet the actual needs of the project. The numerical calculation model can provide strong support for the study of the formation of an artificial freezing temperature field under the action of groundwater.

4. Engineering Applications

4.1. Study of the Freezing Rule for Single-Row Pipes under the Action of Groundwater. The central wind shaft of Panyi Mine in Huainan Mining Area was constructed by the freezing method. The wellbore passes mainly through Cenozoic alluvium and Permian Shihezi coal-bearing strata. The thickness of the Cenozoic alluvium is 205.8 m, and it is composed mainly of clay and sand. The sand layer is rich in groundwater and is the key control layer of the whole freezing project. The freezing parameters of the central wind shaft in Panyi Mine are shown in Table 3.

We now apply the numerical calculation model established in the previous section to the arrangement of pipes found in the central wind shaft of the Panyi Mine. And the sand-permeable stratum at a depth of 200 m is selected for analysis. The numerical calculation model of stratum freezing under the action of groundwater is constructed as shown in Figure 15.

In this model, the calculated control range is 28 m × 28 m. The initial temperature of both the groundwater and the formation is 20°C. The axis $L1$ is parallel to the direction of the water flow, the axis $L2$ is perpendicular to the direction of the water flow, and the intersection of $L1$ and $L2$ coincides with the center of the freezing pipe arrangement circle. For the convenience of analysis, the left and right intersections of the $L1$ and the freezing pipe arrangement circle are, respectively, defined as the "upstream position" and "downstream position," and the intersection point of $L2$ and the freezing pipe arrangement circle is defined as the "side position."

According to test results of freezing temperature of saturated sand, an effective frozen wall is formed when the temperature of the frozen sand layer reaches −1°C; this means that the −1°C isotherm is the contour of the frozen wall. The distributions of the freezing temperature field under the action of different flow rates at 30 d, 60 d, and 90 d are plotted in Figure 16.

Using the data in Figure 16, we can analyze variations in the artificial freezing temperature field under the action of groundwater with different flow rates. We find that, due to the convective heat transfer of the water flow, part of the cooling capacity of the upstream freezing pipes is carried by the water flow to the downstream region. The end result is that the closure time of the downstream position of the frozen wall is earlier than that of the upstream position. For $t = 30$ d, under the action of groundwater less than 10 m/d, the downstream area of the frozen wall has completed the intersection, while the upstream position of the frozen wall has not been closed. For $t = 60$ d, the downstream area of the frozen wall has been closed, and the upstream position can only be closed under the condition that the flow rate is less

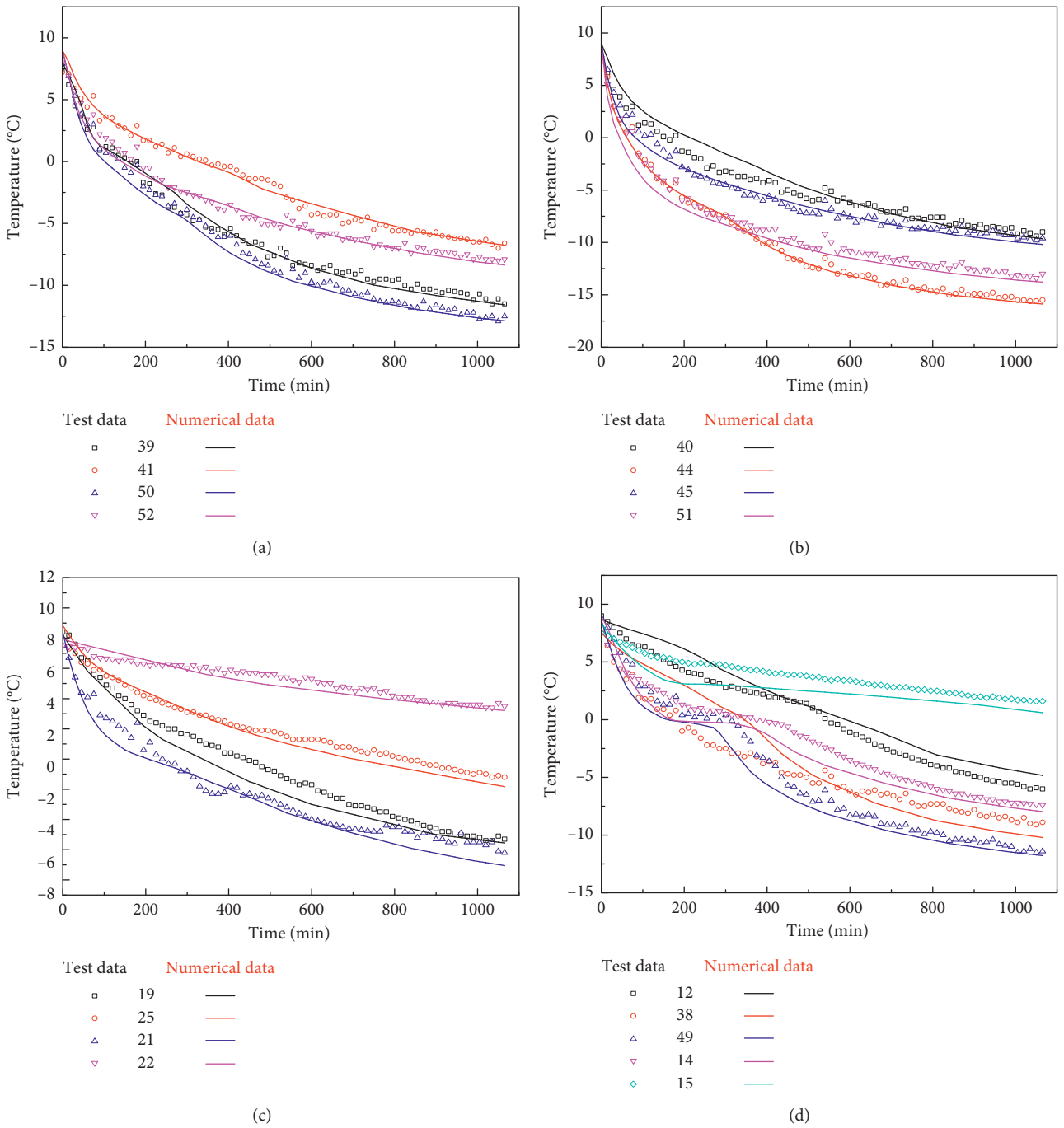

FIGURE 11: Comparison of simulation and test data for measuring point of (a) the inner ring circle, (b) the middle ring circle, (c) the outer ring circle, and (d) the axis ML2 under a flow rate of 5 m/d.

than 7 m/d. For $t = 90$ d, the frozen range of the downstream area has formed a distinct convex shape along the direction of the water flow, and the frozen range on both sides has expanded to the intended excavation position, while the upstream position can only be closed if the groundwater flow rate is less than 9 m/d.

Numerical calculation shows that groundwater flowing at less than 5 m/d has little effect on the freezing temperature of single-row pipes. As a result, in this paper, only the influence of groundwater with a flow rate greater than 5 m/d is studied. Figure 17 shows that the closure time of the frozen wall formed by the single-row freezing pipes increases with the flow rate. The closure time under the action of 5 m/d water flow is 30 d, while the closure time under the action of 11 m/d water flow is 171 d.

Whether the downstream area can be closed plays a decisive role in the formation of the entire frozen wall. After the frozen wall of the downstream zone is closed, there is no longer movement of water throughout the frozen zone inside the circle of the freezing pipe arrangement; as a result,

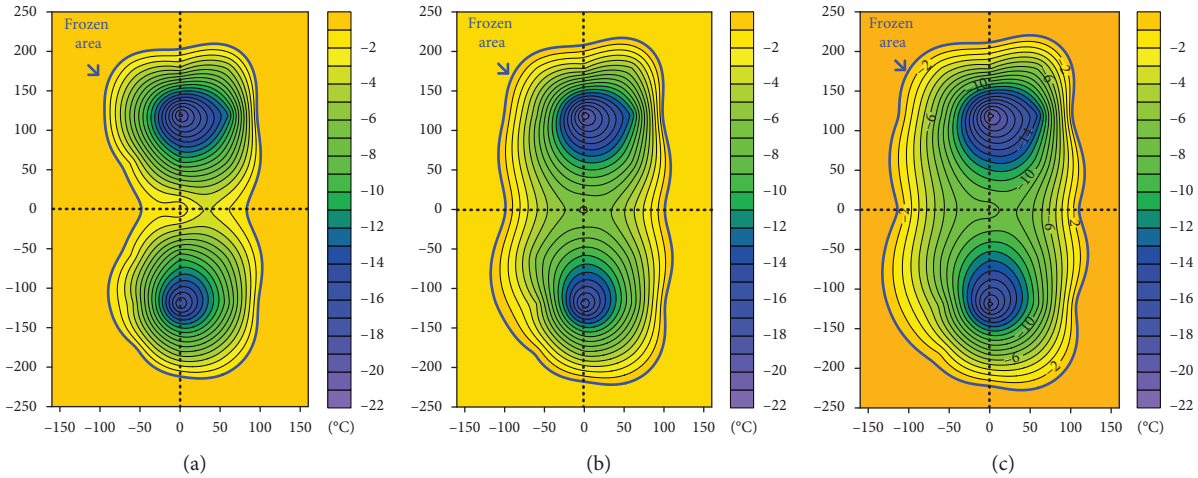

Figure 12: The frozen range of the test when the freezing time is (a) 350 min, (b) 500 min, and (c) 650 min under the action of groundwater moving at 5 m/d.

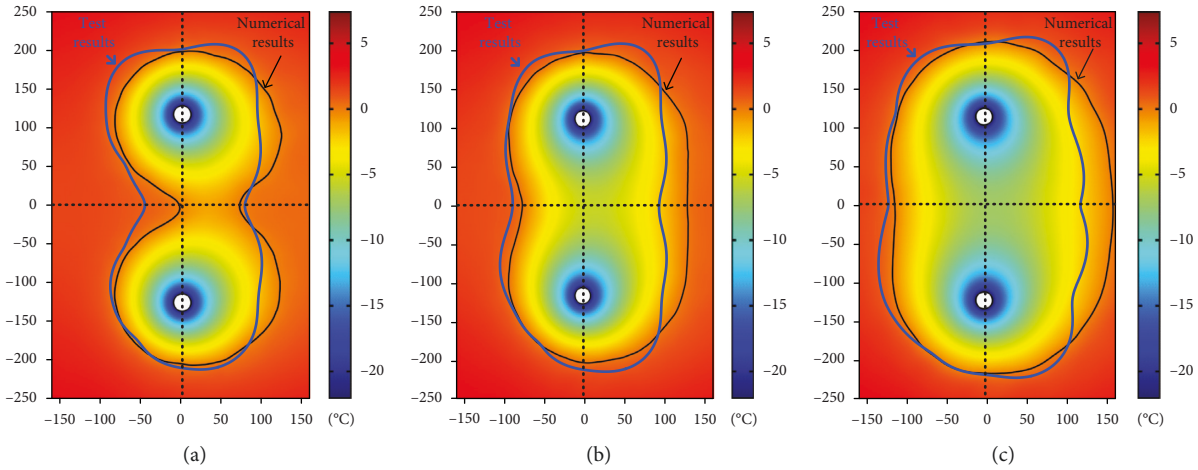

Figure 13: Comparison of numerical calculation frozen range with test results when the freezing time is (a) 350 min, (b) 500 min, and (c) 650 min under the action of groundwater moving at 5 m/d.

the effect of water flow on the freezing temperature field is weakened. Therefore, as long as the frozen wall in the downstream position can complete the intersection, the entire frozen wall will be closed. Through numerical calculation, we find that the closure time of the frozen wall at the downstream location shows a parabolic relationship with the water flow velocity. When the water flow velocity is less than 7 m/d, the closure time of the frozen wall in the downstream region decreases with increasing flow velocity; when the flow velocity is greater than 7 m/d, the closure time increases with increasing flow velocity. The reasons for this phenomenon are as follows: due to convective heat transfer, part of the cooling released by the freezing pipes is used to reduce the temperature of the water flow. When this part of the low-temperature water flows through a higher temperature region, part of the cooling capacity is transferred to this area, and the water flow becomes the flow medium of the heat. This realizes the process of transferring the cooling capacity of the upstream freezing pipes to the downstream area. Therefore, when the water flow velocity is within a certain range, the increase of the flow velocity promotes the process of energy transfer. However, as the flow rate is further increased, the replenishing cold from upstream cannot compensate for the energy loss caused by the convective heat transfer of the water stream to the downstream region. The effect of this part of the heat from the upstream on the freezing process in the downstream area is weakened. When the groundwater flow rate is further increased, the closure time of the frozen wall in the downstream area increases.

In fact, when the flow rate of groundwater is large, the unfrozen area in the upstream position is still subjected to the impact of a large water flow after the downstream frozen wall is closed; this position will not be closed until the internal extent of the freeze pipe arrangement circle is frozen. This process requires continuous cooling for a long time, resulting in large energy losses. During actual construction, the soil inside the pipe arrangement is not allowed to

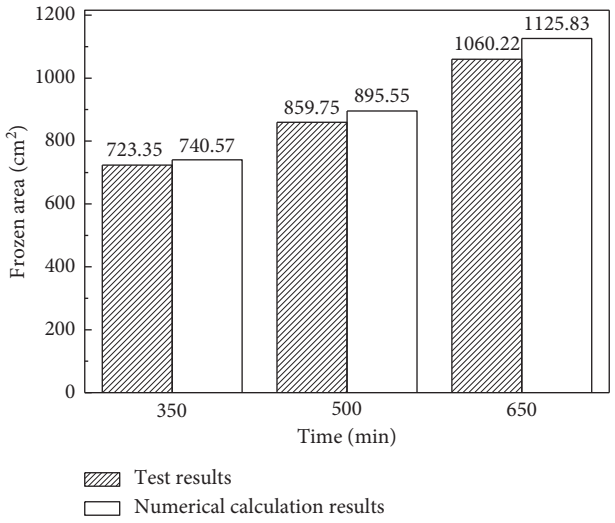

Figure 14: Comparison of the frozen range of numerical calculations with test result when the freezing time is 350, 500, and 650 min under the action of groundwater moving at 5 m/d.

Table 3: Freezing parameters of central wind shaft in Panyi Mine.

Parameters		Value	Unit
Inner diameter of the wellbore		6	m
Diameter of the excavation boundary		8	m
Freezing pipe	Diameter of the arrangement area	14	m
	Quantity	38	1
	Spacing	1.15	m
	Temperature	−32	℃
	Size of freezing pipe	159 × 6	mm

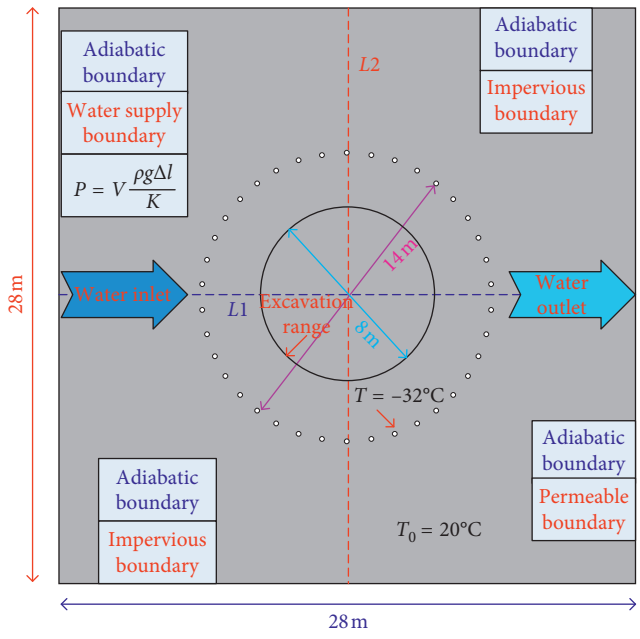

Figure 15: Geometric model and boundary conditions for numerical calculation based on the freezing parameters of central wind shaft in Panyi Mine.

completely frozen, in order to prevent adverse effects on the excavation of the soil and the construction of the wellbore. Therefore, it is necessary to comprehensively consider the above factors in determining the water flow rate allowed by the freezing method. In the calculations herein, we find that for single-row freezing pipes, the maximum flow rate is 10 m/d.

Figure 18 shows the development law of the thickness of the frozen wall under different flow rates at a freezing time of 90 d. Through comparative analysis, we find that the groundwater flow rate has the most significant effect on the thickness of the frozen wall at the upstream position; the thickness of the frozen wall of this position decreases sharply with the increase of the water flow velocity. When the water flow velocity is greater than 9 m/d, the thickness of the frozen wall at this position is 0, indicating that the frozen wall in the upstream position cannot be closed within 90 d. The frozen wall on both sides is less affected by the flow rate. When the groundwater flow rate is increased from 5 m/d to 12 m/d, the thickness of the frozen wall in this area decreases with the increase of the flow velocity, but the decrease is not obvious. Due to the superposition effect of the cold volume from the upstream and downstream regions, the thickness of the frozen wall in the downstream region is always greater than the thickness of the frozen wall at other locations when the freezing time reaches 90 d.

It can be seen from Figure 19 that when the initial flow rate of groundwater is large, the flow rate will undergo the following changes as the freezing time increases: (1) In the first stabilization phase, the frozen area and the resistance to water flow are small. The groundwater flow rate will stabilize near the initial flow rate. Since the placement of the freezing pipes has a certain influence on the permeability of the soil, the initial flow rate in the middle position of the adjacent freezing pipes of the downstream region is slightly larger than the design rate. (2) The second stage involves a rapid increase in flow rate. Since the permeability of the frozen area is small, the water flow can only pass through the unfrozen area in the middle of the two adjacent freezing pipes. Therefore, under a constant pressure head, the smaller the seepage area, the greater the water flow rate. (3) The next stage is a slow growth phase. When the frozen wall formed by the adjacent freezing pipes is about to be closed, the water flow rate at the midpoint of the line connecting the two freezing pipes increases with the increase of the freezing time. As can be seen from Figure 20, once the water flow speed increases to a certain value, it decreases sharply to 0, and this turning point is the closure time of the frozen wall. The reason for this change in the flow rate is that as the volume of the frozen column formed by the adjacent two freezing pipes increases, the permeable region of the cross section decreases continuously, but the water pressure from the upstream does not change, resulting in a gradually increasing water flow. Through the calculations in this paper, we find that groundwater with an initial flow rate of 10 m/d can reach 7 times the initial flow rate at the moment of closure.

We now analyze the closure time of the frozen wall for different pipe spacings (Figure 21). Through comparative

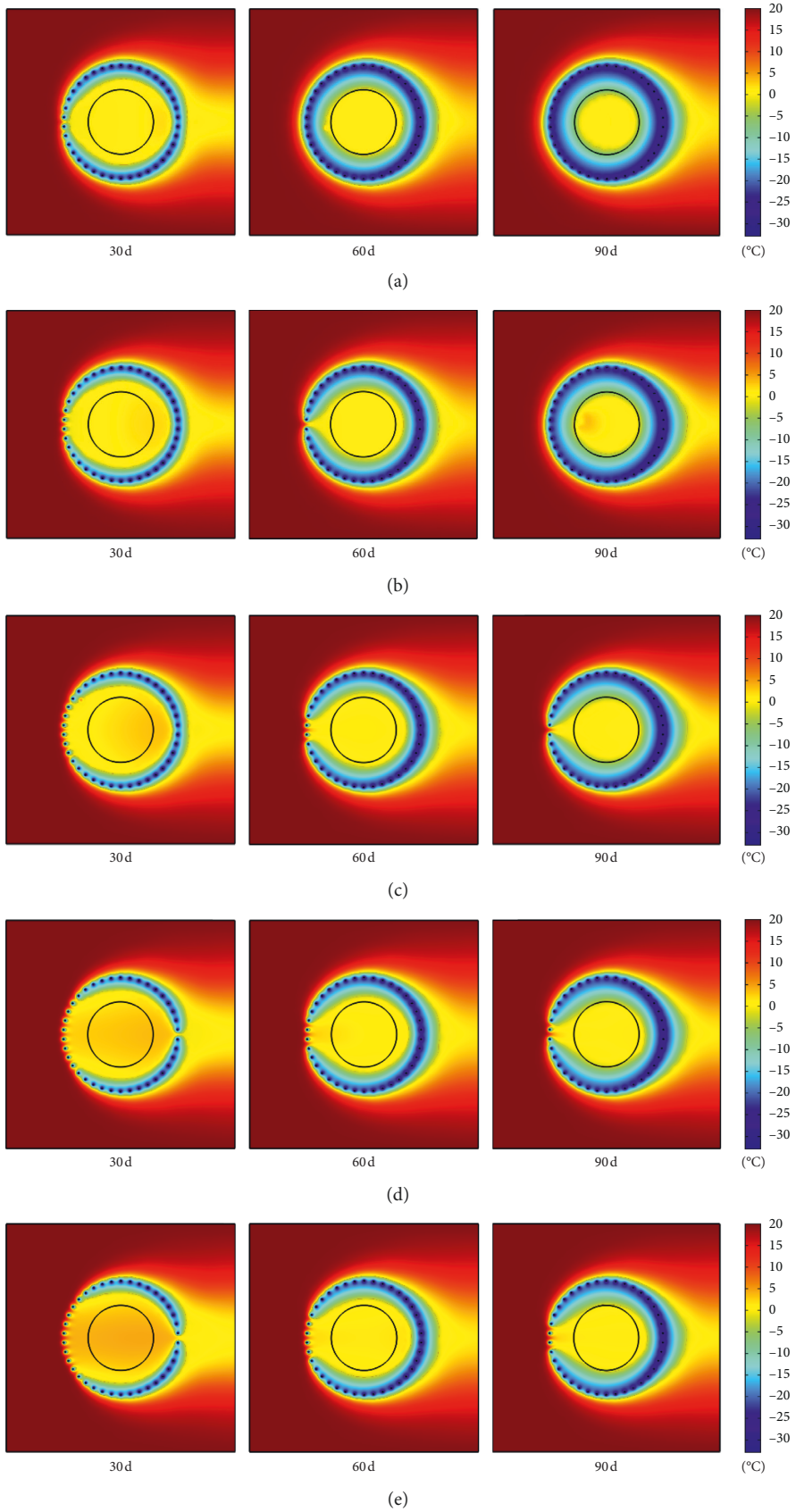

Figure 16: The variation of freezing temperature field of single-row pipes with time under the action of groundwater with a flow rate of (a) 5 m/d; (b) 7 m/d; (c) 9 m/d; (d) 10 m/d; (e) 11 m/d.

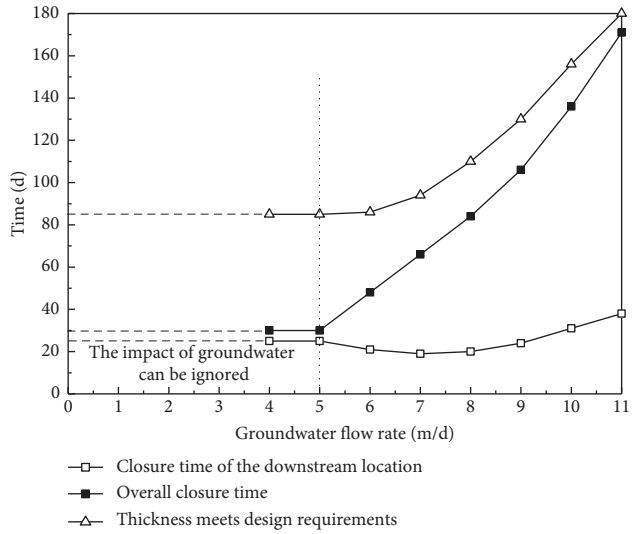

Figure 17: The variation of time required for the downstream location, the overall location of the frozen wall to be closed, and the thickness of the frozen wall to meet design requirement with groundwater flow rate.

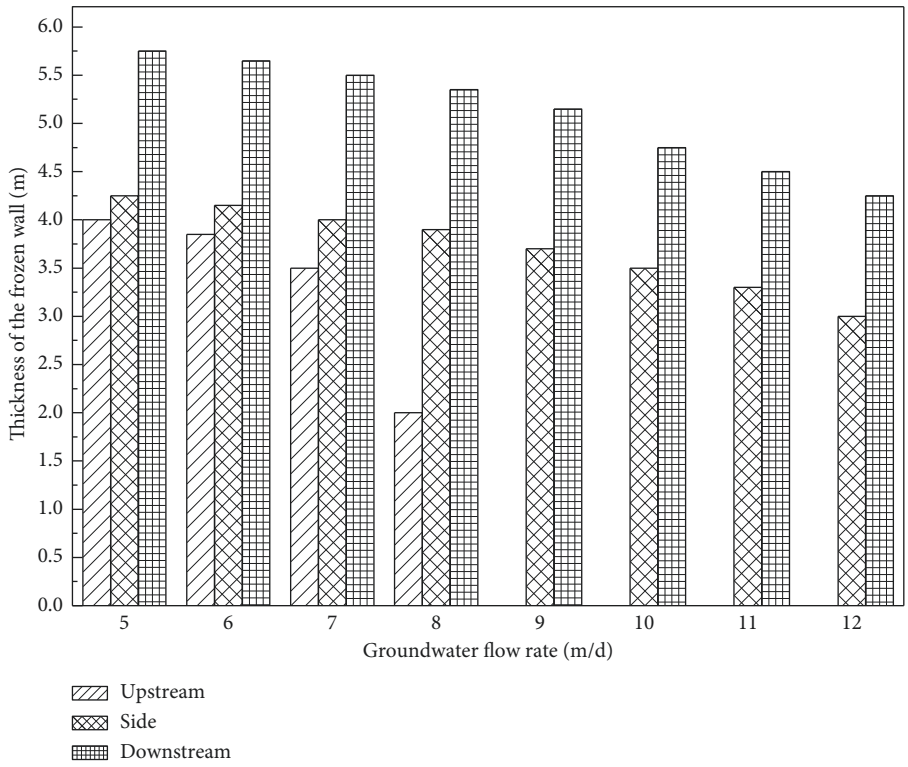

Figure 18: The effect of groundwater flow rate on the thickness of the frozen wall at upstream, side, and downstream locations when the freezing time is 90 day.

analysis, we find that the spacing of the freezing pipes has a significant influence on the final closure time of the frozen wall. Under the action of groundwater with a flow rate of 5 m/d, when the spacing of the freezing pipes is reduced from 1.15 m to 1.05 m, the closure time of the entire frozen wall is decreased by 11 d, and when the spacing of the freezing pipes is increased from 1.15 m to 1.30 m, the closure time of the entire frozen wall is increased by 20 d. With the increase in the flow rate, the influence of the change of the freezing pipe spacing on the freezing efficiency of the frozen wall becomes more apparent. Under the action of groundwater with a flow rate of 9 m/d, when the spacing of

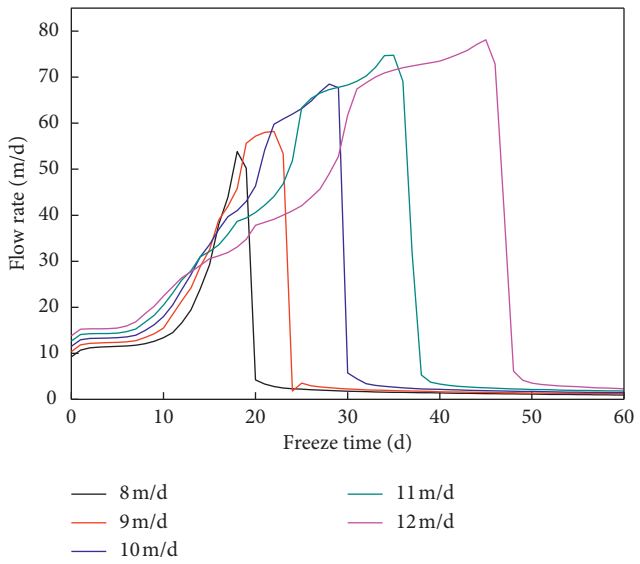

Figure 19: The variation of groundwater flow rate with time in the freezing process of porous media.

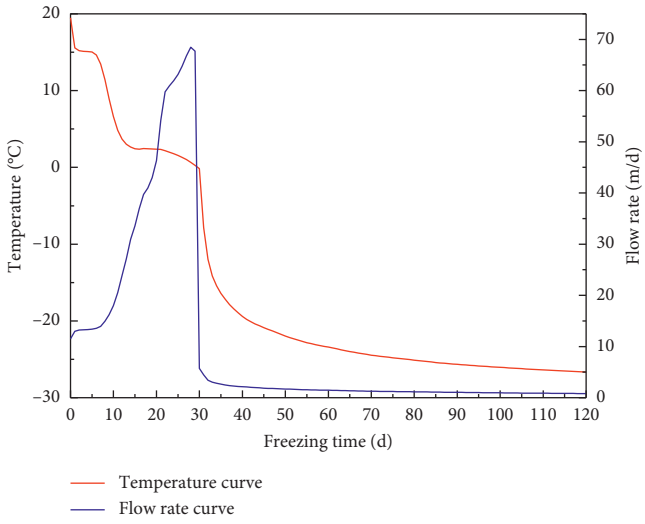

Figure 20: The variation of temperature and groundwater flow rate in the middle position between the two freezing pipes with time during the freezing process of porous media.

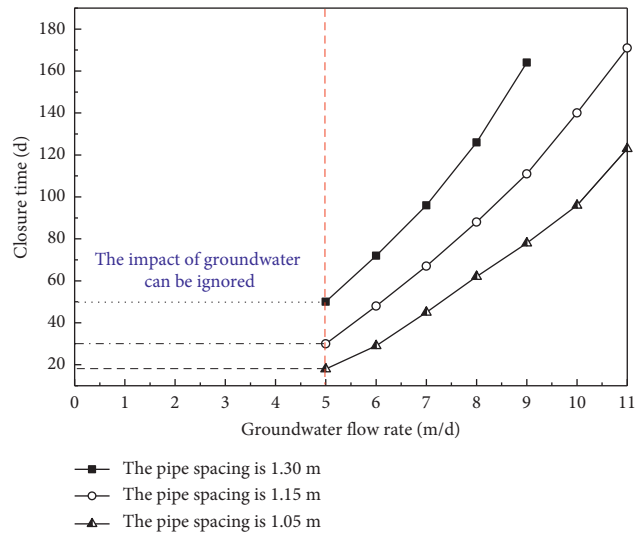

Figure 21: Variation law of closure time of frozen wall corresponding to different freezing pipe spacing.

Table 4: Freezing parameters of wind well in Zhangji Mine.

Parameters		Value	Unit
Inner diameter of the wellbore		7	m
Diameter of the excavation boundary		9	m
Auxiliary freezing pipe	Diameter of the arrangement area	13	m
	Quantity	18	1
	Spacing	2.27	m
	Temperature	−32	°C
	Size of freezing pipe	159 × 6	mm
Main freezing pipe	Diameter of the arrangement area	17	m
	Quantity	42	1
	Spacing	1.27	m
	Temperature	−32	°C
	Size of freezing pipe	159 × 6	mm
Row spacing		2	m

the freezing pipes is reduced from 1.15 m to 1.05 m, the closure time of the entire frozen wall is decreased by 52 d, and when the spacing of the freezing pipes is increased from 1.15 m to 1.30 m, the closure time of the entire frozen wall is increased by 34 d. When the flow rate of groundwater reaches 10 m/d, the frozen wall formed by the freezing scheme with the freezing pipe spacing of 1.30 m cannot been closed within 180 d. Therefore, when there is a large flow rate of groundwater in the local layer, the spacing of the freezing pipes should be reduced in the design of the freezing scheme to improve the freezing efficiency of the entire region. We conclude that when the single-row pipe arrangement is adopted, the spacing of the freezing pipes should not be greater than 1.3 m. However, considering the possible existence of freezing pipe deflection, the spacing of the freezing pipes should not be less than 1 m. Therefore, the spacing of the freezing pipes can be set to 1–1.3 m.

4.2. Study on the Freezing Law of Double-Row Pipe under the Action of Groundwater with Different Flow Rates. The wind well in the north area of Zhangji Mine in Huainan Mining Area was constructed by the freezing method. The wind well intersects Quaternary sediments to a depth of 271.25 m and Permian strata from 271.25~1067.80 m; the total thickness of these Permian sediments is 796.55 m. The bedrock weathering zone has a bottom boundary of 317 m and a thickness of 45.75 m, and the strong weathering zone has a depth of 293.25 m and a thickness of 22 m. At the depth range of 380 m–430 m is a water-rich sand layer, which is the key control layer of the whole freezing project. The freezing scheme design parameters are shown in Table 4.

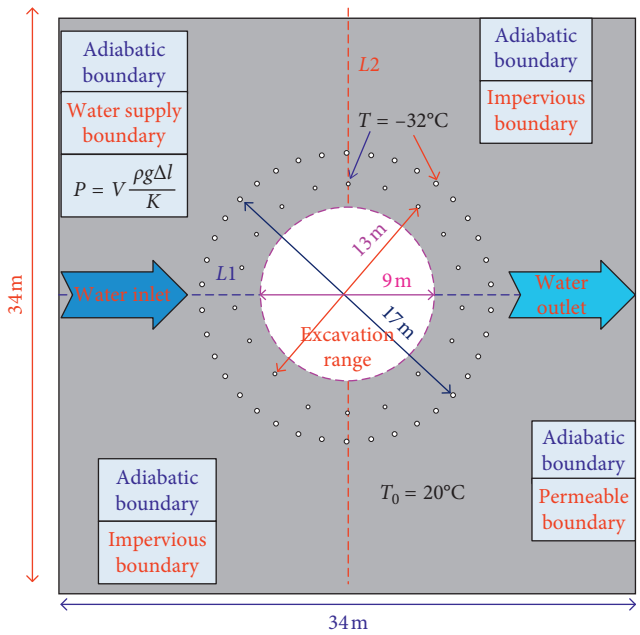

Figure 22: Geometric model and boundary conditions for numerical calculation based on the freezing parameters of central wind shaft in Zhangji Mine.

Based on the design parameters of the freezing scheme, the sand-permeable stratum at a depth of 400 m is selected for analysis, and the numerical calculation model of the double-row pipes stratum freezing under the action of groundwater is constructed as shown in Figure 22.

In this calculation model, the calculated control range is 34 m × 34 m. The initial temperature of the groundwater and the formation is 20°C. The temperature of the freezing pipe is −32°C. The axis $L1$ is parallel to the direction of the water flow, the axis $L2$ is perpendicular to the direction of the water flow, and the intersection of $L1$ and $L2$ coincides with the center of the freezing pipe arrangement circle. For the convenience of analysis, the left and right intersections of the $L1$ and the main freezing pipe arrangement circle are, respectively, called the "upstream outer ring position" and the "downstream outer ring position," and the left and right intersections of $L1$ and the auxiliary freezing pipe arrangement circle are, respectively, the "upstream inner position" and "downstream inner ring position."

Using Figures 23 and 24, the variation law of temperature field formed by double-row freezing pipes under the action of groundwater with different flow rates can be analyzed.

In the case that there is no significant difference in the spacing of the main freezing pipes, since a circle of auxiliary freezing pipes is arranged inside an arrangement ring of the main freezing pipes, the resistance of the entire frozen area to groundwater is significantly improved. Groundwater with a flow rate below 10 m/d does not have a significant effect on the freezing time of the frozen wall formed by double-row freezing pipes, and when the groundwater flow rate reaches 20 m/d, a frozen wall can still form successfully. When the freezing time reaches 30 d, the outer ring area of the frozen wall downstream under the action of groundwater with a flow rate less than 20 m/d has already been closed, and the frozen wall formed by the side inner-ring freezing pipes has been connected to the frozen wall formed by the outer-ring freezing pipes. Increases in the flow rate have a significant effect on the frozen wall in the downstream area, but the frozen walls on both sides do not change significantly.

When the freezing time reaches 60 d, the frozen area under the action of groundwater with a flow rate of less than 14 m/d has been closed, and the extent of the frozen wall is close to the intended excavation boundary. When the flow rate is greater than 14 m/d, the frozen wall of the upstream region is not closed, and as the flow rate increases, the unfrozen region increases. When the freezing time reaches 90 d, the frozen area under the action of groundwater with a flow rate of less than 16 m/d has been closed, and the extent of the frozen wall has exceeded the control boundary of the proposed excavation area. Under the action of groundwater with a flow rate greater than 16 m/d, the frozen area of the upstream position is not closed, but the frozen range on both sides has developed to the inside of the boundary to be excavated.

Figure 24 shows the closure times of different positions of the frozen wall. We find that the closure time of the downstream outer ring position is earlier than that of the downstream inner ring and the upstream position. When the water flows through this position, it has passed the precooling action and the blocking action of the three rows of freezing pipes, and the convective heat transfer effect of the water flow with the frozen area is weakened, so the closure time of the position is less affected by the flow rate. When the water flow rate is less than 14 m/d, the closure time at this position remains unchanged at 17 d. When the groundwater flow rate is greater than 14 m/d, the closure time increases with increasing flow rate. When the groundwater flow rate reaches 20 m/d, the closure time of the downstream outer ring position is 34 d. The closure time of the position of the outer ring and the inner ring upstream maintains the same development trend throughout the freezing process. When the flow rate is low, the influence of the water flow on the freezing efficiency is small. Since the spacing of the auxiliary freezing pipes is larger than that of the main freezing pipes, the closure time of the upstream outer ring position is earlier than that of the inner ring position. With increasing flow rate, the convective heat transfer of the water flow causes the cooling capacity of the freezing pipes at the outer ring position upstream to be largely lost, while the cooling loss of the frozen region at the upstream inner ring position is small. Therefore, the closure time of the position of the upstream inner ring is earlier than that of the outer ring area.

However, since the row spacing between the freezing pipes is small, after the frozen wall formed by the inner ring pipes is closed, the water flow bypasses the frozen zone and flows to the downstream zone, and the influence of the water flow on the action area of the freezing pipes of upstream outer ring is weakened. Therefore, the frozen wall at this position is closed in a short time after the closure of the frozen wall of the upstream inner ring. When the

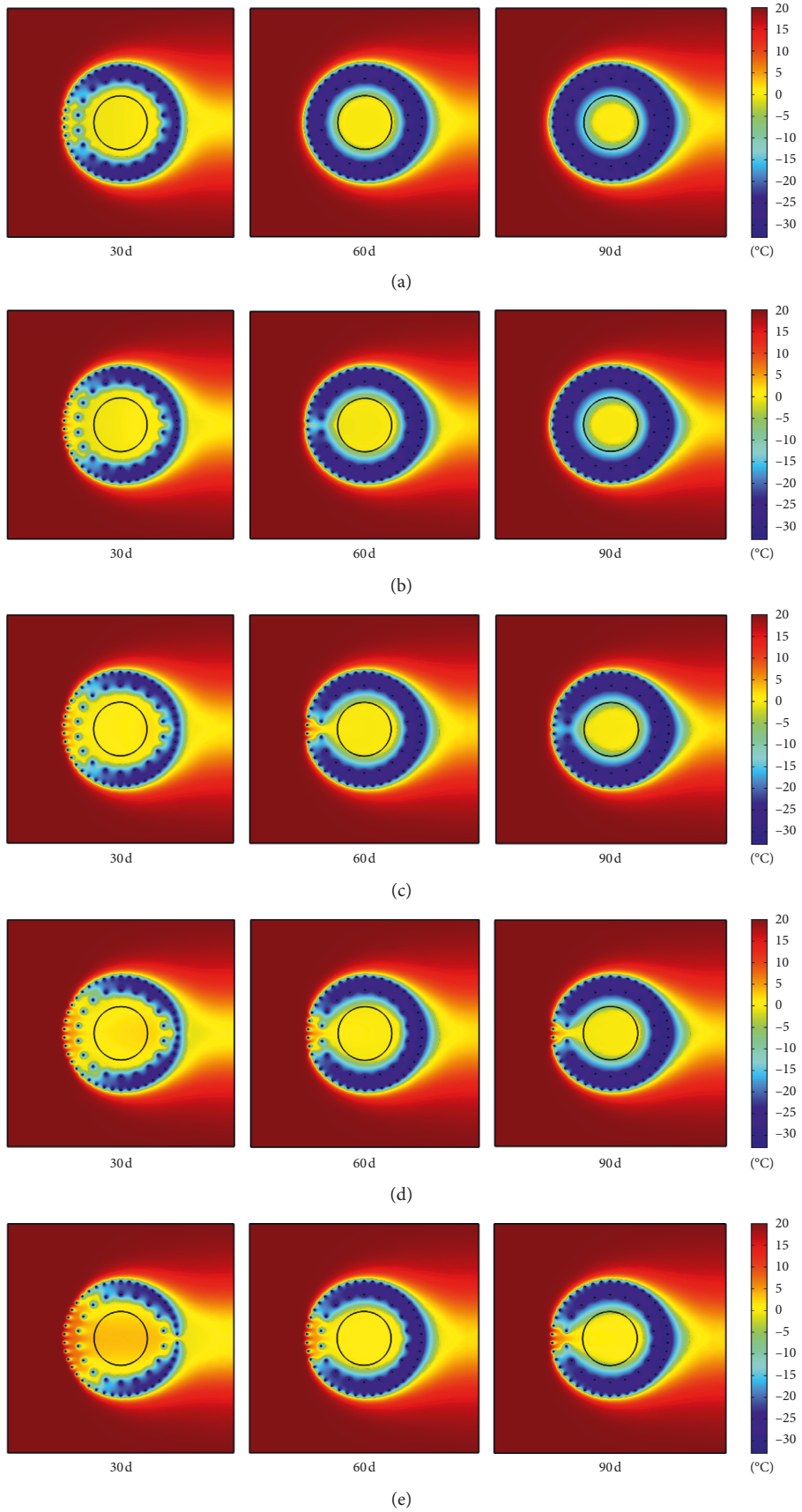

Figure 23: The variation of freezing temperature field of double-row pipes with time under the action of groundwater with a flow rate of (a) 10 m/d, (b) 14 m/d, (c) 16 m/d, (d) 18 m/d, and (e) 20 m/d.

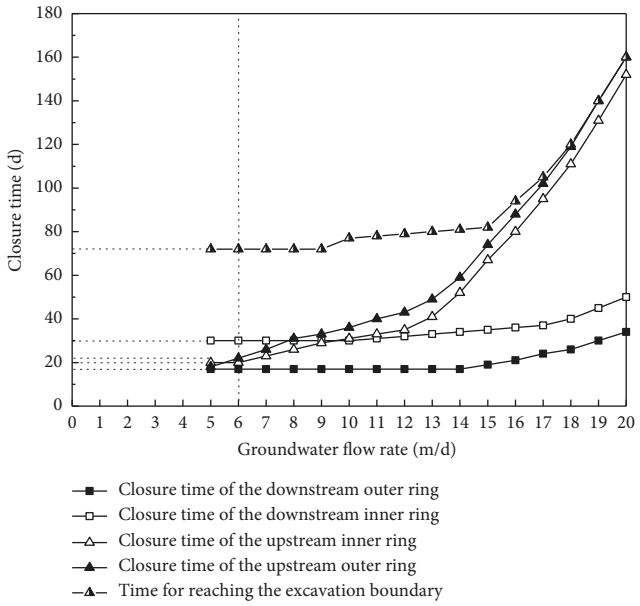

Figure 24: The time required for the downstream outer ring, downstream inner ring, upstream outer ring, and upstream inner ring of frozen wall to be closed and the time for reaching the excavation boundary under the action of groundwater with different flow rates.

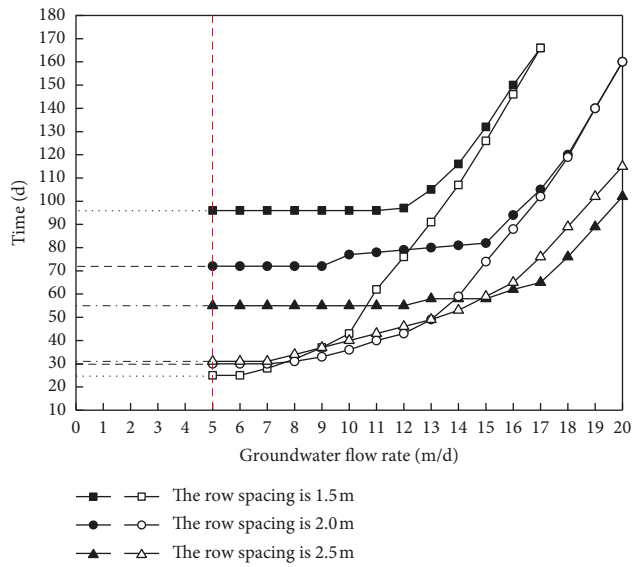

Figure 25: The closure time of the frozen wall and the time to reach the excavation boundary with different row spacings.

groundwater flow rate is greater than 10 m/d, the intersection time of the downstream inner ring position is earlier than that of the upstream position. After the frozen wall is closed, the unfrozen area inside the frozen wall is no longer affected by flowing groundwater; therefore, the time when the frozen area reaches the intended excavation boundary will not change significantly under the flow velocity within 15 m/d. When the flow rate is further increased, the interval between the closure time of the frozen wall of the upstream position and downstream area is longer. Therefore, before the frozen wall in the upstream position is closed, the frozen areas on both sides and downstream have developed to the position to be excavated. In this case, the closure time of the frozen wall of the upstream outer ring is basically the same as the time when the entire frozen wall extends to the boundary to be excavated.

To study the influence of the row spacing of the freezing pipes on the development law of the freezing temperature field, the row spacing is adjusted to 2.5 m and 1.5 m while keeping the number of auxiliary freezing pipes unchanged. The closure time and the time when the frozen wall develops to the boundary to be excavated corresponding to the two cases are compared with those of the original freezing scheme (Figure 25; the curve formed by the solid figure represents the variation of the time required for the frozen wall to reach the excavation boundary with the flow rate, and the curve formed by the hollow figure represents the variation law of the closure time of the frozen wall with the flow rate).

According to Figure 25, the influence of the row spacing on the closure time of the frozen wall can be found. Under the action of groundwater with a small flow rate, when the row spacing increases, the time to complete freezing becomes longer. The reason is that when the groundwater flow rate is small, the time when the frozen wall formed by the main freezing pipes and the freezing wall formed by the auxiliary freezing pipes are integrated is the main factor affecting the final closure time of the entire frozen wall. When the spacing of the rows is increased, intersection of the two takes longer, which leads to a longer closure time of the entire frozen wall.

Under the action of groundwater with a large flow rate, when the row spacing increases, the closure time of the entire frozen wall becomes shorter. The reason for this is that as the groundwater flow rate increases, the intersecting time of the frozen wall formed by the upstream main freezing pipes becomes the main factor affecting the closure time of the entire frozen wall. The increase of the row spacing leads to the reduction of the pipe spacing of the auxiliary freezing pipes, and the intersection time of the frozen wall formed by the auxiliary freezing pipes becomes shorter. After that, the impact of the water flow on the frozen zone of the main freezing pipes is weakened, thereby increasing the freezing efficiency of the main freezing pipe and shortening the closure time of the entire frozen wall.

It can be seen from Figure 25 that the larger the row spacing, the shorter the time required for the frozen wall to develop to the excavation boundary. The reason is that after the row spacing is increased, the distance between the auxiliary freezing pipe arrangement circle and the excavation boundary is shortened, so the time required for the frozen wall to expand to the excavation boundary is reduced.

Further analysis shows that when the row spacing of the freezing pipes is large, it takes a long time for the frozen wall formed by the auxiliary freezing pipes to intersect with the frozen wall formed by the main freezing pipes, resulting in the excessive expansion of the frozen wall to the interior of the excavation boundary in the late stage of freezing. At the same time, due to the large spacing between the rows, the

temperature of the frozen soil between the main freezing pipe arrangement ring and the auxiliary freezing pipe arrangement ring is relatively high, and the overall strength of the frozen wall cannot meet the design requirements, which adversely affects the later excavation. When the row spacing of the freezing pipe is small, the cooling capacity will be concentrated near the freezing pipe arrangement circle, and the time required for the freezing wall to reach the design thickness becomes long, which causes waste of energy and delays the construction period of the excavation.

In order to achieve a reasonable distribution of cooling capacity and ensure that the strength and thickness of the frozen wall meet the design requirements, the row spacing of the freezing pipes should be controlled within a reasonable range. Through calculation, the reasonable range of the row spacing of the double-row freezing pipe design scheme is 2~2.5 m.

5. Conclusions and Recommendations

We constructed a numerical calculation model of hydrothermal coupling based on the law of conservation of energy and mass. This model considers groundwater flow, heat change during the freezing process, and the influence of the absolute porosity reduction on seepage during the freezing process. The accuracy of the model was verified by large-scale laboratory tests. Based on the actual layout scheme of the frozen pipes, numerical calculation models of the freezing temperature field of the single-row pipes and double-row pipes under the action of groundwater were constructed. The conclusions drawn from this research are as follows:

(1) Groundwater with a flow rate of less than 5 m/d does not have a significant effect on the artificial freezing temperature field. The layout scheme of single-row freezing pipes is suitable for the formation of freezing under the action of the groundwater with a flow rate of less than 10 m/d, while the layout scheme of double-row freezing pipes is suitable for formation freezing under the action of the groundwater with a flow rate of less than 20 m/d.

(2) During the development of the freezing temperature field of the single-row pipes, the groundwater flow rate increases as the range of the unfrozen area decreases because groundwater flows through the middle of the frozen area between the adjacent two freezing pipes. When the frozen wall is about to be closed, the groundwater flow rate at this position can reach 5 to 7 times the initial flow rate, resulting in slower expansion of the freezing range just before closure.

(3) During the freezing process, the frozen range upstream is most affected by the water flow; increasing water flow will cause the frozen area upstream to decrease sharply, while the frozen wall areas on both sides are less affected by the water flow. Therefore, in the design of the arrangement of the freezing pipes, the installation density of the freezing pipes in the upstream regions should be appropriately increased, thereby improving the freezing efficiency of the entire freezing pipe action area.

(4) The pipe spacing and the spacing of the rows have significant effects on the formation of the entire frozen wall. In the design of the single-row pipes, a reasonable range of pipe spacing is 1–1.3 m. In the design of the double-row pipes, a reasonable range of the row spacing is 2–2.5 m.

(5) A "group-pipe effect" will occur, when the three freezing pipes are arranged in a triangle. In the future research, we will study the formation law of this "group-pipe effect" by changing the row spacing and the pipe spacing under the action of groundwater with different flow rates.

Data Availability

The data used to support the findings of this study are available from the corresponding author upon request.

Conflicts of Interest

The authors declare that they have no conflicts of interest.

Acknowledgments

This work was supported by the National Natural Science Foundation of China (grant nos. 51878005 and 51374010) and National Science and Technology Major Project (no. 2016YFC0600902-01).

References

[1] G. Russo, A. Corbo, F. Cavuoto, and S. Autuori, "Artificial ground freezing to excavate a tunnel in sandy soil. measurements and back analysis," *Tunnelling and Underground Space Technology*, vol. 50, pp. 226–238, 2015.

[2] X.-D. Hu, T. Fang, and Y.-G. Han, "Mathematical solution of steady-state temperature field of circular frozen wall by single-circle-piped freezing," *Cold Regions Science and Technology*, vol. 148, pp. 96–103, 2018.

[3] D. Li, X. Yang, and J. Chen, "A study of triaxial creep test and yield criterion of artificial frozen soil under unloading stress paths," *Cold Regions Science and Technology*, vol. 141, pp. 163–170, 2017.

[4] E. Pimentel, S. Papakonstantinou, and G. Anagnostou, "Numerical interpretation of temperature distributions from three ground freezing applications in urban tunnelling," *Tunnelling and Underground Space Technology*, vol. 28, no. 1, pp. 57–69, 2012.

[5] A. M. Haxaire, M. Aukenthaler, and R. B. J. Brinkgreve, "Application of a thermo-hydro-mechanical model for freezing and thawing," *Procedia Engineering*, vol. 191, pp. 74–81, 2017.

[6] K. M. Neaupane, T. Yamabe, and R. Yoshinaka, "Simulation of a fully coupled thermo-hydro-mechanical system in freezing and thawing rock," *International Journal of Rock Mechanics and Mining Sciences*, vol. 36, no. 5, pp. 563–580, 1999.

[7] G. M. Xu, *Study on mechanical charateristics of rock at low temperature, damage due to freezing and thawing and mutiphysical coupling problems of rock in cold Regions*, PhD thesis, Institute of Rock and Soil Mechanics, Chinese Academy of Science, Xiaohongshan, China, 2006.

[8] X. M. Zhou, M. S. Wang, and X. Z. Zhang, "Model test research on the formation of freezing wall in seepage ground," *Journal of China Coal Society*, vol. 30, no. 2, pp. 196–201, 2005.

[9] R. C. Huang, B. M. Chang, Y. S. Tsaic et al., "Influence of seepage flow on temperature field around an artificial frozen soil through model testing and numerical simulations," in *Proceedings of the 18th Southeast Asian Geotechnical Conference (18SEAGC) & Inaugural AGSSEA Conference (1AGSSEA)*, pp. 973–978, Singapore, May 2013.

[10] L. Y. Lao, Z. Q. Ji, L. L. Huang et al., "Research on the temperature field of a partially freezing sand barrier with groundwater seepage," *Sciences in Cold and Arid Regions*, vol. 9, no. 3, pp. 280–288, 2017.

[11] Z. H. Wang, X. R. Zhu, G. X. Zhu et al., "The experimental researches on the g round freezing with liquid nitrogen under water flowing," *Journal of Zhejiang University(Natural Science)*, vol. 32, no. 5, pp. 534–540, 1998.

[12] M. Vitel, A. Rouabhi, M. Tijani, and F. Guérin, "Modeling heat transfer between a freeze pipe and the surrounding ground during artificial ground freezing activities," *Computers and Geotechnics*, vol. 63, pp. 99–111, 2015.

[13] G. Anagnostou, A. Sres, and E. Pimentel, "Large-scale laboratory tests on artificial ground freezing under seepage-flow conditions," *Géotechnique*, vol. 62, no. 3, pp. 227–241, 2012.

[14] P. Yang and A. R. Pi, "Study on the effects of large groundwater flow velocity on the formation of frozen wall," *Chinese Journal of Geotechnical Engineering*, vol. 23, no. 2, pp. 167–171, 2001.

[15] J. Gao, M. M. Feng, and W. H. Yang, "Research on distribution law of frozen temperature field of fractured rock mass with groundwater seepage," *Journal of Mining and Safety Engineering*, vol. 30, no. 1, pp. 68–73, 2013.

[16] J. G. Liu, Q. Liu, D. D. Zhou et al., "Influence of groundwater transverse horizontal flow velocity on the formation of artificial horizontal freezing wall," *Journal of Basic Science and Engineering*, vol. 25, no. 2, pp. 258–265, 2017.

[17] M. Vitel, A. Rouabhi, M. Tijani, and F. Guérin, "Modeling heat and mass transfer during ground freezing subjected to high seepage velocities," *Computers and Geotechnics*, vol. 73, pp. 1–15, 2016.

[18] M. Vitel, A. Rouabhi, M. Tijani, and F. Guérin, "Thermo-hydraulic modeling of artificial ground freezing: application to an underground mine in fractured sandstone," *Computers and Geotechnics*, vol. 75, pp. 80–92, 2016.

[19] M. A. Alzoubi, A. Nie-Rouquette, and A. P. Sasmito, "Conjugate heat transfer in artificial ground freezing using enthalpy-porosity method: experiments and model validation," *International Journal of Heat and Mass Transfer*, vol. 126, pp. 740–752, 2018.

[20] M. A. Alzoubi and A. P. Sasmito, "Development and validation of enthalpy-porosity method for artificial ground freezing under seepage conditions," in *5th Joint US-European Fluids Engineering Division Summer Meeting*, pp. 1–9, Montreal, Canada, June 2018.

[21] J. Lin, H. Cheng, H.-B. Cai, B. Tang, and G.-Y. Cao, "Effect of seepage velocity on formation of shaft frozen wall in loose aquifer," *Advances in Materials Science and Engineering*, vol. 2018, Article ID 2307157, 11 pages, 2018.

[22] S. B. Huang, Y. L. Guo, Y. Z. Liu, L. H. Ke et al., "Study on the influence of water flow on temperature around freeze pipes and its distribution optimization during artificial ground freezing," *Applied Thermal Engineering*, vol. 135, pp. 435–445, 2018.

[23] S. B. Huang, Q. S. Liu, A. P. Cheng et al., "A fully coupled thermo-hydro-mechanical model including the determination of coupling parameters for freezing rock," *International Journal of Rock Mechanics and Mining Sciences*, vol. 103, 2018.

[24] S. B. Huang, Q. S. Liu, A. P. Cheng et al., "A coupled hydro-thermal model of fractured rock mass under low temperature and its numerical analysis," *Rock and Soil Mechanics*, vol. 39, no. 2, pp. 735–744, 2018.

[25] M. Ahmed, M.-M. Zhou, and M. Zaki Abdelrehim, "Optimization of artificial ground freezing in tunneling in the presence of seepage flow," *Computers and Geotechnics*, vol. 75, 2016.

Hindawi
Advances in Materials Science and Engineering
Volume 2019, Article ID 7681760, 8 pages
https://doi.org/10.1155/2019/7681760

Research Article

Longitudinal Reservoir Evaluation Technique for Tight Oil Reservoirs

Yutian Luo,[1,2,3] **Zhengming Yang**,[1,3] **Zhenxing Tang**,[4] **Sibin Zhou**,[5] **Jinwei Wu**,[5] **and Qianhua Xiao**[6]

[1]*University of Chinese Academy of Sciences, Beijing 100049, China*
[2]*Institute of Porous Flow and Fluid Mechanics, Chinese Academy of Sciences, Langfang 065007, China*
[3]*Research Institute of Petroleum Exploration and Development, Petrochina, Langfang, Hebei 065007, China*
[4]*Exploration and Development Research Institute, Jilin Oilfield Company, Songyuan 138001, China*
[5]*Exploration and Development Research Institute of Sinopec North China Branch, Zhengzhou 450006, China*
[6]*Chongqing University of Science and Technology, Chongqing 401331, China*

Correspondence should be addressed to Yutian Luo; luoyutian@petrochina.com.cn

Received 23 September 2018; Revised 3 November 2018; Accepted 5 December 2018; Published 6 January 2019

Guest Editor: Jianchao Cai

Reservoir evaluation is a method for classifying reservoirs and the description of heterogeneity quantitatively. In this study, according to the characteristics of longitudinal physical properties of tight oil reservoirs, advanced experimental techniques such as nuclear magnetic resonance, high pressure mercury intrusion, and X-ray diffraction were adopted; the flow capacity, reservoir capacity, ability to build an effective displacement system, and the ability to resist damage in reservoir reconstruction were considered as evaluation indexes; average throat radius, percentage of movable fluid, start-up pressure gradient, and the content of clay minerals were taken as the evaluation parameters. On the above basis, a longitudinal evaluation technique for tight oil reservoirs was established. The reservoir was divided into four categories by using this method. The reservoirs with a depth 2306.54 m–2362.07 m were mainly type I and II reservoirs, and the reservoirs with a depth of 2362.07 m–2391.30 m were mainly reservoirs of type II and III. The most effective development was water injection in the upper section and gas injection in the lower section.

1. Introduction

China has large reserves of tight oil, and the tight oil reserves in the onshore basin are about 20.0×10^8 t, which are mainly distributed in the Ordos, Songliao, Junggar, and Sichuan basins [1–3]. At the end of the "12th Five-Year Plan," the major oil fields have been explored for the large-scale development of tight oil reservoirs. During the "13th Five-Year Plan" period, the tight oil reservoirs will become an important substitute energy source in China [4]. The primary problem that constrains the effective development of tight oil was how to accurately describe the heterogeneity of tight oil reservoirs. The physical properties of tight oil reservoirs in different oil fields in China were significantly different, and the reservoir porosity and permeability were extremely low [5, 6]. In the evaluation of low-permeability and tight oil reservoirs, Chinese scholars have done a lot of research. Yang et al. and Zhang et al. used a five-parameter method to evaluate the low-permeability reservoirs [7, 8]. Xiao used a six-parameter method to evaluate the tight oil reservoirs [9]. Jia et al. put forward 10 geological parameters to evaluate the tight oil reservoirs [10]. Zou et al. presented the six-property method for the evaluation, considering the geological and engineering factors of the reservoir [11]. The above research studies mainly focused on the differences among reservoirs in different oil fields or blocks. The evaluation parameters are generally calculated based on the mean values of reservoir physical properties, without taking the physical property parameter variations of the tight reservoirs in the longitudinal section into consideration. Therefore, the accurate description of the tight reservoirs can hardly be obtained. In this study, the multiparameters that reflect the most

significant longitudinal heterogeneity of the tight reservoirs were adopted to evaluate the tight reservoirs. The throat radius curve was plotted to describe the change of reservoir seepage capacity, the percentage curve of the movable fluid was plotted to show the change of fluid storage capacity, the pressure gradient curve was used to present the variation of reservoir displacement capacity, and the clay percentage curve was employed to explain the variation of difficulty in the reservoir energy supplement. Based on the comprehensive reservoir evaluation result, the development mode was determined, and the development "sweet spot" [12] areas in the tight reservoirs were preferred. Different types of reservoirs are suitable for different injection media. Hence, it is very important to study reservoir properties. For example, Jia et al. evaluated the effects of CO_2, CH_4, and N_2 injection on shale oil recovery [13].

2. Materials and Methods

2.1. Rock Samples. In this study, taking the tight sandstone of K1q4 of Jilin Oilfield in Songliao Basin as the research object, the rock cores were collected from the same layer of three adjacent wells (namely, No. 1 well, Qian262 Well; No. 2 well, Qian 246 Well; and No. 3 well, Qian21 Well), with the coring depth of 2,309 m, 2,321 m, and 2,371 m, respectively. Rock samples have a porosity of 13.14%–15.20% and a permeability of $(0.39–1.86) \times 10^{-3}\ \mu m^2$, which was typical for the tight reservoir.

2.2. Experimental Methodology. Scanning electron microscopy (SEM) was often used to capture high-resolution images that recognize rock structural features, mineral types, and reservoir spatial characteristics. It can not only observe the microscopic characteristics of rock samples under high magnification, but can also qualitatively and semiquantitatively analyze different components in the sample. A Zeissbeam-540 FIB scanning electron microscope (Zeiss, Germany) was employed to study the pore and mineral characteristics of tight rock samples, with a magnification of 100 times. Electron microscopy was used for visual observation of pores.

Pore distribution characteristics of tight rock samples were studied using an ASPE 730 rate-controlled mercury intrusion instrument manufactured by US Coretest. These tests were conducted with a mercury-injection pressure of 0–1000 psi (about 7 MPa), a mercury-penetration speed of 0.00005 mL/min, a contact angle of 140°, an interfacial tension factor of 485 dyn/cm, and a physical size of approximately 1.5 cm^3. During rate-controlled mercury intrusion, mercury can be injected into pore volumes of rocks under extremely low mercury-penetration speed (0.00005 ml/min) without changing the surface tension or contact angle to ensure quasistatic mercury intrusion processes [14, 15]. In accordance with changes in mercury-penetration pressures, data related to pore structures could be acquired. With the distribution of pore throats and quantities of pores known directly, pore radius, pore throat radius, and other characteristic parameters of microscopic pore structures in rocks could be obtained. Rate-controlled mercury intrusion was used to quantitatively describe the size of the pores.

The fluid distribution of pores in tight rocks was studied using the RecCore 2500 NMR instrument independently developed by the Institute of Porous Flow and Fluid Mechanics, Chinese Academy of Sciences. These tests were conducted with a resonance frequency of 2.38 MHz, an echo time of 0.3 ms, a recovery time of 6000 ms, an echo number of 2048, and an experimental temperature of 25°C. Since the oil or water was rich in hydrogen nuclei and had a nuclear magnetic moment, the nuclear magnetic moment would generate energy-level splitting in the applied static magnetic field. If a specific radio frequency magnetic field was applied, the nuclear magnetic moment would undergo an absorption transition, resulting in a nuclear magnetic resonance phenomenon. NMR was used to retrieve pore structure information of tight reservoirs by testing T_2 (transverse relaxation time) spectrum of saturated oil or water in rock cores. We used a paramagnetic substance dissolved in water to eliminate the water signal in NMR. This method could distinguish water and oil in tight reservoirs. NMR was used to describe the law of fluid occurrence in pores.

3. Results and Discussion

3.1. Development Characteristics and Evaluation Difficulties of Tight Reservoirs. Because tight oil reservoirs were characterized by source generation and source accumulation in situ and it had short-term migration, the heterogeneity of the pore distribution was relatively strong [5, 8, 16]. The results of the permeability test using different gases were significantly different [17]. In keeping with the conventional test method, in this paper, the permeability was tested using N_2. According to the SEM images of tight rock cores (shown in Figure 1; the porosity and permeability were tested using industry standard methods), it was found that the lower the porosity of the core, the more microscopic pores the rock contains and the poorer the pore connectivity, and the cement was mainly composed of an illite-smectite mixed layer and was mixed with a small amount of chlorite. With the increase in permeability, the core structure loosened increasingly, large pores appeared gradually, the number of pores increased significantly, and the connectivity became better.

The difference between reservoirs was relatively small in the horizontal plane in the same depth. Through comparison of the tight cores collected from different depths, the difference between reservoirs was significant in the longitudinal plane. As shown in Table 1, the variation of rock porosity ranges from 0.33% to 2.52%, with an average of 1.32%; the variation of permeability ranges from 7.14% to 27.96%, with an average of 16.39%. As shown in Table 2, the variation of rock porosity ranges from 11.20% to 13.27%, with an average of 12.19%; the variation of permeability ranges from 68.66% to 79.03%, with an average of 73.11%. The difference between tight reservoirs in the longitudinal direction was much larger than that in the horizontal direction; it was therefore inapplicable to evaluate the tight reservoir using porosity and permeability.

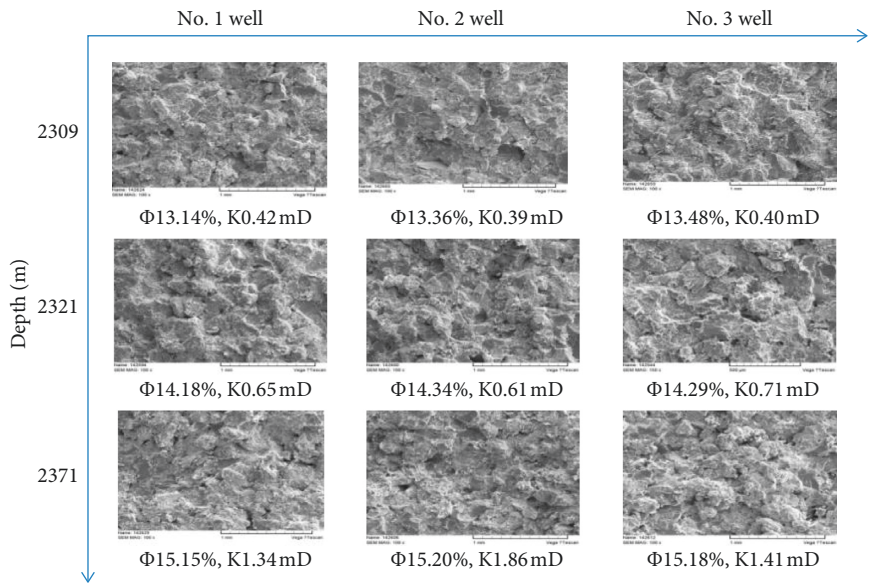

Figure 1: Scanning electron microscope images of tight reservoirs.

Table 1: Variation of porosity and permeability of tight reservoirs in the horizontal direction.

Depth (m)	Horizontal porosity average (mD)	Horizontal porosity variation (%)	Horizontal permeability average (mD)	Horizontal permeability variation (%)
2,309	13.33	2.52	0.40	7.14
2,321	14.27	1.12	0.66	14.08
2,371	15.18	0.33	1.54	27.96

Table 2: Variation of porosity and permeability of tight reservoirs in the longitudinal direction.

Well no.	Longitudinal porosity average (%)	Longitudinal porosity variation (%)	Longitudinal permeability average (%)	Longitudinal permeability variation (%)
1	14.16	13.27	0.80	68.66
2	14.30	12.11	0.95	79.03
3	14.32	11.20	0.84	71.63

In order to study the pore distribution of the tight reservoir, the core samples of Qian262 Well was continuously collected for mercury intrusion experiments. According to the mercury intrusion test results, the pore distribution curves at different scales were plotted, as shown in Figure 2(a), and the pore size was divided into five intervals using nuclear magnetic and centrifugal methods in the literature [18]. Namely, the first was nanopores with radius less than 25 nm, whose fluid cannot be developed; the second was nanopores with radius of 25–50 nm, whose fluid can be exploited by osmotic and displacement; the third was nanopores with radius of 50–100 nm, whose fluid can be mined by gas injection; the fourth was submicron pores with radius of 0.1–1 μm, whose fluid can be developed by a water injection-mixed surfactant; and the fifth was micropores with radius larger than 1 μm, whose fluid can be exploited by water injection. As seen from Figure 2(a), the pore distribution of the tight reservoir varies sharply; the third type of pores with radius of 50–100 nm has the largest variation, with the lowest content of 1.5% and the highest content of 44.6%; the content of the first type of pores with radius less than 25 nm accounts for 20%–40%; the reservoir also contains considerable amounts of the fourth type of pores with radius of 0.1–1 μm, and there was an extremely small amount of the fifth type of pores with radius larger than 1 μm.

Nuclear magnetic resonance (NMR) tests were carried out to measure the fluid content in different sizes of the pores [19, 20]. The result is shown in Figure 2(b). It was observed that the difference in fluid distribution in the reservoir was also obvious. The fluid in the nanopores accounts for about 60%, and it is as high as 90% in some depths. In addition, about 10% of the fluid exists in the micropores and 30% fluid in the submicron pores. It can be seen from Figure 2 that it was difficult to describe accurately the distribution of pores and fluids in tight reservoirs by a simple number. Since the formation of tight reservoirs mainly depends on self-generation and self-storing or short-term migration [18], the physical properties of tight reservoirs were not as

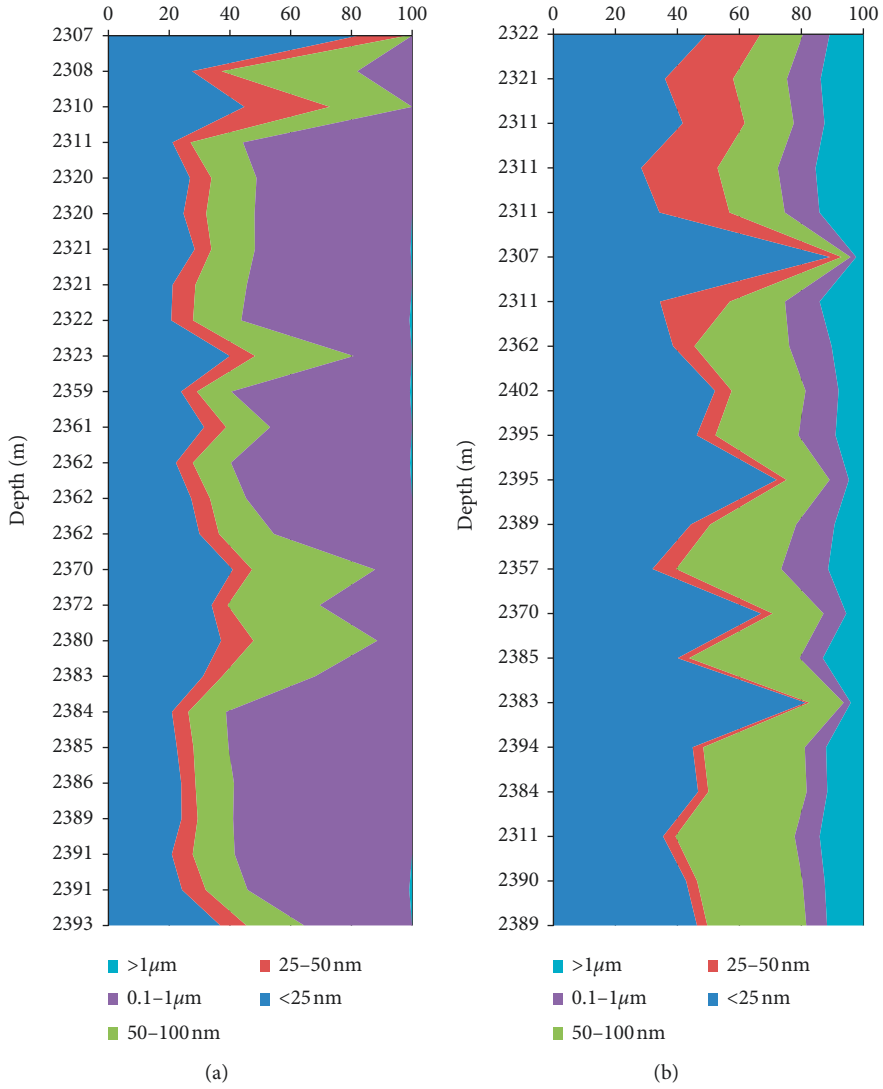

Figure 2: Pore distribution characteristics of tight reservoirs at different scales. (a) Pore distribution at different scales. (b) Fluid distribution in different pore spaces.

uniform as those of conventional sandstone reservoirs, causing dramatic changes in reservoir pores and fluid. Therefore, multiparameter evaluation of tight reservoirs with different depths was necessary.

3.2. Longitudinal Multiparameter Comprehensive Evaluation for Tight Oil Reservoirs. Four parameters were selected to characterize the longitudinal changes of reservoirs: (1) Average throat radius, whose distribution presents the change of reservoir seepage capacity [16]; (2) Percentage of movable fluid, whose distribution explains the change of occurrence characteristics of the reservoir fluid and determines the development potential of the reservoirs [21–23]. The movable fluid of the tight reservoir corresponds to the amount of fluid measured by nuclear magnetic resonance at a centrifugal force of 417 psi; (3) The start-up pressure gradient, whose distribution characterizes the difficulty degree in establishing an effective displacement system for the reservoir [24, 25]; and (4) The content of clay mineral, whose distribution shows the reservoir damage suffered from water injection [26–28]. In the reservoir evaluation in different blocks, some scholars introduced parameters such as brittleness index and pressure coefficient. However, for the same reservoir, these parameters have little change in the longitudinal direction and cannot well reflect the physical properties of the tight reservoir. Therefore, this study did not consider these evaluation parameters.

According to the test and analysis results of tight sandstone cores collected from K1q4 of the Songliao Basin, the classification evaluation intervals of each parameter were divided into four categories, as shown in Table 3. The conventional reservoir evaluation methods only obtain the evaluation results based on the single parameter, ignoring the comprehensive evaluation and the influence of various parameters on the comprehensive evaluation results. In this study, selecting the appropriate parameters [13] for evaluation the comprehensive evaluation results were divided

Table 3: Longitudinal evaluation interval of tight reservoirs.

Classification interval	Throat radius (μm)	Movable fluids saturation (%)	Starting pressure gradient (MPa/m)	Clay minerals (%)	Comprehensive evaluation
I	0.6–0.8	60–75	0–0.3	0–5.0	>5.0
II	0.4–0.6	45–60	0.3–0.6	5.0–10.0	3.5–5.0
III	0.2–0.4	30–45	0.6–0.9	10.0–15.0	1.5–3.5
IV	0–0.2	15–30	0.9–1.2	15.0–20.0	0–1.5

into four categories accordingly, and a comprehensive evaluation grading calculation formula was formed as follows:

$$D = \ln\left(\alpha * \frac{(r_0/r_{sta}) * (s_0/s_{sta})}{(\lambda_0/\lambda_{sta}) * (m_0/m_{sta})}\right), \quad (1)$$

where D was the comprehensive evaluation result; r_0 was the average throat radius, μm; r_{sta} was the evaluation limit of average throat radius, μm; s_0 was the percentage of the movable fluid, %; s_{sta} was the evaluation limit of the percentage of the movable fluid, %; λ_0 was the start-up pressure gradient, MPa/m; λ_{sta} was the evaluation limit of the start-up pressure gradient, MPa/m; m_0 was the content of clay mineral, %; m_{sta} was the evaluation limit of the content of clay mineral, %; and α was the reservoir influence factor.

In order to compare the changes of each parameter in the reservoir, the graded evaluation results of each parameter were normalized, as shown in formulas (2) and (3).

When the evaluation parameters were positively correlated with the comprehensive evaluation results,

$$D_N = \frac{P_0}{P_{max} - P_{min}}. \quad (2)$$

When the evaluation parameters were negatively correlated with the comprehensive evaluation results,

$$D_N = 1 - \frac{P_0}{P_{max} - P_{min}}, \quad (3)$$

where D_N was the normalized evaluation result of single parameter; P_0 was the single parameter value; P_{max} was the upper limit of single parameter evaluation; and P_{min} was the lower limit of single parameter evaluation.

The classification results of the evaluation parameters were placed in the same coordinate system to analyze the changes between the parameters. The sampling cores were collected from the tight sandstone of K1q4 of Jilin Oilfield in Songliao Basin, with a depth of 2,306.5–2,391.3 m, and mercury intrusion test, nuclear magnetic resonance test, percolation curve test, and X-ray diffraction measurement were carried out. The parameters that vary with reservoir depth were obtained, including the throat radius, the percentage of movable fluid, the start-up pressure gradient, and the content of clay mineral. Longitudinal subsection parameter evaluation results and comprehensive evaluation results of tight oil reservoirs were plotted according to formulas (1)–(3), as shown in Figure 3.

It can be seen from Figure 3 that the throat radius values in the longitudinal direction of the tight reservoir were mainly categorized into type IV reservoir, and the fluctuation range was small, indicating that the reservoir was relatively tight, the pore throat was small, and the seepage capacity was poor. The percentage values of the movable fluid were mainly categorized into type III, type II, and type I reservoirs, and the fluctuation range crosses three intervals, indicating that the occurrence difference of the reservoir fluids was large. The start-up pressure gradient was dominated by type III, II, and I reservoirs, indicating the difficulty degree of reservoir development was relatively higher, and attention should be paid to water channeling and gas channeling when replenishing energy. Clay mineral content was mainly dominated by type III and type II reservoirs, and attention should be paid to reservoir damage during development. There were five reservoir types (I-IV) in the longitudinal comprehensive evaluation of the tight reservoir, and the fluctuation range was extremely large. In the development of tight reservoirs, a rational plan and the development modes should be made according to the longitudinal comprehensive evaluation curve of the reservoir.

3.3. Optimization of Development Modes Adopting Longitudinal Evaluation of Tight Oil Reservoirs. The longitudinal distribution of tight oil reservoirs varies a lot. The recovery of reservoirs with different evaluation results was also quite different using water injection or gas injection, as shown in Figure 4. Figure 4(a) shows the time-dependent recovery curve of four different types of reservoirs with water injection. The recovery of the four types of reservoirs increased rapidly in the early stage but remained stable in the later period. Type I reached the final recovery first, and type IV was the slowest. Figure 4(b) presents the time-dependent recovery curve of four different types of reservoirs with nitrogen injection. The evaluation results showed that the recovery degree of the reservoirs with better evaluation results increased rapidly in the early stage and then gradually slowed down after a certain period of development. In the later period of development, the recovery degree of poor reservoirs with poorer evaluation results was larger than that of the reservoirs with better evaluation results. The type IV reservoir had the highest recovery degree, the type I reservoir had the lowest recovery degree, and type II and III reservoirs were in the middle.

It can be seen from Table 4 that the recovery ratios of the different types of reservoirs adopting different development modes vary significantly. In the case of all reservoir

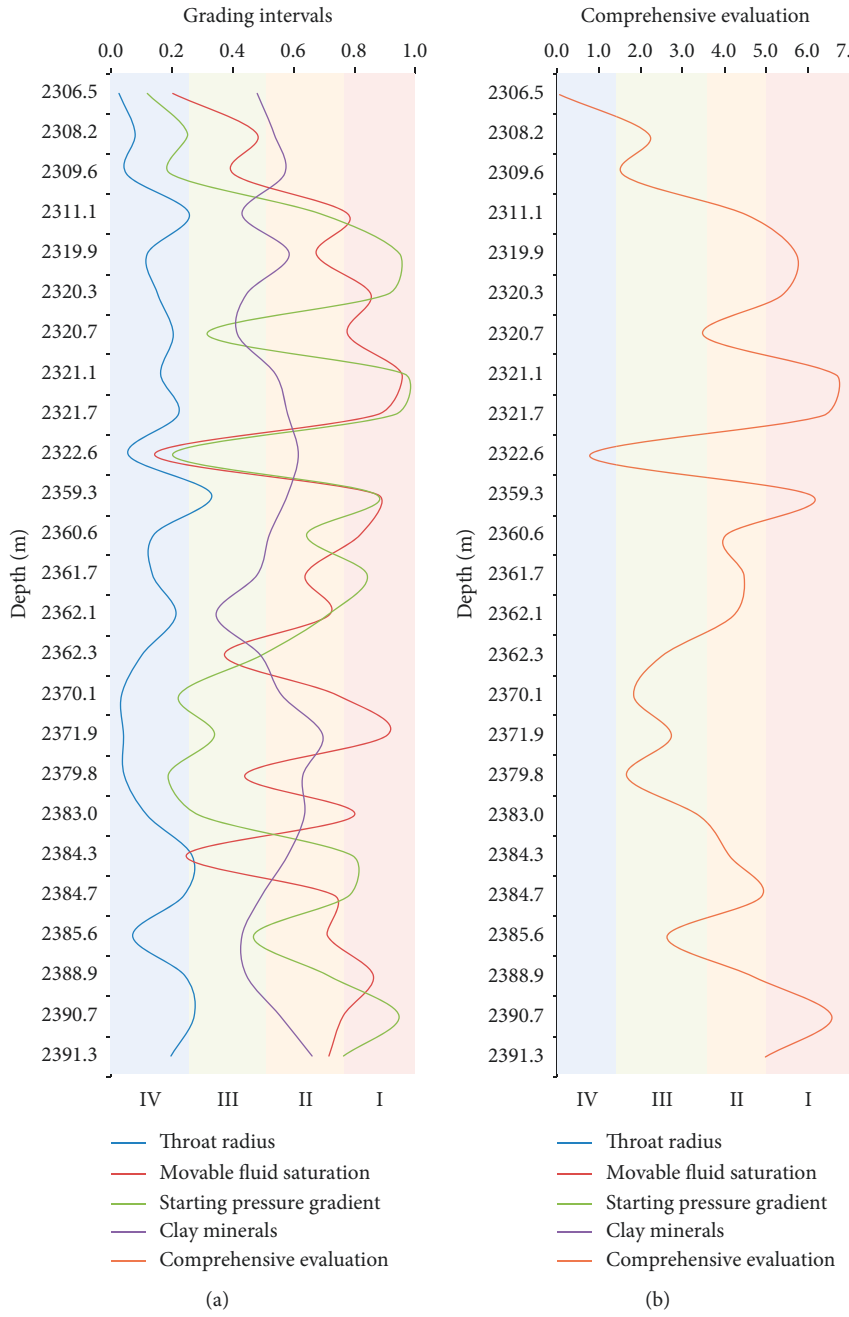

Figure 3: Comprehensive evaluation results and longitudinal grading evaluation results of tight reservoirs.

types involved, type I reservoir was most suitable for water injection development, and type IV reservoir was most suitable for gas injection development. Taking the tight oil reservoir studied in this paper as an example, the reservoirs with a depth of 2,306.54–2,362.07 m were mainly dominated by type I and II reservoirs, and the reservoirs with a depth of 2,362.07–2,391.30 m were mainly dominated by type II and III reservoirs. Through comparison of water injection in the whole reservoir, gas injection in the whole reservoir, water injection in the upper reservoir and gas injection in the lower reservoir, and gas injection in the upper reservoir and water injection in the lower reservoir, the final recovery ratio of the tight oil reservoir under different development modes can be obtained according to formula (4), as shown in Table 5:

$$E_R = \sum_{i=1}^{4} E_{R_i} * h_i, \tag{4}$$

where E_R was the recovery of the tight oil reservoir, %; E_{R_i} was the recovery corresponding to type I, type II, type III, and type IV reservoirs, %; h_i was the effective thickness corresponding to type I, type II, type III, and type IV reservoirs, m.

In the case of all reservoir types involved, the highest recovery (70.66%) can be obtained under the development

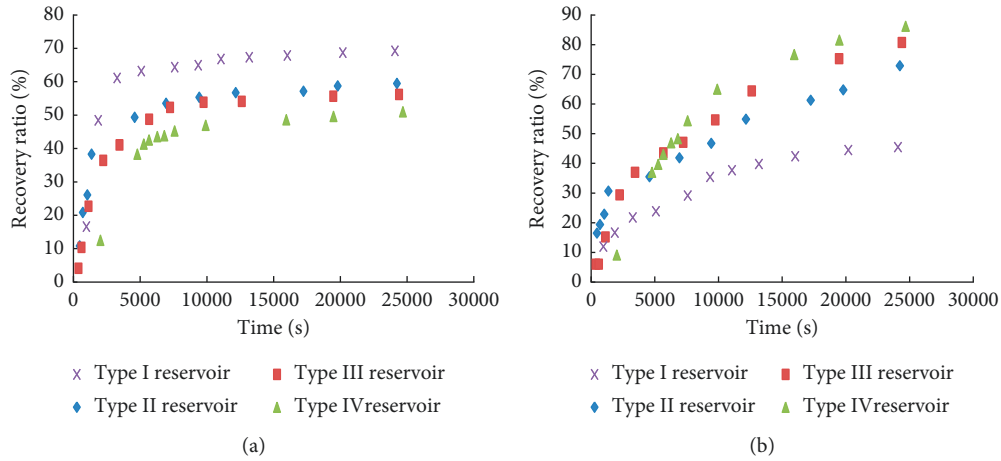

Figure 4: Recovery curve of tight reservoirs with water injection/gas injection. (a) Time-dependent recovery curve of tight reservoirs with water injection. (b) Time-dependent recovery curve of tight reservoirs with nitrogen injection.

Table 4: Recovery of different types of reservoirs.

Development mode	Type I (%)	Type II (%)	Type III (%)	Type IV (%)
Water injection	69.23	59.48	56.15	50.97
Gas injection	45.43	67.17	80.72	86.16

Table 5: Recovery of reservoirs under different development modes.

Different development mode	Water injection	Gas injection	Upper water/lower gas	Upper gas/lower water
Recovery ratio (%)	63.98	59.62	70.66	52.94

mode of water injection in the upper reservoir and gas injection in the lower reservoir; the recovery was 63.98% using the water injection method and the recovery using the gas injection mode or gas injection in the upper reservoir and water injection in the lower reservoir were both lower than those of the previous two modes.

4. Conclusions

Microscopic pore structure, fluid occurrence conditions, start-up pressure gradient, and the content of clay minerals in the longitudinal direction of tight reservoirs were analyzed in this study. Each parameter represented a physical property of the reservoir, and these parameters were independent of each other and did not affect each other, so the evaluation results obtained in this way were objective. The longitudinal evaluation method for tight reservoirs was proposed, and the optimal development mode was selected according to reservoir evaluation results. Three innovations of this study are summarized as follows:

(1) The longitudinal variations of the microscopic pore structure were bigger than the horizontal variations. The longitudinal variations of porosity and permeability were 12.19% and 73.11%, respectively. The horizontal variations of porosity and permeability were 1.32% and 16.39%, respectively. In tight oil reservoirs, the nanopores dominate and control about 60% of the flow space, the submicron pores account for about 30% of the flow space, which is the main part in the development, and the micropores were few.

(2) Four parameters, including average throat radius, the percentage of movable fluid, start-up pressure gradient, and the content of clay mineral, were applied to evaluate the reservoir. Seepage capacity, development potential of the reservoirs, the difficulty degree in development, and the reservoir damage suffered from water injection, and the four-parameter evaluation results were normalized to obtain the influence degree of different factors on the reservoir physical property. The depth-dependent comprehensive evaluation results and grading evaluation results were plotted.

(3) The recovery of tight reservoirs under different development modes was compared. According to the longitudinal comprehensive evaluation curve and the recovery, the most appropriate development method for each type of reservoir would be chosen. It can be known that the highest recovery was obtained when the mode of water injection in the upper reservoir and gas injection reservoir was adopted.

Data Availability

The data used to support the findings of this study are available from the corresponding author upon request.

Conflicts of Interest

The authors declare that they have no conflicts of interest.

Acknowledgments

We gratefully acknowledge the financial supports from the National Science and Technology Major Project (No.

2016ZX05048-001), the National Science and Technology Major Project (No. 2017ZX05069-003), and the National Natural Science Foundation of China (grant 51604053).

References

[1] S. Y. Hu, R. K. Zhu, S. T. Wu et al., "Profitable exploration and development of continental tight oil in China," *Petroleum Exploration and Development*, vol. 45, no. 4, pp. 737–748, 2018.

[2] S. J. Wang, R. J. Wei, Q. L. Guo et al., "New advance in resource evaluation of tight oil," *Acta Petrolei Sinica*, vol. 35, no. 6, pp. 1095–1105, 2014.

[3] J. H. Du, H. Q. He, J. Z. Li et al., "Progress in China's tight oil exploration and challenges," *China Petroleum Exploration*, vol. 19, no. 1, pp. 1–9, 2014.

[4] G. G. Wu, H. Fang, Z. Han et al., "Growth features of measured oil initially in place & gas initially in place during the 12th five-year plan and its outlook for the 13th five-year plan in China," *Acta Petrolei Sinica*, vol. 37, no. 9, pp. 1145–1151, 2016.

[5] Y. T. Luo, Z. M. Yang, Y. He et al., "The research of lithology characteristics and effective development in tight oil reservoir," *Unconventional Oil and Gas*, vol. 1, no. 1, pp. 47–54, 2014.

[6] H. Cander, *What are Unconventional Resources*, AAPG Annual Convention and Exhibition, Long Beach, CA, USA, 2012.

[7] Z. M. Yang, Y. Z. Zhang, M. Q. Hao et al., "Comprehensive evaluation of reservoir in low permeability oilfields," *Acta Petrolei Sinica*, vol. 27, no. 2, pp. 64–67, 2006.

[8] Z. H. Zhang, Z. M. Yang, X. G. Liu et al., "A grading evaluation method for low-permeability reservoirs and its application," *Acta Petrolei Sinica*, vol. 33, no. 3, pp. 437–441, 2012.

[9] Q. H. Xiao, *The Reservoir Evaluation and Porous Flow Mechanism for Typical Tight Oil Fields*, Institute of Porous Flow and Fluid Mechanics, University of Chinese Academy of Sciences, Langfang, China, 2015.

[10] C. Z. Jia, C. N. Zou, J. Z. Li et al., "Assessment criteria, main types, basic features and resource prospects of the tight oil in China," *Acta Petrolei Sinica*, vol. 33, no. 3, pp. 343–350, 2012.

[11] C. N. Zou, R. K. Zhu, S. T. Wu et al., "Type, characteristics, genesis and prospects of conventional and unconventional hydrocarbon accumulations: taking tight oil and tight gas in China as an instance," *Acta Petrolei Sinica*, vol. 33, no. 2, pp. 173–187, 2012.

[12] Z. Yang, L. H. Hou, S. Z. Tao et al., "Formation conditions and "sweet spot"evaluation of tight oil and shale oil," *Petroleum Exploration and Development*, vol. 42, no. 5, pp. 555–565, 2015.

[13] B. Jia, J. S. Tsau, and R. Barati, "A review of the current progress of CO2 injection EOR and carbon storage in shale oil reservoirs," *Fuel*, vol. 236, pp. 404–427, 2019.

[14] W. R. Purcell, "Capillary pressures—their measurement using mercury and the calculation of permeability therefrom," *Journal of Petroleum Technology*, vol. 1, no. 2, pp. 39–48, 2013.

[15] B. F. Swanson and B. F. Swanson, "A simple correlation between permeabilities and mercury capillary pressures," *Journal of Petroleum Technology*, vol. 33, no. 12, pp. 2498–2504, 2013.

[16] A. Hakami, A. Al-Mubarak, K. Al-Ramadan, C. Kurison, and I. Leyva, "Characterization of carbonate mudrocks of the jurassic tuwaiq mountain formation, jafurah basin, Saudi arabia: implications for unconventional reservoir potential evaluation," *Journal of Natural Gas Science and Engineering*, vol. 33, pp. 1149–1168, 2016.

[17] B. Jia, J. S. Tsau, and R. Barati, "Different flow behaviors of low-pressure and high-pressure carbon dioxide in shales," *SPE Journal*, vol. 23, no. 4, pp. 1452–1468, 2018.

[18] Z. M. Yang, R. Z. Yu, Z. X. Su et al., "Numerical simulation of the nonlinear flow in ultra-low permeability reservoirs," *Petroleum Exploration and Development*, vol. 37, no. 1, pp. 94–98, 2010.

[19] D. P. Li, *The Development of the Low Permeability Sandstone Oil Field*, Petroleum Industry Press, Beijing, China, 1997.

[20] Z. M. Yang, Y. T. Luo, Y. He et al., "Study on occurrence feature of fluid and effective development in tight sandstone oil reservoir," *Journal of Southwest Petroleum University (Science & Technology Edition)*, vol. 37, no. 3, pp. 85–92, 2015.

[21] W. M. Wang, H. K. Guo, and Z. H. Ye, "The Evaluation of development potential in low permeability oilfield by the aid of NMR movable fluid detecting technology," *Acta Petrolei Sinica*, vol. 22, no. 6, pp. 40–44, 2001.

[22] D. O. Seevers, "A nuelear magnetic method for determining the permeability of sandstones," in *Proceedings of Annual Logging SymPosium Transaetions*, Soeiety of Professional Well Log Analysts, Tulsa, OK, USA, May 1966.

[23] R. J. S. Brown and I. Fatt, "Measurement of fraetional wettability of oil fields' rocks by the nuclear magnetic relaxation method," in *Proceedings of Fall Meeting of the Petroleum Branch of AIME, SPE-743-G*, Soeiety of Petroleum Engineers, Los Angeles, CA, USA, October 1956.

[24] Y. Shi, Z. M. Yang, and Y. Z. Huang, "Study on non-linear seepage flow model for low-permeability reservoir," *Acta Petrolei Sinica*, vol. 30, no. 5, pp. 731–734, 2009.

[25] C. Dabbouk, A. Liaqat, G. Williams, and G. Beattie, "Waterflood in vuggy layer of a middle east reservoir-displacement physics understood," in *Proceedings of Abu Dhabi International Petroleum Exhibition and Conference*, Abu Dhabi, UAE, October 2002.

[26] S. B. Peng, X. Yin, J. C. Zhang et al., "Evolutionary pattern of clay mineral and rock sensitivity in water-flooding reservoir," *Acta Petrolei Sinica*, vol. 27, no. 4, pp. 71–75, 2006.

[27] Y. T. Luo and Z. Yang, "Advantageous reservoir characterization technology in extra low permeability oil reservoirs," *Journal of Engineering*, vol. 2017, Article ID 6705263, 9 pages, 2017.

[28] H. Karimaie and O. Torsæter, "Effect of injection rate, initial water saturation and gravity on water injection in slightly water-wet fractured porous media," *Journal of Petroleum Science and Engineering*, vol. 58, no. 1-2, pp. 293–308, 2007.

Hindawi
Advances in Materials Science and Engineering
Volume 2018, Article ID 9565240, 31 pages
https://doi.org/10.1155/2018/9565240

Review Article

Critical Review of Fluid Flow Physics at Micro- to Nano-scale Porous Media Applications in the Energy Sector

Harpreet Singh [1] **and Rho Shin Myong** [2]

[1]*National Energy Technology Laboratory, Morgantown, WV, USA*
[2]*School of Mechanical and Aerospace Engineering and ACTRC, Gyeongsang National University, Jinju, Republic of Korea*

Correspondence should be addressed to Harpreet Singh; harpreet.singh@netl.doe.gov

Received 12 September 2018; Accepted 18 October 2018; Published 4 December 2018

Academic Editor: Giorgio Pia

While there is a consensus in the literature that embracing nanodevices and nanomaterials helps in improving the efficiency and performance, the reason for the better performance is mostly subscribed to the nanosized material/structure of the system without sufficiently acknowledging the role of fluid flow mechanisms in these systems. This is evident from the literature review of fluid flow modeling in various energy-related applications, which reveals that the fundamental understanding of fluid transport at micro- and nanoscale is not adequately adapted in models. Incomplete or insufficient physics for the fluid flow can lead to untapped potential of these applications that can be used to increase their performance. This paper reviews the current state of research for the physics of gas and liquid flow at micro- and nanoscale and identified critical gaps to improve fluid flow modeling in four different applications related to the energy sector. The review for gas flow focuses on fundamentals of gas flow at rarefied conditions, the velocity slip, and temperature jump conditions. The review for liquid flow provides fundamental flow regimes of liquid flow, and liquid slip models as a function of key modeling parameters. The four porous media applications from energy sector considered in this review are (i) electrokinetic energy conversion devices, (ii) membrane-based water desalination through reverse osmosis, (iii) shale reservoirs, and (iv) hydrogen storage, respectively. Review of fluid flow modeling literature from these applications reveals that further improvements can be made by (i) modeling slip length as a function of key parameters, (ii) coupling the dependency of wettability and slip, (iii) using a reservoir-on-chip approach that can enable capturing the sub-continuum effects contributing to fluid flow in shale reservoirs, and (iv) including Knudsen diffusion and slip in the governing equations of hydrogen gas storage.

1. Introduction

World's energy demand is expected to grow approximately by 25–37% between 2014 and 2040 per some estimates [1, 2]. In order to secure the future energy supply while also reducing the global carbon footprints, new avenues are being explored to produce energy that is efficient and clean. Some major technologies that are either already contributing to this objective or can potentially contribute in the future include (i) electrokinetic energy conversion devices that power wide variety of applications, (ii) water desalination using synthetically created nanosized membranes, (iii) extraction of hydrocarbons from ultra-tight shale formations, and (iv) storage of hydrogen. Optimum utilization of these technologies requires understanding of fluid transport at micro- to nanosized pores and developing theoretical models that capture the physics of fluid flow at these scales to predict their performance. Understanding the material of the medium together with the physics of fluid flow is important because they are often coupled together in addition to the importance of their role independently; for instance, properties of a rock matrix (material) are important in shale to locate regions with hydrocarbons as well as in designing a hydraulic fracturing job that is strongly affected by the rock's material properties. As another example, properties of the material are used to control the performance of electrokinetic devices. While it is evident from the literature that more emphasis is given to studying the material of these

systems, similar emphasis must be given to study the physics of fluid flow. Incomplete or insufficient physics for the fluid flow can lead to untapped potential of these applications that can be used to increase their performance.

This paper reviews the current state of research for the physics of gas and liquid flow at micro- and nanoscale and identified critical gaps to improve fluid flow modeling in four different applications related to the energy sector. The review for gas flow focuses on fundamentals of gas flow at rarefied conditions, the velocity slip, and temperature jump conditions. The review for liquid flow provides fundamental flow regimes of liquid flow, and liquid slip models as a function of key modeling parameters. The four applications from energy sector considered in this review are (i) electrokinetic energy conversion devices, (ii) membrane-based water desalination through reverse osmosis, (iii) shale reservoirs, and (iv) hydrogen storage, respectively. The structure of this paper is divided into three sections: gas flow, liquid flow, and relevant applications in the energy sector, respectively.

2. Gas Flow

The flow of gas in micro/nanoscale medium is usually a function of the ratio of the molecular mean free path of a gas molecule to characteristic length of the medium; this function is referred to as the *Knudsen number*. In such mediums, collisions between a molecule and wall dominate over intermolecule collisions, which causes each molecule to act independently and control the gas properties [3], a condition often referred as *rarefied gas flow*. As a result, gas slips over the wall surface in case of flow, whereas in case of heat transfer this leads to jump in temperature. Knudsen's pioneering experimental and theoretical work [4, 5] on rarefied gas flows showed that the compressible form of the Navier–Stokes–Fourier (NSF) model [6–8] is inadequate in describing rarefied gas flows subject to the no-slip boundary condition. One of the challenges in modeling these systems is that the assumption of continuum scale does not apply because the characteristic length scale of the medium approaches the mean free path (MFP) of the molecules.

2.1. Fundamentals

2.1.1. Rarefaction and Slip Effect. Rarefaction effect in microsystems is a function of mean free path (MFP) of the gas. Usually the degree of rarefaction effect is characterized by the Knudsen number, which is defined as the ratio of the molecular mean free path (MFP) of a gas molecule to characteristic length of the medium:

$$\mathrm{Kn} = \frac{\lambda}{s}, \qquad \lambda = \mathrm{MFP} = \frac{k_B T}{\sqrt{2}\pi\sigma^2 p}, \tag{1}$$

where s is characteristic length of the medium, σ is diameter of a molecule, k_B is the Boltzmann constant, T is absolute temperature, p is pressure, and λ is MFP.

The Kn provides a direct indication whether the continuum approach for a flow of gas in a medium is applicable or not. Beyond the continuum approach, the flow is no longer near equilibrium; the assumptions of the no-slip boundary condition, thermodynamic equilibrium, and linear relation between the stress and the rate of strain fail. As the Kn increases, the rarefaction effect becomes more prominent which results in the following:

(i) Flow slippage at the wall
(ii) Flow is no long in thermodynamic equilibrium
(iii) Transfer of momentum from the bulk fluid region to the walls
(iv) Increase in mass flow rate
(v) The appropriate flow and heat transfer models depend on the range of Kn

2.1.2. Compressibility Effect. A change in pressure causes the gas properties to change in order to satisfy mass balance. For example, if the density of the gas decreases due to decrease in pressure, then it causes the gas to accelerate. Colin [9] recommended that compressibility effect is important for gas microflows when Mach number (Ma) is greater than 0.2, while Li and Guo [10] demonstrated experimentally that for an average Ma < 0.3 the effect of compressibility is negligible. The compressibility and rarefaction phenomena in gas microflows are generally coupled together, and they can have an opposite effect on each other in the slip flow and early transition regimes based on the magnitude of Reynolds number (Re):

$$\mathrm{Kn} = c\sqrt{\frac{\pi\gamma}{2}}\,\frac{\mathrm{Ma}}{\mathrm{Re}}, \tag{2}$$

where γ is the ratio of specific heats of a gas. In the above expression, $c = 1$ as given by Colin [9], whereas $c = \lambda/s$ in Zhang et al. [11].

Tang et al. [12] demonstrated experimentally that the compressibility effect causes the gas flow characteristics to deviate from conventional laminar flow at high Re regime (about Re = 2000). In general, it has been demonstrated [13, 14] that the compressibility effect results in negative curvature of the pressure distribution, while the rarefaction effect weakens the negative curvature.

2.1.3. Flow Regimes. On the basis of the Knudsen number, different flow regimes with their physics and applicable models can be defined as shown in Table 1. In the case of rarefied gas flow, continuum models are applicable for $\mathrm{Kn} \leq 0.01$, and for $\mathrm{Kn} \geq 10$ free-molecular models should be used. However, neither continuum models nor free-molecular models can be used for Kn lying in the intermediate range between the continuum and free-molecular flow regimes.

Using the general definition of the Knudsen number that is defined as the ratio of the MFP of a gas molecule to characteristic length of the medium, and the mathematical formulation of MFP, we can write Kn as a function of the characteristic length of the flowing medium (s) and the average flowing pressure in that medium (p) as follows:

Table 1: Different flow regimes as a function of Knudsen number.

Kn		Flow regime	Physics	Applicable models
Lower bound	Upper bound			
0	10^{-2}	Continuum (no slip flow)	Thermodynamic equilibrium and no-slip at the boundary	(1) Navier–Stokes equations, (2) Euler equations, (3) LBM
10^{-2}	10^{-1}	Slip flow	Nonequilibrium effects dominate near the walls. Assumptions of no-slip boundary condition, thermodynamic equilibrium, and linear stress-strain relationship fail	(1) Navier–Stokes equations with slip velocity and temperature jump boundary conditions, (2) Boltzmann gas-kinetic equation, (3) DSMC, (4) Burnett equations, (5) LBM, (6) gas-kinetic scheme, (7) method of moments
10^{-1}	10	Transition flow	Rarefaction effects dominate and slip models become more complex. Assumptions of no-slip boundary condition, thermodynamic equilibrium, and linear stress-strain relationship fail	(1) Navier–Stokes equations with slip velocity and temperature jump boundary conditions, (2) Boltzmann gas-kinetic equation, (3) DSMC, (4) Burnett equations, (5) LBM, (6) gas-kinetic scheme, (7) method of moments
10	∞	Free-molecule flow	Collisions between gas molecules and boundary surface become dominant compared to intermolecular collisions. Assumptions of no-slip boundary condition, thermodynamic equilibrium, and linear stress-strain relationship fail	(1) Boltzmann gas-kinetic equation, (2) DSMC method

Flow regimes as a function of medium and flow parameters.

$$\mathrm{Kn} = \frac{k_B T}{s\sqrt{2}\pi\sigma^2 p} = f(s, p). \tag{3}$$

The Kn is estimated from the above equation for various characteristic lengths and average flowing pressures, and the corresponding flow regimes using the values of Kn are plotted as a function of characteristic lengths and flowing pressures as shown in Figure 1.

Another measure of Kn was proposed by Tsien [15] that was based on thickness (δ) of the boundary layer on the flowing medium as $\mathrm{Kn} = \lambda/\delta$, where $\delta \propto s/\sqrt{\mathrm{Re}}$. Here Re is Reynold's number for the characteristic length s and is defined as $\mathrm{Re} = \rho u s/\mu$, where $\rho, u,$ and μ are fluid's density, velocity, and viscosity, respectively. Using these relationships, Kn for the boundary layer thickness (δ) can be defined in terms of the freestream Mach number (M) and Reynold's number as follows:

$$\mathrm{Kn}_\delta = \frac{\lambda}{\delta} = \frac{M}{\mathrm{Re}_\delta} \sim \frac{M}{\sqrt{\mathrm{Re}}}. \tag{4}$$

The Kn is estimated from the above equation for various M and Re, and the corresponding flow regimes using the values of Kn are plotted as a function of M and Re as shown in Figure 2.

It must be noted that Tsien's parameter (Kn_δ) reduces to the ordinary Kn defined for the characteristic length in the free-molecular flow regime where $\mathrm{Re} \ll 1$, such that $\delta \approx s$ that results in $\mathrm{Kn}_\delta = \mathrm{Kn}$.

For flows with large amounts of nonequilibrium, modifying boundary conditions of continuum equations to account for slip will not eliminate all sources of errors. For example, the pressure tensor in more rarefied flows turns anisotropic, whereas the derivation of continuum equations assumes an isotropic pressure field [16, 17]. In those cases, it is recommended to use higher-order equations such as Burnett [18] equations and super-Burnett equations [19]. However, in some specific cases N-S equations with slight correction can be used to match data for a high Kn number regime (0.04–8.3) as shown by some authors [20, 21].

2.1.4. Accommodation Coefficients. The accommodation coefficients describe the macroscopic estimate of the fraction of momentum and energy transfer between the impinging/incident gas molecules and the boundary wall surface; therefore, their values vary between unity (complete accommodation of gas molecules with no reflection) and zero (complete reflection of gas molecules with no accommodation on the solid surface). These two accommodation coefficients for momentum and energy transfer [22] are key parameters in the estimation of slip velocity and temperature jump, respectively. A smaller value of accommodation coefficient would lead to higher velocity slip and temperature jump, because in that case the gas molecules are less affected by the solid surface.

(1) Tangential Momentum Accommodation Coefficient. This coefficient defines the fraction of momentum transfer between the incident gas molecules and the boundary wall surface:

$$\sigma_u = \frac{\tau_i - \tau_r}{\tau_i} = 1 - \frac{\tau_r}{\tau_i}, \tag{5}$$

where σ_u is tangential momentum accommodation coefficient (TMAC), τ_i is the tangential momentum of the incident gas molecules, and τ_r is the tangential momentum of the reflected gas molecules. It can be seen that $\sigma_u = 1$ if the reflected component of the tangential momentum of the gas molecules is zero (or fully diffusive), and $\sigma_u = 0$ if the tangential momentum of the reflected molecules is equal to the tangential momentum of the incident molecules (or fully reflective/specular).

Agrawal and Prabhu [23] presented the values of TMAC as a function of gas rarefaction magnitude (Kn) by using the data reported by various researchers in the literature for both monoatomic and diatomic gases. By fitting a curve to this

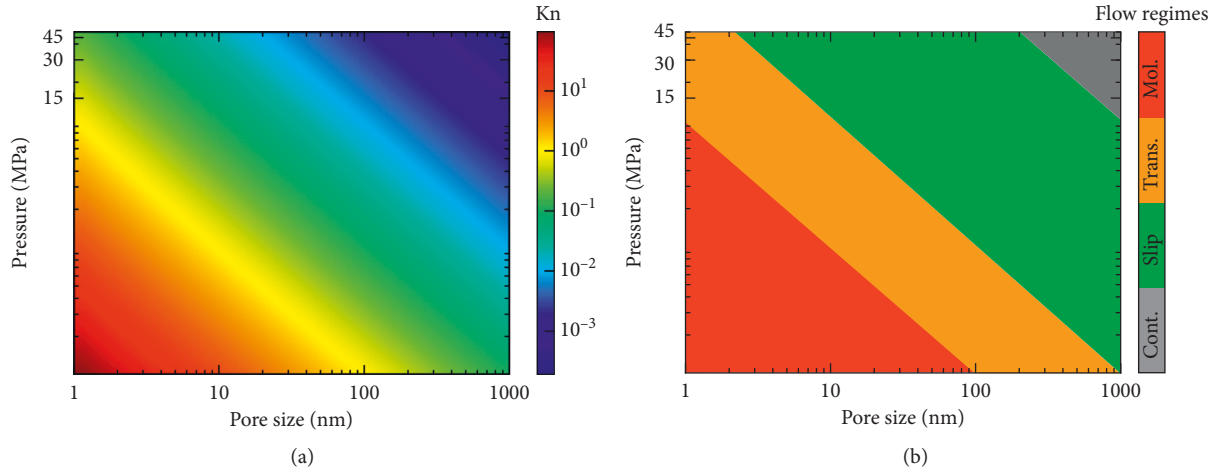

FIGURE 1: (a) Variation of Kn values as a function of channel height and pressure, and (b) graphical representation of corresponding gas flow regimes. Here, Cont., Slip, Trans., and Mol. represent continuum flow regime, slip flow regime, transition flow regime, and molecular flow regime, respectively.

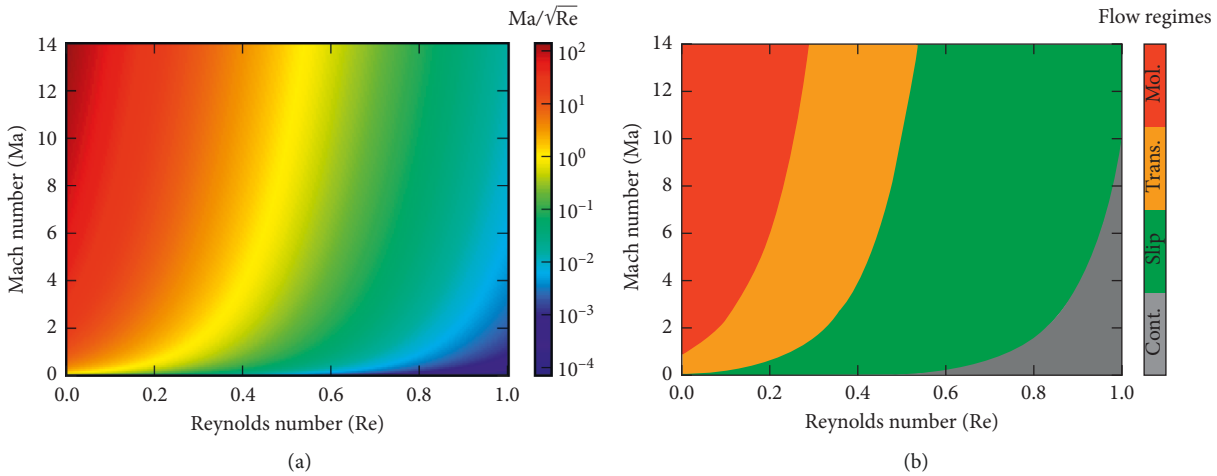

FIGURE 2: (a) Variation of $\mathrm{Ma}/\sqrt{\mathrm{Re}}$ values as a function of Re and Ma, and (b) graphical representation of corresponding gas flow regimes. Here, Cont., Slip, Trans., and Mol. represent continuum flow regime, slip flow regime, transition flow regime, and molecular flow regime, respectively.

data, they obtained and proposed the following expression for the TMAC:

$$\sigma_u = 1 - \log\left(1 + \mathrm{Kn}^{0.7}\right). \tag{6}$$

(2) Thermal Accommodation Coefficient. This coefficient defines the fraction of kinetic energy transfer between the incident gas molecules and the boundary wall surface. For a molecular beam type measurement, thermal accommodation coefficient is defined as follows:

$$\sigma_T = \frac{E_i - E_r}{E_i - E_s}, \tag{7}$$

where σ_T is *thermal accommodation coefficient* (TAC), E_i and E_r are the kinetic energies (for the normal component of velocity) of incoming and reflected gas molecules, respectively, and E_s is the kinetic energy that would be produced by a diffusive reflection at the temperature of the solid surface (T_s). Another definition of TAC that is directly related to measurement of temperatures is defined as follows:

$$\sigma_T = \frac{T_i - T_r}{T_i - T_s}, \tag{8}$$

where T_i, T_r, and T_s are the temperatures of the incident gas molecules, reflected gas molecules, and solid surface, respectively.

Song and Yovanovich [24] presented the values of TAC as a function of gas molecular weight (M_g) and T_s by using the data reported by various researchers in the literature for both monoatomic, diatomic, and polyatomic gases. By fitting a curve to this data, they obtained and proposed the following expression for the TAC:

$$\sigma_T = \exp\left[C_0\left(\frac{T_s - T_0}{T_0}\right)\right]\left(\frac{M_g^*}{C_1 + M_g^*}\right) + \left\{1 - \exp\left[C_0\left(\frac{T_s - T_0}{T_0}\right)\right]\right\}\left\{\frac{2.4\mu}{(1+\mu)^2}\right\}, \tag{9}$$

where $C_0 = -0.57$ (dimensionless), $C_1 = 6.8$ (g/mole), M_s is molecular weight of solid, $\mu = M_g/M_s$, $T_0 = 273$K, and M_g^* is defined as follows:

$$M_g^* = \begin{cases} M_g, & \text{for monoatomic gas,} \\ 1.4M_g, & \text{for dia/polyatomic gases.} \end{cases} \quad (10)$$

2.1.5. Knudsen Layer. As the flow deviates from the continuum regime, a sublayer with thickness of few mean free paths (MFPs) starts to develop from the wall of the medium such that it starts to become dominant between the bulk of the fluid and the wall of the medium (Figure 3). The molecules within the KL collide more with the boundary wall than with other molecules [25], and this results in fluid (i) having nonzero velocity at the boundary surface and (ii) exhibiting non-Newtonian properties, thus introducing discontinuity in fluid properties between the bulk fluid and the KL.

The flow in the *Knudsen layer* (KL) cannot be analyzed with conventional N-S equations, which does not account for certain slip and jump conditions expressing conservation of momentum, mass, and energy. The flow within the KL is typically regarded as being governed by the linearized Boltzmann gas-kinetic equation (LBE) [26–29] or by direct simulation Monte Carlo (DSMC) method [30–32]. Velocity slip results in increasing the mass flow rate by approximately 70%, and about one-third of this increase in flow rate is contributed by the non-Newtonian structure of the KL [33]. Therefore, accurate characterization of the KL is important in modeling of gas flow through microsystems.

(1) Description of Flow in Knudsen Layer. Accurate simulation of rarefied flow effects requires accurate description and modeling of the KL. For this, it is important to know the performance of parameters at the nonequilibrium state within the KL. The flow within the KL can be described by three different approaches: (i) wall-function method, (ii) higher-order continuum method, and (iii) power-law method.

The wall-function [33–35] is independent of the accommodation coefficient and is valid for planar surfaces up to Kn of 0.1. This function predicts the velocity gradient at the wall to be 1.7.

Higher-order continuum models [33, 36] derived from the linear Boltzmann equation (LBE) [18, 19, 33] and truncated at disparate orders have been used to describe the flow in KL. One of the motivations for the development of these higher-order hydrodynamic models to simulate rarefied flows was to reduce the prohibitive computational demand of the DSMC method [37, 38]. However, there are questions regarding validity of these models [39] and in accurately capturing the KL [33, 40]. Additionally, these models cannot treat the boundary conditions at the wall [41, 42].

Power-law model proposed by Lilley and Sader [40, 43] can be used to accurately describe the flow within the KL, and they suggest that this method describes a general physical phenomenon. The power-law model was derived by using the solution of LBE and DSMC, and it depicts the physics of velocity gradient not captured by the wall-function method [44] and the higher-order continuum method [33].

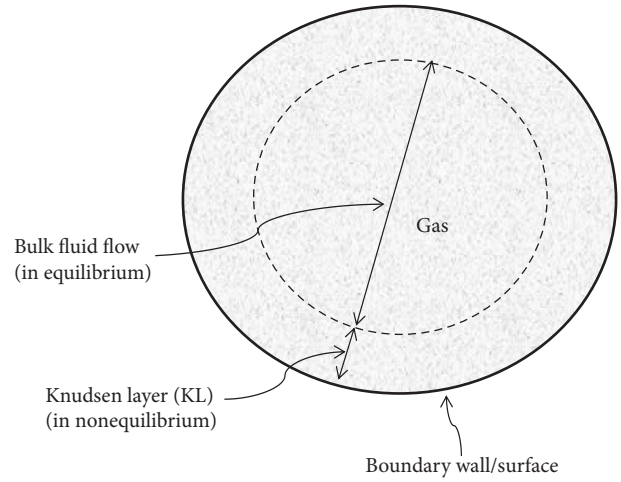

Figure 3: Schematic of the Knudsen layer near a boundary wall. The property in KL is discontinuous across which certain slip and jump conditions expressing conservation of momentum, mass, and energy are applied. The KL region is in nonequilibrium, whereas the bulk fluid flow region is in equilibrium.

(2) Thickness of Knudsen Layer. Lockerby et al. [33] presented the thicknesses of KL calculated from eight different models that used three different solution approaches of kinetic theory, higher-order continuum models, and molecular dynamics (MD) simulation. The thickness of KL obtained from these eight models varied between 0.9 λ and 4.9 λ. Gusarov and Smurov [45] presented the following expression to estimate an approximate value of KL thickness (l_c):

$$l_c = \frac{k_B T}{\pi d^2 p}, \quad (11)$$

where k_B is the Boltzmann constant, T is the absolute temperature, and p is the gas pressure.

2.2. Slip and Jump. Knudsen's pioneering experimental and theoretical work [4, 5] on rarefied gas flows showed that the compressible form of the Navier–Stokes–Fourier model [6–8] is inadequate in describing rarefied fluid flows subject to the no-slip boundary condition. A common way to model the flow of rarefied gas is to modify the no-slip and no-jump boundary conditions in continuum models by revising the basic equations of momentum, mass, and heat transfer. There have been a number of approaches to account for slip boundary conditions through the Maxwell slip (1878), second-order slip [46], and Langmuir slip [47–49]. Maxwell boundary slip condition is the first-order approximation from kinetic theory of gases that has been widely used along with its derived forms in the past 135 years. One challenge in most gas flows at micro- and nanometer scale is the wide range of Knudsen numbers and the lack of a general slip model that can be applicable from the slip regime to the transition regime. Under this scenario, a different approach using molecular models that simulate the gas flow at the

molecular level can be adopted. For example, one of most commonly used molecular simulation models is the Boltzmann gas-kinetic model [26–28], as well as many approximate methods based on particle and moments [50] like direct simulation Monte Carlo (DSMC) method and Burnett equations set [18, 26], respectively.

Several studies on theory [16, 46, 51–53], Zhang et al. [11], and experimental data [54–57] of gaseous slip flow have cumulatively added to the knowledge base of gaseous slip. Below, we briefly review the fundamentals of velocity slip and temperature jump in terms of their governing equations and provide references for further discussions on these topics.

2.2.1. Velocity Slip. Although the concept of slip was first proposed by Navier in his model in which the magnitude of the fluid velocity is proportional to the magnitude of the flow shear rate, Maxwell [58] was the first person to quantify the slip length of a gas flowing over a solid boundary surface. According to Maxwell [58], for a dilute, ideal monoatomic gas, the first-order slip condition can be described as follows:

$$u_{\text{slip}} = u_{\text{t}} - u_{\text{w}} = \frac{2-\sigma_{\text{u}}}{\sigma_{\text{u}}}\lambda\left(\frac{\partial u_{\text{t}}}{\partial z}\right)_{\text{w}} + \frac{3}{4}\frac{\mu}{\rho T}\left(\frac{\partial T}{\partial x}\right)_{\text{w}}, \quad (12)$$

where σ_{u} is TMAC, u_{slip} is the gas slip velocity at the wall, u_{t} is the gas velocity in the tangential direction, λ is the mean free path of the gas molecules, u_{w} is the velocity of the solid wall, ρ and T are the density and temperature of the gas, respectively, and subscript w represents wall surface. The directional axes are represented as x, y, and z with respect to the direction of the flow. The second term on the right hand side represents the effect of thermal creep due to an axial temperature gradient, and it provides slip to the velocity at the wall in the presence of varying temperature.

In case of a medium with curvature, the gas slip velocity at the wall can be expressed by adding an additional derivative of the gas velocity in z-direction as follows [59, 60]:

$$u_{\text{slip}} = u_{\text{t}} - u_{\text{w}} = \frac{2-\sigma_{\text{u}}}{\sigma_{\text{u}}}\lambda\left(\frac{\partial u_{\text{t}}}{\partial z} + \frac{\partial u_z}{\partial x}\right)_{\text{w}} + \frac{3}{4}\frac{\mu}{\rho T}\left(\frac{\partial T}{\partial x}\right)_{\text{w}}. \quad (13)$$

Colin [61] suggested that for significantly rough surfaces, expression for slip velocity on curved surfaces is equally applicable. Other authors who studied the effect of roughness on rarified gas flow through microchannels [62, 63] made three important conclusions regarding the impact of surface roughness on the flow behavior of gas: (i) the flow behavior in the transition regime is more sensitive to the roughness height than that in the slip flow regime, (ii) influence of roughness height on the flow behavior is more significant than that of fractal dimension, and (iii) presence of surface roughness reduces the gas slip at the boundary wall irrespective of the flow regime. Pelević and van der Meer [64] studied the effect of surface roughness on heat transfer in microflows and reported that the roughness has a marginal effect in increasing heat transfer in microflows. For further readings on various approaches to model gaseous slip flow, readers can refer to the reviews by Cao et al. [16] and Zhang et al. [11].

(1) Measurement of Gas Slip Velocity. Despite the presence of different correction coefficients [9] to account for slip flow at the boundary, there is no consensus on the most appropriate equation that can account for gas slip [65]. Additionally, accurate values of TMAC are generally not well known in the literature as it is a function of type of gas, material, and degree of rarefaction. These limitations are usually accounted by experimental data on slip length of rarefied gas flows that is defined by Maxwell's equation in its simplest form for an isothermal surface as follows:

$$u_{\text{slip}} = \frac{2-\sigma_{\text{u}}}{\sigma_{\text{u}}}\lambda\left(\frac{\partial u_{\text{t}}}{\partial z}\right)_{\text{w}} = b\left(\frac{\partial u_{\text{t}}}{\partial z}\right)_{\text{w}}, \quad (14)$$

where $b = ((2-\sigma_{\text{u}})/\sigma_{\text{u}})\lambda$, which is called as the slip length of rarefied gas flow. Maali et al. [65] reviewed the experimental techniques used to measure the slip length and TMAC for gas flow on isothermal surface. These techniques are Millikan experiment, rotating body techniques, mass flow rate measurements, and atomic force microscopy method, respectively. The gas slip is measured indirectly from these experimental techniques by using slip length, which is deduced from the measurement of the velocity of the drop in the Millikan method, the deflection of the cylinder in rotating body technique, the mass flow rate in rarefied gas flow through microchannels, and the force in atomic force microscopy method, respectively. For detailed discussion on these experimental techniques and their use in measuring gas slip, readers can refer to the review by Maali et al. [65].

2.2.2. Temperature Jump. Similar to the velocity slip expressions presented above, temperature jump boundary conditions can be written as follows:

$$T_{\text{jump}} = T_{\text{g}} - T_{\text{w}} = \frac{2-\sigma_{\text{T}}}{\sigma_{\text{T}}}\frac{2\gamma}{\gamma+1}\frac{\lambda}{Pr}\left(\frac{\partial T}{\partial z}\right)_{\text{w}}, \quad (15)$$

where σ_{T} is thermal accommodation coefficient, T_{jump} is the temperature jump at the wall, T_{g} is the gas temperature, T_{w} is the temperature of the solid wall, γ is specific heat ratio, and Pr is the Prandtl number. For further discussions on temperature jump, readers can refer to the reviews by Sharipov [56] and Colin [61].

2.2.3. Second-Order Velocity Slip and Temperature Jump. The linear velocity slip equation (12) and temperature jump equation (15) were obtained from the original (nonlinear) models in which the velocity slip and temperature jump are assumed directly proportional to the degree of non-equilibrium near the wall surface [60]:

$$u_{\text{slip}} = u_{\text{t}} - u_{\text{w}} = \frac{2-\sigma_{\text{u}}}{\sigma_{\text{u}}}\lambda\left(\frac{\Pi}{\mu}\right)_{\text{w}} + \frac{3}{4}\frac{(\gamma-1)}{\gamma/\text{Pr}}\left(\frac{Q_x}{p}\right)_{\text{w}},$$

$$T_{\text{jump}} = T_{\text{g}} - T_{\text{w}} = \frac{2-\sigma_{\text{T}}}{\sigma_{\text{T}}}\frac{2\gamma}{\gamma+1}\frac{\lambda}{\text{Pr}}\left(\frac{Q_z}{k}\right)_{\text{w}}. \quad (16)$$

Only after the degree of nonequilibrium is taken as linear with the first-order accuracy (that is, shear stress $\Pi \sim (\partial u_t/\partial z)$, tangential heat flux $Q_x \sim (\partial T/\partial x)$, and normal heat flux $Q_z \sim (\partial T/\partial z)$), the models are reduced to the well-known first-order models (Equations (12) and (15)). Therefore, if the linear constitutive relations are replaced by higher-order relations like the second-order constitutive relations, the resulting models become a second-order velocity slip and temperature jump. Such models were recently developed by Myong [66] and were applied to the theoretical analysis of the gaseous Knudsen layer in Couette flow. It was shown that the velocity gradient singularity in the Knudsen layer can be explained within the continuum framework, when the nonlinearity of the constitutive model is morphed into the determination of the velocity slip in the second-order slip and jump model. Also, the smaller velocity slip and shear stress are shown to be caused by the shear-thinning property of the second-order constitutive model, that is, vanishing effective viscosity at high Knudsen number.

2.3. Knudsen Diffusion. Diffusive transport in micro- and nanoscale mediums can occur through three different mechanisms: (i) molecular bulk diffusion, (ii) surface diffusion (sorption), and (iii) Knudsen diffusion [67]. The proportion of each of this mechanism depends on the magnitude of the Knudsen number (Kn), and Knudsen diffusion is an important mode of diffusion for large Kn such that the molecules interact more often with the walls of the medium than with each other.

The molar flow rate of gas molecules in one direction of an axis ($\dot{n}^{\pm}$) is defined from ensemble averaging Einstein's equation over a large enough number of molecules [68], and it is given as follows [69]:

$$\dot{n}^{\pm} = \pm\frac{1}{6}\lambda A\overline{v}\frac{\partial c}{\partial x}. \tag{17}$$

The entire molar flow rate ($\dot{n}$) from the two opposite directions across an axis would be

$$\dot{n} = \frac{1}{6}\lambda A\overline{v}\frac{\partial c}{\partial x} - \left(-\frac{1}{6}\lambda A\overline{v}\frac{\partial c}{\partial x}\right) = \frac{1}{3}\lambda A\overline{v}\frac{\partial c}{\partial x}, \tag{18}$$

where λ is the mean free path, A is the cross-sectional area, $\overline{v}$ is the average velocity of gas molecules, and c is the gas concentration in mole per unit volume. Now, the diffusive flux of the gas would be

$$J = \frac{\dot{n}}{A} = \frac{1}{3}\lambda\overline{v}\frac{\partial c}{\partial x} = -D\frac{\partial c}{\partial x}, \tag{19}$$

where $D\,(=(1/3)\lambda\overline{v})$ is the coefficient of diffusion that varies with the kind of diffusion mechanism; for Knudsen diffusion, D would be equivalent to diffusion coefficient for Knudsen diffusion if λ is replaced by characteristic length of the medium (s) and $\overline{v}$ follows Maxwellian distribution equal to $\sqrt{(8RT/\pi M)}$:

$$D_{\mathrm{Kn}} = \frac{1}{3}s\sqrt{(8RT/\pi M)}, \tag{20}$$

where M is the molar mass of gas, R is the universal gas constant, and T is the temperature.

The resistances of these three diffusive fluxes exist in series, so the effective diffusive flux as a result of these three mechanisms is the harmonic average [70, 71]:

$$\frac{1}{J_{\mathrm{eff}}} = \frac{1}{J_{\mathrm{m}}} + \frac{1}{J_{\mathrm{Kn}}} + \frac{1}{J_{\mathrm{sorp}}}, \tag{21}$$

where J_{eff} is the effective flux that is the harmonic average of flux due to molecular diffusion (J_{m}), flux due to Knudsen diffusion (J_{Kn}), and the flux due to sorption (J_{sorp}).

3. Liquid Flow

3.1. Fundamentals. Unlike the well-developed kinetic theory for gases, no such molecular level transport theory exists for liquids because of which it is difficult to predict molecular effects in liquids. Even though a detailed molecular theory for the thermal conductivity of monatomic liquids was developed more than half a century ago [72], the means to implement it for practical calculations have not been developed. As a result of that gap, some rough theories and empirical estimation methods are used instead [73], and one that is generally used quite often was proposed by Bridgman [74] to predict the energy transport in pure liquids. Bridgman [74] assumed the molecules of a liquid are arranged in cubic lattice, with a center-to-center spacing (δ) given by

$$\delta = \left(\frac{\overline{V}}{N_{\mathrm{A}}}\right)^{1/3}, \tag{22}$$

where $\overline{V}$ is the molar volume and N_{A} is Avogadro's number. He further hypothesized that the energy transfers from one lattice plane to the next plane with a sonic velocity v_{s} for a given liquid, and by rearranging the thermal conductivity from the rigid-sphere gas theory he derived the following equation that is known as *Bridgman's equation*:

$$k = 3\left(\frac{N_{\mathrm{A}}}{\overline{V}}\right)^{2/3}\kappa v_{\mathrm{s}}. \tag{23}$$

The above equation shows good agreement with experimental data even for polyatomic liquids, but later it was suggested that a slightly lower coefficient value of 2.80 instead of 3 gives a better agreement with the data. Here, the velocity of low-frequency sound is given as follows:

$$v_{\mathrm{s}} = \sqrt{\frac{C_{\mathrm{p}}}{C_{\mathrm{V}}}\left(\frac{\partial p}{\partial \rho}\right)_{\mathrm{T}}}, \tag{24}$$

where $C_{\mathrm{p}}/C_{\mathrm{V}}$ is the ratio of heat capacities that is nearly unity for liquids (except near the critical point) and $(\partial p/\partial\rho)_{\mathrm{T}}$ can be determined from isothermal compressibility measurements of change in density (ρ) with the corresponding change in pressure (p) of the liquid.

3.1.1. Flow Regimes. The flow regimes in gases are based on the concept of Kn, which is the ratio of the mean free path of a molecule to the characteristic length of the medium. The spacing between molecules in liquids is much smaller than the spacing between molecules in gases, so the concept of mean free path and the flow regimes based on Kn are not

valid in liquids. Because of the lack of a well-developed molecular theory for liquids, no flow regimes have been proposed for liquids in the literature. However, there is one study by Liu and Li [75] that talks about the liquid flow regimes in nanochannels. Liu and Li [75] investigated the liquid motion as a function of four parameters (fluid-fluid binding energy ε_{ff}, fluid-solid wall binding energy ε_{fw}, temperature of the system T, and external driving force F_e corresponding to the pressure drop along the channel) by using nonequilibrium molecular dynamics simulations (NEMDs). They define two dimensionless numbers to understand the competing effect between the liquid-liquid interaction and liquid-surface interaction as $[\varepsilon_{ff}/k_BT]$ and $[(\varepsilon_{fw}/k_BT) \times (\varepsilon_{fw}/F_e\sigma_{fw})]$, respectively, where k_B is the Boltzmann constant and σ_{fw} is the collision diameter (separation) at which the potential vanishes. They compute the flux using liquid argon and liquid helium flowing through a channel made of silver walls at temperatures varying from 100 K to 300 K and pressure difference varying from 33 MPa to 132 MPa. They find liquid flux values as a function of these two dimensionless numbers and illustrate their results by dividing them into different regimes, each associated with a distinct mechanism. The authors noted that the relation of the four parameters was not clear if the slip length was used instead of flux. The reason why slip length may not directly relate to the flow is because the density and viscosity of the confined fluid are nonuniform.

Using the data from the study of Liu and Li [75], we graphically illustrate the flow regimes in liquid in Figure 4 and summarize them theoretically in Table 2.

3.2. Liquid Slip. Fundamental understanding of the mechanisms that control liquid slip is still elusive. Unlike gases, the concept of mean free path is not useful for liquids because the average distance between liquid molecules is comparable to the molecular diameter. Even though it is believed unanimously that the flow enhancement in nanoscale systems is caused by liquid slip velocity at the solid surface [76, 77], the debate on understanding its mechanisms mostly revolves around four key parameters. Many theories have been developed to associate liquid slip length (L_s) as a function of liquid properties [78, 79], interaction strength between the fluid and wall material [80–84], wettability of the medium [77, 85–89], surface roughness [90–95], and liquid shear rate [81, 86, 96–100].

3.2.1. Physical Mechanisms of Liquid Slip. The physical mechanisms behind the slip are still elusive, though there are few studies [101–107] that conjecture the reasons behind the liquid slip as due to the presence of either (i) a depleted water layer or (ii) an effective air gap at the wall formed by the nanobubbles. Another approach to hypothesize liquid slip is based on intermolecular forces affecting the momentum transport from the liquid to the wall [16]. Barring two studies [81, 108], there are no molecular-based theories to characterize this process [109, 110]. Lichter et al. [81] and Martini et al. [108] attribute the slip mechanism to hopping of liquid atoms from one equilibrium site to another, which follows Arrhenius dynamics based on the rate of hopping.

3.2.2. Slip Length. The slip velocity of the liquid at the surface boundary is characterized by an averaged property of all the liquid molecules called slip length (L_s), which is defined as the linearly extrapolated perpendicular distance from the surface boundary where fluid velocity becomes zero. In other words, slip length is the perpendicular distance from the solid boundary, outside the region of liquid flow, where the no-flow boundary condition is achieved. Figure 5 shows a schematic to illustrate the concept of slip for liquid flow; this figure shows three types of flow from left to right that indicate flow with no slip, flow with partial slip, and flow with full slip, respectively.

Navier first introduced the linear boundary condition that is considered to be the standard and most basic characterization of liquid slip. Theoretically, liquid slip velocity (v_s) is defined as follows:

$$v_s = L_s n \cdot \left[\frac{dv_x(z)}{dz} + \left(\frac{dv_x(z)}{dz}\right)^T\right] \cdot (1 - nn). \tag{25}$$

Pressure gradient-driven fluid velocity (v_x) in the presence of slip can then be theoretically calculated as follows [111]:

$$v_x = \frac{h^2}{12\eta}\left(-\frac{dP}{dx}\right)\left(1 + \frac{6L_s}{h}\right), \tag{26}$$

where L_s is the slip length, n denotes the normal to the surface along the z direction, v_s is the slip velocity at the surface, v_x is the liquid velocity in a channel, η is liquid shear viscosity, (dP/dx) is the pressure gradient along x-direction, and h is the height of the channel.

Research on liquid slip started with a focus on slip over smooth and hydrophobic surfaces [79, 105, 112, 113], but there has been an increasing evidence of liquid slip at different types of surface, including rough surface [90, 114] and hydrophilic surface [88, 115, 116]. Recent progress in liquid slip has broadened to various other parameters that have shown to influence liquid slip, and as a result, there is a continuous effort in developing appropriate models to characterize the slip on different types of surfaces and under different conditions. Below, we review the progress of liquid slip models as a function of (i) surface wettability, (ii) surface property, (iii) shear rate, and (iv) surface roughness.

(1) Effect of Surface Wettability. The liquid slip at nanoscale is greatly affected by the surface *wettability* of the medium. Macroscopically, the wettability of a surface is classified as wetting, nonwetting, or neutral depending on the contact angle formed by a liquid droplet with the surface. A surface forming contact angles larger than 90° with a liquid is termed as nonwetting, whereas a surface forming contact angles smaller than 90° with a liquid is termed as wetting fluid. A surface forming contact angle equal to 90° with a liquid is termed as neutral. Nonwetting surfaces are known to have a high disposition towards introducing liquid slip

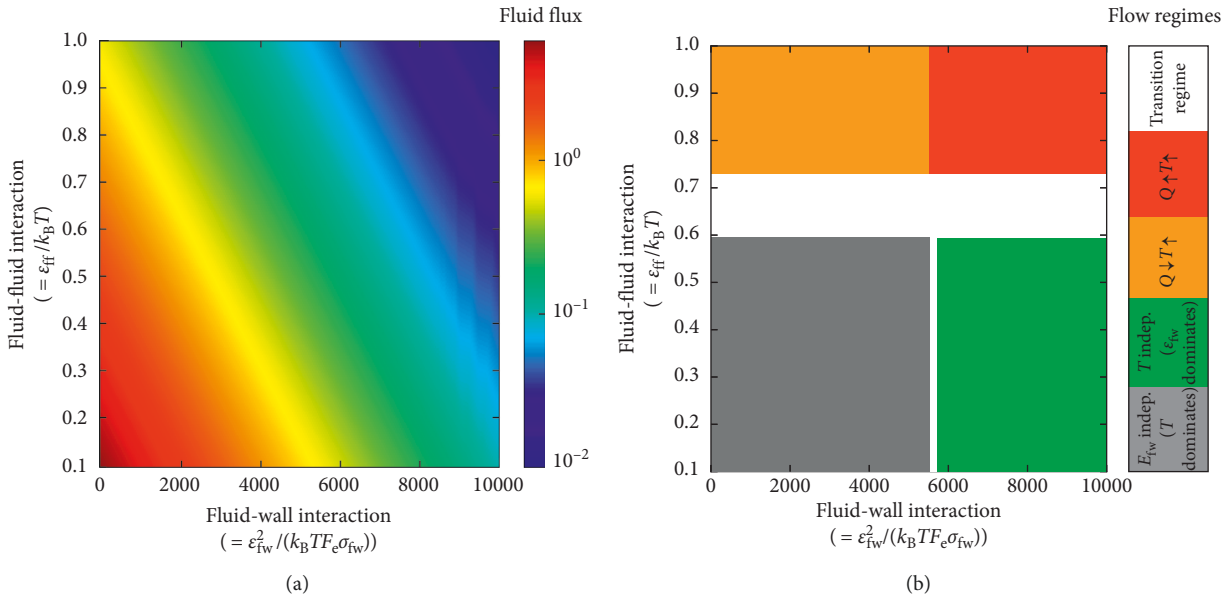

Figure 4: (a) Variation of flux values as a function of fluid-wall interaction and fluid-fluid interaction, and (b) graphical representation of corresponding liquid flow regimes.

Table 2: Different flow regimes as a function of liquid/solid binding force.

Interaction between		Flux	Flow regime	Physics
Liquid-liquid	Liquid-solid			
Low	Low	High	Flux independent of solid-fluid binding force and increases with decreasing temperature	Surface effects are weak with no liquid adsorption. Flux is dominated by the temperature-driven friction between the solid and the liquid
Low	High	Intermediate	Flux independent of temperature and dependent on solid-fluid binding force	Surface effects become strong and liquid adsorption starts to take place that results in increasing fluid density close to the solid surface
High	Low	Intermediate	Flux independent of solid-fluid interaction and increases with decreasing temperature	Surface effects are weak with no liquid adsorption. Flux is dominated by the temperature-driven friction between the solid and the liquid
High	High	Low	Flux independent of solid-fluid interaction and increases with increasing temperature	Surface effects become strong and liquid adsorption starts to take place that results in increasing fluid density close to the solid surface. Flux is enhanced with increasing temperature as it results in desorption of the fluid molecules that merge together with the bulk liquid

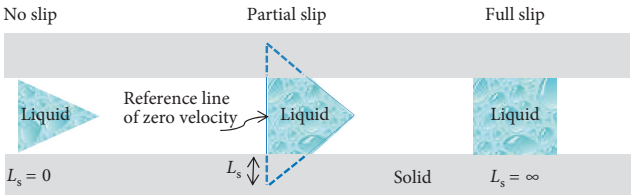

Figure 5: Schematic to illustrate liquid slip on a stationary solid surface.

[77, 86, 87, 117]. For example, hydrodynamic slip length of simple liquids flowing on smooth nonwetting surfaces (also referred as hydrophobic surfaces in the context of water as a liquid) is typically 20 nm in mediums with size varying from one to several hundreds of nanometers [112]. On the other hand, disposition of wetting surfaces in introducing slip is not as straight forward as it is for the nonwetting surfaces. There are reports [118] that suggest wetting surfaces are neutral in their disposition to introduce liquid slip, whereas others [88] have demonstrated that the wettability factor alone is not necessary to attain liquid slip and that it should be combined with the strength of the solid-fluid interactions. For example, if there is favorable sorption sites that are separated from each other by well-defined sub-nanometer distances, no slip takes place. However, liquid slip can occur if those favorable sorption sites are close to each other, provided liquid-solid attractions are not too strong. That is because nonwetting surfaces such as graphite are usually characterized by uniform distributions of fluid molecules, while the wetting surfaces such as crystalline silica are characterized by discontinuous sorption sites with high affinity for adsorbing fluid molecules.

Voronov et al. [89] found that the slip length grows if the surface's wettability is turned into more wetting by modifying the fluid-wall interfacial energy through affinity strength parameters. Gao and McCarthy [119] demonstrated experimentally that static contact angle of a fluid on a surface should not be the sole criteria to characterize the nature of wettability in order to determine the tendency of a liquid to slip. Instead, they suggested that contact angle hysteresis should be used to determine the nonwetting vs. wetting behavior of a surface.

It is believed that Tolstoi [87] was the first person to propose the liquid slip by linking the macroscopic thermodynamics concept at the molecular scale. He quantified the mobility of liquid molecules with the surface energies ($= \sigma^2\gamma$) through spreading coefficient ($= \gamma(1-\cos\theta)$) as follows:

$$\frac{L_s}{\sigma} \sim \exp\left[\frac{\alpha\sigma^2\gamma(1-\cos\theta)}{k_B T}\right] - 1, \tag{27}$$

where α is a dimensionless geometrical parameter of first order that represents the microcavity area within the solid, σ is molecular diameter, γ is the surface tension between the liquid and the surface, θ is the equilibrium/static contact angle, T is the absolute temperature, k_B is the Boltzmann constant. Another theory [85, 120, 121] that describes liquid slip at the molecular level with thermodynamic equilibrium uses the Green-Kubo relation and fluctuation-dissipation theorem (linear regression of fluctuations) and is given by the following equation:

$$\frac{L_s}{\sigma} \sim \frac{D^*}{S_t c_{LS}^2 \rho_c \sigma^3}, \tag{28}$$

where $D^* = (D_p/D_0)$, D_p is the collective molecular diffusion coefficient, D_0 is the bulk diffusion coefficient, S_t is a factor that represents first molecular layer structure, ρ_c is the fluid density at the first molecular layer, σ is the molecular diameter, and c_{LS} is the dimensionless coefficient for solid-liquid Lennard-Jones potential.

Huang et al. [122] and Sendner et al. [116] studied the slip length of shear-driven water on various hydrophobic surfaces using nonequilibrium molecular dynamic simulations (NEMDs). They show that the slip length as a function of different surfaces (both organic-like silane monolayers and inorganic-like Lennard-Jones models) can be characterized using the static contact angle (θ) of the surface as shown below, which they describe as the crucial parameter in controlling the water slippage:

$$L_s \propto (1+\cos\theta)^{-2}. \tag{29}$$

The authors demonstrate that their formula can also be obtained from the linear response theory by using the LJ fluid-solid energy parameter and the Young-Laplace equation. Their estimated slippage length varies from a few nanometers to tens of nanometers. They also proposed the following scaling expression for slip length as a function of liquid depletion length, which they define as the layer between the water and the solid surface occupied by the gas:

$$L_s \propto \delta^4, \tag{30}$$

where δ is the thickness of liquid depletion and given by

$$\delta = \int_0^\infty \left[1 - \frac{\rho_s(z)}{\rho_s^b} - \frac{\rho_l(z)}{\rho_l^b}\right] dz, \tag{31}$$

where $\rho_s(z)$ and $\rho_l(z)$ are the densities of the solid and liquid along the height of the channel, whereas ρ_s^b and ρ_l^b are the bulk densities of the solid and liquid, respectively.

Bakli and Chakraborty [123] presented a constitutive model to describe the nanopore imbibition characteristics of water as a function of the dynamic slip length using NEMDs. Their derived slip length depends on the contact angle and an acceleration parameter that comes from the pressure gradients due to capillary forces. They show that for low acceleration values, their model approaches the model given by Huang et al. [122]:

$$\begin{aligned} L_s &= \frac{A_1(a)}{[1+\cos(\theta)]^2} - A_2(a), \\ a &= \frac{\gamma\cos(\theta)}{\rho R L}, \\ a^* &= \frac{\gamma\cos(\theta)}{\eta L(dL/dt)}, \\ a^*_{\text{rough}} &= a^*_{\text{smooth}} + \overline{a}, \\ \overline{a} &= 0.35\exp(-0.6N), \end{aligned} \tag{32}$$

where L is the capillary imbibition length at time t, N is the parameter representing the surface roughness (lower value represents higher roughness), a is the imbibition driving acceleration parameter, a^* is the dimensionless form of a, $\overline{a}$ is a deceleration parameter to mimic flow hindrance due to surface roughness, and $A_1(a)$ and $A_2(a)$ are functions of a.

(2) Effect of Shear Rate. The effect of shear rate on slip length has been investigated experimentally by many researchers [90, 96, 97, 99, 100] and observed to depend on the shear rate. In such a scenario where slip length is found to depend on the shear rate, the slip boundary condition proposed by Navier, and presented earlier, shows a nonlinear behavior with shear rate. Although several slip length relationships have been proposed as a function of shear rate, the relationship proposed by Priezjev [98] is an important one as it accounts for the solid-fluid interaction strength that is crucial in micro- or nanoporous media. Priezjev [98] proposed slip length for smooth surfaces as a function of shear rate that predicts that the slip length increases nonlinearly with the shear rate for weak solid-fluid interactions provided that the solid-liquid interface forms a discrete structure, whereas if the solid-fluid interaction increases, the slip length becomes linearly proportional to the shear rate:

$$Q_{\text{slip}} = \frac{2}{3}\frac{\rho f_x h^3}{\mu} + 2hV_s. \tag{33}$$

The above equation can be normalized in terms of the no-slip flow rate as follows:

$$Q_{\text{slip}} = Q_{\text{no-slip}}\left(1 + 6\frac{L_s}{2h}\right), \tag{34}$$

where f_x is an externally applied force in the x direction, ρ is the fluid density, h is the distance between the confining solid walls, μ is the fluid viscosity, V_s is the fluid velocity at the confining parallel walls that can also be written as $V_s = v(-h) = v(h)$, and Q_{slip} and $Q_{\text{no-slip}}$ are the flow rates due to slip and no-slip boundary conditions, respectively. The term $2hV_s$ in the above equation represents the correction to the flow rate due to slip boundary conditions. Priezjev [98] reported that the fluid viscosity, shown below, was found to be shear rate ($\dot{\gamma}$) independent in the range of $\dot{\gamma} \leq 0.16\tau^{-1}$, where τ is the characteristic Lennard-Jones (LJ) time:

$$\mu = (2.2 \pm 0.2)\varepsilon\tau\sigma^{-3}, \tag{35}$$

where ε and σ represent the energy and length scales of the fluid phase.

(3) Effect of Surface Roughness. Even though most of the solids are naturally rough at micro- to nanoscale, slip length of liquid as a function of surface roughness is not well studied [16, 124]. The problem of calculating slip as a function of surface roughness is challenging [16, 125, 126] because of four reasons: (i) controlling surface roughness in a natural and a realistic manner at nanometer scale is not easy, (ii) surface roughness can introduce changes to some interfacial properties such as interfacial forces, wettability, and trapped gases, which may be undesirable, (iii) rough surface will introduce undulating boundaries that will introduce complexities in making correct interpretations with respect to varying boundary positions, and (iv) there is no analytical characterization for the nonperiodic and natural randomness of surface roughness.

Although several slip length relationships have been proposed as a function of surface roughness, two relationships by Lund et al. [127] and Misra and Bakli [128] are discussed here because of their simplicity and effectiveness.

Lund et al. [127] derived an expression of effective slip length on a surface with periodic roughness in terms of intrinsic slip length and contact area of the surface, using steady-state Stokes flow and homogenization method. Their derived effective slip length represents the harmonic mean weighted by the area of contact between surface and fluid as follows:

$$L_{\text{eff}} = \left\langle \frac{\sqrt{1+s^2}}{L_s} \right\rangle^{-1}, \tag{36}$$

where L_s is the intrinsic slip length, s is the slope, and $\sqrt{1+s^2} = (1/L)\int_0^L \sqrt{1+s^2}dx$ is the arc length of the surface function over one period, normalized by the length of the period (L). For a flat surface ($s = 0$), the above expression reduces to the intrinsic slip length. Their result is applicable for rough surfaces where $L \ll (L_s)_{\min}$.

Misra and Bakli [128] recently proposed an expression of effective slip length for slippage of water considering coupled effect of the surface chemistry and surface roughness by performing molecular dynamics simulations. They found that the slip length without surface roughness match closely with the result of $(1 + \cos\theta)^2$ proposed by Huang et al. [122] for smooth surface, while the presence of surface roughness always reduces the effective slip length as follows:

$$L_{\text{eff}} = \frac{k}{(1+\cos\theta)^2(1+\alpha^*)^2},$$
$$\alpha^* = \frac{\sum|f(x,y) - \overline{f(x,y)}|}{N}, \tag{37}$$

where k is the constant of proportionality and α^* is a parameter that characterizes the roughness of a surface through its amplitude N and roughness function $f(x, y)$ that modifies the attractive part of the Lennard-Jones (LJ) potential.

(4) Electrokinetic Effects. The amount of liquid slip on a surface is found to be affected by the presence of a charged surface and/or liquids with charged ions such as electrolytes. The presence of charge leads to attraction of oppositely charged ions and repulsion of similarly charged ions, and in the presence of a charged surface, this leads to the formation of a charged interfacial layer near the surface. The fluid flow in the presence of charge (also referred to as *electrokinetic phenomenon*) is centrally connected to the key concept of *electrical double layer* (EDL) that is made up of a *stern* layer and a *diffuse* layer as illustrated in Figure 6. Stern layer is the width of a layer close to the surface where the underlying solid surface charge (cations or anions) attracts the opposite charge of the solvent/liquid to form a layer of highly concentrated ions, whereas the diffuse layer is the width of a layer starting from the stern layer and ending where the electrokinetic potential goes to zero.

The electrokinetic effects result in enhanced solid-fluid interaction close to the surface, which may also influence the liquid slip flow and consequently the overall fluid transport. Two examples of electrokinetic flows relevant here are electro-osmosis (liquid flow induced by application of an electric field) and streaming currents (electric current induced by application of a pressure gradient).

The surface-fluid interaction due to electrokinetic effects is more complex than the surface-fluid interaction without any charge. Research on this area is sparse due to limited applications that have surface charge present. Out of the few models that exist in the literature, models proposed by Joly et al. [129] and Choudhary et al. [130] are discussed here because of parameters that are directly related to the electrokinetic effects and solid-fluid interaction compared to other models where the parameters are not that apparent.

Joly et al. [129] explored the effect of surface charge to solid-liquid interfacial friction and its effect on the slip length boundary condition. They study the hydrodynamics of liquid coupled with electrostatics within the EDL using molecular dynamics simulations. Their study found that the presence of surface charge on the solid-liquid interface enhances the frictional force between the solid-liquid and as a result decreases the slip length.

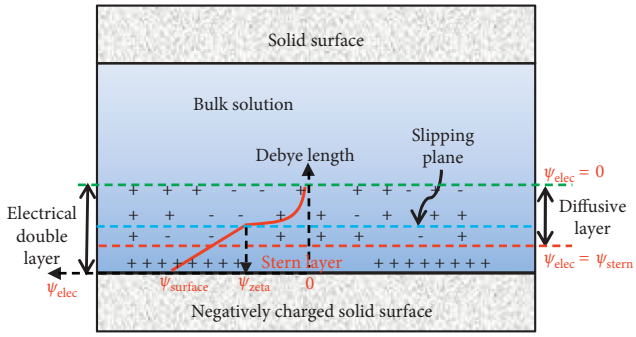

FIGURE 6: Schematic of a flow in a channel with electrokinetic effects.

$$L_{\text{eff}} = \frac{L_s}{1 + (1/\alpha)\left((\sigma d^2)/e\right)^2 \left(l_B/d^2\right) L_s}, \tag{38}$$

where L_s is the slip length without considering surface charge, $\alpha\,(\approx 1)$ is a numerical factor, σ is the surface charge density, d is the equilibrium distance of Lennard-Jones potential, e is the elementary charge, and l_B (~0.7 nm in water at room temperature) is the Bjerrum length that represents a length scale below which electrostatic interactions dominate thermal effects.

Choudhary et al. [130] studied the liquid slip for electro-osmotic flow through a nanochannel with hydrophobic walls of sinusoidally varying slippage using an asymptotic theory that uses the ratio of pattern amplitude (perpendicular to the applied electric field) to the average slip as a parameter. They proposed the following analytical expression for effective slip that can be used to design slip through engineered variations in topography and/or chemistry:

$$\overline{L}_{\text{eff}} = \overline{L}_s - \alpha^2 \frac{\overline{L}_s^2 \overline{k}_s}{2} \left[\frac{\sinh\left(\overline{k}_s\right)(1+\cos\theta)}{2\left\{\cosh\left(\overline{k}_s\right) + \overline{L}_s.\overline{k}_s \sinh\left(\overline{k}_s\right)\right\}} + \frac{\cosh\left(\overline{k}_s\right)(1-\cos\theta)}{2\left\{\sinh\left(\overline{k}_s\right) + \overline{L}_s.\overline{k}_s \cosh\left(\overline{k}_s\right)\right\}} \right], \tag{39}$$

where $\overline{L}_{\text{eff}}$ is the dimensionless effective slip length due to electrokinetic effects and $\overline{L}_s$ is the dimensionless average slip length $(= L_s(x)/h)$ that is equal to $L_{s0}\left\{1 + \alpha\cos\left(\overline{k}_s\overline{x} + \theta\right)\right\}$ and $L_{s0}\left\{1 + \alpha\cos\left(\overline{k}_s\overline{x}\right)\right\}$ on the top and bottom walls of the channel with height $2h$, respectively. Here, L_{s0} is the average slip length without electrokinetic effects, α is the dimensionless amplitude $(= a/L_{s0})$ of the pattern on either walls charged to facilitate electro-osmosis flow, $\overline{k}_s$ is the wavenumber, and θ is the phase angle between the slip waves on the two walls.

4. Porous Media Applications in the Energy Sector

In this section, the above-reviewed knowledge on gas and liquid flow at micro- to nanoscale is used to critically examine the modeling gaps in four different porous media applications from the energy sector and how that can be improved. Specifically, for each application we provide a brief introduction in context of its importance, a brief literature review on that application with the present state of progress, followed by identification of critical gaps and proposed approach to improve modeling at micro- and nanoscale in each application. The four applications from energy sector considered here are (i) electrokinetic energy conversion devices, (ii) membrane-based water desalination through reverse osmosis, (iii) shale reservoirs, and (iv) hydrogen storage, respectively.

4.1. Energy Conversion through Electrokinetics

4.1.1. Introduction. Increasing demand for energy has led to harnessing of energy from various forms such as mechanical, chemical, internal, electrical, thermal, etc. and various other combinations. To utilize these various sources of energy, micro- and nanofluidics provide the capability of converting energy from one form to another form to cater to different applications. Energy conversion is possible through electrokinetics, which is a term used to describe different transport mechanisms in the presence of an electric field and liquid flow through a medium. Electrokinetics can be used for energy conversion in four different ways: (i) drive liquid by applying an electric potential (*electro-osmosis*), (ii) transport and separate particles by applying an electric potential (*electrophoresis*), (iii) generate electric potential by pressure gradient-driven liquid flow (*streaming potential*), and (iv) generate electric potential by movement of charged particles under gravitational or centrifugal force (*sedimentation potential*). In particular, micro- and nanofluidics have found application in converting energy from heat, electrical, chemical/biochemical, pressure, etc. to electrical energy using micro- and nanoscale technologies with a wide range of efficiencies varying from 3% for streaming potential devices [131] to 60% for micro-fuel cells [132].

4.1.2. Literature Review. Electric double layer (~1 nm thickness) is a common phenomenon in small energy conversion devices that are increasingly based on nanostructured materials. As an example to illustrate the scale at which fluids flow in electrokinetic devices, Figure 7 shows transmission electron microscope images of carbon composites [133, 134] with application in electrochemical energy conversion.

The electrokinetic effects at confined scales result in enhanced solid-fluid interaction close to the surface, which may also influence the liquid slip flow and consequently the overall fluid transport. The amount of liquid slip on a surface is found to be affected by the presence of a charged surface and/or liquids with charged ions such as electrolytes. Two examples of electrokinetic flows relevant here are electro-osmosis (liquid flow induced by application of an electric field) and streaming currents (electric current induced by application of a pressure gradient).

(1) Key Challenge. One of the key challenges in the design of electrokinetic energy conversion devices is their low

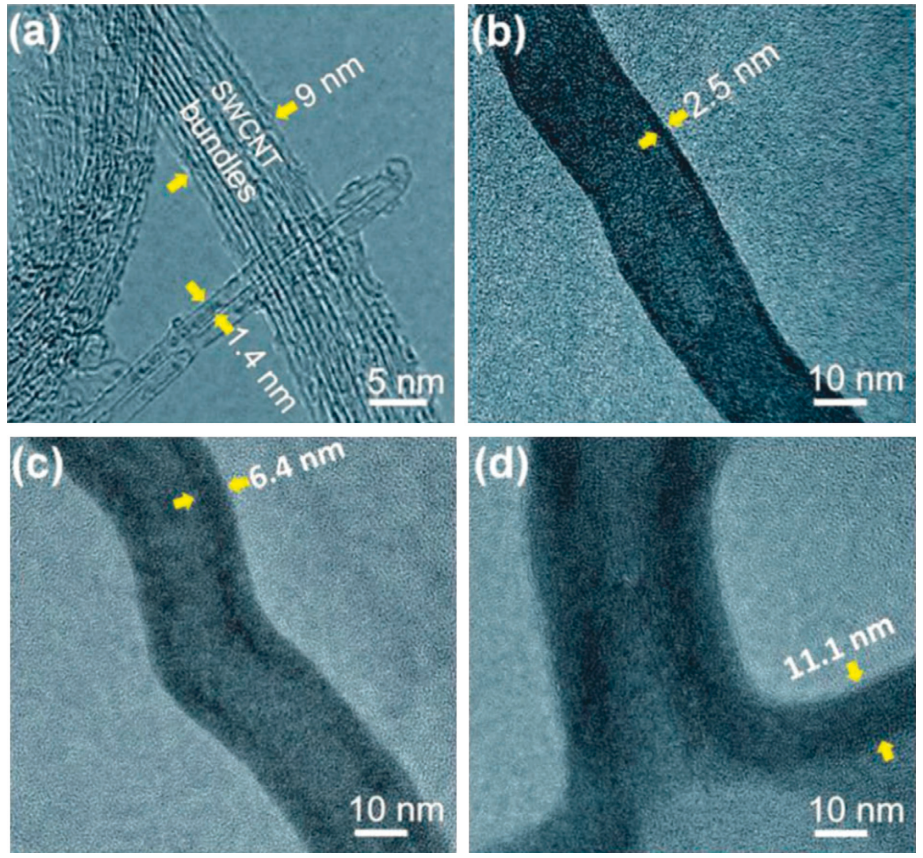

FIGURE 7: Transmission electron microscope images of carbon composites for application in electrochemical energy conversion [133, 134].

conversion efficiencies. The maximum efficiency of energy conversion ($\eta_{\max}$), which is defined as the ratio of the output power to the input power, is given as follows:

$$\eta_{\max} = \frac{\text{Power}_{\text{output}}}{\text{Power}_{\text{input}}}. \tag{40}$$

(2) Governing Equations. The mathematical theory used to model the transport in the presence of chemical potential (due to surface charge and charged ions in the solution), externally applied electric potential, and hydrostatic potential is briefly reviewed below. The chemical potential and ionic concentrations in the diffuse part of the EDL are governed by the Poisson-Boltzmann equation as follows:

$$\nabla^2\psi(y) = -\frac{1}{\varepsilon}\rho(y) = -\frac{e}{\varepsilon}\sum_{i=1}^{N}\left[z_i c_i \exp\left(-\frac{ez_i\psi(y)}{k_B T}\right)\right], \tag{41}$$

where $\psi(y)$ is the potential in the EDL due to surface charge and the charged ions in the solution, y is the radial distance from the surface of the channel, $\rho(y)$ is the volume charge density of all the ions present in the neighborhood of the surface, e is the unit charge, ε is the permittivity of the liquid, c_i and z_i are the concentration and the ionic valence of the i^{th} ionic species, respectively, k_B is the Boltzmann constant, and T is the absolute temperature.

The Poisson-Boltzmann equation does not have a general analytical solution, but its solutions are available for specific cases [135]. For our interest, we consider the solution for a flat surface with a low potential (ψ_{surface}) at its surface for which the above equation can be linearized based on the Debye-Hückel approximation to obtain the following solution:

$$\psi(y) = \psi_{\text{surface}}\exp(-\kappa y),$$
$$\lambda_D = \kappa^{-1} = \sqrt{\frac{\varepsilon k_B T}{N_A e^2 \sum_{i=1}^{N}\left(z_i^2 c_i\right)}}, \tag{42}$$

where κ^{-1} is called the Debye length (λ_D) that gives a measure of the EDL and N_A is the Avogadro number. The Debye length is independent of the charge on the solid surface and increases as the solute ion concentration in the solution becomes dilute such that λ_D for a solution without electrolytes can be considered as infinitely thick. Typical values of λ_D can vary from $\sim$3nm to $\sim$300nm for electrolytes with ionic concentration of 10^{-2}M and 10^{-6}M, respectively [135].

The above-defined definitions are finally used to describe the solvent and solute transport in the presence of hydrostatic, chemical, and electric potential within a micro- or a nanochannel of width $2h$ as follows.

(i) Solvent Transport. The solvent flux across the channel due to hydrostatic potential and electric potential is the sum of

the average of the fluxes due to these two potentials and given as follows [136, 137]:

$$\begin{aligned}\langle v_s\rangle &= \frac{1}{h}\int_0^h v_s(y)dy,\\ \langle v_s\rangle &= \frac{1}{h}\int_0^h \underbrace{\left[\frac{1}{2\eta}\left(y^2-2hy\right)\frac{dP}{dx}\right]}_{\substack{\text{flow due to}\\ \text{hydrostatic potential}}} dy\\ &\quad + \frac{1}{h}\int_0^h \underbrace{\left[\frac{\varepsilon}{\eta}\{\zeta-\psi(y)\}\frac{d\phi}{dx}\right]}_{\substack{\text{flow due to}\\ \text{electric potential}}} dy,\end{aligned} \tag{43}$$

where $\langle v_s\rangle$ is the average solvent velocity, ζ is the electric potential at the slipping plane (also called *zeta* potential), $\psi(y)$ is the potential in the EDL, η is the solution viscosity, ε is the permittivity of the solution, and ϕ is an externally applied electric potential.

(ii) Solute Transport. The solute flux across the channel is given as the averaged sum of the flux due to hydrostatic potential, flux due to diffusion, and flux due to electric potential. The solute transport in the presence of these three mechanisms is also called the Nernst-Planck equation and given as follows [137–139]:

$$\begin{aligned}\langle J\rangle &= \frac{1}{h}\int_0^h \underbrace{c(y)v_s(y)}_{\substack{\text{flux due to}\\ \text{hydrostatic potential}}} dy - \frac{1}{h}\int_0^h \underbrace{\left[D_\infty\frac{dc(y)}{dx}\right]}_{\substack{\text{flux due to}\\ \text{diffusion}}} dy\\ &\quad - \frac{1}{h}\int_0^h \underbrace{\left[\frac{zeD_\infty}{k_BT}c(y)\frac{d\phi}{dx}\right]}_{\substack{\text{flux due to}\\ \text{electric potential}}} dy,\end{aligned} \tag{44}$$

where $\langle J\rangle$ is the area-averaged solute flux, D_∞ is the diffusion coefficient of the solute in the free solution, $c(y)$ is the solute concentration at distance y from the surface, and ze is the ionic charge.

(iii) Solute Partitioning. Solute ions experience electric, chemical, and surface forces that vary in magnitude based on the size and charge on the ions; therefore, this leads to nonuniform distribution of ions along the width of the flowing medium. This partitioning of the solute ions can be characterized through the ratio of the average solute concentration ($\langle c\rangle$) to the bulk concentration (c_0) in the solution, which is also referred to as the partitioning coefficient β_{part} [140]:

$$\beta_{\text{part}} = \frac{\langle c\rangle}{c_0} = \frac{1}{h}\int_{\sim 0}^{h-r} \exp\left\{-\frac{E(y)}{k_BT}\right\}dy, \tag{45}$$

where β_{part} is the solute partition coefficient that is the measure of ion permeability-selectivity of the pore, r is the radius of the spherical solute, and E is the electrostatic interaction potential. It should be noted that when the confinement width becomes comparable to the Debye length, the overlapped EDL gets deformed significantly due to steric effects and in that case the modified Poisson-Boltzmann equation must be employed [141]. When the transport of solute through the medium is strongly dependent on solute size and independent of frictional and hydrostatic (convective) forces, in that case [137, 142],

$$\beta_{\text{part}} = 1 - \frac{r}{h}. \tag{46}$$

(iv) Conversion Efficiency. The maximum efficiency of energy conversion ($\eta_{\max}$) is defined as the ratio of the output power to the input power; however, some researchers [143–145] also use an alternate measure for the conversion efficiency using a measure called electrokinetic *figure of merit* [146], which is based on phenomenological transport equations. The following equation is an alternate form for the maximum efficiency in terms of *figure of merit* (β):

$$\eta_{\max} = \frac{\sqrt{1+\beta}-1}{\sqrt{1+\beta}+1}, \tag{47}$$

where $\beta = ((\nu^2\sigma)/k_H)$. Here, ν, σ, and k_H are the streaming potential coefficient, the ion conductivity, and the hydraulic permeability, respectively.

4.1.3. Critical Gaps and Proposed Approach. About a decade ago it was hypothesized [147, 148] that the efficiencies of the energy conversion devices based on electrokinetic effects can be optimized by enhancing the liquid slip. A theoretical study by Davidson and Xuan [143] showed that the efficiency of electrokinetic energy conversion devices is almost a linear function of slip length for small values of zeta potentials. Even though there is a consensus that liquid slip plays a strong role in the device efficiency among the electrokinetic energy research community, some issues remain in regard to understanding of slip length as a function of key device parameters and its relationship with flux.

(1) Slip Length as a Function of Device Parameters. In the electrokinetic energy research community, performance of the device is predicted by either completely neglecting the slip [149, 150] or an assumed value of slip length used by others [143, 148, 151, 152] that is independent of the surface and flow conditions. Further, some researchers [153, 154] suggested that the slip length increases as the surface becomes slippery, or in other words slip length increases on surfaces with low friction coefficient. However, this suggestion is contrary to the observations reported by researchers [155–158] in the field of liquid slip who reported that the surface friction results in increase in the effective viscosity that consequently increases the liquid slip length [156]. This result, even though counterintuitive in nature, is supported by experimental observations [90, 96, 99, 159]. Therefore, as noted by others [160], there is a lack of understanding about the liquid slip length when it comes to predicting the conversion efficiencies. Developing the

fundamental understanding of liquid slip as a function of key device parameters presents an opportunity of increasing the efficiency of energy conversion devices by exploiting their potential of developing large slip lengths. For instance, we discussed many slip length models earlier as a function of surface wettability, surface friction, shear rate, surface roughness, and electrokinetic effects that can be used to either estimate the slip lengths for a given device or design the device parameters for a given slip length.

(2) Slip Length vs. Flux. Following theoretical considerations initiated by some studies [143, 147, 148], it is now believed by most researchers that the efficiency of energy conversion devices can be increased by increasing the liquid slip length. In this regard, some comments were made on how to optimally exploit this potential. Having said that, the arguments made in favor of slip are theoretical in nature, and there are no experimental studies specific to energy conversion devices that verify the amplified values of conversion efficiencies predicted theoretically and usually cited by many authors [137, 153]. The objective of this note is to caution that a theoretical definition of liquid slip where flux is proportional to the slip length ($v_x \propto 1 + 6L_s/h$) may not be universally true. To support this hypothesis, we refer to the experimental study of Liu and Li [75] who measured the flux and slip length for liquid argon and liquid helium in nanochannels of various widths and noted that the relation of slip length to flux was not clear from the data. They attributed this reason to nonuniform distribution of density and viscosity of the confined fluid.

4.2. Membrane-Based Water Desalination

4.2.1. Introduction. Currently, there are 4 major sources of water that can be used for water desalination and treatment, i.e., produced water from oil and gas wells, brackish groundwater, municipal wastewater, and seawater, respectively. Out of these, seawater is a source with continuous and large amounts of saline water that can be potentially desalinated and supplied to various applications on large scale as illustrated in Figure 8.

Desalination using the membrane-based reverse osmosis process is a potentially attractive technology that can be used to desalinate enormous amount of seawater. Reverse osmosis (RO) is considered to be a leading technology for desalination primarily because of its relatively low cost (one-half to one-third of the cost of distillation) due to relatively low energy consumption (1.8 kW·h/m^3) that contributes to about 44% of production capacity in the world [161]. RO uses a semipermeable membrane to stop the contaminants at the level of 0.1 nm to 1 nm by applying hydrostatic pressure to overcome osmotic pressure, which is a chemical potential developed due to salinity difference of the solvents that drives the solvent from an aqueous solution of low salt concentration to an aqueous solution of high salt concentration. In the RO, the movement of solvent from low concentration to high concentration due to chemical potential is reversed by applying an external pressure.

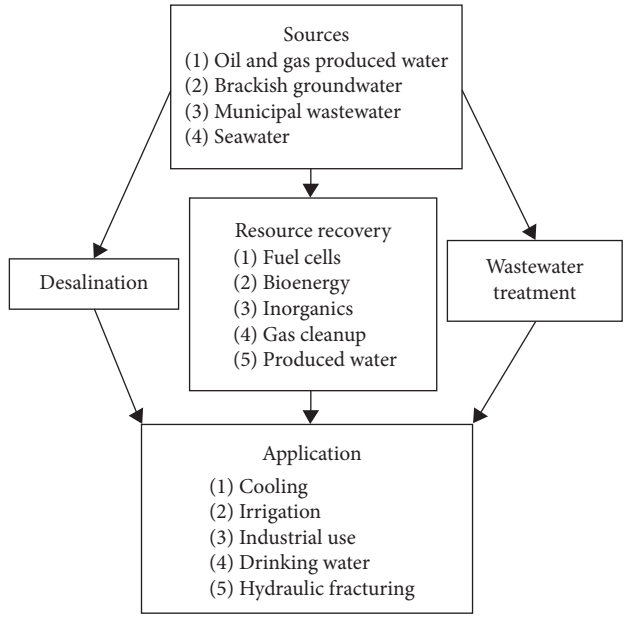

Figure 8: Role of water in the energy sector.

4.2.2. Literature Review. The study by Nair et al. [162] was the first to discover that graphene oxide has the membrane properties suitable for desalination, i.e., unique water permeation pathway and retention for other gases and ions/solutes. The water flows through the multiple layers of graphene oxide through two-dimensional capillaries formed by closely spaced graphene sheets where the salt ions are retained on the sheets as shown in Figure 9.

Conventional understanding of the flow fluid through pores suggests that this dual-task is paradoxical in nature, but development of nanomaterials such as carbon nanotubes (CNTs), boron nitride nanotubes (BNNTs), and graphene that show unconventional fluid transport behavior due to their smallest possible pore volumes combined with ionic dehydration [163], electrokinetic effects [164], and size exclusion [165] properties provide opportunity for their application in optimizing two coupled tasks of desalination mentioned above. Specifically, high selective-solute retention and high permeability to water is achieved by drilling sub-nanometer holes through the solid-state nanomaterials such as graphene by using focus ion beam [166, 167] or oxygen plasma etching process [168]. The water molecules are too big to pass through graphene's fine mesh without making holes/pores in the graphene sheet and poking these sub-nanometer holes uniformly is another challenge. Additionally, in order to drive satisfactory magnitude of water flux through these nanopores, a large pressure difference is required that cannot be solely achieved by osmotic pressure. However, compared to the fine mesh of nanoporous graphene, Nair et al. [162] proposed graphene oxide membrane as an alternate to the graphene because graphene oxide relies on its naturally occurring tortuous path to flow out water (Figure 9), unlike the challenging task of artificially poking holes through graphene for creating a path to flow out water. Other than this major advantage of graphene oxide, there are several other reasons as presented by You et al. [169] that

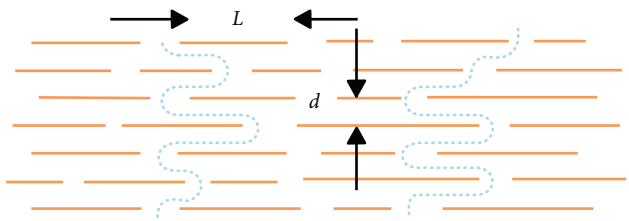

Figure 9: Graphene oxide membrane with nanopores [162].

make graphene oxide a preferred choice over nanoporous graphene.

(1) Key Challenge. One of the key design challenges in the desalination technology using RO membranes is the binding of the following two conditions: (i) increasing retention for selective solutes through sieving using small nanometer-sized apertures, and (ii) allowing large flux of pure water to pass through the membrane by increasing membrane permeability. These two challenges can be visualized through a schematic [170] in Figure 10 that shows the nanosized pores of the graphene membrane and water molecules with salt are comparable to each other.

Finally, a recent study by Werber et al. [171] questioned and critiqued the coupled-importance of a high selective-solute retention, and high water permeability in the desalination performance. They suggest that increased water permeability seems to have little impact on the efficiency and that increased retention of selective solutes should be the most important measure for desalination efficiency. The water/salt selectivity tradeoff relationship is based on empirical relationship [172] that is still continued to be used [173] because of incomplete theoretical understanding of many physical/chemical processes that occur during desalination through membrane-based RO.

(2) Governing Equations. Most of the studies use the simple convective flux and diffusive flux to model the transport of water and solute, respectively, through the nanoscale membranes as reviewed by Werber et al. [174]:

$$J_w = A(\Delta P - \Delta\pi_m),$$
$$J_s = B\Delta c_m, \tag{48}$$

where $A = (P_w V_w/\delta_m R_g T)$ and $B = (P_s/\delta_m)$. Here, $A$and$B$ are the permeability coefficients for water and solute, respectively, P_w and P_s are the diffusive permeability for water and solute, respectively, V_w is the molar volume of water, R_g is the gas constant, T is the absolute temperature, ΔP is the applied hydraulic pressure difference across the membrane, $\Delta\pi_m$ is the osmotic pressure difference across the active layer, and δ_m is the active layer thickness of the membrane. Werber et al. [174] suggest that the coefficients A and B together define the selective layer performance of nonporous membranes.

4.2.3. Critical Gaps and Proposed Approach. Despite the rapid progress made in developing nanomaterials for membranes, very little research has been performed in modeling the flow of water and solute retention through graphene-based membranes. Based on above discussions of liquid flow at nanoscale, water and solute transport in graphene-based membranes should be a strong function of wettability and slip length. The strong effect of membrane wettability and slip length on water permeability and volumetric flux was shown recently by Shahbabaei et al. [175] and Chen et al. [176], respectively, through molecular dynamics simulations. Werber et al. [174] reviewed important polymeric membrane materials as a measure of controlling the wettability from an experimental perspective. Therefore, in this regard it is important to understand how wettability may affect the slip length and a method to model the effect of their coupled behavior on flux.

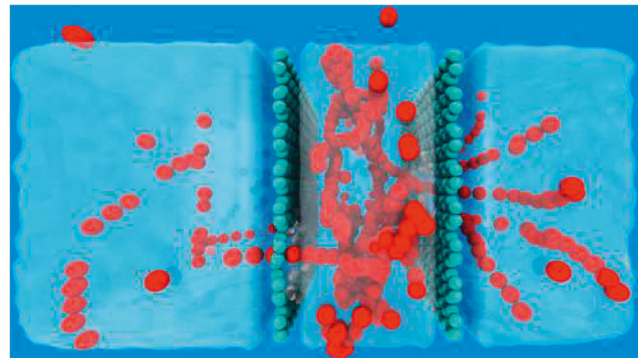

Figure 10: Schematic of RO membrane with nanopores [170].

(1) Coupled Effect of Slip Length and Wettability. Bakli and Chakraborty (2012) presented a constitutive model to describe the liquid filling of water in nanopores as a function of the dynamic slip length that changes with the contact angle and the fluid acceleration due to pressure gradient as follows:

$$L_s = \frac{A_1(a)}{[1+\cos(\theta)]^2} - A_2(a),$$
$$a = \frac{\gamma\cos(\theta)}{\rho RL}, \tag{49}$$
$$a^* = \frac{\gamma\cos(\theta)}{\eta L(dL/dt)},$$

where L_s is the slip length, L is the water filling length at time t, N is the parameter representing the surface roughness (lower value represents higher roughness), a is the imbibition driving acceleration parameter, a^* is the dimensionless form of a, and $A_1(a)$ and $A_2(a)$ are functions of a.

Parobek and Liu [177] reviewed the wettability of graphene and found that the intrinsic wettability of graphene based on advancing contact angle measurements suggests that graphene is a nonwetting (hydrophobic) material and its wettability is independent of the substrate underneath graphene and the number of graphene layers. Based on our earlier discussions, it is known that slip lengths on the order of tens of nanometers are observed on hydrophobic (nonwetting) surfaces that can go up to hundreds of nanometers

[178, 179] for super-hydrophobic surfaces. Therefore, the hydrophobic nature of graphene further emphasizes the need to incorporate the slip length in modeling the flux of water, which can be obtained using the Hagen-Poiseuille (HP) equation for cylindrical-shaped capillary or using the HP equation modified for geometric corrections and slip flow through capillaries of different shapes:

$$q = c\frac{\pi\left(r^4 + 4r^3 L_s\right)}{8\mu}.\frac{1}{L_0}, \tag{50}$$

where c is a geometry correction factor [180] to account for different shapes and eccentricity of capillaries ($k = 1$, 1.43, and 1.98 for capillaries with circular, square, and equilateral triangle cross-sections, respectively), r is the pore radius, μ is the water viscosity, L_s is the slip length, and L_0 is the capillary length within the membrane.

4.3. Shale Reservoirs

4.3.1. Introduction. Shales are unconventional rocks that are both the source and the reservoir for oil and gas resources. Economical production from shale formations requires creating hydraulic fractures by pumping large volume of water (~2–6 million gallons) at high pressure. Shale rocks are predominantly composed of consolidated clay-sized particles with a high organic content [181, 182] that result in extremely small pore sizes with 80% of pores in the range of 2 nm to 15 nm [183, 184]. Because of their extremely small pore sizes, shale rocks present an opportunity to apply the fundamentals of nanoscale fluid flow physics over existing conventional theories of porous media fluid flow.

4.3.2. Literature Review. The typical characteristics of a shale reservoir include low porosity, low permeability [185, 186], complex network of matrix-fracture systems [187–191], and heterogeneous mineralogy [181, 182, 192–195], and the combination of these characteristics presents a unique challenge in understanding the fluid flow and fluid-rock and fluid-fluid interactions in these reservoirs. Following theoretical considerations, some studies explored the fluid flow in these reservoirs as a function of convection, slip flow, Knudsen diffusion [196–201], surface diffusion/sorption [202–210], rock-mechanics [189, 211–215], and osmosis [216–218]. Unlike conventional reservoir rocks, shales are typically oil-wet or mixed-wet as discussed in a review by Singh [218] for various shale rocks across the world [219–222]. The wettability of shales cannot be characterized by the macroscopic method of measuring contact angle because of the nontrivial effect of line tension in nanopores, and to account for this effect, a modified contact angle method was discussed in a review by Singh [218].

Other areas that have recently caught interest due to their importance in understanding the fluid behavior in shale or increasing the productivity are (i) spontaneous imbibition in shales [218, 223–225], (ii) thermodynamic phase behavior of fluids inside shales as a function of pressure drawdown during production [226–231], (iii) alternate fracturing fluids [232–237] for better reservoir stimulation and to avoid water usage, and (iv) enhancing oil recovery by injection of fluids [238–240].

(1) Key Challenge. The knowledge about fluid flow in shale reservoirs is still at its infancy compared to our knowledge of fluid flow in conventional oil and gas reservoirs that has been rigorously tested over several decades. The key challenge in production from shale reservoirs is developing verifiable theories that describe flow and mechanics from these extremely tigh pore spaces, which are heterogeneous in terms of the mineralogical composition and pore structure.

4.3.3. Critical Gaps and Proposed Approach. Even though the importance of shale reservoirs as a source of hydrocarbon production continues to increase with time, the production of fluids from these reservoirs remain poorly understood at the pore level and that drives many researchers to look at these problems from continuum perspective at the reservoir scale [241]. From a theoretical perspective, there are many transport mechanisms that seem to be contributing to the hydrocarbon production from the shale rocks. A better understanding to characterize those mechanisms in terms of their contribution to the flow, the period for which they remain activated, and their likely place of origin in the reservoir can be useful to optimize the production from these reservoirs. In this regard, we can elaborate this into three specific questions: (i) What is the contribution of each transport mechanism in the total production? (ii) At what point of time and for how long during a reservoir's life do these mechanisms remain activated? (iii) What is the contribution of different sections of reservoir, such as matrix, natural fractures, and hydraulic fractures, in the transport of hydrocarbons?

(1) Reservoir-on-Chip Approach. It is clear from the discussions in the literature that ultra-tight nanopore structure of the shales plays a major role in controlling the transport of fluids and their production, but despite this consensus most of the experimental studies focus on investigating the fluid transport from a continuum perspective using core-scale experiments [219, 242–246]. The core-scale investigations can be employed to explore the flow due to interaction between matrix and fractures; however, the appropriate way to investigate nanoscale transport mechanisms would be through the nanofluidics (e.g., chip-based models) framework. Recently, there has been some effort [159, 226, 247–252] in investigating the transport from nanopores using some innovative ideas that mimic the heterogeneous nanopore and fracture network through the reservoir-on-chip approach as illustrated in Figure 11. A more realistic network of matrix and fracture mimicking actual core images can be developed synthetically using micro-CT images, characterizing the fracture and matrix system in those images using an image processing software and fabricating the processed images using standard lithography techniques [247, 253]. The features of fracture network from the CT images can be patterned and etched using deep reactive ion

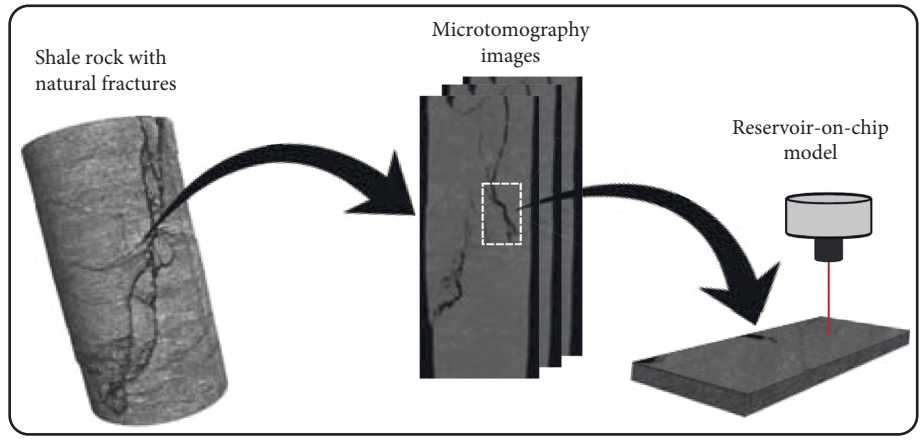

(a)

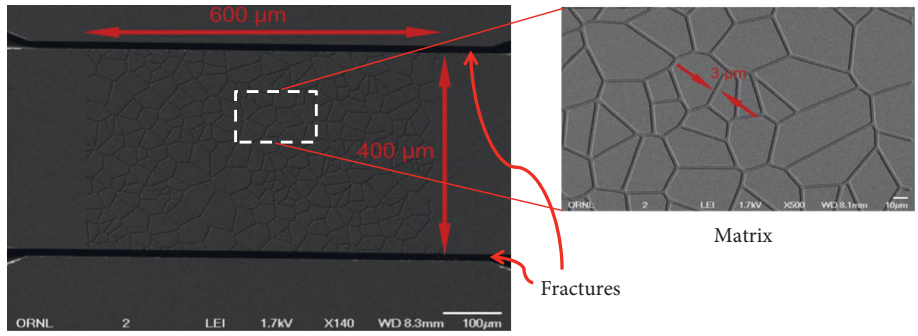

(b)

Figure 11: Schematic illustrating (a) a reservoir-on-chip framework and (b) a micromodel with a network of fractures and heterogeneous pores (inset) (adapted after [252] and [248], respectively).

etching. An innovative and sophisticated reservoir-on-chip model was developed by Gerami et al. [247] to study coal reservoirs, and a similar approach can be adopted to develop a reservoir-on-chip model for shale rocks.

(2) Contribution of Liquid Slip to Total Flow. Discovery of slip flow's contribution in enhancing performance in other micro- and nanoscale applications, for instance, energy conversion devices [143, 148], has been acknowledged with great enthusiasm by others [153] in their field. However, similar interest has not been visible in the research community studying flow from shale reservoirs, despite some theoretical studies that illustrated the importance of gas slip in shale [196, 206, 254]. Until now, there have been no experimental studies to investigate the theoretical contribution of gas slip to the total flux. Theoretical studies considering slip flow of oil and its contribution to total flux are still evading. Perhaps, the major reason why micro- and nanoscale transport mechanisms such as slip flow have not been experimentally investigated by shale research community is because of the general inclination to perform experiments using continuum scale cores that are not suitable to investigate the fluid slip. Therefore, it is suggested that to study the micro- and nanoscale transport mechanisms in shale rocks, an emphasis must be given to employ the reservoir-on-chip approach discussed earlier. Following that, a systematic approach can be adopted to study the effect of gas and liquid slip on the total flow. As a starting point, well-established theories on liquid slip can be used to verify their applicability in shales; for instance, it can be investigated whether slip length (L_s) for oil varies as $L_s \propto (1 + \cos\theta)^{-2}$ in synthetically fabricated chips mimicking shale rock structure by varying its wettability (θ). If the surface of the fabricated chip has been characterized with some roughness function $f(x, y)$, then a modified expression for slip length accounting for roughness [128] can be used as follows:

$$L_s = \frac{k}{(1 + \cos\theta)^2 (1 + \alpha^*)^2}, \qquad \alpha^* = \frac{\sum |f(x, y) - \overline{f(x, y)}|}{N}, \tag{51}$$

where k is the constant of proportionality and α^* is a parameter that characterizes the roughness of a surface through its amplitude N and roughness function $f(x, y)$. Now, the flow rate as a function of slip length would be given as follows:

$$Q_{slip} = Q_{no-slip}\left(1 + 6\frac{L_s}{2h}\right), \tag{52}$$

where h is the distance between the confining pore walls and Q_{slip} and $Q_{no-slip}$ are the flow rates due to slip and no-slip boundary conditions, respectively.

(3) Contribution of Evaporation to Water Loss. Hydraulic fracturing requires injecting large volume of water (~2–6 million gallons); however, on average, only 6–10% of the injected water is recovered in the US across all shale plays [255]. This abundant retention of fracturing fluid inside the shale formations is a cause of major concern because it keeps the hydrocarbons from flowing out of the reservoir by reducing the relative permeability of the hydrocarbons inside the formation. Singh [218] reviewed the process of water uptake by shales and suggested evaporation as one of the possible mechanisms that may be contributing to loss of water in shales. To support their hypothesis, they provided three characteristics associated with shale formations that could facilitate evaporation of water: (1) gas expansion, (2) water droplets formed at asperities or cavities in fractures, and (3) pore confinement. Since the hypothesis of water loss in shales due to evaporation has not been investigated before, it can be tested using the reservoir-on-chip approach with the network of small pores and fractures. Among the three characteristics noted above that could be facilitating evaporation, gas expansion seems to be the most intuitive source and can be mimicked by injecting gas into the water saturated chip with a network of matrix pores and fractures under reservoir conditions. The process of fabricating such a chip and other experimental devices needed to test this process can be set up based on the reservoir-on-chip model developed by Gerami et al. [247] to study coal reservoirs and shown in Figure 12.

Keeping track of water saturation and its phase change with time can indicate whether expansion of gas as it moves from pores to fractures results in evaporating some water. The phase change can be studied using direct visual observation of water phase behavior due to light scattering, a method that has been reliably tested for vapor detection by Yang et al. [256] and more recently in the context of shales by Ally et al. [227] to study the fluid phase behavior in nanopores.

4.4. Hydrogen Storage

4.4.1. Introduction. Hydrogen-based energy is one of the promising sources of energy [257] because hydrogen is a zero-emission fuel and can provide solutions to many versatile problems such as predictable supply that is not dependent on weather conditions, its capability to integrate within existing infrastructure developed for other forms of energy, and its applications in many different industries [258, 259]. As such, hydrogen-based energy solutions have versatile applications, such as sources of power [260] (fuel cells [261]) in transportation [262, 263] and as a commodity in many industrial processes [264]. Figure 13 shows a general illustration of a hydrogen energy system with sources, production, storage, and its applications. Among all sources of hydrogen production worldwide, 95% of the hydrogen production comes from nonrenewable sources [265] such as natural gas, coal, gasoline, diesel fuels, etc.

Among various steps in the hydrogen energy system, hydrogen storage is a major challenge and a key enabling technology for the advancement of the hydrogen energy-based applications.

4.4.2. Literature Review. Hydrogen can be stored either physically (as compressed gas or liquid) or chemically (on the surfaces of solid materials by adsorption or within the solid materials by absorption). Exploiting hydrogen energy on commercial scale as planned by the US Department of Energy through portable power sources, fuel cells, and transportation requires a compact system that can store hydrogen on these applications. The fundamental difficulty in achieving this task is low energy density per unit volume of hydrogen, which means hydrogen needs relatively larger volume to pack same amount of energy compared to other fuels. The storage of hydrogen can be divided in three sectors [266–269], namely: (i) high-pressured gaseous state, (ii) cryogenic liquid state, and (iii) solid state. Because of the low storage efficiency of liquid and gaseous hydrogen, research efforts to develop storage technologies have focused towards increasing the density of hydrogen either through chemical storage technology using new materials [270–273] or through physical storage using compression [274–276].

Even though some researchers [271] suggest that the chemical method is more efficient in storing hydrogen than the physical method, they do not provide a comparison or a reference to support such a claim. However, Petitpas et al. [275] provided an objective comparison between the two storage methods, i.e., physical storage and chemical storage, which suggested that at low pressures the density of stored hydrogen through the chemical method is significantly higher than the density of hydrogen stored through the physical method. As the pressure is increased, the density of hydrogen through the chemical method starts to flatten, whereas the density of hydrogen through the physical method continues to increase, eventually overtaking the density of hydrogen stored through the chemical method at a breakeven pressure beyond which the density of hydrogen stored through the physical method remains larger than the hydrogen stored through the chemical method (Figure 14). They reported that this breakeven pressure strongly depends on temperature.

Since the choice of hydrogen storage technology would depend on the end application, Petitpas et al. [275] suggested that the conditions relevant to a specific application may supersede the chemistry and physics required to enhance the hydrogen density. For instance, the added mass of the adsorbent for chemical storage may discourage the use of this storage technology in the case of weight-sensitive applications, whereas in the case of storage by compression the use of higher pressures may discourage its use for some applications where high pressure is a safety concern. Additionally, the cryogenic temperature needed for both techniques could be discouraging in the absence of liquid hydrogen (or liquid nitrogen for 80 K fueling). Petitpas et al. [275] also compared the use of a "hybrid" system that can store hydrogen by both compression and adsorbent and found that they can store 10% to 20% (with metal-organic framework as the sorbent) more hydrogen compared to storage by compression alone.

Despite the variation in density of stored hydrogen by the two approaches, the research on hydrogen storage in past few years has mostly focused on chemical storage by

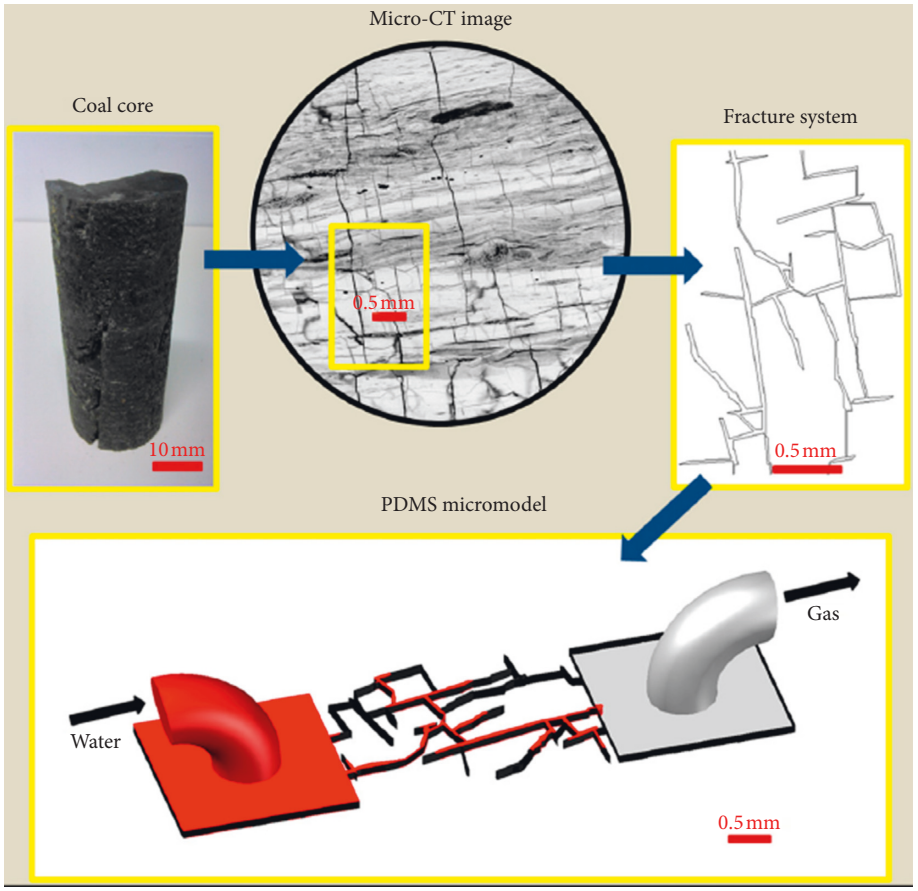

Figure 12: Reservoir-on-chip model used to depict the fracture structure in a coal reservoir [247].

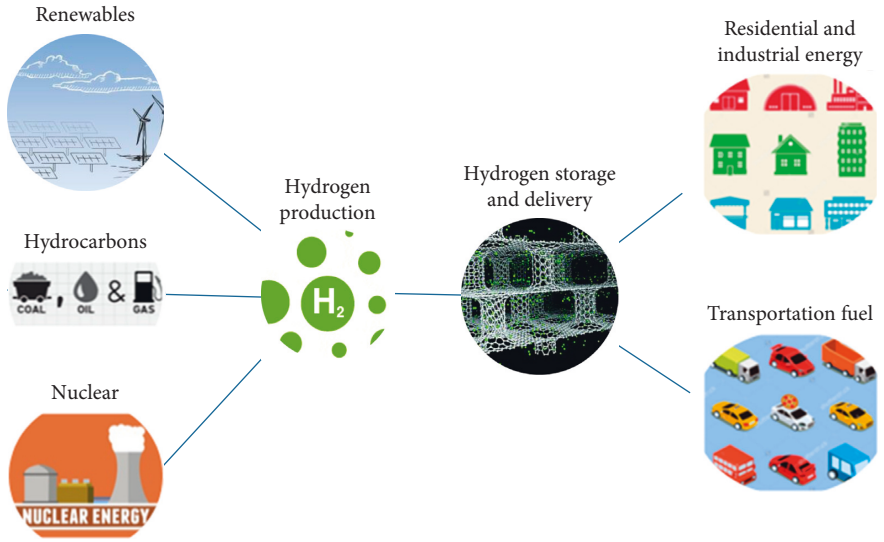

Figure 13: Schematic representing a hydrogen energy system. About 95% of the hydrogen currently produced across the world comes from nonrenewable sources.

adsorbents because of its expected use in many commercial and portable applications that may have safety concerns related to high pressure. Therefore, below we review the modeling scheme to store hydrogen by adsorption on porous and deformable materials.

(1) Key Challenge. Increasing the efficiency of hydrogen storage is one of the major challenges in the application of hydrogen for consumer applications such as transportation. Figure 15 shows a schematic comparing the volumetric scale of storage space required for 4 kg of

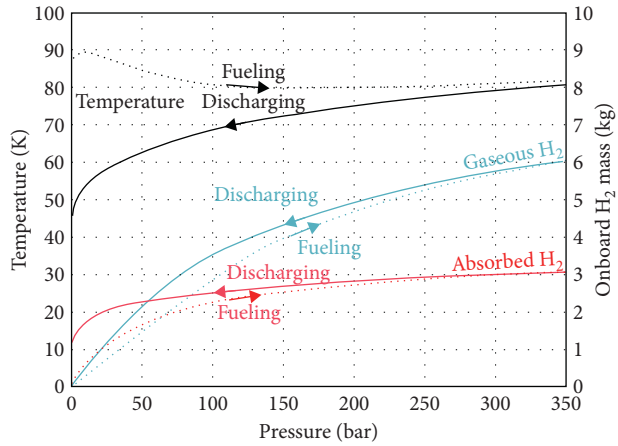

Figure 14: Comparison of physical and chemical storage capacities [275].

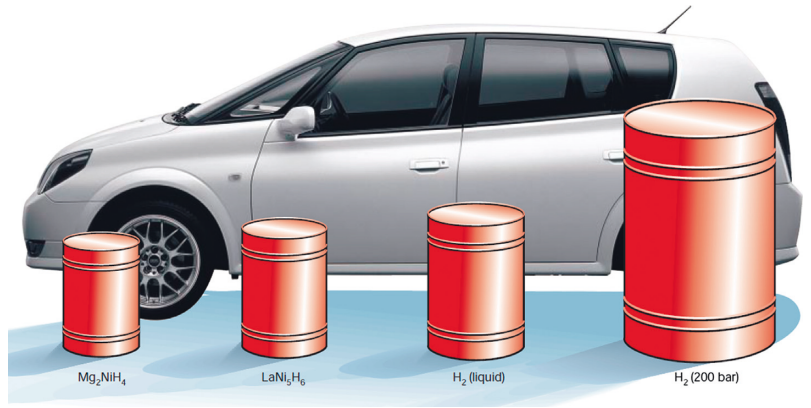

Figure 15: Schematic representation of the volumetric scale of storage space required for 4 kg of hydrogen with different modes of storage [259, 268]. Car image is a courtesy of Toyota press information, 33rd Tokyo Motor Show.

hydrogen storage in different materials and storage methods.

(2) Governing Equations. The governing equations for the storage of hydrogen follow the conservation of mass and energy.

Mass balance:

$$\frac{\partial\left(\phi\rho_g\right)}{\partial t} + \nabla.\left(\phi\rho_g u\right) = -\frac{\partial s_m}{\partial t}, \qquad \frac{\partial s_m}{\partial t} = \frac{\partial\left[(1-\phi)\rho_s\right]}{\partial t} = \frac{\partial\rho_s}{\partial t} - \frac{\partial\left(\phi\rho_s\right)}{\partial t}, \tag{53}$$

where ρ_g is the hydrogen gas density, ϕ is the porosity of the adsorbent, u is the hydrogen gas velocity that is computed using either Navier–Stokes equation or Darcy's law, s_m is the mass of hydrogen adsorbed or desorbed per unit volume of the sorbent, and ρ_s is the density of the sorbent.

Energy balance:

$$\frac{\partial\left(\overline{\rho c_p}T\right)}{\partial t} + \nabla.\left(\rho_g c_{p,g} u T\right) = \nabla.\left(k_{eff}\nabla T\right) + \frac{\partial s_T}{\partial t}, \tag{54}$$

where $\overline{\rho c_p}$ is the effective heat capacity, k_{eff} is the effective thermal conductivity [277], T is the temperature, and s_T is the product of the enthalpy change (as a result of sorption).

4.4.3. Critical Gaps and Proposed Approach. Even though the experimental research on developing superior nanostructured adsorbents [271, 273, 278, 279] for hydrogen storage continues to increase with time, the same effort has not been devoted to model the transport of hydrogen in these nanostructured porous materials. For instance, transport of hydrogen is modeled using only the continuum scale transport [277, 280–283] with no contribution of nanoscale transport mechanisms despite the role of nanoconfinement [273, 284] as an effective strategy in modifying the hydrogen storage performance. From a theoretical perspective, transport of hydrogen in nanoporous mediums is controlled by two more mechanisms (Knudsen diffusion and slip flow) other than viscous/convective flow, heat transfer, and sorption (surface diffusion). A better understanding to characterize the transport mechanisms at

nanoscale in terms of their contribution to the storage and the operating conditions for which they remain activated can be useful to optimize the storage of hydrogen in nanostructured materials. In this regard, we discuss two transport mechanisms of Knudsen diffusion and slip flow at nanoscale and how they can be added in the governing equations to model hydrogen storage.

(1) Accounting for Slip Flow and Knudsen Diffusion in Total Flux. The flow behavior at the *continuum* regime is governed by the Navier–Stokes equations; however, as Kn increases beyond the range of the continuum regime, the no-slip boundary conditions start to break such that the N-S equations should be modified to account for slip boundary conditions or molecular models should be employed. Another transport mechanism that plays an important role when the mean free path of the gas molecules is larger than or equal to the pore size is the form of diffusive transport called Knudsen diffusion. Diffusive transport in micro- and nanopores can occur through three different mechanisms: (i) bulk diffusion, (ii) surface diffusion (sorption), and (iii) Knudsen diffusion [67]. The proportion of each mechanism depends on the magnitude of the Knudsen number (Kn), and for large Kn, the molecules interact more often with the pore walls than with each other. Typical nanoporous materials for storing hydrogen have pore size that can vary from less than 1 nm to about 10 nm [270, 271, 273, 285, 286] for varied materials ranging from carbons, zeolites, metal-organic framework (MOF), complex hydrides, etc., whereas mean free path of hydrogen molecules at ambient conditions estimated from kinetic theory is about 160 nm. Therefore, it is evident from this comparison that Knudsen diffusion may have an important role to play in the transport of hydrogen.

(i) Slip Flow and Knudsen Diffusion: The convective mass flow in the presence of slip boundary conditions and diffusive mass flow in the presence of Knudsen diffusion is given as follows [69]:

$$\dot{m}_{\mathrm{C}} = \frac{MuA}{RT}\frac{p_0}{l},$$

$$\dot{m}_{\mathrm{D}} = D_{\mathrm{Kn}}\left(\frac{MA}{RT}\frac{\Delta p}{l}\right) = \left(\frac{1}{3}s\sqrt{\frac{8RT}{\pi M}}\right)\left(\frac{MA}{RT}\frac{\Delta p}{l}\right), \tag{55}$$

$$s = \begin{cases} \dfrac{4h}{\pi}, & \text{channel shaped pores,} \\ 2r, & \text{tube shaped pores.} \end{cases}$$

The solution of the Navier–Stokes equation and slip flow boundary conditions are used to solve for hydrogen velocity due to convective flux for two pore shapes of channels and tubes, respectively, as follows:

$$u = \begin{cases} \dfrac{2}{h}\displaystyle\int_{-h/2}^{h/2}\left(\frac{1}{2\mu}\frac{\partial p}{\partial x}y^2 + c_1 y + c_2\right)dy, & \text{channel-shaped pores,} \\ \dfrac{1}{\pi r^{*2}}\displaystyle\int_0^{r^*}\left[\frac{1}{4\mu}\frac{\partial p}{\partial x}r^2 + c_3\ln(r) + c_4\right]2\pi r dr, & \text{tube-shaped pores,} \end{cases}$$

$$u_{\mathrm{slip}} = \begin{cases} \dfrac{2-\sigma_{\mathrm{u}}}{\sigma_{\mathrm{u}}}\lambda\left(\dfrac{\partial u}{\partial y}\right)_{y=h}, & \text{channel-shaped pores,} \\ \dfrac{2-\sigma_{\mathrm{u}}}{\sigma_{\mathrm{u}}}\lambda\left(\dfrac{\partial u}{\partial r}\right)_{r=r^*}, & \text{tube-shaped pores,} \end{cases} \tag{56}$$

where $\dot{m}_{\mathrm{D}}$ is the diffusive mass flow, D_{Kn} is the Knudsen diffusion coefficient, s is the characteristic length, p is the pressure, u is the hydrogen velocity due to convective flux, σ_{u} is TMAC, λ is the mean free path, p_0 is the outlet pressure, M is the molar mass, A is the cross-sectional area of the medium, h is the height of the channel-shaped pore, r^* is the radius of a cylindrical-shaped pore, l is the length of the medium, R is the universal gas constant, T is the temperature, and c_1, c_2, c_3, and c_4 are constants from integration of the Navier–Stokes equation.

The total flux is the sum of the mass flow due to convective flux (including slip flow) and diffusive flux (from Knudsen diffusion), eventually leading to an effective velocity of hydrogen molecules (u_{eff}) that can be substituted in place of u in the mass balance equation for hydrogen:

$$\begin{aligned} \dot{m} &= \dot{m}_{\mathrm{C}} + \dot{m}_{\mathrm{D}}, \\ \Rightarrow \dot{m} &= \left(\frac{MuA}{RT}\frac{p_0}{l}\right) + \left(D_{\mathrm{Kn}}\frac{MA}{RT}\frac{\Delta p}{l}\right), \\ u_{\mathrm{eff}} &= \frac{\dot{m}}{\rho_{\mathrm{g}}A}, \\ u_{\mathrm{eff}} &= \frac{M}{\rho_{\mathrm{g}}RTl}\left(up_0 + D_{\mathrm{Kn}}\Delta p\right). \end{aligned} \tag{57}$$

5. Conclusions

While there is a consensus in the literature that embracing nanodevices and nanomaterials helps in improving the

efficiency and performance, the reason for the better performance is mostly subscribed to the nanosized material/structure of the system without sufficiently acknowledging the role of fluid flow mechanisms in these systems. This is evident from the literature review of fluid flow modeling in various energy-related applications, which reveals that the fundamental understanding of fluid transport at micro- and nanoscale is not adequately adapted in models. Incomplete or insufficient physics for the fluid flow can lead to untapped potential of these applications that can be used to increase their performance. This paper reviewed the current state of research for the physics of gas and liquid flow at micro- and nanoscale and identified critical gaps to improve fluid flow modeling in four different applications related to the energy sector. The review for gas flow focused on fundamentals of gas flow at rarefied conditions, the velocity slip, and temperature jump conditions. The review for liquid flow provided fundamental flow regimes of liquid flow, and liquid slip models as a function of various parameters at micro- and nanoscale. Regarding porous media applications in the energy sector, this review identified critical gaps to improve fluid flow modeling in each of the four different applications. The four applications from the energy sector considered in this review are (i) electrokinetic energy conversion devices, (ii) membrane-based water desalination through reverse osmosis, (iii) shale reservoirs, and (iv) hydrogen storage, respectively. For electrokinetic energy conversion, it was found that further improvements can be made in terms of modeling slip length as a function of key device parameters and its relationship with flux. For membrane-based water desalination, it was found that further improvements can be made if water and solute transport in graphene-based membranes are modeled by coupling the dependency of wettability and slip length in addition to typical flux from convective and diffusive flows. For shale reservoirs, it was found that researchers explore the issue at continuum scale than at pore scale, which can generally mask the phenomena contributing to flow from micro- to nanoscale; in that regard, we proposed using a reservoir-on-chip approach that can enable capturing the subcontinuum effects contributing to fluid flow in shale reservoirs. Additionally, the reservoir-on-chip approach can be used to estimate the contribution of liquid slip to total flow and the role of evaporation in the loss of fracturing water in shales. For hydrogen storage, it was found that further improvements can be made by including Knudsen diffusion and slip in the governing equations of hydrogen storage.

While many experiments have been conducted to understand the contribution of some mechanisms (e.g., slip length) at micro- and nanoscale, there are just few studies that have looked at the combined effect of material properties and the size of the flowing medium on fluid flow. The coupled effect of material properties and the flow at micro- to nanoscale is important in shale rocks and electrokinetic devices where the amount of fluid flux, important for performance, is controlled by the properties of the material in addition to the scale of the flowing medium. Future work on coupled impact of material properties and flowing medium size would be an important contribution for these two applications.

Conflicts of Interest

The authors declare that they have no conflicts of interest.

Acknowledgments

This research was supported in part by the National Energy Technology Laboratory Research Participation Program, sponsored by the U.S. Department of Energy and administered by the Oak Ridge Institute for Science and Education. R. S. M. acknowledges the support from the National Research Foundation of Korea funded by the Ministry of Education, Science and Technology (NRF 2017-R1A2B2007634 and 2017-R1A5A1015311), South Korea.

References

[1] F. Aloulou, "World tight oil production to more than double from 2015 to 2040," in *International Energy Outlook 2016*, U.S. Energy Information Administration, Washington, DC, USA, 2016.

[2] BP PLC, "2016 energy outlook," in *BP Energy Outlook*, BP PLC, London, UK, 2016.

[3] E. H. Kennard, *Kinetic Theory of Gases: With an Introduction to Statistical Mechanics*, McGraw-Hill, New York, NY, USA, 1938.

[4] M. Knudsen, "The law of the molecular flow and viscosity of gases moving through tubes," *Annals of Physics*, vol. 28, pp. 75–130, 1909.

[5] W. Steckelmacher, "Knudsen flow 75 years on: the current state of the art for flow of rarefied gases in tubes and systems," *Reports on Progress in Physics*, vol. 49, no. 10, pp. 1083–1107, 1986.

[6] R. B. Bird, W. E. Stewart, and E. N. Lightfoot, *Transport Phenomena*, John Wiley & Sons, Hoboken, NJ, USA, 2006.

[7] S. R. de Groot, P. Mazur, and A. L. King, "Non-equilibrium thermodynamics," *American Journal of Physics*, vol. 31, no. 7, pp. 558-559, 1963.

[8] L. D. Landau and E. M. Lifshitz, "Fluid mechanics," in *Course of Theoretical Physics*, Pergamon Press, Oxford, UK, 1987.

[9] S. Colin, "Rarefaction and compressibility effects on steady and transient gas flows in microchannels," *Microfluidics and Nanofluidics*, vol. 1, no. 3, pp. 268–279, 2004.

[10] D. Li and Guo, "Characteristics of frictional resistance for gas flow in microtubes," in *Proceedings of Symposium on Energy Engineering in the 21st Century*, vol. 1–6, pp. 658–664, Paris, France, January 2000.

[11] W.-M. Zhang, G. Meng, and X. Wei, "A review on slip models for gas microflows," *Microfluidics and Nanofluidics*, vol. 13, no. 6, pp. 845–882, 2012.

[12] G. H. Tang, Z. Li, Y. L. He, and W. Q. Tao, "Experimental study of compressibility, roughness and rarefaction influences on microchannel flow," *International Journal of Heat and Mass Transfer*, vol. 50, no. 11-12, pp. 2282–2295, 2007.

[13] T. Lee and C.-L. Lin, "Rarefaction and compressibility effects of the lattice-Boltzmann-equation method in a gas microchannel," *Physical Review E*, vol. 71, no. 4, article 046706, 2005.

[14] C. Y. Lim, C. Shu, X. D. Niu, and Y. T. Chew, "Application of lattice Boltzmann method to simulate microchannel flows," *Physics of Fluids*, vol. 14, no. 7, pp. 2299–2308, 2002.

[15] H.-S. Tsien, "Superaerodynamics, mechanics of rarefied gases," *Journal of the Aeronautical Sciences*, vol. 13, no. 12, pp. 653–664, 1946.

[16] B.-Y. Cao, J. Sun, M. Chen, and Z.-Y. Guo, "Molecular momentum transport at fluid-solid interfaces in MEMS/NEMS: a review," *International Journal of Molecular Sciences*, vol. 10, no. 11, pp. 4638–4706, 2009.

[17] A. J. Lofthouse, L. C. Scalabrin, and I. D. Boyd, "Velocity slip and temperature jump in hypersonic aerothermodynamics," *Journal of Thermophysics and Heat Transfer*, vol. 22, no. 1, pp. 38–49, 2008.

[18] D. Burnett, "The distribution of velocities in a slightly non-uniform gas," *Proceedings of the London Mathematical Society*, vol. s2-39, no. 1, pp. 385–430, 1935.

[19] M. S. Shavaliyev, "Super-Burnett corrections to the stress tensor and the heat flux in a gas of Maxwellian molecules," *Journal of Applied Mathematics and Mechanics*, vol. 57, no. 3, pp. 573–576, 1993.

[20] A. Agrawal and S. V. Prabhu, "Deduction of slip coefficient in slip and transition regimes from existing cylindrical Couette flow data," *Experimental Thermal and Fluid Science*, vol. 32, no. 4, pp. 991–996, 2008.

[21] N. Dongari, A. Agrawal, and A. Agrawal, "Analytical solution of gaseous slip flow in long microchannels," *International Journal of Heat and Mass Transfer*, vol. 50, no. 17-18, pp. 3411–3421, 2007.

[22] C. Cercignani and M. Lampis, "Kinetic models for gas-surface interactions," *Transport Theory and Statistical Physics*, vol. 1, no. 2, pp. 101–114, 1971.

[23] A. Agrawal and S. V. Prabhu, "Survey on measurement of tangential momentum accommodation coefficient," *Journal of Vacuum Science and Technology A: Vacuum, Surfaces, and Films*, vol. 26, no. 4, pp. 634–645, 2008.

[24] S. Song and M. M. Yovanovich, "Correlation of thermal accommodation coefficient for 'engineering' surfaces," in *Fundamentals of Conduction and Recent Developments in Contact Resistance*, pp. 107–116, American Society of Mechanical Engineers, New York, NY, USA, 1987, Proceedings of the Twenty-Fourth National Heat Transfer Conference and Exhibition, Pittsburgh, PA, USA, 1987 (A88-18501 05-34).

[25] M. A. Gallis, J. R. Torczynski, D. J. Rader, M. Tij, and A. Santos, "Normal solutions of the Boltzmann equation for highly nonequilibrium Fourier flow and Couette flow," *Physics of Fluids*, vol. 18, no. 1, article 017104, 2006.

[26] S. Chapman and T. G. Cowling, *The Mathematical Theory of Non-Uniform Gases: An Account of the Kinetic Theory of Viscosity, Thermal Conduction and Diffusion in Gases*, Cambridge University Press, Cambridge, UK, 1970.

[27] M. Gad-el-Hak, "The fluid mechanics of microdevices—the Freeman scholar lecture," *Journal of Fluids Engineering*, vol. 121, no. 1, p. 5, 1999.

[28] C.-M. Ho and Y.-C. Tai, "Micro-electro-mechanical-systems (MEMS) and fluid flows," *Annual Review of Fluid Mechanics*, vol. 30, no. 1, pp. 579–612, 1998.

[29] S. K. Loyalka, N. Petrellis, and T. S. Storvick, "Some numerical results for the BGK model: thermal creep and viscous slip problems with arbitrary accomodation at the surface," *Physics of Fluids*, vol. 18, no. 9, pp. 1094–1099, 1975.

[30] G. A. Bird, "Approach to translational equilibrium in a rigid sphere gas," *Physics of Fluids*, vol. 6, no. 10, pp. 1518-1519, 1963.

[31] G. A. Bird, "Monte Carlo simulation of gas flows," *Annual Review of Fluid Mechanics*, vol. 10, no. 1, pp. 11–31, 1978.

[32] G. A. Bird, *Molecular Gas Dynamics and the Direct Simulation of Gas Flows*, Clarendon Press, Oxford, UK, 1998.

[33] D. A. Lockerby, J. M. Reese, and M. A. Gallis, "The usefulness of higher-order constitutive relations for describing the Knudsen layer," *Physics of Fluids*, vol. 17, no. 10, article 100609, 2005.

[34] C. Cercignani, *Rarefied Gas Dynamics: From Basic Concepts to Actual Calculations*, Cambridge University Press, Cambridge, UK, 2000.

[35] L. O'Hare, D. A. Lockerby, J. M. Reese, and D. R. Emerson, "Near-wall effects in rarefied gas micro-flows: some modern hydrodynamic approaches," *International Journal of Heat and Fluid Flow*, vol. 28, no. 1, pp. 37–43, 2007.

[36] Z. Guo, B. Shi, T. S. Zhao, and C. Zheng, "Discrete effects on boundary conditions for the lattice Boltzmann equation in simulating microscale gas flows," *Physical Review E*, vol. 76, no. 5, article 056704, 2007.

[37] J. M. Reese, M. A. Gallis, and D. A. Lockerby, "New directions in fluid dynamics: non-equilibrium aerodynamic and microsystem flows," *Philosophical Transactions of the Royal Society of London A: Mathematical, Physical and Engineering Sciences*, vol. 361, no. 1813, pp. 2967–2988, 2003.

[38] M. Torrilhon and H. Struchtrup, "Boundary conditions for regularized 13-moment-equations for micro-channel-flows," *Journal of Computational Physics*, vol. 227, no. 3, pp. 1982–2011, 2008.

[39] C. Cercignani, "The Boltzmann equation and its applications," in *Applied Mathematical Sciences*, Vol. 67, Springer, New York, NY, USA, 1988.

[40] C. R. Lilley and J. E. Sader, "Velocity profile in the Knudsen layer according to the Boltzmann equation," *Proceedings of the Royal Society of London A: Mathematical, Physical and Engineering Sciences*, vol. 464, no. 2096, pp. 2015–2035, 2008.

[41] X. J. Gu and D. R. Emerson, "A computational strategy for the regularized 13 moment equations with enhanced wall-boundary conditions," *Journal of Computational Physics*, vol. 225, no. 1, pp. 263–283, 2007.

[42] H. Struchtrup and M. Torrilhon, "Higher-order effects in rarefied channel flows," *Physical Review E*, vol. 78, no. 6, article 046301, 2008.

[43] C. R. Lilley and J. E. Sader, "Velocity gradient singularity and structure of the velocity profile in the Knudsen layer according to the Boltzmann equation," *Physical Review E*, vol. 76, no. 2, article 026315, 2007.

[44] D. A. Lockerby, J. M. Reese, and M. A. Gallis, "Capturing the Knudsen layer in continuum-fluid models of non-equilibrium gas flows," *AIAA Journal*, vol. 43, no. 6, pp. 1391–1393, 2005.

[45] A. V. Gusarov and I. Smurov, "Gas-dynamic boundary conditions of evaporation and condensation: numerical analysis of the Knudsen layer," *Physics of Fluids*, vol. 14, no. 12, pp. 4242–4255, 2002.

[46] A. Beskok and G. E. Karniadakis, "A model for flows in channels, pipes, and ducts at micro and nano scales," *Microscale Thermophysical Engineering*, vol. 3, no. 1, pp. 43–77, 1999.

[47] R. Myong, "Velocity-slip effect in low-speed microscale gas flows," in *Proceedings of 35th AIAA Thermophysics Conference*, American Institute of Aeronautics and Astronautics, Denver, CO, USA, June 2001.

[48] R. S. Myong, "A computational method for Eu's generalized hydrodynamic equations of rarefied and microscale gasdynamics," *Journal of Computational Physics*, vol. 168, no. 1, pp. 47–72, 2001.

[49] R. S. Myong, "Gaseous slip models based on the Langmuir adsorption isotherm," *Physics of Fluids*, vol. 16, no. 1, pp. 104–117, 2004.

[50] R. K. Agarwal, K.-Y. Yun, and R. Balakrishnan, "Beyond Navier–Stokes: Burnett equations for flows in the continuum–transition regime," *Physics of Fluids*, vol. 13, no. 10, pp. 3061–3085, 2001.

[51] R. W. Barber and D. R. Emerson, "Challenges in modeling gas-phase flow in microchannels: from slip to transition," *Heat Transfer Engineering*, vol. 27, no. 4, pp. 3–12, 2006.

[52] G. E. Karniadakis, A. Beskok, and N. Aluru, *Microflows: Fundamentals and Simulation*, Springer, New York, NY, USA, 2001.

[53] G. E. Karniadakis, A. Beskok, and N. Aluru, *Microflows and Nanoflows: Fundamentals and Simulation*, Springer Science and Business Media, Berlin, Germany, 2005.

[54] P. Roy, N. K. Anand, and D. Banerjee, "Liquid slip and heat transfer in rotating rectangular microchannels," *International Journal of Heat and Mass Transfer*, vol. 62, pp. 184–199, 2013.

[55] S. Roy, R. Raju, H. F. Chuang, B. A. Cruden, and M. Meyyappan, "Modeling gas flow through microchannels and nanopores," *Journal of Applied Physics*, vol. 93, no. 8, pp. 4870–4879, 2003.

[56] F. Sharipov, "Data on the velocity slip and temperature jump on a gas-solid interface," *Journal of Physical and Chemical Reference Data*, vol. 40, no. 2, article 023101, 2011.

[57] F. Sharipov and V. Seleznev, "Data on internal rarefied gas flows," *Journal of Physical and Chemical Reference Data*, vol. 27, no. 3, pp. 657–706, 1998.

[58] J. Maxwell, *On Stresses in Rarefied Gases Arising from Inequalities of Temperature*, Royal Society of London, London, UK, 1878.

[59] R. W. Barber, Y. Sun, X. J. Gu, and D. R. Emerson, "Isothermal slip flow over curved surfaces," *Vacuum*, vol. 76, no. 1, pp. 73–81, 2004.

[60] D. A. Lockerby, J. M. Reese, D. R. Emerson, and R. W. Barber, "Velocity boundary condition at solid walls in rarefied gas calculations," *Physical Review E*, vol. 70, no. 1, article 017303, 2004.

[61] S. Colin, "Gas microflows in the slip flow regime: a critical review on convective heat transfer," *Journal of Heat Transfer*, vol. 134, no. 2, article 020908, 2011.

[62] Z. Deng, Y. Chen, and C. Shao, "Gas flow through rough microchannels in the transition flow regime," *Physical Review E*, vol. 93, no. 1, article 013128, 2016.

[63] C. Zhang, Y. Chen, Z. Deng, and M. Shi, "Role of rough surface topography on gas slip flow in microchannels," *Physical Review E*, vol. 86, no. 1, article 016319, 2012.

[64] N. Pelević and T. H. van der Meer, "Heat transfer and pressure drop in microchannels with random roughness," *International Journal of Thermal Sciences*, vol. 99, pp. 125–135, 2016.

[65] A. Maali, S. Colin, and B. Bhushan, "Slip length measurement of gas flow," *Nanotechnology*, vol. 27, no. 37, article 374004, 2016.

[66] R. S. Myong, "Theoretical description of the gaseous Knudsen layer in Couette flow based on the second-order constitutive and slip-jump models," *Physics of Fluids*, vol. 28, no. 1, article 012002, 2016.

[67] E. L. Cussler, *Diffusion: Mass Transfer in Fluid Systems*, Cambridge University Press, Cambridge, UK, 2009.

[68] K. Malek and M.-O. Coppens, "Knudsen self- and Fickian diffusion in rough nanoporous media," *Journal of Chemical Physics*, vol. 119, no. 5, pp. 2801–2811, 2003.

[69] T. Veltzke and J. Thöming, "An analytically predictive model for moderately rarefied gas flow," *Journal of Fluid Mechanics*, vol. 698, pp. 406–422, 2012.

[70] W. He, W. Lv, and J. H. Dickerson, "Gas diffusion mechanisms and models," in *Gas Transport in Solid Oxide Fuel Cells*, pp. 9–17, Springer International Publishing, Cham, Switzerland, 2014.

[71] F. Zhao, T. J. Armstrong, and A. V. Virkar, "Measurement of O_2-N_2 effective diffusivity in porous media at high temperatures using an electrochemical cell," *Journal of the Electrochemical Society*, vol. 150, no. 3, p. A249, 2003.

[72] J. H. Irving and J. G. Kirkwood, "The statistical mechanical theory of transport processes. IV. The equations of hydrodynamics," *Journal of Chemical Physics*, vol. 18, no. 6, pp. 817–829, 1950.

[73] R. Reid, J. Prausnitz, and B. Poling, *The Properties of Gases and Liquids*, McGraw-Hill, New York, NY, USA, 1987.

[74] P. W. Bridgman, "The thermal conductivity of liquids under pressure," *Proceedings of the American Academy of Arts and Sciences*, vol. 59, no. 7, pp. 141–169, 1923.

[75] C. Liu and Z. Li, "Flow regimes and parameter dependence in nanochannel flows," *Physical Review E*, vol. 80, no. 3, article 036302, 2009.

[76] J. K. Holt, H. G. Park, Y. Wang et al., "Fast mass transport through sub-2-nanometer carbon nanotubes," *Science*, vol. 312, no. 5776, pp. 1034–1037, 2006.

[77] M. Majumder, N. Chopra, R. Andrews, and B. J. Hinds, "Nanoscale hydrodynamics: enhanced flow in carbon nanotubes," *Nature*, vol. 438, no. 7064, p. 44, 2005.

[78] S. P. McBride and B. M. Law, "Viscosity-dependent liquid slip at molecularly smooth hydrophobic surfaces," *Physical Review E*, vol. 80, no. 6, article 060601, 2009.

[79] O. I. Vinogradova, "Drainage of a thin liquid film confined between hydrophobic surfaces," *Langmuir*, vol. 11, no. 6, pp. 2213–2220, 1995.

[80] L. Joly, G. Tocci, S. Merabia, and A. Michaelides, "Strong coupling between nanofluidic transport and interfacial chemistry: how defect reactivity controls liquid–solid friction through hydrogen bonding," *Journal of Physical Chemistry Letters*, vol. 7, no. 7, pp. 1381–1386, 2016.

[81] S. Lichter, A. Martini, R. Q. Snurr, and Q. Wang, "Liquid slip in nanoscale channels as a rate process," *Physical Review Letters*, vol. 98, no. 22, article 226001, 2007.

[82] G. Tocci, L. Joly, and A. Michaelides, "Friction of water on graphene and hexagonal boron nitride from ab initio methods: very different slippage despite very similar interface structures," *Nano Letters*, vol. 14, no. 12, pp. 6872–6877, 2014.

[83] J. Yang and D. Y. Kwok, "Effect of liquid slip in electrokinetic parallel-plate microchannel flow," *Journal of Colloid and Interface Science*, vol. 260, no. 1, pp. 225–233, 2003.

[84] J. Zhang and D. Y. Kwok, "Apparent slip over a solid-liquid interface with a no-slip boundary condition," *Physical Review E*, vol. 70, no. 5, article 056701, 2004.

[85] J.-L. Barrat and L. Bocquet, "Influence of wetting properties on hydrodynamic boundary conditions at a fluid/solid interface," *Faraday Discussions*, vol. 112, pp. 119–128, 1999.

[86] X. Chen, G. Cao, A. Han et al., "Nanoscale fluid transport: size and rate effects," *Nano Letters*, vol. 8, no. 9, pp. 2988–2992, 2008.

[87] T. D. Blake, "Slip between a liquid and a solid: D.M. Tolstoi's (1952) theory reconsidered," *Colloids and Surfaces*, vol. 47, pp. 135–145, 1990.

[88] T. A. Ho, D. V. Papavassiliou, L. L. Lee, and A. Striolo, "Liquid water can slip on a hydrophilic surface," *Proceedings of the National Academy of Sciences*, vol. 108, no. 39, pp. 16170–16175, 2011.

[89] R. S. Voronov, D. V. Papavassiliou, and L. L. Lee, "Boundary slip and wetting properties of interfaces: correlation of the contact angle with the slip length," *Journal of Chemical Physics*, vol. 124, no. 20, article 204701, 2006.

[90] E. Bonaccurso, H.-J. Butt, and V. S. J. Craig, "Surface roughness and hydrodynamic boundary slip of a Newtonian fluid in a completely wetting system," *Physical Review Letters*, vol. 90, no. 14, article 144501, 2003.

[91] Y. Chen, D. M. Kalyon, and E. Bayramli, "Effects of surface roughness and the chemical structure of materials of construction on wall slip behavior of linear low density polyethylene in capillary flow," *Journal of Applied Polymer Science*, vol. 50, no. 7, pp. 1169–1177, 1993.

[92] H. Hervet and L. Léger, "Flow with slip at the wall: from simple to complex fluids," *Comptes Rendus Physique*, vol. 4, no. 2, pp. 241–249, 2003.

[93] R. Pit, H. Hervet, and L. Léger, "Direct experimental evidence of slip in hexadecane: solid interfaces," *Physical Review Letters*, vol. 85, no. 5, pp. 980–983, 2000.

[94] J. R. Seth, M. Cloitre, and R. T. Bonnecaze, "Influence of short-range forces on wall-slip in microgel pastes," *Journal of Rheology*, vol. 52, no. 5, pp. 1241–1268, 2008.

[95] B. Woolford, D. Maynes, and B. W. Webb, "Liquid flow through microchannels with grooved walls under wetting and superhydrophobic conditions," *Microfluidics and Nanofluidics*, vol. 7, no. 1, pp. 121–135, 2008.

[96] V. S. J. Craig, C. Neto, and D. R. M. Williams, "Shear-dependent boundary slip in an aqueous Newtonian liquid," *Physical Review Letters*, vol. 87, no. 5, article 054504, 2001.

[97] C. L. Henry, C. Neto, D. R. Evans, S. Biggs, and V. S. J. Craig, "The effect of surfactant adsorption on liquid boundary slippage," *Physica A: Statistical Mechanics and its Applications*, vol. 339, no. 1-2, pp. 60–65, 2004.

[98] N. V. Priezjev, "Rate-dependent slip boundary conditions for simple fluids," *Physical Review E*, vol. 75, no. 5, article 051605, 2007.

[99] Y. Zhu and S. Granick, "Rate-dependent slip of Newtonian liquid at smooth surfaces," *Physical Review Letters*, vol. 87, no. 9, article 096105, 2001.

[100] Y. Zhu and S. Granick, "Limits of the hydrodynamic no-slip boundary condition," *Physical Review Letters*, vol. 88, no. 10, article 106102, 2002.

[101] P. G. de Gennes, "On fluid/wall slippage," *Langmuir*, vol. 18, no. 9, pp. 3413-3414, 2002.

[102] S. Granick, Y. Zhu, and H. Lee, "Slippery questions about complex fluids flowing past solids," *Nature Materials*, vol. 2, no. 4, pp. 221–227, 2003.

[103] A. C. Simonsen, P. L. Hansen, and B. Klösgen, "Nanobubbles give evidence of incomplete wetting at a hydrophobic interface," *Journal of Colloid and Interface Science*, vol. 273, no. 1, pp. 291–299, 2004.

[104] J. W. G. Tyrrell and P. Attard, "Images of nanobubbles on hydrophobic surfaces and their interactions," *Physical Review Letters*, vol. 87, no. 17, article 176104, 2001.

[105] O. I. Vinogradova, "Slippage of water over hydrophobic surfaces," *International Journal of Mineral Processing*, vol. 56, no. 1–4, pp. 31–60, 1999.

[106] X. H. Zhang, N. Maeda, and V. S. J. Craig, "Physical properties of nanobubbles on hydrophobic surfaces in water and aqueous solutions," *Langmuir*, vol. 22, no. 11, pp. 5025–5035, 2006.

[107] X. H. Zhang, A. Khan, and W. A. Ducker, "A nanoscale gas state," *Physical Review Letters*, vol. 98, no. 13, article 136101, 2007.

[108] A. Martini, A. Roxin, R. Q. Snurr, Q. Wang, and S. Lichter, "Molecular mechanisms of liquid slip," *Journal of Fluid Mechanics*, vol. 600, pp. 257–269, 2008.

[109] M. Gad-el-Hak, "Liquids: the holy grail of microfluidic modeling," *Physics of Fluids*, vol. 17, no. 10, article 100612, 2005.

[110] X. Liang, "Some effects of interface on fluid flow and heat transfer on micro- and nanoscale," *Chinese Science Bulletin*, vol. 52, no. 18, pp. 2457–2472, 2007.

[111] W. Sparreboom, A. van den Berg, and J. C. T. Eijkel, "Transport in nanofluidic systems: a review of theory and applications," *New Journal of Physics*, vol. 12, no. 1, article 015004, 2010.

[112] C. Cottin-Bizonne, B. Cross, A. Steinberger, and E. Charlaix, "Boundary slip on smooth hydrophobic surfaces: intrinsic effects and possible artifacts," *Physical Review Letters*, vol. 94, no. 5, article 056102, 2005.

[113] E. Lauga and M. P. Brenner, "Dynamic mechanisms for apparent slip on hydrophobic surfaces," *Physical Review E*, vol. 70, no. 2, article 026311, 2004.

[114] A. Lee and H.-Y. Kim, "Does liquid slippage within a rough channel always increase the flow rate?," *Physics of Fluids*, vol. 26, no. 7, article 072002, 2014.

[115] N. J. Lund, *Effective Slip Lengths for Stokes Flow over Rough, Mixed-Slip Surfaces*, 2015, http://researcharchive.vuw.ac.nz/xmlui/handle/10063/4162.

[116] C. Sendner, D. Horinek, L. Bocquet, and R. R. Netz, "Interfacial water at hydrophobic and hydrophilic surfaces: slip, viscosity, and diffusion," *Langmuir*, vol. 25, no. 18, pp. 10768–10781, 2009.

[117] J.-L. Barrat and L. Bocquet, "Large slip effect at a nonwetting fluid-solid interface," *Physical Review Letters*, vol. 82, no. 23, pp. 4671–4674, 1999.

[118] U. Raviv, P. Laurat, and J. Klein, "Fluidity of water confined to subnanometre films," *Nature*, vol. 413, no. 6851, pp. 51–54, 2001.

[119] L. Gao and T. J. McCarthy, "Teflon is hydrophilic. Comments on definitions of hydrophobic, shear versus tensile hydrophobicity, and wettability characterization," *Langmuir*, vol. 24, no. 17, pp. 9183–9188, 2008.

[120] L. Bocquet and J.-L. Barrat, "Hydrodynamic boundary conditions and correlation functions of confined fluids," *Physical Review Letters*, vol. 70, no. 18, pp. 2726–2729, 1993.

[121] L. Bocquet and J.-L. Barrat, "Hydrodynamic boundary conditions, correlation functions, and Kubo relations for confined fluids," *Physical Review E*, vol. 49, no. 4, pp. 3079–3092, 1994.

[122] D. M. Huang, C. Sendner, D. Horinek, R. R. Netz, and L. Bocquet, "Water slippage versus contact angle: a quasiuniversal relationship," *Physical Review Letters*, vol. 101, no. 22, article 226101, 2008.

[123] C. Bakli and S. Chakraborty, "Capillary filling dynamics of water in nanopores," *Applied Physics Letters*, vol. 101, no. 15, article 153112, 2012.

[124] C. Neto, D. R. Evans, E. Bonaccurso, H.-J. Butt, and V. S. J. Craig, "Boundary slip in Newtonian liquids: a review of experimental studies," *Reports on Progress in Physics*, vol. 68, no. 12, pp. 2859–2897, 2005.

[125] C. Cottin-Bizonne, J.-L. Barrat, L. Bocquet, and E. Charlaix, "Low-friction flows of liquid at nanopatterned interfaces," *Nature Materials*, vol. 2, no. 4, pp. 237–240, 2003.

[126] C. Cottin-Bizonne, C. Barentin, E. Charlaix, L. Bocquet, and J.-L. Barrat, "Dynamics of simple liquids at heterogeneous surfaces : molecular dynamics simulations and

hydrodynamic description," *European Physical Journal E*, vol. 15, no. 4, pp. 427–438, 2004.

[127] N. J. Lund, X. P. Zhang, K. Mahelona, and S. C. Hendy, "Calculation of effective slip on rough chemically heterogeneous surfaces using a homogenization approach," *Physical Review E*, vol. 86, no. 4, article 046303, 2012.

[128] C. A. Misra and C. Bakli, "On the comparability of chemical structure and roughness of nanochannels in altering fluid slippage," 2016, http://arxiv.org/abs/1605.02479.

[129] L. Joly, C. Ybert, E. Trizac, and L. Bocquet, "Liquid friction on charged surfaces: from hydrodynamic slippage to electrokinetics," *Journal of Chemical Physics*, vol. 125, no. 20, article 204716, 2006.

[130] J. N. Choudhary, S. Datta, and S. Jain, "Effective slip in nanoscale flows through thin channels with sinusoidal patterns of wall wettability," *Microfluidics and Nanofluidics*, vol. 18, no. 5-6, pp. 931–942, 2014.

[131] Y. Xie, X. Wang, J. Xue, K. Jin, L. Chen, and Y. Wang, "Electric energy generation in single track-etched nanopores," *Applied Physics Letters*, vol. 93, no. 16, article 163116, 2008.

[132] S. M. Mitrovski, L. C. C. Elliott, and R. G. Nuzzo, "Microfluidic devices for energy conversion: planar integration and performance of a passive, fully immersed H2-O2 fuel cell," *Langmuir*, vol. 20, no. 17, pp. 6974–6976, 2004.

[133] X. Meng, X. Wang, D. Geng, C. Ozgit-Akgun, N. Schneider, and J. W. Elam, "Atomic layer deposition for nanomaterial synthesis and functionalization in energy technology," *Materials Horizons*, vol. 4, no. 2, pp. 133–154, 2017.

[134] X. Meng, K. He, D. Su et al., "Gallium sulfide–single-walled carbon nanotube composites: high-performance anodes for lithium-ion batteries," *Advanced Functional Materials*, vol. 24, no. 34, pp. 5435–5442, 2014.

[135] C. Zhao and C. Yang, "Advances in electrokinetics and their applications in micro/nano fluidics," *Microfluidics and Nanofluidics*, vol. 13, no. 2, pp. 179–203, 2012.

[136] D. Burgreen and F. R. Nakache, "Electrokinetic flow in ultrafine capillary slits," *Journal of Physical Chemistry*, vol. 68, no. 5, pp. 1084–1091, 1964.

[137] W. Sparreboom, A. van den Berg, and J. C. T. Eijkel, "Principles and applications of nanofluidic transport," *Nature Nanotechnology*, vol. 4, no. 11, pp. 713–720, 2009.

[138] W. R. Bowen and H. Mukhtar, "Characterisation and prediction of separation performance of nanofiltration membranes," *Journal of Membrane Science*, vol. 112, no. 2, pp. 263–274, 1996.

[139] W. M. Deen, "Hindered transport of large molecules in liquid-filled pores," *AIChE Journal*, vol. 33, no. 9, pp. 1409–1425, 1987.

[140] F. G. Smith and W. M. Deen, "Electrostatic effects on the partitioning of spherical colloids between dilute bulk solution and cylindrical pores," *Journal of Colloid and Interface Science*, vol. 91, no. 2, pp. 571–590, 1983.

[141] Rajni, J. M. Oh, and I. S. Kang, "Ion size effects on the osmotic pressure and electrocapillarity in a nanoslit: symmetric and asymmetric ion sizes," *Physical Review E*, vol. 93, no. 6, article 063112, 2016.

[142] J. C. Giddings, E. Kucera, C. P. Russell, and M. N. Myers, "Statistical theory for the equilibrium distribution of rigid molecules in inert porous networks. Exclusion chromatography," *Journal of Physical Chemistry*, vol. 72, no. 13, pp. 4397–4408, 1968.

[143] C. Davidson and X. Xuan, "Electrokinetic energy conversion in slip nanochannels," *Journal of Power Sources*, vol. 179, no. 1, pp. 297–300, 2008.

[144] S. Haldrup, J. Catalano, M. Hinge, G. V. Jensen, J. S. Pedersen, and A. Bentien, "Tailoring membrane nanostructure and charge density for high electrokinetic energy conversion efficiency," *ACS Nano*, vol. 10, no. 2, pp. 2415–2423, 2016.

[145] X. Xuan and D. Li, "Thermodynamic analysis of electrokinetic energy conversion," *Journal of Power Sources*, vol. 156, no. 2, pp. 677–684, 2006.

[146] F. A. Morrison Jr. and J. F. Osterle, "Electrokinetic energy conversion in ultrafine capillaries," *Journal of Chemical Physics*, vol. 43, no. 6, pp. 2111–2115, 1965.

[147] S. Pennathur, J. Eijkel, and A. Berg, "Energy conversion in microsystems: is there a role for micro/nanofluidics?," *Lab on a Chip*, vol. 7, no. 10, p. 1234, 2007.

[148] Y. Ren and D. Stein, "Slip-enhanced electrokinetic energy conversion in nanofluidic channels," *Nanotechnology*, vol. 19, no. 19, article 195707, 2008.

[149] F. H. J. van der Heyden, D. J. Bonthuis, D. Stein, C. Meyer, and C. Dekker, "Electrokinetic energy conversion efficiency in nanofluidic channels," *Nano Letters*, vol. 6, no. 10, pp. 2232–2237, 2006.

[150] P. B. Peters, R. van Roij, M. Z. Bazant, and P. M. Biesheuvel, "Analysis of electrolyte transport through charged nanopores," *Physical Review E*, vol. 93, no. 5, article 053108, 2016.

[151] F. J. Diez, G. Hernaiz, J. J. Miranda, and M. Sureda, "On the capabilities of nano electrokinetic thrusters for space propulsion," *Acta Astronautica*, vol. 83, pp. 97–107, 2013.

[152] G. Seshadri and T. Baier, "Effect of electro-osmotic flow on energy conversion on superhydrophobic surfaces," *Physics of Fluids*, vol. 25, no. 4, article 042002, 2013.

[153] L. Bocquet and E. Charlaix, "Nanofluidics, from bulk to interfaces," *Chemical Society Reviews*, vol. 39, no. 3, pp. 1073–1095, 2010.

[154] C. I. Bouzigues, P. Tabeling, and L. Bocquet, "Nanofluidics in the Debye layer at hydrophilic and hydrophobic surfaces," *Physical Review Letters*, vol. 101, no. 11, article 114503, 2008.

[155] E. Bertrand, T. D. Blake, and J. D. Coninck, "Influence of solid?liquid interactions on dynamic wetting: a molecular dynamics study," *Journal of Physics: Condensed Matter*, vol. 21, no. 46, article 464124, 2009.

[156] S. Lichter, A. Roxin, and S. Mandre, "Mechanisms for liquid slip at solid surfaces," *Physical Review Letters*, vol. 93, no. 8, article 086001, 2004.

[157] M. R. Stukan, P. Ligneul, J. P. Crawshaw, and E. S. Boek, "Spontaneous imbibition in nanopores of different roughness and wettability," *Langmuir*, vol. 26, no. 16, pp. 13342–13352, 2010.

[158] S. Supple and N. Quirke, "Molecular dynamics of transient oil flows in nanopores I: imbibition speeds for single wall carbon nanotubes," *Journal of Chemical Physics*, vol. 121, no. 17, pp. 8571–8579, 2004.

[159] S. Kelly, C. Torres-Verdín, and M. T. Balhoff, "Anomalous liquid imbibition at the nanoscale: the critical role of interfacial deformations," *Nanoscale*, vol. 8, no. 5, pp. 2751–2767, 2016.

[160] C. Bakli and S. Chakraborty, "Electrokinetic energy conversion in nanofluidic channels: addressing the loose ends in nanodevice efficiency," *Electrophoresis*, vol. 36, no. 5, pp. 675–681, 2015.

[161] L. F. Greenlee, D. F. Lawler, B. D. Freeman, B. Marrot, and P. Moulin, "Reverse osmosis desalination: water sources,

technology, and today's challenges," *Water Research*, vol. 43, no. 9, pp. 2317–2348, 2009.

[162] R. R. Nair, H. A. Wu, P. N. Jayaram, I. V. Grigorieva, and A. K. Geim, "Unimpeded permeation of water through helium-leak-tight graphene-based membranes," *Science*, vol. 335, no. 6067, pp. 442–444, 2012.

[163] M. E. Suk and N. R. Aluru, "Ion transport in sub-5-nm graphene nanopores," *Journal of Chemical Physics*, vol. 140, no. 8, article 084707, 2014.

[164] D. G. Luchinsky, R. Tindjong, I. Kaufman, P. V. E. McClintock, and R. S. Eisenberg, "Self-consistent analytic solution for the current and the access resistance in open ion channels," *Physical Review E*, vol. 80, no. 2, article 021925, 2009.

[165] M. Thomas, B. Corry, and T. A. Hilder, "What have we learnt about the mechanisms of rapid water transport, ion rejection and selectivity in nanopores from molecular simulation?," *Small*, vol. 10, no. 8, pp. 1453–1465, 2014.

[166] C. Dekker, "Solid-state nanopores," *Nature Nanotechnology*, vol. 2, no. 4, pp. 209–215, 2007.

[167] D. P. Hoogerheide, S. Garaj, and J. A. Golovchenko, "Probing surface charge fluctuations with solid-state nanopores," *Physical Review Letters*, vol. 102, no. 25, article 256804, 2009.

[168] S. P. Surwade, S. N. Smirnov, I. V. Vlassiouk et al., "Water desalination using nanoporous single-layer graphene," *Nature Nanotechnology*, vol. 10, no. 5, pp. 459–464, 2015.

[169] Y. You, V. Sahajwalla, M. Yoshimura, and R. K. Joshi, "Graphene and graphene oxide for desalination," *Nanoscale*, vol. 8, no. 1, pp. 117–119, 2015.

[170] D. Cohen-Tanugi, L.-C. Lin, and J. C. Grossman, "Multilayer nanoporous graphene membranes for water desalination," *Nano Letters*, vol. 16, no. 2, pp. 1027–1033, 2016.

[171] J. R. Werber, C. O. Osuji, and M. Elimelech, "Materials for next-generation desalination and water purification membranes," *Nature Reviews Materials*, vol. 1, no. 5, article 16018, 2016.

[172] G. M. Geise, H. B. Park, A. C. Sagle, B. D. Freeman, and J. E. McGrath, "Water permeability and water/salt selectivity tradeoff in polymers for desalination," *Journal of Membrane Science*, vol. 369, no. 1-2, pp. 130–138, 2011.

[173] H. Zhang and G. M. Geise, "Modeling the water permeability and water/salt selectivity tradeoff in polymer membranes," *Journal of Membrane Science*, vol. 520, pp. 790–800, 2016.

[174] J. R. Werber, A. Deshmukh, and M. Elimelech, "The critical need for increased selectivity, not increased water permeability, for desalination membranes," *Environmental Science and Technology Letters*, vol. 3, no. 4, pp. 112–120, 2016.

[175] M. Shahbabaei, D. Tang, and D. Kim, "Simulation insight into water transport mechanisms through multilayer graphene-based membrane," *Computational Materials Science*, vol. 128, pp. 87–97, 2017.

[176] B. Chen, H. Jiang, X. Liu, and X. Hu, "Observation and analysis of water transport through graphene oxide Interlamination," *Journal of Physical Chemistry C*, vol. 121, no. 2, pp. 1321–1328, 2017.

[177] D. Parobek and H. Liu, "Wettability of graphene," *2D Materials*, vol. 2, no. 3, article 032001, 2015.

[178] P. Joseph, C. Cottin-Bizonne, J.-M. Benoît et al., "Slippage of water past superhydrophobic carbon nanotube forests in microchannels," *Physical Review Letters*, vol. 97, no. 15, article 156104, 2006.

[179] C. Lee, C.-H. Choi, and C.-J. Kim, "Structured surfaces for a giant liquid slip," *Physical Review Letters*, vol. 101, no. 6, article 064501, 2008.

[180] J. Cai, E. Perfect, C.-L. Cheng, and X. Hu, "Generalized modeling of spontaneous imbibition based on hagen–Poiseuille flow in tortuous capillaries with variably shaped apertures," *Langmuir*, vol. 30, no. 18, pp. 5142–5151, 2014.

[181] M. J. Wilson, M. V. Shaldybin, and L. Wilson, "Clay mineralogy and unconventional hydrocarbon shale reservoirs in the USA. I. Occurrence and interpretation of mixed-layer R3 ordered illite/smectite," *Earth-Science Reviews*, vol. 158, pp. 31–50, 2016.

[182] M. J. Wilson, L. Wilson, and M. V. Shaldybin, "Clay mineralogy and unconventional hydrocarbon shale reservoirs in the USA. II. Implications of predominantly illitic clays on the physico-chemical properties of shales," *Earth-Science Reviews*, vol. 158, pp. 1–8, 2016.

[183] T. J. Katsube, "Petrophysical characteristics of shales from the Scotian shelf," *Geophysics*, vol. 56, no. 10, pp. 1681–1689, 1991.

[184] T. J. Katsube and M. A. Williamson, "Effects of diagenesis on shale nano-pore structure and implications for sealing capacity," *Clay Minerals*, vol. 29, no. 4, pp. 451–461, 1994.

[185] F. Javadpour, "Nanopores and apparent permeability of gas flow in mudrocks (shales and siltstone)," *Journal of Canadian Petroleum Technology*, vol. 48, no. 8, pp. 16–21, 2009.

[186] A. Wasaki and I. Y. Akkutlu, "Permeability of organic-rich shale," *SPE Journal*, vol. 20, no. 6, pp. 1384–1396, 2015.

[187] J. F. W. Gale, S. E. Laubach, J. E. Olson, P. Eichhubl, and A. Fall, "Natural fractures in shale: a review and new observations," *AAPG Bulletin*, vol. 98, no. 11, pp. 2165–2216, 2014.

[188] H. Singh and J. Cai, "Screening improved recovery methods in tight-oil formations by injecting and producing through fractures," *International Journal of Heat and Mass Transfer*, vol. 116, pp. 977–993, 2018.

[189] H. Singh and J. Cai, "A feature-based stochastic permeability of shale: part 1—validation and two-phase permeability in a utica shale sample," *Transport in Porous Media*, pp. 1–34, 2018.

[190] H. Singh and J. Cai, "A feature-based stochastic permeability of shale: part 2–predicting field-scale permeability," *Transport in Porous Media*, pp. 1–18, 2018.

[191] W. Wei and Y. Xia, "Geometrical, fractal and hydraulic properties of fractured reservoirs: a mini-review," *Advances in Geo-Energy Research*, vol. 1, no. 1, pp. 31–38, 2017.

[192] L. Chen, Z. Jiang, K. Liu, and F. Gao, "Quantitative characterization of micropore structure for organic-rich Lower Silurian shale in the Upper Yangtze Platform, South China: implications for shale gas adsorption capacity," *Advances in Geo-Energy Research*, vol. 1, no. 2, pp. 112–123, 2017.

[193] J. A. Chermak and M. E. Schreiber, "Mineralogy and trace element geochemistry of gas shales in the United States: environmental implications," *International Journal of Coal Geology*, vol. 126, pp. 32–44, 2014.

[194] S. Huang, Y. Wu, X. Meng, L. Liu, and W. Ji, "Recent advances on microscopic pore characteristics of low permeability sandstone reservoirs," *Advances in Geo-Energy Research*, vol. 2, no. 2, pp. 122–134, 2018.

[195] D. Wood and B. Hazra, "Pyrolysis S2-peak characteristics of Raniganj shales (India) reflect complex combinations of kerogen kinetics and other processes related to different levels of thermal maturity," *Advances in Geo-Energy Research*, vol. 2, no. 4, pp. 343–368, 2018.

[196] H. Darabi, A. Ettehad, F. Javadpour, and K. Sepehrnoori, "Gas flow in ultra-tight shale strata," *Journal of Fluid Mechanics*, vol. 710, pp. 641–658, 2012.

[197] F. Javadpour, M. McClure, and M. E. Naraghi, "Slip-corrected liquid permeability and its effect on hydraulic fracturing and fluid loss in shale," *Fuel*, vol. 160, pp. 549–559, 2015.

[198] M. Kazemi and A. Takbiri-Borujeni, "An analytical model for shale gas permeability," *International Journal of Coal Geology*, vol. 146, pp. 188–197, 2015.

[199] H. Singh and P. Azom, *Integration of Nonempirical Shale Permeability Model in a Dual-Continuum Reservoir Simulator*, 2013, https://www.onepetro.org/conference-paper/SPE-167125-MS.

[200] H. Singh and F. Javadpour, "A new non-empirical approach to model transport of fluids in shale gas reservoirs," in *Proceedings of Unconventional Resources Technology Conference*, pp. 1258–1273, Denver, CO, USA, August 2013.

[201] H. Singh, F. Javadpour, A. Ettehadtavakkol, and H. Darabi, "Nonempirical apparent permeability of shale," *SPE Reservoir Evaluation and Engineering*, vol. 17, no. 3, pp. 414–424, 2014.

[202] F. Javadpour and H. Singh, "Authors' reply to comment by Xu Tang on the paper "Langmuir slip-Langmuir sorption permeability model of shale"," *Fuel*, vol. 181, p. 1096, 2016.

[203] Z.-Z. Li, T. Min, Q. Kang, Y.-L. He, and W.-Q. Tao, "Investigation of methane adsorption and its effect on gas transport in shale matrix through microscale and mesoscale simulations," *International Journal of Heat and Mass Transfer*, vol. 98, pp. 675–686, 2016.

[204] E. M. Myshakin, H. Singh, S. Sanguinito, G. Bromhal, and A. L. Goodman, "Numerical estimations of storage efficiency for the prospective CO2 storage resource of shales," *International Journal of Greenhouse Gas Control*, vol. 76, pp. 24–31, 2018.

[205] D. Orozco and R. Aguilera, *A Material Balance Equation for Stress-Sensitive Shale Gas Reservoirs Considering the Contribution of Free, Adsorbed and Dissolved Gas*, 2015, https://www.onepetro.org/conference-paper/SPE-175964-MS.

[206] H. Singh and F. Javadpour, "Langmuir slip-Langmuir sorption permeability model of shale," *Fuel*, vol. 164, pp. 28–37, 2016.

[207] J. Wang, L. Chen, Q. Kang, and S. S. Rahman, "Permeability prediction of organic shale with generalized lattice Boltzmann model considering surface diffusion effect," 2016, http://arxiv.org/abs/1601.00704.

[208] K. Wu, X. Li, C. Wang, W. Yu, and Z. Chen, "Model for surface diffusion of adsorbed gas in nanopores of shale gas reservoirs," *Industrial and Engineering Chemistry Research*, vol. 54, no. 12, pp. 3225–3236, 2015.

[209] T. Wu and D. Zhang, "Impact of adsorption on gas transport in nanopores," *Scientific Reports*, vol. 6, no. 1, article 23629, 2016.

[210] Z. Yang, W. Wang, M. Dong et al., "A model of dynamic adsorption–diffusion for modeling gas transport and storage in shale," *Fuel*, vol. 173, pp. 115–128, 2016.

[211] P. Cao, J. Liu, and Y.-K. Leong, "A fully coupled multiscale shale deformation-gas transport model for the evaluation of shale gas extraction," *Fuel*, vol. 178, pp. 103–117, 2016.

[212] H. Wang and M. Marongiu-Porcu, "Impact of shale-gas apparent permeability on production: combined effects of non-Darcy flow/gas-slippage, desorption, and geomechanics," *SPE Reservoir Evaluation and Engineering*, vol. 18, no. 4, pp. 495–507, 2015.

[213] K. Wu, X. Li, C. Guo, C. Wang, and Z. Chen, "A unified model for gas transfer in nanopores of shale-gas reservoirs: coupling pore diffusion and surface diffusion," *SPE Journal*, vol. 21, no. 5, pp. 1583–1611, 2016.

[214] L. Yang, H. Ge, Y. Shen et al., "Imbibition inducing tensile fractures and its influence on in-situ stress analyses: a case study of shale gas drilling," *Journal of Natural Gas Science and Engineering*, vol. 26, pp. 927–939, 2015.

[215] W. Yu and K. Sepehrnoori, "Simulation of gas desorption and geomechanics effects for unconventional gas reservoirs," *Fuel*, vol. 116, pp. 455–464, 2014.

[216] P. Fakcharoenphol, B. Kurtoglu, H. Kazemi, S. Charoenwongsa, and Y.-S. Wu, *The Effect of Osmotic Pressure on Improve Oil Recovery from Fractured Shale Formations*, 2014, https://www.onepetro.org/conference-paper/SPE-168998-MS.

[217] P. Fakcharoenphol, B. Kurtoglu, H. Kazemi, S. Charoenwongsa, and Y.-S. Wu, "The effect of chemical osmosis on oil and gas production from fractured shale formations," in *Fluid Dynamics in Complex Fractured-Porous Systems*, B. Faybishenko, S. M. Benson, and J. E. Gale, Eds., pp. 85–97, John Wiley & Sons, Hoboken, NJ, USA, 2015.

[218] H. Singh, "A critical review of water uptake by shales," *Journal of Natural Gas Science and Engineering*, vol. 34, pp. 751–766, 2016.

[219] L. Liang, D. Luo, X. Liu, and J. Xiong, "Experimental study on the wettability and adsorption characteristics of Longmaxi Formation shale in the Sichuan Basin, China," *Journal of Natural Gas Science and Engineering*, vol. 33, pp. 1107–1118, 2016.

[220] H. Roshan, A. Z. Al-Yaseri, M. Sarmadivaleh, and S. Iglauer, "On wettability of shale rocks," *Journal of Colloid and Interface Science*, vol. 475, pp. 104–111, 2016.

[221] D. Wang, R. Butler, J. Zhang, and R. Seright, "Wettability survey in bakken shale with surfactant-formulation imbibition," *SPE Reservoir Evaluation and Engineering*, vol. 15, no. 6, pp. 695–705, 2012.

[222] M. Xu and H. Dehghanpour, "Advances in understanding wettability of gas shales," *Energy and Fuels*, vol. 28, no. 7, pp. 4362–4375, 2014.

[223] Q. Meng, H. Liu, and J. Wang, "A critical review on fundamental mechanisms of spontaneous imbibition and the impact of boundary condition, fluid viscosity and wettability," *Advances in Geo-Energy Research*, vol. 1, no. 1, pp. 1–17, 2017.

[224] X. Wang and J. J. Sheng, "A self-similar analytical solution of spontaneous and forced imbibition in porous media," *Advances in Geo-Energy Research*, vol. 2, no. 3, pp. 260–268, 2018.

[225] M. R. Yassin, H. Dehghanpour, J. Wood, and Q. Lan, "A theory for relative permeability of unconventional rocks with dual-wettability pore network," *SPE Journal*, vol. 21, no. 6, pp. 1970–1980, 2016.

[226] M. Alfi, H. Nasrabadi, and D. Banerjee, "Experimental investigation of confinement effect on phase behavior of hexane, heptane and octane using lab-on-a-chip technology," *Fluid Phase Equilibria*, vol. 423, pp. 25–33, 2016.

[227] J. Ally, S. Molla, and F. Mostowfi, "Condensation in nanoporous packed beds," *Langmuir*, vol. 32, no. 18, pp. 4494–4499, 2016.

[228] B. T. Bui, H.-H. Liu, J. Chen, and A. N. Tutuncu, "Effect of capillary condensation on gas transport in shale: a pore-scale model study," *SPE Journal*, vol. 21, no. 2, pp. 601–612, 2016.

[229] A. W. Islam, T. W. Patzek, and A. Y. Sun, "Thermodynamics phase changes of nanopore fluids," *Journal of Natural Gas Science and Engineering*, vol. 25, pp. 134–139, 2015.

[230] B. Jin and H. Nasrabadi, "Phase behavior of multi-component hydrocarbon systems in nano-pores using gauge-GCMC molecular simulation," *Fluid Phase Equilibria*, vol. 425, pp. 324–334, 2016.

[231] M. Sarvestani, F. Rashidi, and S. A. Mousavi Dehghani, "A production data analysis model for gas/condensate reservoirs," *Journal of Petroleum Science and Engineering*, vol. 141, pp. 52–69, 2016.

[232] R. Barati and J.-T. Liang, "A review of fracturing fluid systems used for hydraulic fracturing of oil and gas wells," *Journal of Applied Polymer Science*, vol. 131, no. 16, 2014.

[233] T. Jacobs, "Energized fractures: shale revolution revisits the energized fracture," *Journal of Petroleum Technology*, vol. 66, no. 6, pp. 48–56, 2014.

[234] J. Lu, J.-P. Nicot, P. J. Mickler, L. H. Ribeiro, and R. Darvari, "Alteration of Bakken reservoir rock during CO_2-based fracturing—an autoclave reaction experiment," *Journal of Unconventional Oil and Gas Resources*, vol. 14, pp. 72–85, 2016.

[235] A. Qajar, Z. Xue, A. J. Worthen et al., "Modeling fracture propagation and cleanup for dry nanoparticle-stabilized-foam fracturing fluids," *Journal of Petroleum Science and Engineering*, vol. 146, pp. 210–221, 2016.

[236] L. H. Ribeiro, H. Li, and J. E. Bryant, "Use of a CO_2-hybrid fracturing design to enhance production from unpropped-fracture networks," *SPE Production and Operations*, vol. 32, no. 1, pp. 28–40, 2016.

[237] Z. Wang, B. Sun, and X. Sun, "Calculation of temperature in fracture for carbon dioxide fracturing," *SPE Journal*, vol. 21, no. 5, pp. 1491–1500, 2016.

[238] D. Sanchez-Rivera, K. Mohanty, and M. Balhoff, "Reservoir simulation and optimization of huff-and-puff operations in the bakken shale," *Fuel*, vol. 147, pp. 82–94, 2015.

[239] H. Singh and J. Cai, "A mechanistic model for multi-scale sorption dynamics in shale," *Fuel*, vol. 234, pp. 996–1014, 2018.

[240] P. Zhu, M. T. Balhoff, and K. K. Mohanty, "Compositional modeling of fracture-to-fracture miscible gas injection in an oil-rich shale," *Journal of Petroleum Science and Engineering*, vol. 152, pp. 628–638, 2017.

[241] T. W. Patzek, F. Male, and M. Marder, "Gas production in the Barnett Shale obeys a simple scaling theory," *Proceedings of the National Academy of Sciences of the United States of America*, vol. 110, no. 49, pp. 19731–19736, 2013.

[242] S. A. Hosseini, F. Javadpour, and G. E. Michael, "Novel analytical core-sample analysis indicates higher gas content in shale-gas reservoirs," *SPE Journal*, vol. 20, no. 6, pp. 1397–1408, 2015.

[243] H. Roshan, S. Ehsani, C. E. Marjo, M. S. Andersen, and R. I. Acworth, "Mechanisms of water adsorption into partially saturated fractured shales: an experimental study," *Fuel*, vol. 159, pp. 628–637, 2015.

[244] Q. Sang, Y. Li, Z. Yang, C. Zhu, J. Yao, and M. Dong, "Experimental investigation of gas production processes in shale," *International Journal of Coal Geology*, vol. 159, pp. 30–47, 2016.

[245] W. Yuan, Z. Pan, X. Li et al., "Experimental study and modelling of methane adsorption and diffusion in shale," *Fuel*, vol. 117, pp. 509–519, 2014.

[246] A. Zolfaghari, H. Dehghanpour, M. Noel, and D. Bearinger, "Laboratory and field analysis of flowback water from gas shales," *Journal of Unconventional Oil and Gas Resources*, vol. 14, pp. 113–127, 2016.

[247] A. Gerami, P. Mostaghimi, R. T. Armstrong, A. Zamani, and M. E. Warkiani, "A microfluidic framework for studying relative permeability in coal," *International Journal of Coal Geology*, vol. 159, pp. 183–193, 2016.

[248] K. He, L. Xu, Y. Gao et al., *Validating Surfactant Performance in the Eagle Ford Shale: A Correlation between the Reservoir-on-a-Chip Approach and Enhanced Well Productivity*, 2014, https://www.onepetro.org/conference-paper/SPE-169147-MS.

[249] J. Jiménez-Martínez, M. L. Porter, J. D. Hyman, J. W. Carey, and H. S. Viswanathan, "Mixing in a three-phase system: enhanced production of oil-wet reservoirs by CO_2 injection," *Geophysical Research Letters*, vol. 43, no. 1, pp. 196–205, 2016.

[250] S. Kelly, H. El-Sobky, C. Torres-Verdín, and M. T. Balhoff, "Assessing the utility of FIB-SEM images for shale digital rock physics," *Advances in Water Resources*, vol. 95, pp. 302–316, 2015.

[251] S. A. Kelly, *Using nanofluidics and microscopy to study unconventional pore-scale transport phenomena*, Ph.D. thesis, University of Texas at Austin, Austin, TX, USA, 2015.

[252] M. L. Porter, J. Jiménez-Martínez, R. Martinez, Q. McCulloch, J. W. Carey, and H. S. Viswanathan, "Geo-material microfluidics at reservoir conditions for subsurface energy resource applications," *Lab on a Chip*, vol. 15, no. 20, pp. 4044–4053, 2015.

[253] M. Warkiani, C.-P. Lou, and H.-Q. Gong, "Fabrication of multi-layer polymeric micro-sieve having narrow slot pores with conventional ultraviolet-lithography and micro-fabrication techniques," *Biomicrofluidics*, vol. 5, no. 3, article 036504, 2011.

[254] M. E. Naraghi and F. Javadpour, "A stochastic permeability model for the shale-gas systems," *International Journal of Coal Geology*, vol. 140, pp. 111–124, 2015.

[255] I. Vandecasteele, I. M. Rivero, S. Sala et al., "Impact of shale gas development on water resources: a case study in northern Poland," *Environmental Management*, vol. 55, no. 6, pp. 1285–1299, 2015.

[256] H. Yang, P. Jiang, and B. Jiang, "Vapor detection enabled by self-assembled colloidal photonic crystals," *Journal of Colloid and Interface Science*, vol. 370, no. 1, pp. 11–18, 2012.

[257] J. Keller, L. Klebanoff, S. Schoenung, and M. Gillie, "The need for hydrogen-based energy technologies in the 21st century," in *Hydrogen Storage Technology*, CRC Press, Boca Raton, FL, USA, pp. 3–30, 2012.

[258] Q. Lai, M. Paskevicius, D. A. Sheppard et al., "Hydrogen storage materials for mobile and stationary applications: current state of the art," *ChemSusChem*, vol. 8, no. 17, pp. 2789–2825, 2015.

[259] L. Schlapbach and A. Züttel, "Hydrogen-storage materials for mobile applications," *Nature*, vol. 414, no. 6861, pp. 353–358, 2001.

[260] N. A. A. Rusman and M. Dahari, "A review on the current progress of metal hydrides material for solid-state hydrogen storage applications," *International Journal of Hydrogen Energy*, vol. 41, no. 28, pp. 12108–12126, 2016.

[261] W. Liu, C. J. Webb, and E. M. Gray, "Review of hydrogen storage in AB3 alloys targeting stationary fuel cell applications," *International Journal of Hydrogen Energy*, vol. 41, no. 5, pp. 3485–3507, 2016.

[262] I. Dincer and C. Acar, "A review on potential use of hydrogen in aviation applications," *International Journal of Sustainable Aviation*, vol. 2, no. 1, pp. 74–100, 2016.

[263] L. Klebanoff, J. Keller, M. Fronk, and P. Scott, "Hydrogen conversion technologies and automotive applications," in *Hydrogen Storage Technology*, CRC Press, Boca Raton, FL, USA, pp. 31–62, 2012.

[264] B. Decourt, B. Lajoie, R. Debarre, and O. Soupa, "Hydrogen-based energy conversion," in *Energy Transition*, Schlumberger and SBC Energy Institute, Houston, TX, USA, 2014.

[265] R. Amirante, E. Cassone, E. Distaso, and P. Tamburrano, "Overview on recent developments in energy storage: mechanical, electrochemical and hydrogen technologies," *Energy Conversion and Management*, vol. 132, pp. 372–387, 2017.

[266] M. Sterlinleohudson, D. Pukazhselvan, G. Irene Sheeja, and O. N. Srivastava, "Studies on synthesis and dehydrogenation behavior of magnesium alanate and magnesium–sodium alanate mixture," *International Journal of Hydrogen Energy*, vol. 32, no. 18, pp. 4933–4938, 2007.

[267] I. P. Jain, "Hydrogen the fuel for 21st century," *International Journal of Hydrogen Energy*, vol. 34, no. 17, pp. 7368–7378, 2009.

[268] T. Sadhasivam, H.-T. Kim, S. Jung, S.-H. Roh, J.-H. Park, and H.-Y. Jung, "Dimensional effects of nanostructured Mg/MgH2 for hydrogen storage applications: a review," *Renewable and Sustainable Energy Reviews*, vol. 72, pp. 523–534, 2017.

[269] B. Sakintuna, F. Lamari-Darkrim, and M. Hirscher, "Metal hydride materials for solid hydrogen storage: a review," *International Journal of Hydrogen Energy*, vol. 32, no. 9, pp. 1121–1140, 2007.

[270] E. Callini, Z. Ö. K. Atakli, B. C. Hauback et al., "Complex and liquid hydrides for energy storage," *Applied Physics A*, vol. 122, no. 4, p. 353, 2016.

[271] E. Callini, K.-F. Aguey-Zinsou, R. Ahuja et al., "Nanostructured materials for solid-state hydrogen storage: a review of the achievement of COST Action MP1103," *International Journal of Hydrogen Energy*, vol. 41, no. 32, pp. 14404–14428, 2016.

[272] N. Z. Khafidz, Z. Yaakob, K. L. Lim, and S. N. Timmiati, "The kinetics of lightweight solid-state hydrogen storage materials: a review," *International Journal of Hydrogen Energy*, vol. 41, no. 30, pp. 13131–13151, 2016.

[273] H. Wang, H. J. Lin, W. T. Cai, L. Z. Ouyang, and M. Zhu, "Tuning kinetics and thermodynamics of hydrogen storage in light metal element based systems—a review of recent progress," *Journal of Alloys and Compounds*, vol. 658, pp. 280–300, 2016.

[274] T. Kampitsch and O. Kircher, "Cryo-compressed hydrogen storage," in *Fuel Cells : Data, Facts and Figures*, D. Stolten, R. C. Samsun, and N. Garland, Eds., pp. 162–174, Wiley-VCH Verlag GmbH and Co. KGaA, Weinheim, Germany, 2016.

[275] G. Petitpas, P. Bénard, L. E. Klebanoff, J. Xiao, and S. Aceves, "A comparative analysis of the cryo-compression and cryo-adsorption hydrogen storage methods," *International Journal of Hydrogen Energy*, vol. 39, no. 20, pp. 10564–10584, 2014.

[276] J. Xiao, P. Bénard, and R. Chahine, "Charge-discharge cycle thermodynamics for compression hydrogen storage system," *International Journal of Hydrogen Energy*, vol. 41, no. 12, pp. 5531–5539, 2016.

[277] S. Kyoung, S. Ferekh, G. Gwak, A. Jo, and H. Ju, "Three-dimensional modeling and simulation of hydrogen desorption in metal hydride hydrogen storage vessels," *International Journal of Hydrogen Energy*, vol. 40, no. 41, pp. 14322–14330, 2015.

[278] Y. Gao, Y. Chen, C. Zhong, Z. Zhang, Y. Xie, and S. Zhang, "Electron and phonon properties and gas storage in carbon honeycombs," *Nanoscale*, vol. 8, no. 26, pp. 12863–12868, 2016.

[279] N. V. Krainyukova and E. N. Zubarev, "Carbon honeycomb high capacity storage for gaseous and liquid species," *Physical Review Letters*, vol. 116, no. 5, article 055501, 2016.

[280] B. Hardy, C. Corgnale, R. Chahine et al., "Modeling of adsorbent based hydrogen storage systems," *International Journal of Hydrogen Energy*, vol. 37, no. 7, pp. 5691–5705, 2012.

[281] Y. Kaplan and T. N. Veziroglu, "Mathematical modelling of hydrogen storage in a LaNi5 hydride bed," *International Journal of Energy Research*, vol. 27, no. 11, pp. 1027–1038, 2003.

[282] S. Mellouli, F. Askri, H. Dhaou, A. Jemni, and S. Ben Nasrallah, "A study of the thermal behavior of a deformable metal-hydride bed," *International Journal of Hydrogen Energy*, vol. 41, no. 3, pp. 1711–1724, 2016.

[283] S. S. Mohammadshahi, E. M. Gray, and C. J. Webb, "A review of mathematical modelling of metal-hydride systems for hydrogen storage applications," *International Journal of Hydrogen Energy*, vol. 41, no. 5, pp. 3470–3484, 2016.

[284] S. Zheng, F. Fang, G. Zhou et al., "Hydrogen storage properties of space-confined NaAlH4 nanoparticles in ordered mesoporous silica," *Chemistry of Materials*, vol. 20, no. 12, pp. 3954–3958, 2008.

[285] I. Cabria, M. J. López, and J. A. Alonso, "The optimum average nanopore size for hydrogen storage in carbon nanoporous materials," *Carbon*, vol. 45, no. 13, pp. 2649–2658, 2007.

[286] S. Tedds, A. Walton, D. P. Broom, and D. Book, "Characterisation of porous hydrogen storage materials: carbons, zeolites, MOFs and PIMs," *Faraday Discussions*, vol. 151, pp. 75–94, 2011.

Hindawi
Advances in Materials Science and Engineering
Volume 2018, Article ID 2656425, 14 pages
https://doi.org/10.1155/2018/2656425

Research Article

Molding of Polymeric Composite Reinforced with Glass Fiber and Ceramic Inserts: Mathematical Modeling and Simulation

Túlio R. N. Porto, Wanderley F. A. Júnior, Antonio G. B. De Lima, Wanderson M. P. B. De Lima, and Hallyson G. G. M. Lima

Department of Mechanical Engineering, Federal University of Campina Grande, Campina Grande 58429-900, Brazil

Correspondence should be addressed to Túlio R. N. Porto; trnporto@gmail.com

Received 24 August 2018; Accepted 4 October 2018; Published 1 November 2018

Academic Editor: Giorgio Pia

This work provides a numerical study of a polymer composite manufacturing by using liquid composite material molding. Simulation of resin flow into a porous media comprising fiber perform (reinforcement) inserted in a mold with preallocated ceramic inserts has been performed, using the Ansys FLUENT® software. Results of resin volumetric fraction, stream lines and pressure distribution inside the mold, and mass flow rate (inlet and outlet gates) of the resin, as a function of filling time, have been presented and discussed. Results show that the number of inserts affects the filling time whereas the distance between them has no influence in a process.

1. Introduction

Composite is a material originating from the joining of two or more different component materials, exhibiting specific properties that are not observed in the constituent phases, acting separately [1].

Most of composites are described as having a matrix phase and a dispersed phase (reinforcement). The matrix is the continuous phase, which is responsible to transfer the stresses exerted on the part. Polymeric matrices are the most used in the composite material production.

Polymers are called thermosets when, after cure reaction, they have a molecular structure that does not allow process reversibility and thermoplastics, when the molecular structure, presented before cure, can be achieved as the polymer is remelted. The epoxy resin is a thermosetting polymer that has better thermal, electrical, and mechanical properties than the other polymer matrices, working in the range of −60 to 180°C [2].

The reinforcement of the composite may consist of continuously disposed, discontinuous, aligned or random fibers, particles, with different sizes and structures, either laminated or in sandwich-panels [1, 3].

Due to the ability of the composites to merge different properties in a single material, they have various applications. In the aeronautical and naval sector, there is a great demand for materials that present lightness associated with high mechanical resistance. Thus, the application of polymer composites to structural components of aircraft and vessels is constantly increasing. Currently, internal, external, wing ribs, landing gear doors, flaps, structural parts, and aircraft leading edges are being made of composite materials consisting of continuous fibers in a thermoset polymer matrix [4]. Vessels are able to associate low weight and maintenance cost with high wear resistance when they are manufactured by composites reinforced. In the scope of the armored structures, composites are processed from the union of ceramic inserts and reinforcing fibers, imbedded in a polymer matrix. This composition promotes to the armored equipment, both structural properties, sufficient to support high loads, as well as protection against ballistic attacks and reduction on the equipment weight [5–8].

The fiber-reinforced composites constitute a porous medium. Interconnected voids between the fibers are distributed along the preform through which the resin flows during the filling mold. The pore geometry and its

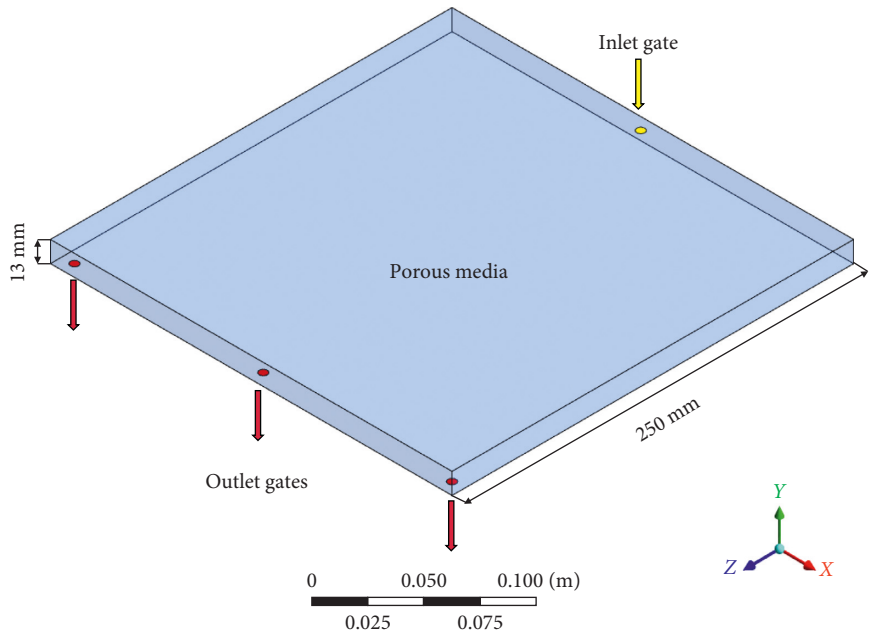

Figure 1: The geometry of the physical problem studied.

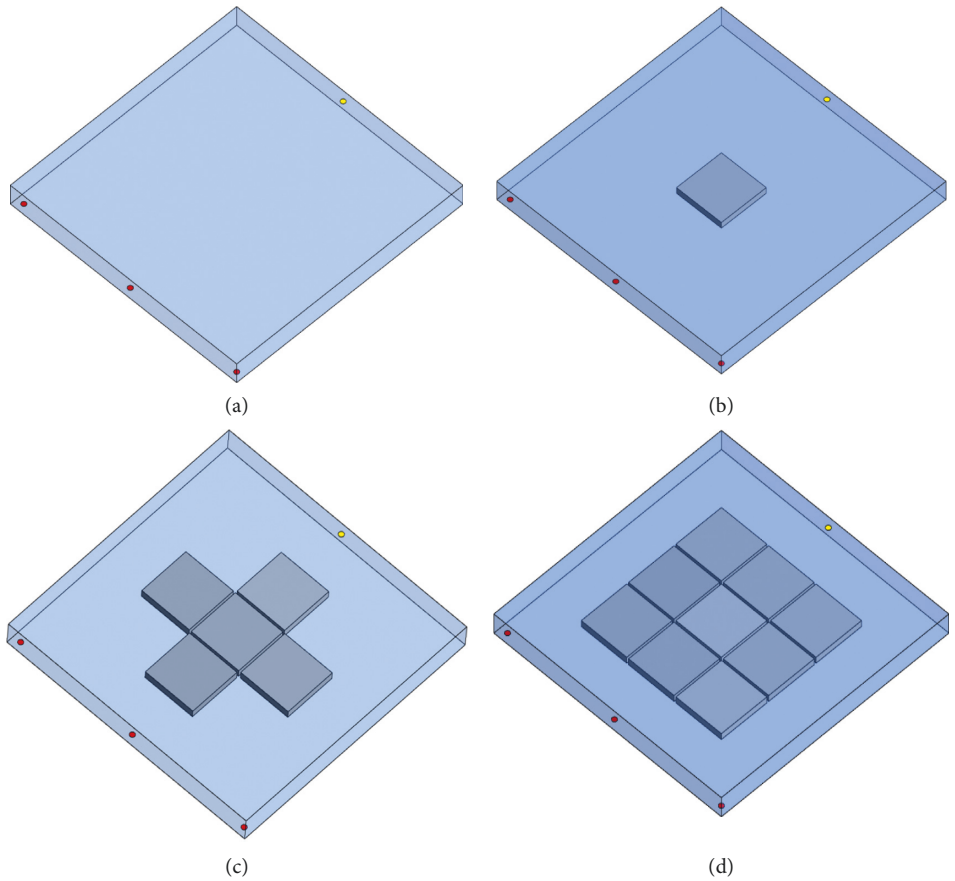

Figure 2: Continued.

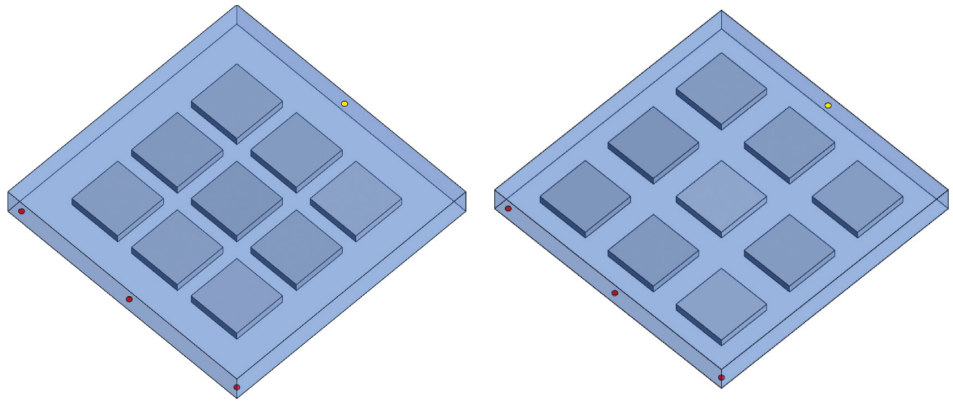

(e) (f)

Figure 2: Reinforcement configuration with 0 (a), 1 (b), 5 (c), and 9 (d) ceramic inserts 2 mm apart and in the case of 9 inserts, with 15 mm apart (e) and 25 mm apart (f).

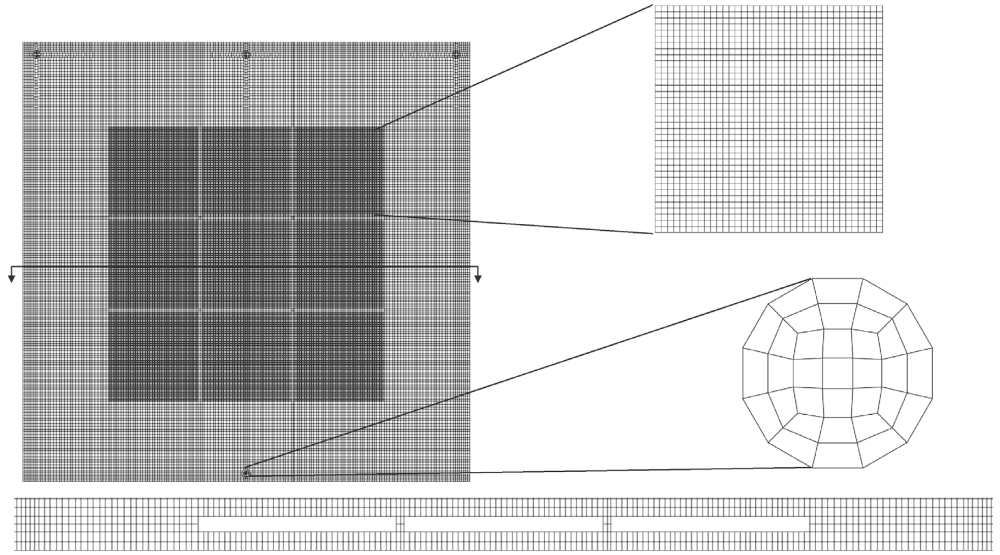

Figure 3: Numerical mesh and details of inserts and outlet gate.

distribution, described by the porosity and permeability of the medium, measured empirically, the density and viscosity of the resin, and the pressures and velocities, established at the inlet and outlet of the mold, characterize the flow in the porous medium and its mechanical properties [9–13].

Historically, the composites were produced by the manual lamination process. In this process, laminated layers are manually produced using reinforcements previously impregnated with the matrix material [14]. Due to the high costs and the operator's ability dependence, associated with the manual lamination process, developments in manufacturing with the aim of promoting reductions in process costs and in the number of failures are increasing. For this, the technique of liquid composite molding (MLC) was developed. In this technique, liquid resin is injected into a closed mold, where the reinforcement is preallocated, under specific conditions of pressure, velocity, and temperature. As the resin fills the mold cavity, impregnating the preform and cure process are finished, the composite is produced [15]. In general, the liquid phase (polymer) is mixed with a chemical hardener before to be injected into the mold. In addition, the shape of the part, the mold temperature, and the maximum injection time depend on thermal and mechanical properties of the matrix. In order to adapt the different specifications, required by the manufacturing projects, the MLC technique was subdivided in resin transfer molding (RTM), vacuum-assisted resin transfer molding (VARTM), resin transfer molding light (RTML), and compressed resin transfer molding (CRTM) [16–19].

During the molding process, a multiphase flow is observed along the mold. A resin-air interface develops inside the mold as the liquid resin is injected into the mold and air, which previously occupied the entire porous volume is repelled through the strategically projected outlets. In the course of the process, the interface extension decreases as air is removed from the mold and phase mixture regions are observed to promote dispersed air bubbles in the polymer

matrix. After the curing process, these bubbles correspond to voids in the solidified part, which give rise to cracks in the composite, drastically reducing the composite mechanical strength. Thus, the transient control of the fluid flow and the pressure distributions along the molded part are directly associated with the quality of the composite. These fluid dynamics parameters are dependent on the composite geometry, the reinforcement and the resin physical properties, the distribution of injectors and air outlets, and their relative pressures and velocity that potentiate the flow [16].

Experiments have shown that undesired results, such as voids inside the mold, high injection times, mold deformations, displacement and deformation of the preform, in locations near the injection points, are influenced by the flow behaviour. In this way, an accurate knowledge of the transport phenomena associated with the flow type to currently control the process is necessary in order to have a structure with desired mechanical properties.

In the search for optimize industrial processes, numerical simulation is characterized as a fundamental tool. From the discretized physical conservation equations, the fluid dynamics aspects of processes such as composite molding can be described and analyzed in order to predict the best operating conditions and the physical implications of the mold and reinforcement geometries used. The prior knowledge of how the flow occurs significantly reduces the logistical venture and costs that would have been used to obtain experimental results. As the computational tool is validated, numerical results are enabling to guiding the industrial processes.

In this sense, the present work carries out a computational study of the resin transfer molding process during the manufacturing of a composite composed by an epoxy resin polymer matrix, reinforced with glass fiber and ceramic inserts. As contribution in this research area, the description of the multiphase flow fronts, rate relative results of the resin and air volume fractions over the time, the resin mass flow at the mold inlet, and the pressures and velocities distributions inside the mold are numerically obtained. In addition, the numerical study allowed to evaluate the influence of the number of inserts and the distance between them in the mold filling process.

2. Mathematical Modeling

2.1. The Physical Problem and the Geometry. As shown in Figure 1, the physical problem consists of the filling, by injection of resin, of a square closed mold, with 250 mm of side and 13 mm thickness; the mold is composed by three air outlets with 5 mm diameter, distributed symmetrically on one side of the mold lower surface, 112.5 mm apart; one inlet on the opposite side, on the mold upper surface, with 5 mm diameter. A preform of glass fibers is allocated in the mold cavity, forming a porous medium, through which the resin passes during filling process.

The influence of the square-base prismatic ceramic inserts, with 50 mm of side and 4 mm of thickness, placed between the fibers and centered on the mold thickness, on the multiphase flow behaviour, will be analyzed. Figure 2 illustrates different configurations of composite reinforcements, relative to the number of inserts and the distances between them. The cases referring to the 0, 1, 5, and 9 inserts, with a distance of 2 mm between them, are presented in Figures 2(a)–2(d), respectively. The cases referring to the variations in the distance between the inserts of 15 and 25 mm for 9 inserts are shown, respectively, in Figures 2(e) and 2(f).

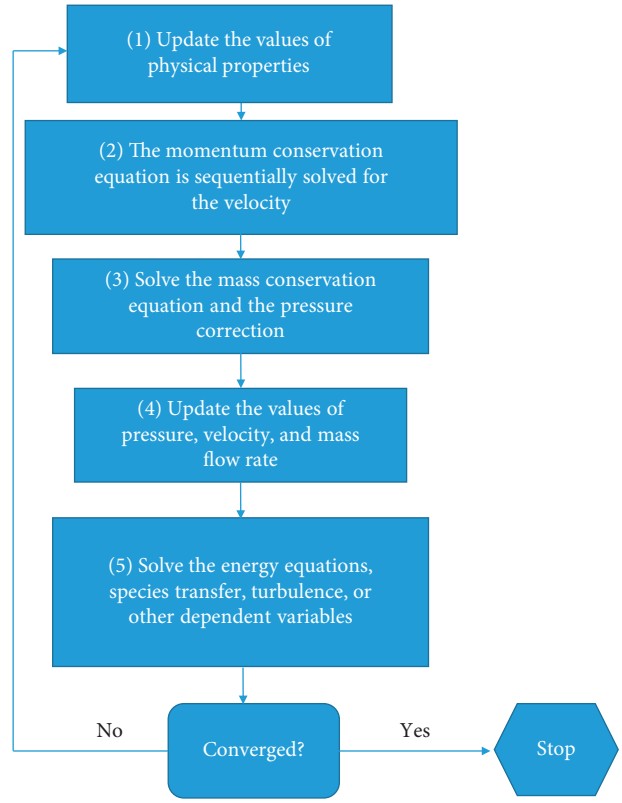

Figure 4: SIMPLE pressure-based solution method.

Table 1: Simulated cases.

Case	Number of inserts	Distances between the inserts (mm)
1	9	25
2	0	—
3	1	2
4	5	2
5	9	2
6	9	15

Table 2: The two physical properties of the fluid phases at 25°C and 1 atm.

Properties	Viscosity (Pa·s)	Density (kg/m^3)
Air	$1.7984e^{-05}$	1.2257
Resin	0.35	1200

2.2. The Mathematical Model. Among the mathematical models used to describe the multiphase flow, the volume of

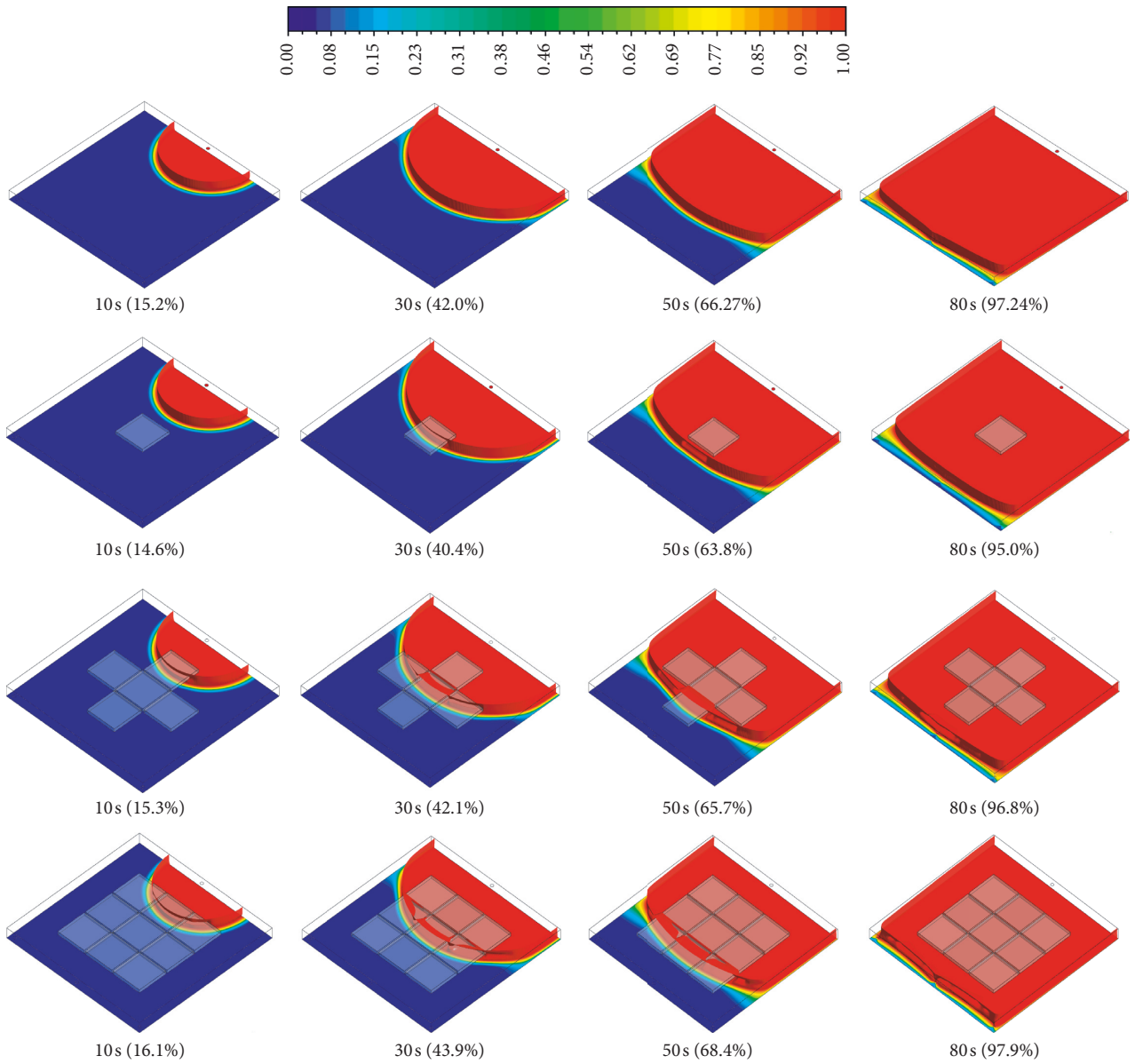

Figure 5: Distribution of the resin volumetric fraction inside the mold containing 0, 1, 5 and 9 insert spaced 2 mm apart, at different instants of process.

Fluid (VOF) model is suitable for composite molding processes. This model, through the solution of the conservation equations of mass and momentum, is able to trace the interfaces of a flow composed of two or more immiscible fluids with great accuracy. As the mold is filled with liquid resin, this model is able to specify the air and resin flow rates and the interface location between these fluids. In this way, it is possible to identify the resin front in the mold and the regions with air bubbles during the injection process.

2.2.1. Mass Conservation. In the mass conservation equation (Equation (1)), the transient, convective, and source terms are related to the volumetric fraction of the secondary phase "q." Making the calculation for the secondary phases present in the flow, by volumetric completion, the conservative values for the primary phase "p" are obtained:

$$\frac{1}{\rho_q}\left[\frac{\partial\left(\alpha_q\rho_q\right)}{\partial t} + \nabla\cdot\left(\alpha_q\rho_q\vec{v}_q\right) = S_{\alpha q} + \sum_{p=1}^{n}\left(\dot{m}_{pq} - \dot{m}_{qp}\right)\right], \tag{1}$$

where t is the time variable, $S_{\alpha q}$ is the source term relative to "q" phase and its respective volumetric fraction α, and this term is related to the generation or mass sink of phase q. The terms $\dot{m}_{pq}$ and $\dot{m}_{qp}$ are related to mass transfer from phase "p" to phase "q" and from phase "q" to phase "p," respectively, which occurs when there is phase transformation associated to this physical problem.

2.2.2. Momentum Conservation. From the momentum equation solution, the velocity and pressure fields, described along the flow, are obtained, which depend on the instant of analysis, the interactions of the fluid with the geometric structure, as well as the external and internal surface and field forces, to the control volume.

$$\frac{\partial}{\partial t}(\rho\vec{v}) + \nabla\cdot(\rho\vec{v}\vec{v}) = -\nabla p + \nabla\cdot\left[\mu\left(\nabla\vec{v} + \nabla\vec{v}^{T}\right) + \rho\vec{g} + \vec{F}\right]. \quad (2)$$

In Equation (2), $\vec{F}$ is the external force vector, $\vec{g}$ is the gravity acceleration vector, and p is the pressure distributed on the volume control surface. The physical properties inserted in Equation (2) correspond to the mixture of phases, in each control volume. These are measured by a weight average between the constituent phase properties of the flow, described in Equation (3), for example, to density:

$$\rho = \alpha_q\rho_q + \left(1-\alpha_q\right)\rho_p. \quad (3)$$

In this way, the properties and appropriate variables are weighted in each region of the multiphase flow.

2.2.3. The Porous Media Flow. The term of momentum conservation equation, relative to the pressure variation in a physical domain, for fluid flowing through an isotropic porous medium is described by Darcy's empirical law (Equation (4)). In this analysis, the Reynolds number (Equation (5)), a dimensionless value, describing the relationships between the inertial forces in relation to the viscous forces, is calculated as a function of the pore size or the particle diameter (d_p) that constitutes the porous medium, and consequently, their value is very small [12].

$$\nabla P = -\frac{\mu\vec{v}_s}{K}, \quad (4)$$

$$\mathrm{Re} = \frac{\rho v_s d_p}{\mu}. \quad (5)$$

In the Equations (4) and (5), μ is the viscosity of the fluid, $\vec{v}_s$ is the fluid superficial velocity vector, which is determined by considering the porous medium as continuous and neglecting the effects of the geometric details of the porous medium structure, and K is the porous media permeability and can be calculated through Equation (6). This parameter is dependent on the porosity ϕ and the parameter "a" which is related to porous geometric microstructure:

$$K = \frac{\phi^3 d_p^2}{a(1-\phi)^2}. \quad (6)$$

The approach applied in the Ansys Fluent 15.0 software does not treat the porous medium through its geometric variations, but as described in Equation (7), considering the resistance to the flow (σ) that the porous medium represents

$$\sigma = \frac{1}{K}. \quad (7)$$

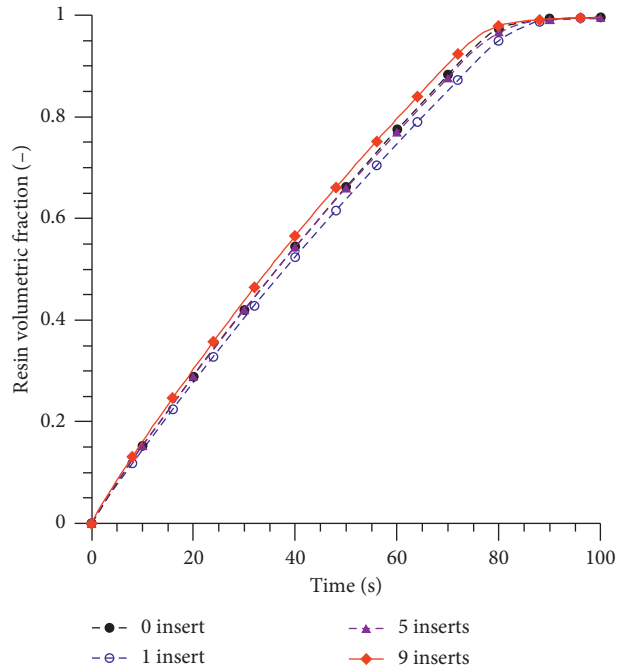

Figure 6: Total volumetric fraction of resin as a function of the filling time (inserts spaced apart with 2 mm).

2.3. Numerical Solution

2.3.1. Numerical Mesh. The molds were described in different meshes, the most refined containing 297,942 elements. The number of elements was enough to describe the process, with considerable precision and physical coherence, presented in the results. Figure 3 illustrates one grid used is this work, produced by the ANSYS ICEM® CDF 15.0 software, with particular emphasis for the inserts surfaces and resin inlet, which was the same used to and air outlets. To reduce the number of elements and consequently the simulation time, the mesh was developed considering only the surfaces of the inserts. No element was treated within its volumes.

2.3.2. Spatial Discretization. In order to obtain the numerical solution of the conservation equations presented, discretization of the governing equations is necessary, that work within differential limits. Therefore, we transform the partial differential equations in algebraic equations, defined for the finite three-dimensional limits of the numerical mesh. Taking Φ as a representative of the transport variables, velocity or pressure, referring to conservation equations of mass and momentum, we have the discretization of the transport general equation, as follows:

$$\frac{\partial(\rho\Phi)}{\partial t}V + \sum_{f=1}^{N_f}\rho_f\Phi_f\vec{v}_f\vec{A}_f = \sum_{f=1}^{N_f}\Gamma_{\Phi_f}\nabla\Phi_f\cdot\vec{A}_f + S_\Phi V, \quad (8)$$

where Γ_Φ is the general term relative to the characteristic physical properties of each conservation equation, $\vec{A}_f$ is the area vector corresponding to the faces (f) of the control volume, S_Φ is the source term per unit of its volume (V), and N_f

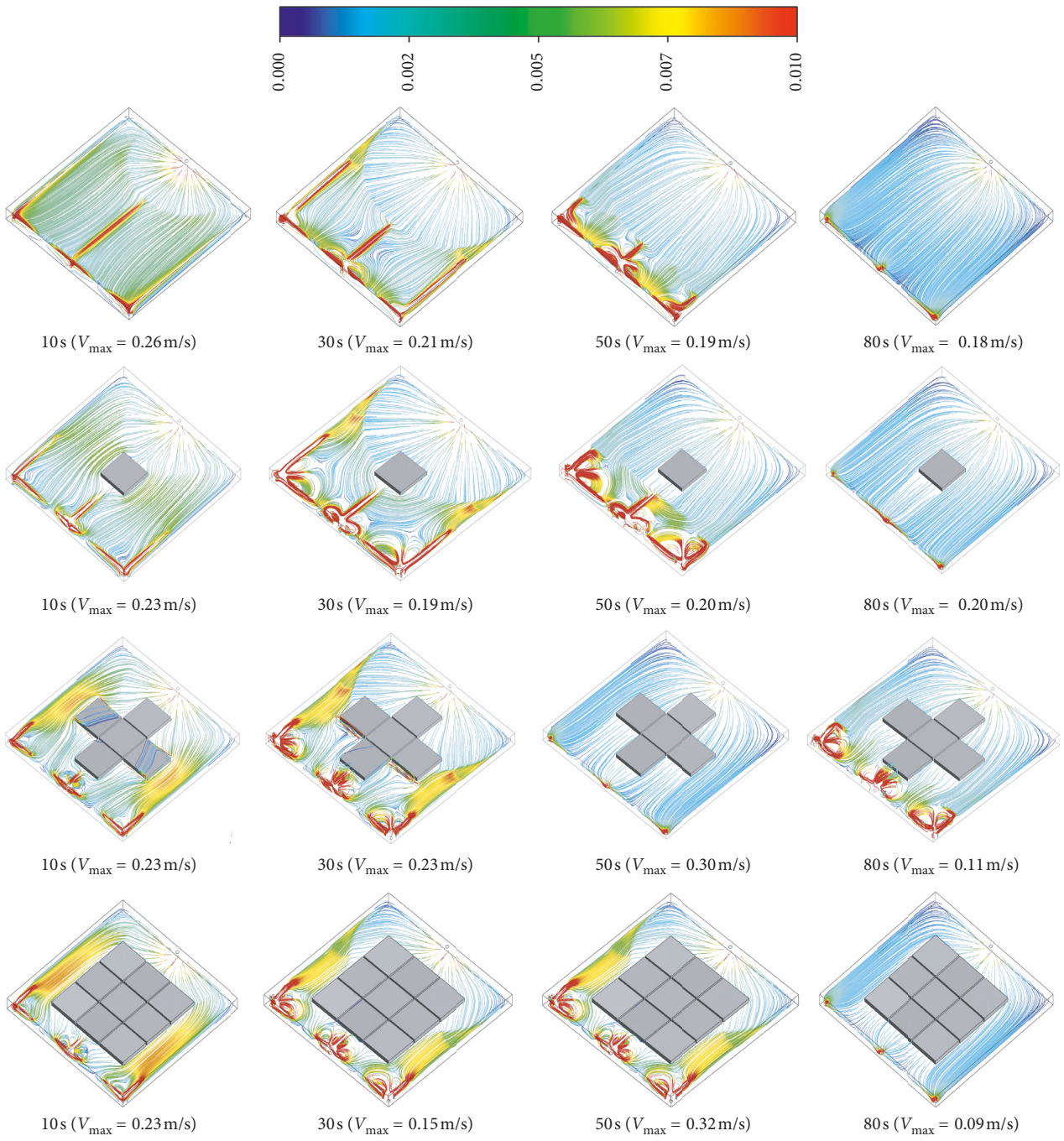

FIGURE 7: Streamlines with velocities (m/s) inside the molds containing 0, 1, 5, and 9 inserts spaced apart with 2 mm, at different instants of process.

is the number of faces in which the conservative equation is analyzed. Knowing the value of the variable Φ in the centroids (c_0, c_1, ..., c_n) of the cells and their values (Φ_f) on each cell faces, solutions of conservation equations can be obtained along the physical space. Herein, we use the least squares cell-based method [20] to determine the gradient $\nabla\Phi$, the quadratic upwind implicit differential convective kinematics (QUICK) method [21] for discretization of the volumetric fraction (continuity), the second-order upwind method [22] for discretization of the continuity equation and the PRESTO [23] for pressure numerical model discretization.

2.3.3. Temporal Discretization. Taking the temporal differential of the general transport equation

$$\frac{\partial \Phi}{\partial t} = F(\Phi), \tag{9}$$

where $F(\Phi)$ incorporates all discretized spatial variables.

Using the implicit method [23] for temporal discretization, Equation (9) can be rewritten as follows:

$$\frac{\Phi^{n+1} - \Phi^n}{\Delta t} = F\left(\Phi^{n+1}\right), \tag{10}$$

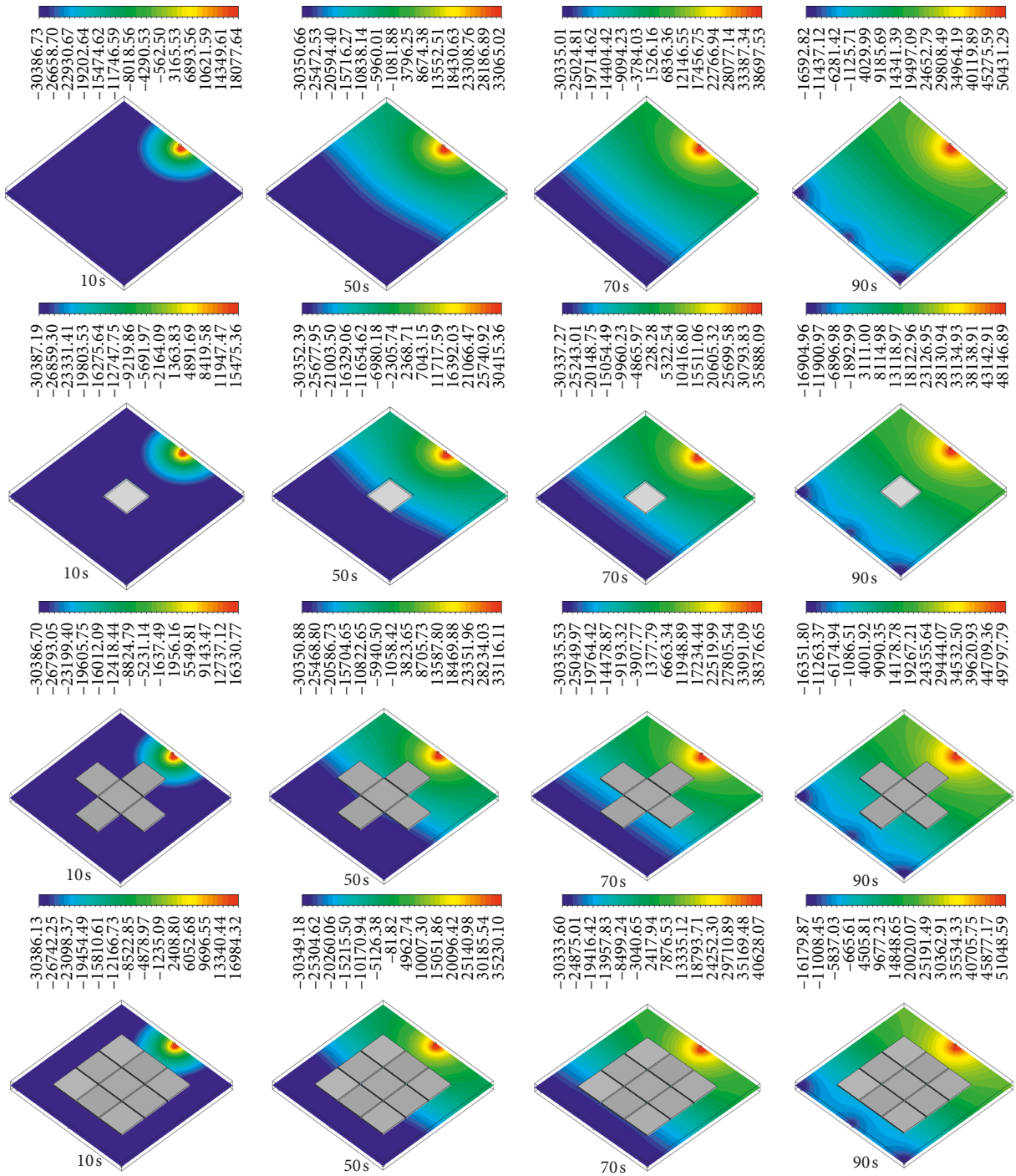

FIGURE 8: Pressure fields, measured (Pa), in the plane $y = 6.5$ mm for different filling times of the molds containing 0, 1, 5, and 9 inserts, spaced apart with 2 mm, for different instants of time.

where Φ^{n+1} refers to the value of the variable Φ, in the central mesh position of the cell, in the later time step and Φ^n, in the current time step. The discretized variables in relation to space are treated in future or later time, $F(\Phi^{n+1})$. Thus, in conjunction of specified initial and boundary conditions, numerical iterations are performed at each time step, and the transient behaviour of conservation equations is obtained.

2.3.4. Solution Procedure. Concerning the fluid flow problem treated here, a pressure-based solution method SIMPLE (semi-implicit method for pressure linked equation) by [24], which is traditionally used in incompressible flow simulations that develop at low velocities, is applied. This method is described by the following solution steps presented in Figure 4.

From the solution of conservation equations, it is possible to describe how the flow occurs during the molding

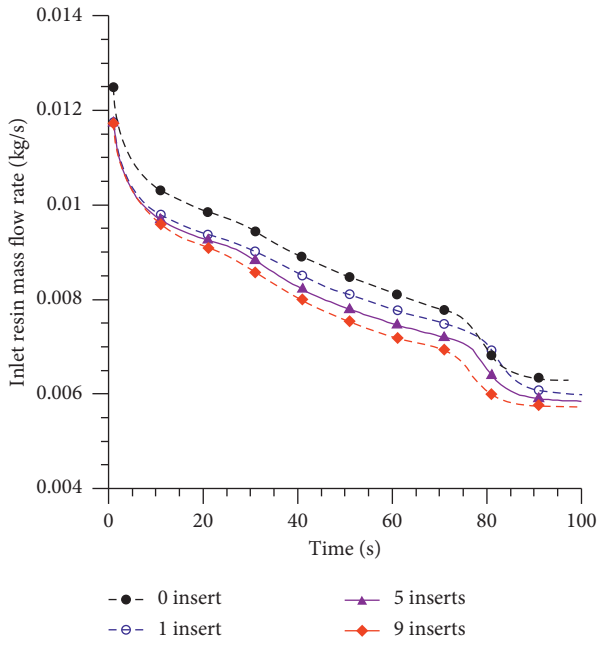

Figure 9: Resin mass flow rate as a function of time at the inlet of the mold containing 0, 1, 5, and 9 inserts, spaced apart with 2 mm.

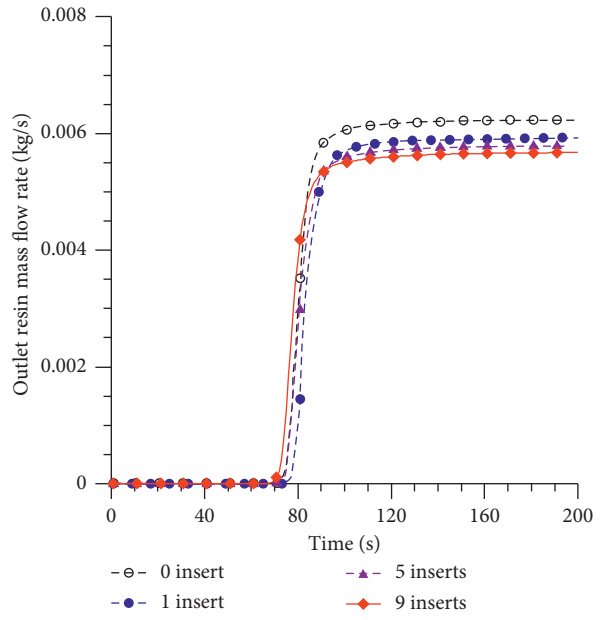

Figure 10: Resin mass flow rates in the outputs of the mold containing 0, 1, 5, and 9 inserts, spaced apart by 2 mm.

process of a fiber-reinforced polymer composite. With this procedure, the pressure fields, velocities, and volume fractions are obtained in each time step time.

2.3.5. Simulated Cases. The 6 cases, described in Table 1, were simulated in a commercial computational program (Ansys FLUENT® 15.0), and the results are presented in the next section. In all situations, the mesh with 297942 elements, a time step of 0.05 seconds with the maximum number of 100 iterations per time step, and convergence criterion for all variables as 10^{-5} were used.

2.3.6. Initial and Boundary Conditions and Fluid Properties. For the solution of the cases, the following initial and boundary conditions were applied:

(a) Prescribed pressure at the resin inlet: 101325 Pa (normal to inlet).

(b) Vacuum pressure at the air outlet: −30397 Pa (normal to outlets).

(c) Resin volumetric fraction in the inlet: 1.

(d) Resin volumetric fraction in the outlet: 0.

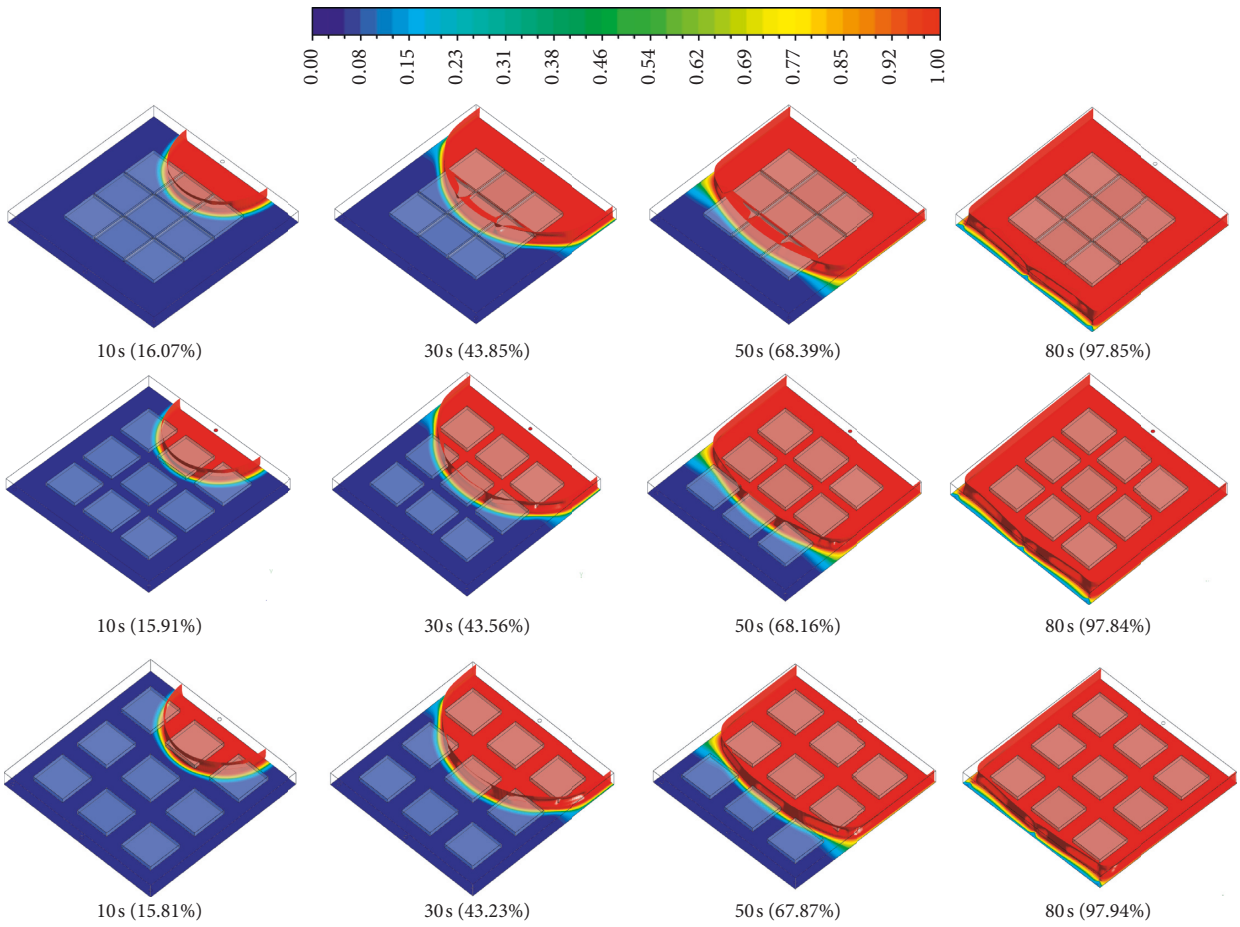

Figure 11: Distribution of the resin volumetric fraction inside the molds containing 9 inserts spaced apart with 2, 15, and 25 mm at different instants of process.

(e) Local gravitational acceleration: 9.81 m/s^2.

(f) Permeability of the porous medium in the x, y, and z directions: $3.89 \cdot 10^{-9}$ m^2. The porous medium structure consists of superimposed glass fibers layers within the mold cavity. Considering that the fibers are traced and that the distances between the layers are small, the permeability in the porous medium is treated as isotropic.

(g) Homogenous porosity: 0.82.

(h) Nonslip condition on the mold and insert walls and top, lateral, and bottom surfaces; this condition can be found as no casting occurs in the mold and the ceramic inserts are impermeable. The roughness of the surfaces was not considered because the flow inside the mold was laminar.

(i) Constant process temperature: 27°C.

In this research, it was considered that the mold is fully filled at room temperature before the curing process development. Under these conditions, the viscosity and temperature variations due to the resin hardening process are neglected. Thus, the fluid properties used on the simulation are described in Table 2.

3. Results and Discussion

In this research, fluid flow in porous media, with emphasis to polymer composite reinforced with fiber and ceramic inserts, is analyzed. Figure 5 illustrates the resin flow fronts at different times. These results show the contours of resin volumetric fraction on $y = 0$ mm plane and the resin-air interface traced throughout the mold volume during filling. From the analyses of this figure, we can see that the porous medium resists to the resin flow into the mold, but this resistance is overcome, due to the high vacuum pressure condition imposed, allowing the mold to be completely filled at 345 s of processing. From Figure 6, it can be seen that, within 80 s, the resin filling rate occurs in intensified way, causing the mold to be filled more than 90% of its capacity. After this period, the resin reaches the air outlets and is expelled from the mold, slowly loading the trapped air fractions, identified by the existence of resin-air interface within the mold, which is reduced in size between $t = 200$ s and $t = 345$ s of process.

The variation of the insert number in a fixed mold volume promotes two effects: (a) resistance to the flow due to the insert barriers; and (b) reduction in the useful cross-sectional area through which the fluid flows, which under small pressure variations promotes the increase in fluid velocity, and thus, the resin advances faster in to the mold.

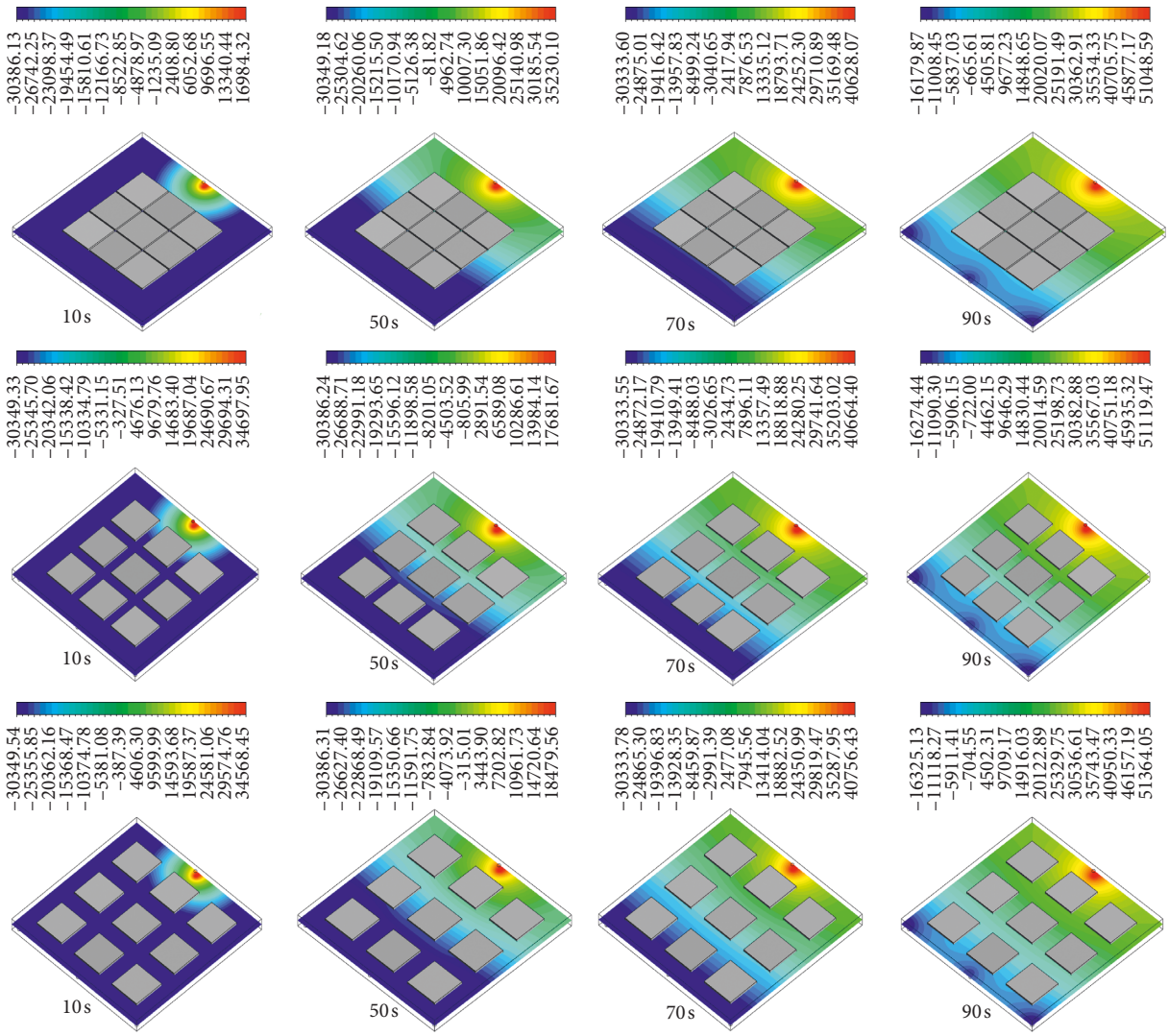

FIGURE 12: Pressure field in the $y = 6.5$ mm plane of the molds containing 9 inserts, spaced apart with 2, 15, and 25 mm at different instants of process.

Qualitatively in Figure 5 and quantitatively in Figure 6, it can be seen that inserts application strongly influences the resin advancement in the interval between 10 and 90 s, a period ahead resin flow takes to pass inserts, centralized in the mold. Thus, it can be observed in Figures 5 and 6, for the case with one insert, the resin velocity is reduced because of the flow resistance effect overriding the geometry effect. For five inserts, there is an increase in the geometric reduction effect compared with the resistance effect, making the 5-insert curve present a higher filling velocity than the case with 1 insert and closing the case with 0 insert. In this sense, when applying nine inserts in the mold cavity, the greatest filling velocity is observed. The number in parenthesis corresponds to percentage of resin into the mold at different process times.

The streamlines describe the intensity, orientation, and direction of a specific flow. Figure 7 shows the results obtained in this research. In order to distinguish the regions of the plane with different levels of flow intensity, the velocities' magnitude was fixed in a range between 0 and 0.01 m/s, described in the single legend of the figure. In these streamlines, regions with velocities' magnitude higher than the 0.01 m/s are not distinguished. However, the maximum velocity at each time, which is above the described range, is presented next to each figure. Thus, the velocity differences between the mold regions, which lie within the given range, indicate important physical characteristics of the flow. In 1 s of process, a streamline structure intensifies towards the mold outputs. This flow comes from the air reaction to the resin injection at the inlet, which occurs from the set pressure conditions at the inlet and outlet. Then, follows the resin advancement from the mold inlet at considerably lower velocities due to its higher viscosity and density. In parallel to that, recirculation of air regions are performed around the mold outputs due to the narrow space that air is confined as the resin advances on the mold. When the mold volume is about 90% filled with the resin, the recirculation regions are extinguished, which occurs because the resin reaches the outlets in this period.

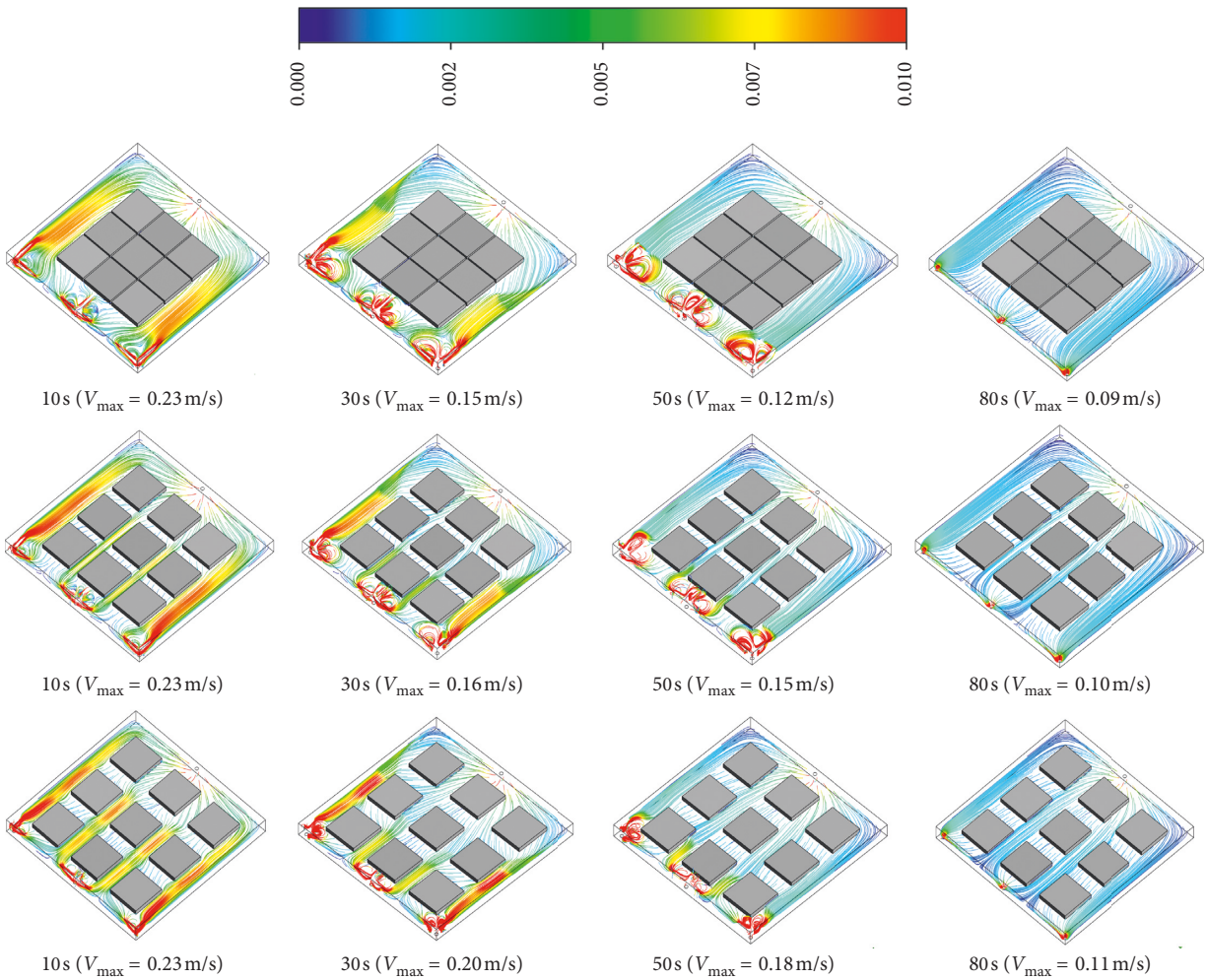

Figure 13: Streamlines with velocities (m/s) inside the molds containing 9 inserts and spaced apart at 2, 15, and 25 mm at different instants of process.

With the ceramic insertion structures in the composites, it is observed that, as the number of inserts is increased, the streamlines are affected by the reduction effects on the cross section area of the mold and the flow resistance. An increase in the recirculation intensity is observed as the inserts are added into the mold until 50 s of processing. Already at 80 s, the velocities of the resin flow are becoming smaller, due to the resistance effect coming from the inserts overlapping at that moment.

Figure 8 illustrates the pressure distribution inside the mold at different moments of molding process. In this figure, the pressure distribution along the central plane of the mold is observed as the mold is being filled by the resin. Initially, the effect of the vacuum pressure (−30386.73 Pa), established at the outputs and homogeneously distributed throughout mold, causes the entering of the resin. It is found that the reddish-toned contours advance in the mold over time, as far as the filling occurs. The advancement of the higher-pressure contours becomes linear ($t > 10$ s) with a small distance from the inlet, due to the effect of the flow resistance increasing, already mentioned. Upon reaching 90 s of processing, the variation of amount of resin into the mold, has been relatively low and, thus, pressure contour profile remains constant until the full-filling the mold. Pressure conditions with small variations are observed when inserts are applied in the mold, which can be observed on the pressure contours legends. This pressure conditions associated with the reductions in the flow areas, due to de presence of inserts into the mold, promoting the different filling times in for each described case.

Resin injection into the mold with constant pressure promotes a reduction in resin flow rate at the mold inlet over time as shown in Figure 9. This is due to the fact that the resistance to scaling increases as the volume of resin, which needs to be moved inside the mold, increases. Because of the low viscosity and density, the air does not offer a high injection resistance, and therefore, the resin flow in the mold inlet at the initial times is relatively high. Subsequently, it decreases, due to the addition of resin, with high viscosity and density, in the porous cavity. This falling rate period occurs, until reaching the permanent regime, around 80 s, when the amount of resin present in the mold is almost constant, as can be observed comparing Figures 9 and 10. In the process, it possible to observe that the resin mass flow

rates in the inlet and outlet are close to 0.006 kg/s. Quantitatively, Figures 9 and 10 also describe the influence of the ceramic structures application on the resin mass flow rates at the mold inlet and outlet along the filling process. It will be seen for the same time that, as the number of inserts is increased in the mold volume, the resin mass flow rate at the mold inlet is reduced. This is due to the increase in the flow resistance imposed by impermeable ceramic structures. Figure 10 illustrates that the resin achieves the mold outputs more rapidly as the number of inserts increases, due to the geometric reduction of the porous volume inside mold, under few variations on the pressure conditions, as the inserts number is varied. In the same figure, it is also observed that the levels at which the resin mass flow rates remain constant at the outputs are greater for the smaller number of inserts inside the mold.

Figure 11 shows the influence of the distance between the inserts in the mold filling time. It is noted that, as the distance between the inserts is reduced, there is a small increase in the resin volumetric fraction at the same instant of time as compared with previous case. This is due to the reducing effect on the cross section area through which multiphase flow occurs, under pressure conditions not sensitive to the geometric variations, as shown in Figure 12, thus increasing the fluid velocity in these narrower regions.

Figure 13 shows that, for the same time, as the distances between the inserts are increased, an increase in the maximum velocity, measured in the plane $y = 6.5$ mm, is observed. What can be seen in streamline structures are small increases on the flow intensity, especially in the initial times, 10 and 30 s, these variations do not influence the filling process because the mass flow rate at the inlet and outlets has no changes as the distances between the inserts are varied, as described in Figures 14 and 15.

4. Conclusions

In the work, fluid flow in porous media has been studied with particular reference to resin flow in a glass fiber preform. From the presented results, the following can be concluded:

The multiphase VOF model, used by Ansys FLUENT® software, is suitable for studying the resin transfer molding process.

The adaptation of the mesh, placing voids instead of the solid ceramic inserts, promoted a reduction in the computational time that does not interfere in the results, since the fluid dynamics process is affected only by the surfaces of the inserts.

Ceramic inserts influence the flow behaviour during the filling of the mold. An increase in the mold filling velocity was verified, as the number of inserts is increased.

The resin mass flow rate at the mold inlet is reduced as it is being filled by resin. In about 80 s of processing, the resin touches the mold outlets and the resin flow in this region is increased until reaching the value of the inlet resin mass flow rate. Both the resin fluxes at the mold inlet and at the mold outlet are inversely proportional, affected as the insert number is increased and are not affected considerably when the distances between them are varied.

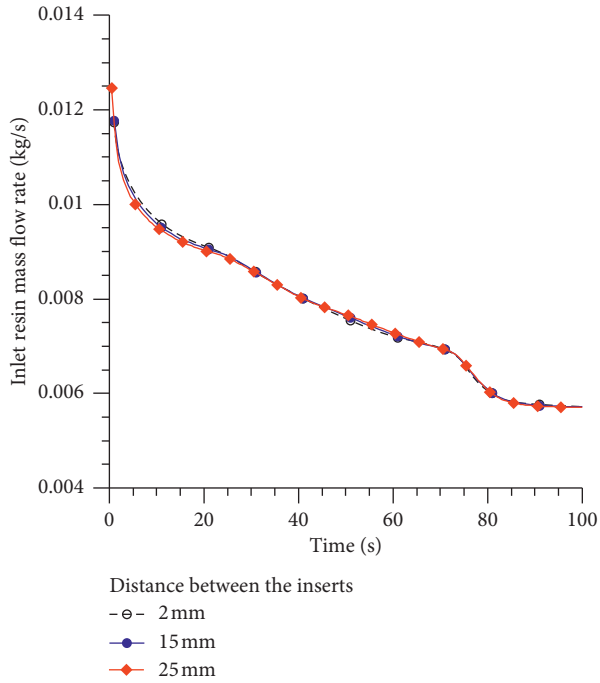

Figure 14: Mass flow rates at the mold inlet with the mold containing 9 inserts spaced apart with 2, 15, and 25 mm at different instants of process.

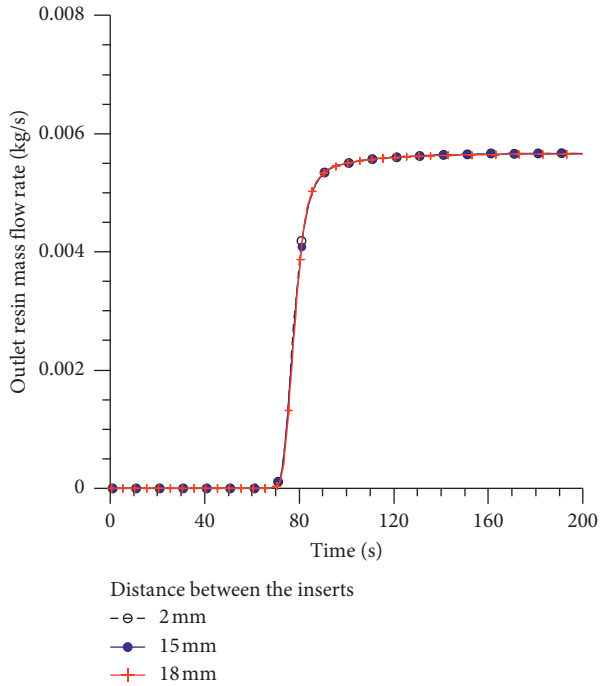

Figure 15: Mass flow rates at the mold outlets with the mold containing 9 inserts spaced apart with 2, 15, and 25 mm at different instants of process.

Data Availability

No data were used to support this study.

Conflicts of Interest

The authors declare that there are no conflicts of interest regarding the publication of this paper.

Acknowledgments

The authors are grateful to CNPq, CAPES, and FINEP (Brazilian Research Agencies) for financial support and to the authors cited in the text who helped in the improvement of this work.

References

[1] W. D. Callister Jr. and D. G. Rethwisch, *Materials Science and Engineering: An Introduction*, John Wiley & Sons, New Jersey, NY, USA, 8th edition, 2010.

[2] S. Tsanzalis, P. Karapappas, A. Vavouliotis et al., "Enhancement of the mechanical performance of an epoxy resin and fiber reinforced epoxy resin composites by the introduction of CNF and PZT particles at the microscale," *Composites Part A: Applied Science and Manufacturing*, vol. 38, no. 4, pp. 1076–1081, 2007.

[3] V. V. Vasilie and E. V. Morozov, *Mechanics and Analysis of Composite Materials*, Elsevier Science, Amsterdam, Netherlands, 1st edition, 2001.

[4] M. C. Rezende and E. C. Botelho, "The use of structural composites in the aerospace industry," *Polímeros*, vol. 10, no. 2, pp. e4–e10, 2000.

[5] Q. Wang, Z. Chen, and Z. Chen, "Design and characteristics of hybrid composite armor subjected to projectile impact," *Materials & Design*, vol. 46, pp. 634–639, 2013.

[6] U. K. Vaidyac, C. Ulven, and H. Ricks, "Acoustic impact evaluation of ballistic damage in VARTM composites," in *Proceedings of Ninth International Congress on Acoustics and Vibration (IIAV)*, pp. 1–8, Kampala, Uganda, July 2002.

[7] C. H. Lee, C. W. Kim, S. U. Yang, and B. M. Ku, "A development of integral composite structure for the ramp of infantry fighting vehicle," in *Proceedings of 23rd International Symposium on Ballistics*, pp. 1–6, Tarragona, Spain, April 2007.

[8] B. K. Fink, "Performance metrics composite integral armor," *Journal of Thermoplastic Composite Materials*, vol. 13, no. 1, pp. 417–431, 2000.

[9] F. A. L. Dullien, "Capillary and viscous effects in porous media," in *Handbook of Porous Media*, K. Vafai, Ed., pp. 53–112, Marcel Dekker, Inc., NewYork, NY, USA, 2000.

[10] C. K. Chen and S. W. Hsiao, "Transport phenomena in enclosed porous cavities," in *Transport Phenomena in Porous Media*, D. B. Inghan and I. Pop, Eds., pp. 40–65, Elsevier Science Ltd., Amsterdam, Netherlands, 1998.

[11] C. M. R. Franco and A. G. B. Lima, "Intermittent drying of porous media: a review," *Diffusion Foundations*, vol. 7, pp. 1–13, 2016.

[12] C. T. Hsu, "Dynamic modeling of convective heat transfer in porous media," in *Handbook of Porous Media*, K. Vafai, Ed., pp. 40–79, Taylor & Francis Group, Didcot, UK, 2005.

[13] M. A. Al-Nimr and M. K. Alkan, "Basic fluid flow problems in porous media," *Journal of Porous Media*, vol. 3, no. 1, pp. 45–59, 2000.

[14] S. Mall, D. W. Katwyk, R. L. Bolick, A. D. Kelkar, and D. C. Davis, "Tension–compression fatigue behaviour of a H-VARTM manufactured unnotched and notched carbon/epoxy composite," *Composite Structures*, vol. 90, no. 2, pp. 201–207, 2009.

[15] S. G. Advani and K. Hsiao, "Transport phenomena in liquid composites molding processes and their roles in process control and optimization," in *Porous Media*, K. Vafai, Ed., pp. 573–606, Taylor & Francis Group, Didcot, UK, 2005.

[16] A. Shojaei, S. R. Ghaffarian, and S. M. H. Karimian, "Modeling and simulation approaches in the resin transfer molding process: a review," *Polymer Composites*, vol. 24, no. 4, pp. 525–544, 2003.

[17] M. K. Yoon, J. Baidoo, J. W. Gillespie Jr., and D. Heider, "Vacuum assisted resin transfer molding (VARTM) process incorporating gravitational effects: a closed-form solution," *Journal of Composite Materials*, vol. 39, no. 24, pp. 2227–2241, 2005.

[18] A. C. Garay, V. Heck, A. J. Zattera, J. A. Souza, and S. C. Amico, "Influence of calcium carbonate on RTM and RTM light processing and properties of molded composites," *Journal of Reinforced Plastic and Composites*, vol. 30, no. 14, pp. 1213–1221, 2011.

[19] R. Chaudhary, M. Pick, O. Geiger, and D. Schimidt, "Compression RTM- a new process for manufacturing high volume continuous fiber reinforced composites," in *Proceedings of 5th International CFK-Valley State Convention*, Stade, Germany, June 2011.

[20] W. K. Anderson and D. L. Bonhaus, "An implicit upwind algorithm for computing turbulent flows on unstructured grids," *Computers & Fluids*, vol. 23, no. 1, pp. 1–21, 1994.

[21] B. P. Leonard and S. Mokhtary, "Ultra-Sharp nonoscillatory convection schemes for high-speed steady multidimensional flow," NASA Technical Memorandum 102568, ICOMP-90-12, NASA, Washington, DC, USA, 1990.

[22] T. J. Barth and D. C. Jespersen, "The design and application of upwind schemes on unstructured meshes," in *Proceedings of 27th Aerospace Sciences Meeting*, Reno, NV, USA, January 1989.

[23] Ansys, *Fluent-Theory Manual*, Ansys, Inc., Canonsburg, PA, USA, 2015.

[24] S. V. Patankar and D. B. Spalding, "Computer analysis of the three-dimensional flow and heat transfer in a steam generator," *Forschung im Ingenieurwesen*, vol. 44, no. 2, pp. 47–52, 1978.

Hindawi
Advances in Materials Science and Engineering
Volume 2018, Article ID 2307157, 11 pages
https://doi.org/10.1155/2018/2307157

Research Article

Effect of Seepage Velocity on Formation of Shaft Frozen Wall in Loose Aquifer

Jian Lin,[1] Hua Cheng ,[1,2,3] Hai-bing Cai,[1] Bin Tang,[1] and Guang-yong Cao[3]

[1]*School of Civil Engineering, Anhui University of Science and Technology, Huainan 232001, China*
[2]*School of Resources and Environmental Engineering, Anhui University, Hefei 230022, China*
[3]*Department of Civil Engineering, Anhui Jianzhu University, Hefei 230601, China*

Correspondence should be addressed to Hua Cheng; hcheng@aust.edu.cn

Received 20 July 2018; Revised 1 September 2018; Accepted 5 September 2018; Published 8 October 2018

Guest Editor: Shimin Liu

This paper addresses the difficult closure of a frozen wall in a coal mine shaft due to excessive seepage velocity in an aquifer when the aquifer is penetrated via the artificial freezing method. Based on hydrothermal coupling theory and considering the effect of decreased absolute porosity on seepage during the freezing process, a mathematical model of hydrothermal full-parameter coupling with a phase change is created. A shaft is used as a prototype, and COMSOL multiphysics finite element software is employed to perform a numerical simulation of the shaft freezing process at various stratum seepage velocities. The numerical simulation results are verified via a comparison with field measurement data. Based on the numerical simulation results, the impact of various underground water seepage velocities on the artificial frozen wall formation process with the seepage-temperature field coupling effect is analysed. Based on the analysis results, the recommended principles of the optimization design for a freezing plan are described as follows: first, the downstream area is closed to enable the water insulation effect, and second, the closure of the upstream area is expedited to reduce the total closure time of a frozen wall.

1. Introduction

Due to core advantages, such as water insulation and temporary support, the artificial freezing method has been extensively applied in geotechnical engineering and become a common method for penetrating an aquifer in a coal mine shaft [1–3]. However, frozen wall closure failure due to excessive aquifer seepage velocity is common in engineering practice [4].

Many researchers have conducted extensive investigation of the freezing problem with high flow velocity. First, based on the Harlan [5] hydrothermal coupling model, a large amount of extension research was conducted. Li et al. [6], Liu et al. [7] and Kurylyk and Watanabe [8] elaborated differences among numerous studies. Vitel et al. [9] suggested that only two studies [9, 10] have performed experimental validation for high flow velocity. Second, based on hydrothermal coupling theory, Yang and Pi [11] created a mathematical model for single-hole freezing front development considering underground water flow and performed a comparative analysis of numerous influencing factors of single-pipe freezing via numeric calculation. Liu et al. [12] performed a qualitative analysis of the effect of horizontal underground water flow on horizontal freezing in a rectangular tunnel. Zhou and Lan [13] briefly analysed the variation of seepage and temperature fields during freezing via the numerical simulation of the artificial freezing process in a seepage stratum. Based on the proposed mathematical model, Marwan et al. [14, 15] employed an ant colony algorithm to optimize the tunnel freezing-hole layout in seepage conditions. However, the theoretical models of this numerical analysis were not validated by experiments, and the relationship between permeability variation and soil state during freezing was not explained. These numerical examples failed to summarize the common law for the effect of a seepage velocity increase on the formation of a shaft artificial frozen wall based on a detailed freezing plan.

Therefore, based on hydrothermal coupling theory and considering the effect of an absolute porosity decrease on seepage during freezing, a mathematical model for

hydrothermal full-parameter coupling with a phase change is created. The combined programming of MATLAB and COMSOL is employed to provide a numerical solution for a coupling mathematical model. A mine shaft double-circle-piped freezing plan is employed as a prototype to perform a numerical simulation and investigate the effect of underground water seepage velocity on frozen wall formation. The focus is the analysis of the effect of the underground water seepage velocity on the seepage field, temperature field, frozen wall closure time, and maximum thickness during freezing. An optimization principle for a high-flow-velocity shaft freezing plan is proposed, which has a significant theoretical and engineering value for solving the problem of the difficult closure of a shaft frozen wall in a loose aquifer with high flow velocity.

In Section 1, the mathematical model for hydrothermal full-parameter coupling with a phase change is created. In Section 2, a mine shaft double-circle-piped freezing plan is employed as a prototype; a combined programming method of MATLAB and COMSOL is employed to obtain a numerical solution. The results are verified with field measurements. In Section 3, based on this model, development patterns of a seepage and temperature field during freezing with different initial seepage velocities (at the step of 1 m/d) are quantitatively investigated. The effect of initial seepage velocity on the frozen wall closure time and effective thickness is analysed.

2. Mathematical Model

Generally, soil in freezing construction is a multiphase system that consists of a soil skeleton, water, air, and ice [16]. As this paper focuses on the effect of shaft underground water seepage on the freezing of a sandy soil layer, the soil is assumed to remain saturated during freezing. Considering the research focus and primary influencing factors, the following assumptions for the mathematical model derivation are presented:

(1) The effect of temperature variation and solute transport-induced density gradient and temperature gradient on the transport of unfrozen water is disregarded. The heat transfer loss of a freezing pipe wall is disregarded.

(2) Unfrozen water transport always satisfies the water flow continuity condition and Darcy's law. The initial state is steady seepage.

(3) A soil layer is a continuous, homogeneous and isotropic porous medium, which satisfies the basic assumption of mixture theory.

(4) The soil skeleton gap is a constant that is unrelated to thermodynamics parameters, ignoring the influence of temperature and pressure on viscosity coefficient of fluid.

2.1. Mathematical Expression for Content of Soil Composition during Freezing. The porosity of the unfrozen state is φ_0; assume that the pore water volume is χ; the volumes of soil compositions are listed in Table 1.

Table 1: Volume of soil composition.

Ice θ_i	Water θ_l	Soil θ_s
$\phi_0(1-\chi)$	$\phi_0\chi$	$1-\phi_0$

After soil freezes, it always contains some liquid water, and the content maintains a dynamic balance with temperature [16]. Based on considerable experimental analysis, the content is determined via formula (1) [16]. Therefore, the pore water volume is represented via formula (2):

$$w_{\mathrm{u}} = w_0\left(\frac{T_{\mathrm{f}}}{T}\right)^b, \tag{1}$$

$$\chi = \begin{cases} 1, & T > T_{\mathrm{f}}, \\ \left(\dfrac{T_{\mathrm{f}}}{\mathrm{T}}\right), & T \le T_{\mathrm{f}}, \end{cases} \tag{2}$$

where w_0 is the initial water volume content in soil; w_{u} is the volume content of unfrozen water in frozen soil; T is the soil temperature, ˚C; T_{f} is the initial soil freezing temperature, ˚C; and b is a constant determined by soil property.

2.2. Creation of Hydrothermal Coupling Control Equation during Freezing. The temperature variation during freezing is a transient heat conduction problem. Based on the basic assumption, ice, water, and soil skeleton coexist in soil during freezing and exhibit different heat transfer characteristics. In addition to heat transfer by conduction, ice heat transfer also includes phase change heat transfer. Water heat transfer includes convective heat transfer, which is induced by liquid water flow. Based on the heat transfer and seepage theory, the temperature and seepage field control equation during freezing that considers a phase change is expressed as [17]

$$\begin{aligned} &\theta_{\mathrm{i}}c_{\mathrm{i}}\rho_{\mathrm{i}}\frac{\partial T}{\partial t} + \phi_0 L_{\mathrm{w}}\rho_{\mathrm{l}}\frac{\partial \chi}{\partial T}\frac{\partial T}{\partial t} + \theta_{\mathrm{l}}c_{\mathrm{l}}\rho_{\mathrm{l}}\frac{\partial T}{\partial t} + \rho_{\mathrm{l}}c_{\mathrm{l}}(\overrightarrow{u}\cdot\nabla T) \\ &\quad + \theta_{\mathrm{s}}c_{\mathrm{s}}\rho_{\mathrm{s}}\frac{\partial T}{\partial t} = \nabla\left((\theta_{\mathrm{i}}k_{\mathrm{i}} + \theta_{\mathrm{l}}k_{\mathrm{l}} + \theta_{\mathrm{s}}k_{\mathrm{s}})\nabla T\right) + Q, \end{aligned} \tag{3}$$

$$\rho_{\mathrm{l}}\left[\alpha_{\mathrm{l}}\phi + \alpha_{\mathrm{s}}(1-\phi)\right]\frac{\partial p}{\partial t} + \nabla\cdot\left(\rho_{\mathrm{l}}\overrightarrow{u}\right) = \rho_{\mathrm{l}}q, \tag{4}$$

$$\overrightarrow{u} = -\frac{K'}{\rho_{\mathrm{l}}g}\nabla p, \tag{5}$$

where t is the time; c_{i}, c_{l}, and c_{s} are the specific heat capacities of ice, water, and the soil skeleton; k_{i}, k_{l}, k_{s} are the thermal conductivities of ice, water, and the soil skeleton; ρ_{i}, ρ_{l}, ρ_{s} are the densities of ice, water, and the soil skeleton; L_{w} is the phase change latent heat of the unit mass of water; $\overrightarrow{u}$ is the relative velocity vector of water; Q is the strength of the equivalent heat source; α_{l} is the compression rate of water; α_{s} is the equivalent compression rate; ϕ is the absolute porosity; p is the seepage pressure; and q is the flow rate.

Based on the relation between permeability and absolute porosity from the servo permeability test [18] and Darcy's law, the hydraulic conductivity during freezing is represented as

$$\frac{K'}{\rho_l g} = \frac{K_0\left(\frac{\phi}{\phi_0}\right)^3}{\mu} = \frac{K_0'}{\rho_l g}\left(\frac{\phi}{\phi_0}\right)^3, \quad (6)$$

where K' is the hydraulic conductivity, K_0' is the hydraulic conductivity for the unfrozen state, and μ is the viscosity coefficient of water.

In saturated soil, the absolute porosity is equal to the volume of liquid water. Therefore, disregarding the variation of the water viscosity coefficient during the cooling period, formulae (4) and (6) are represented as

$$K' = K_0'\left(\frac{\theta_l}{\phi_0}\right)^3, \quad (7)$$

$$\rho_l\left[\alpha_l\theta_l + \alpha_s\left(1-\theta_l\right)\right]\frac{\partial p}{\partial t} + \nabla\cdot\left(\rho_l\vec{u}\right) = \rho_l q. \quad (8)$$

The temperature boundary at the water inlet is the temperature of the water inflow, i.e., equal to the initial soil temperature. The temperature boundary at the freezing pipe wall is the actual temperature measured at the external wall of the freezing pipe. Assume that the convective flux is at the water outlet. The boundary condition is

$$n_d\cdot\left(-k\nabla T\right)\big|_{x=a_2} = 0, \quad (9)$$

where a_2 is the horizontal coordinate of the outlet boundary, and n_d is a vector along the inner normal direction at the water outlet.

As the heat transfer of other boundaries is not considered, other boundaries are treated as adiabatic boundaries. The boundary condition is

$$-n\cdot\left(-k\nabla T\right)\big|_{y=b_1,b_2} = 0, \quad (10)$$

where b_1, b_2 are the boundary vertical coordinates and n is a vector along the inner normal direction of the boundary.

In the calculation, assume that an initial water flow only has a flow velocity from left to right and perpendicular to the boundary, as shown in Figure 1. To form a directional and steady flow velocity in the initial state, the initial condition is

$$p|_{t=0} = p_0, \quad (11)$$

where p_0 is the initial hydraulic pressure distribution, which is obtained via the seepage velocity formula.

Both the inlet and outlet are set to boundaries with a fixed pressure. The corresponding values are determined by the initial pressure distribution. Other boundaries are set as the boundaries without flow:

$$-n\cdot\left(\vec{u}\,p\right)|_{\text{else}} = 0, \quad (12)$$

where n is a vector along the inner normal direction of the boundary.

Formulae (3), (5), (7), and (8) and the boundary conditions comprise the mathematical model for hydrothermal coupling during freezing.

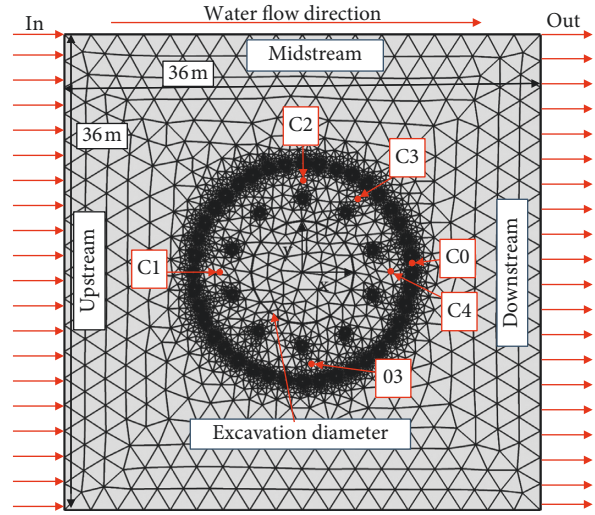

Figure 1: Geometrical model and grid.

3. Numerical Example

The mathematical model considers the variation of each composition, absolute porosity, and permeability for the seepage-temperature coupling effect during freezing. This model also considers the time-dependence of the temperature boundary of the freezing pipe wall. Therefore, the control equation and boundary condition are highly nonlinear. In this paper, based on the interpolation function and the coupling equation developed by MATLAB script language and the combined programming of MATLAB and COMSOL, the transient state solution of the mathematical model for hydrothermal coupling during freezing is obtained by substituting the variables and boundary conditions in the field equation.

Extensive engineering experience reveals that the effect of seepage on freezing is substantially dependent on a freezing plan. Therefore, a main shaft freezing project of a mine in Shangdong is presented as an example in this paper. First, the freezing temperature field for this condition is analysed to validate the mathematical model and solution. Second, based on the effect of different seepage velocities on the freezing process, the effect of the seepage velocity and variation on the closure time and frozen wall thickness during freezing are quantitatively analysed to obtain the critical seepage velocity and common law for the freezing plan. Last, the optimal path of the freezing-hole layout is proposed based on the simulations.

3.1. Engineering Background and Geometrical Model. In the main shaft of a mine in Shangdong, the artificial freezing method is employed to penetrate a 457.78 m thick alluvium; the shaft net diameter is 4.5 m, and the excavation diameter is 7.8 m [19]. The designed active freezing period is 150 days. The diameter of the primary pipe freezing hole is 159 mm; the circle diameter is 16.5 m; 40 holes exist; and the hole spacing is 1.295 m. The secondary pipe freezing-hole

diameter is 133 mm; the circle diameter is 11 m; 10 holes exist; and the hole spacing is 3.45 m [19].

In shaft freezing construction, the geometrical model for frozen wall formation is three-dimensional. If the freezing pipe deflection, nonuniform axial distribution of the freezing pipe wall temperature, and soil heterogeneity during shaft freezing are disregarded, the model is simplified to a two-dimensional model. Therefore, a horizontal section at a depth of 342.5 m is selected for investigation. The shaft centre is defined as the origin; both the model length and the model width are set to 36 m; the seepage direction is perpendicular to the vertical boundary and extends from left to right. The constructed geometrical model and grid for calculation are shown in Figure 1. In the figure, 03, C1, C2, C3, and C4 represent the temperature measurement points with equivalent distance to the shaft centre. Of these points, 03 is the actual temperature measurement hole; C2 and C3 are the intersection points of the freezing-hole boundary with its axial plane for the primary pipe and secondary pipe, respectively; C1 and C4 are the two positions in the axis planes of two secondary pipe freezing holes along the boundary and close to the primary pipe; and C0 is the downstream velocity measurement point, which is the intersection of the axis and the boundary of two freezing holes in the downstream primary pipe.

3.2. Calculation Parameters. Based on actual engineering hydrological data, the seepage velocity is set to 0.5 m/d in the calculations. The initial hydraulic conductivity is 3.656 m/d. The initial soil temperature is 22°C. Assume that the freezing pipe wall does not experience any heat transfer loss and the temperature at pipe outer wall is the brine temperature in the pipe. In the numeric calculation, therefore, the pipe wall temperature is based on the field measurement of the brine temperature. The average field measurement of the brine temperature at the outlet and inlet versus time is shown in Figure 2.

Based on corresponding physical test results and research conclusions in reference [16], the physical parameters are listed as follows: the phase change latent heat of unit mass of water is $334\,kJ/kg$; the initial freezing temperature of saturated soil is −0.02°C; and the constant b determined by the property of saturated soil is 0.61 [16]. Values of other physical parameters in formulae (3) and (6) are listed in Table 2.

3.3. Comparison and Verification of Numerical Calculation Result versus Field Measurement. To validate mathematical model and numerical solution method proposed in this paper, primary pipe closure time, effective frozen wall thickness after active freezing, and field temperature measurement are compared and analysed.

When primary shaft freezes for 150 d, actual measurement of frozen wall thickness is 6.6 m; actual measurement of primary pipe closure time is 22 days [19]. As shown in Figures 3 and 4, from numerical calculation result, the average thickness of the effective frozen wall is 6.54 m after the crude diameter is deducted, and the primary pipe closure time is 22 days, both match well with field measurement. Due to limitation of paper length, only 03 measurement point is selected to compare with actual temperature measurement. Comparison curve of actual measurement data versus numerical simulation is shown in Figure 5. Figure 5 shows that the simulation result and field measurement result have similar temperature variation pattern and amplitude.

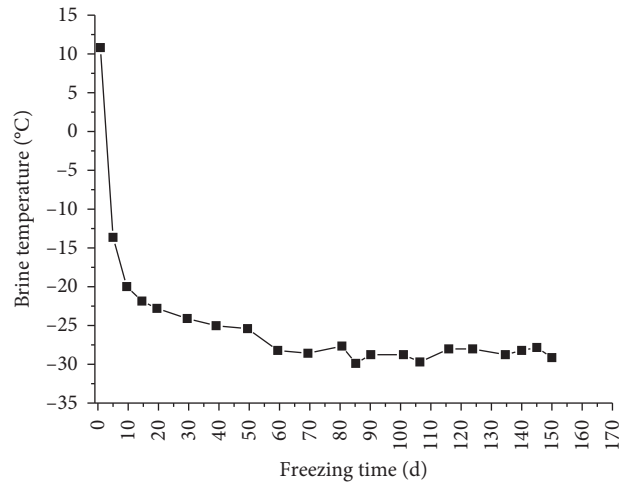

Figure 2: Time dependence of brine temperature.

Comparison results indicate that three numerical calculation results are consistent with the field measurements, which indicates that the numerical calculation results are accurate and valid for extension research.

4. Analysis of Frozen Wall Formation Pattern under Seepage

To investigate the effect of seepage velocity on frozen wall formation, based on the model, the effect of seepage field, temperature field, seepage velocity on the frozen wall closure time, and the effective thickness for different initial seepage velocities (at a step of 1 m/d) during freezing is quantitatively investigated.

During freezing, with the formation of a frozen area, the roundabout flow induced by the water insulation effect of the frozen area along the freezing front will change the seepage velocity and direction. These changes in seepage characteristics affect the coupling with the temperature field. Coupling of the seepage and temperature fields is the main influencing factor of different characteristics of frozen wall formation. To investigate the effect of seepage velocity on frozen wall formation, the characteristics of two fields in seepage-temperature field coupling during freezing should be separately analysed.

4.1. Analysis of Seepage Field during Freezing. Prior to freezing, with the exception of the freezing hole with the roundabout flow, other regions are located in the seepage field with uniform velocity. As freezing continues, the frozen area gradually forms around the freezing hole and the

Table 2: Physical parameters.

Composition	Density (kg·m^{-3})	Heat conductivity, W·(m·K)$^{-1}$	Specific heat, J·(kg·K)$^{-1}$	Initial volume fractions (l)
Water	1000	0.55	4179	—
Ice	918	2.25	2052	—
Soil	1800	2.08	720	0.34

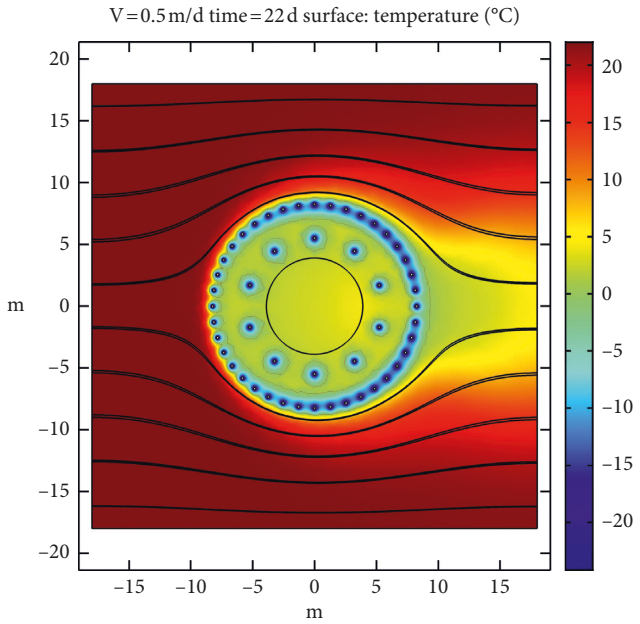

Figure 3: Temperature nephogram when primary pipe closes.

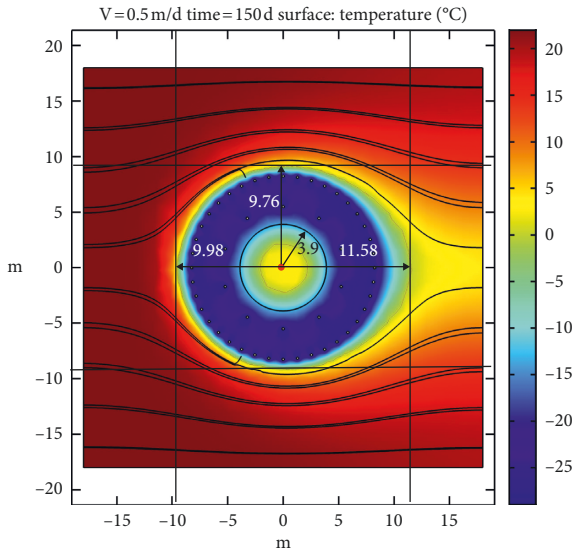

Figure 4: Temperature nephogram after freezing for 150 d.

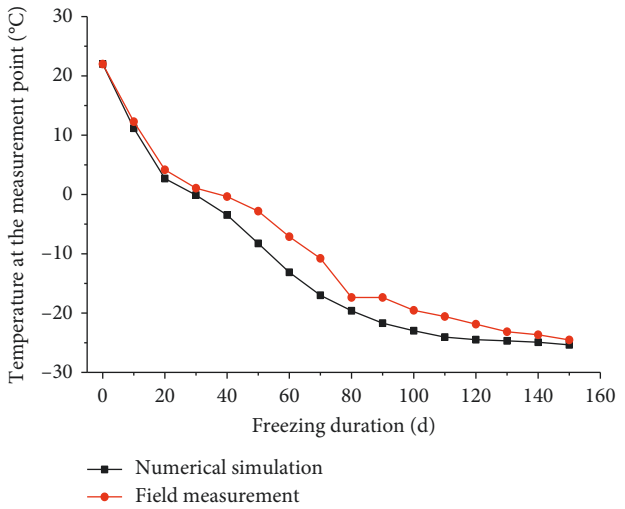

Figure 5: Variation curve of temperature at measurement point versus time.

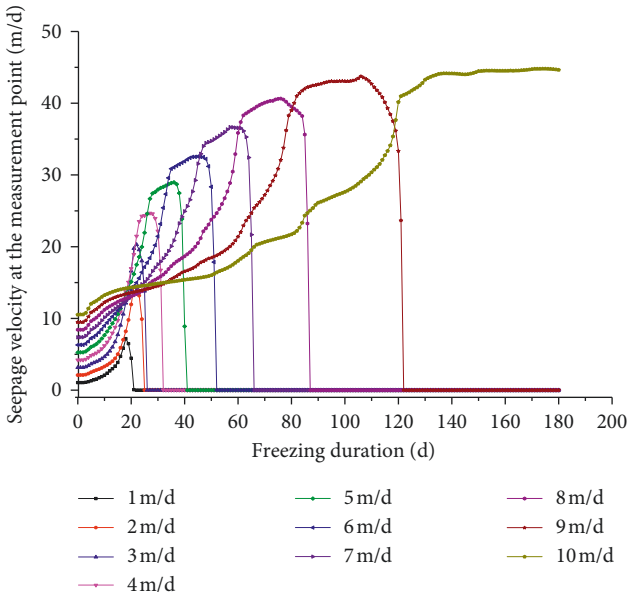

Figure 6: Variation curve of flow velocity at velocity measurement point C0 versus time.

roundabout flow occurs along the freezing front. Then, the frozen regions between the midstream freezing holes are separately connected. In the hole deployment area, a "window" with a wide top and narrow bottom exists. Water flows from the wide "window" and aggregates at the narrow "window", which causes an increase in the flow velocity at the point. When the downstream "window" closes, the seepage velocity at this point rapidly decreases to zero.

As shown in Figure 6, as freezing continues, the seepage velocity at the downstream velocity measurement point gradually increases. Then, the seepage velocity rapidly approaches the peak value. Subsequently, the velocity gradually increases to the peak value and significantly decreases to zero. With an increase in the initial seepage velocity, this pattern changes to a certain extent. As listed in Table 3, the flow velocity duration downstream increases; and both the

Table 3: Comparison of maximum seepage velocity and duration at velocity measurement point.

Initial seepage velocity v_0 (m/d)	Maximum seepage velocity v max (m/d)	$\frac{v_{max}}{v_0}$	Maximum seepage velocity increase (m/d)	Peak duration (d)	Downstream flow velocity duration (d)
1	7.18	7.18	6.18	1	21
2	16.41	7.21	12.41	2	25
3	20.29	6.76	17.29	3	26
4	24.68	6.17	20.68	7	32
5	28.98	5.80	23.98	9	41
6	32.57	5.43	26.57	13	52
7	36.65	5.24	29.65	18	66
8	40.65	5.08	32.65	22	87
9	43.74	4.86	34.74	29	122
10	44.54	4.45	34.54	51	—

peak seepage velocity and its duration at the downstream velocity measurement point increase. The rate of increase of the peak value gradually increases; however, the ratio between the peak seepage velocity to the initial seepage velocity gradually decreases. When initial seepage velocity is 10 m/d, a decrease in the seepage velocity in the calculation period is not exhibits.

As shown in Figure 7, when the downstream "window" closes, a semicircular water insulation frozen area is formed in the hole area. At this moment, the water flow by passes the freezing-hole area, and the seepage velocity in the freezing-hole area is almost zero. The seepage velocity in upstream and downstream areas significantly decreases, which indicates that the water insulation effect of freezing construction is formed.

However, in the midstream area along the tangential direction of flow velocity, the flow velocity exceeds the initial seepage velocity and is approximately two times the initial seepage velocity. The amplitude of the flow velocity increases with an increase in the initial seepage velocity, as listed in Table 4.

This phenomenon indicates that during freezing of a double-circle-piped shaft, the maximum seepage velocity downstream of the freezing-hole deployment area significantly exceeds the initial stratum seepage velocity. The downstream "window closure" and water flow that circumvents the freezing-hole deployment area almost simultaneously occur. After the downstream "window closure", the effect of the seepage velocity on freezing is only reflected in the outward expansion rate of the midstream freezing front. The effect on frozen wall formation in the freezing-hole deployment area is insignificant.

4.2. Effect of Seepage Velocity on Freezing Temperature Field. The frozen wall formation process is the frozen area expansion process induced by the variation in temperature field. The essence of the formation rule is the variation rule of the freezing temperature field. Therefore, an analysis of the effect of seepage velocity on frozen wall formation requires further analysis of the effect of seepage velocity on the freezing temperature field.

An analysis of the temperature field calculation results indicates that when seepage velocity is not considered, the frozen area expands along the freezing pipe in the outer

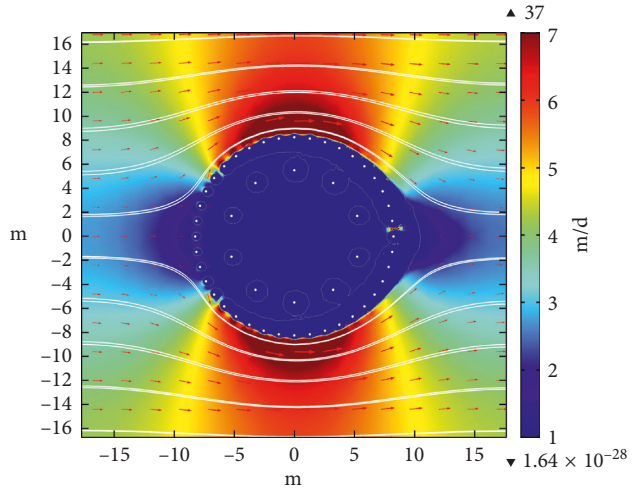

Figure 7: Velocity distribution after 40 d of freezing when initial seepage flow velocity is 5 m/d.

Table 4: Comparison of midstream peak surface seepage velocity after 150 d of freezing.

Initial seepage velocity (m/d)	Maximum seepage velocity (m/d)	Velocity ratio (1)
1	1.52	1.52
2	3.21	1.61
3	5.02	1.67
4	7.43	1.86
5	9.47	1.89
6	11.97	2.00
7	16.12	2.02
8	16.28	2.04
9	21.79	2.42

normal direction in the form of a concentric circle prior to the frozen wall closure. After the frozen wall closure, the frozen area expands along the boundary until a homogeneous frozen wall is formed. Due to the seepage-temperature field coupling effect, as heat transfer between freezing holes changes to the superposition of fluid heat transfer and solid heat transfer, the freezing temperature field demonstrates inhomogeneity. Inhomogeneity increases with seepage flow velocity. As freezing continues, inhomogeneity gradually

decreases after the frozen wall closure. At a particular moment when the seepage velocity increases, the frozen wall undergoes the following sequential states: formation of the entire frozen wall, midstream and downstream "window closure", and frozen wall midstream closure.

To intuitively analyse the effect of the initial seepage velocity in different strata on the freezing temperature field, the calculation results for four key nodes with the same freezing duration are compared and analysed, as shown in Figure 8.

As shown in the nephogram in Figure 8, for the same freezing duration, when the initial stratum seepage velocity is 0 m/d, the primary pipe is closed and closure of the primary and secondary pipes starts, the temperature field is symmetric and homogeneous in the frozen area. When the initial stratum seepage velocity is 5 m/d, the frozen area demonstrates a pattern that displays a thin top and a thick bottom. The temperature of the lower part of midstream is significantly lower than the temperature of the other part. As the seepage velocity increases, the frozen area shrinks, the temperature in the hole area rises and inhomogeneity increases.

The temperature curve in Figure 8 demonstrates the following results. (1) When the flow velocity is zero, two measurement points in the midstream area have identical temperature variation patterns; the temperature variation patterns for the measurement points upstream and downstream are identical. As the measurement points are located in different positions, the temperature of two measurement points in the midstream area is lower than the temperature of the measurement points upstream and downstream. The difference gradually increases when the primary and secondary pipe closure starts and gradually disappears when closure is completed. (2) When the seepage velocity is a nonzero value, the temperature variation at each measurement point demonstrates four distinct phases as follows: (a) before formation of the frozen area around the freezing hole near the measurement point, the temperature rapidly decreases. (b) after formation of the frozen area around the freezing hole near measurement point and before closure of the frozen area, temperature at the measurement point gradually decreases. (c) after the downstream "window closure" and before total frozen wall formation, the temperature at the measurement point rapidly decreases. (d) after total frozen wall formation, the rate of temperature decrease at the measurement point decelerates; the difference between two temperatures at different measurement points is minimal; and the temperature at the downstream measurement point gradually becomes lower than the temperature at other measurement points. The temperatures at the measurement points maintain the following order: C4 < C3 < C1 < C2. (3) As the seepage velocity increases, the durations of phases b and c are prolonged. During a long period, the temperatures at different measurement points maintain the following order: C3 < C2 < C4 < C1. (4) The interval for the temperature at each measurement point to decrease to the phase change temperature increases. However, the increase for each interval at the upstream and downstream measurement points is insignificant. For different seepage velocities, following the order C3, C2, C4, C1, the patterns of temperature variation curve at each measurement point becomes more distinct.

The seepage and temperature field analysis results are described as follows: the seepage-temperature field coupling effect, the primary pipe at the lower part of the midstream area closes. The primary and secondary pipes also closed at the primary surface of the lower part of the midstream area, and the closure expands to the upstream and downstream area as freezing continues. After downstream closes, the impact of the seepage velocity on the freezing process in the freezing-hole deployment area is insignificant. The temperature in the frozen area rapidly decreases, and the difference among the temperatures at different points gradually decreases.

4.3. Variation Pattern of Closure Time for Different Initial Seepage Velocities. Analysis of the individual characteristics of two fields with the seepage-temperature field coupling effect during freezing reveals that the seepage-temperature field coupling effect causes a loss of cooling energy and nonuniform temperature field distribution. As the initial stratum seepage velocity increases, the frozen wall inhomogeneity increases. Midstream freezing holes are gradually connected, and the closure expands towards the downstream and upstream areas until the frozen area between the upstream freezing holes closes to form the entire frozen area. Therefore, the upstream frozen wall closure time is used to represent the formation of the entire frozen area. The variation curve of the frozen wall closure time versus the initial stratum seepage velocity is shown in Figure 9.

As shown in Figure 9, when the initial stratum seepage velocity is within 7 m/d, the increased closure time is always less than 10% of the active freezing period for each 1 m/d increase in the initial stratum seepage velocity. However, when the initial stratum seepage velocity increases from 8 m/d to 9 m/d, the increased closure time is 27% of the active freezing period. When the initial stratum seepage velocity is 10 m/d, the frozen wall cannot close. The upstream and downstream frozen wall closure times increase with the initial stratum seepage velocity and both demonstrate a quasiexponential relation. However, the interval between the upstream closure time and the downstream closure time is not distinct.

The cause of this phenomenon is described as follows: after the midstream frozen area is formed, the downstream frozen area closes, and the resultant water insulation effect reduces the loss of cooling energy in the freezing-hole deployment area and facilitates closure of the entire frozen wall.

4.4. Variation Pattern of Maximum Thickness of Frozen Wall during Active Freezing Period. Due to the underground water seepage effect, before the frozen wall closure, the upstream, midstream, and downstream frozen wall thicknesses along the seepage direction demonstrate a pattern with a thin top and a thick bottom. As the seepage velocity increases, the effective frozen walls in the upstream, midstream, and downstream areas become thinner, which causes an upstream closure failure, and the effective frozen

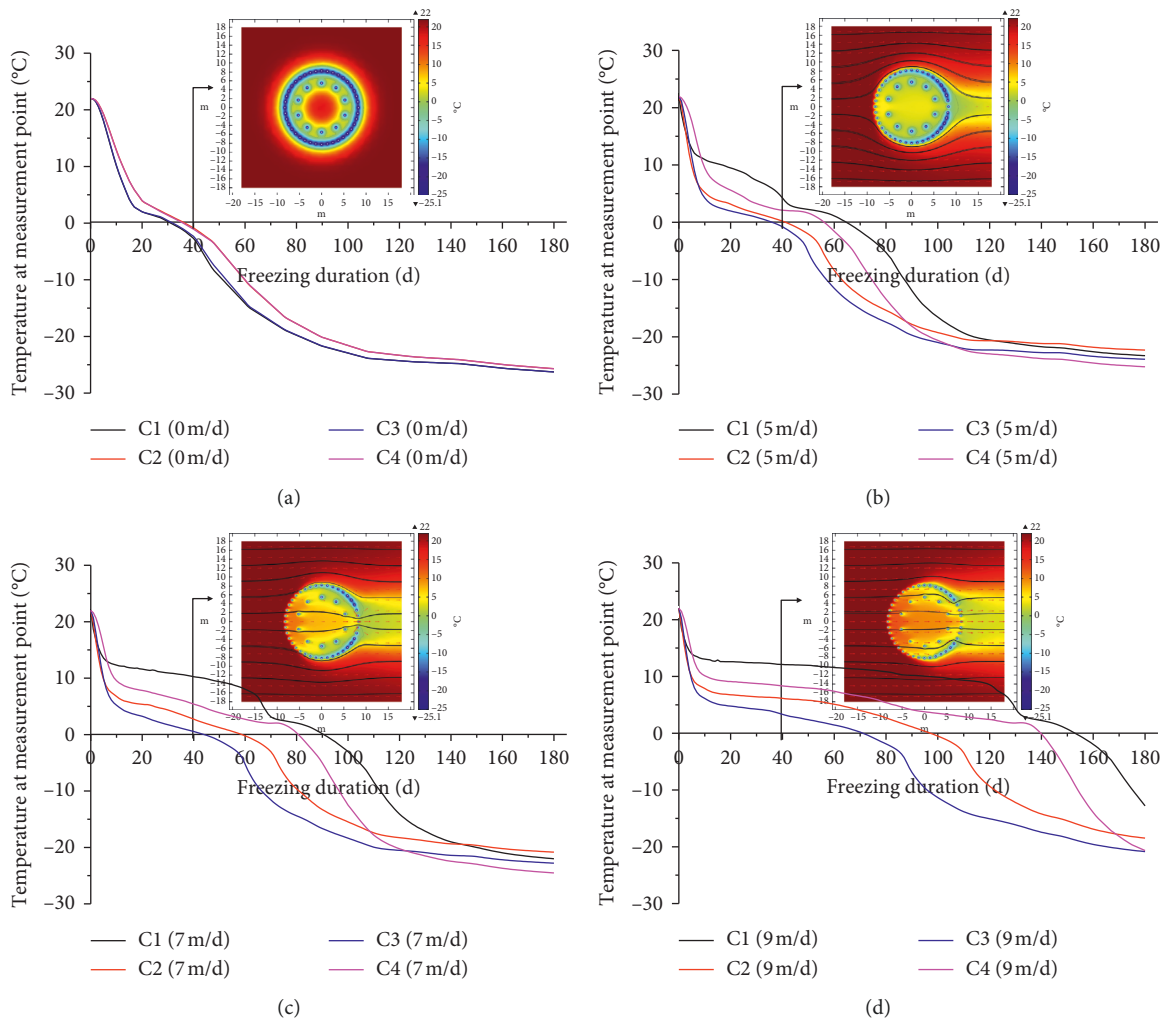

Figure 8: Temperature curve at measurement points for different initial seepage velocities and distribution of frozen area and seepage line after 40 d of freezing. (a)$v = 0$ m/d. (b)$v = 5$ m/d. (c)$v = 7$ m/d and (d)$v = 9$ m/d.

wall cannot be formed. After the frozen wall closure, due to the water insulation effect by the frozen wall, the seepage velocities in the frozen wall interior area and the frozen wall exterior upstream and downstream areas are significantly lower than the initial stratum seepage velocity. However, the seepage velocity in the frozen wall exterior midstream area is approximately two times the initial stratum seepage velocity. Therefore, the freezing front expansion in the frozen wall interior area and the as frozen wall exterior upstream and downstream areas are not affected by the seepage velocity. The freezing front line at the frozen wall interior gradually forms a regular circle. The freezing front expansion in the frozen wall exterior upstream and downstream areas exhibits a similar pattern. However, the frozen wall exterior midstream area remains affected by high flow velocity and expansion decelerates.

Two completely different freezing front expansion patterns before and after the frozen wall closure cause a change in the frozen wall thickness growth trend with an increase in the seepage velocity and freezing time. To reflect the effect of the seepage velocity on freezing, the relation between the frozen wall maximum thickness without removing the crude diameter and the seepage velocity during the active freezing period are analysed in this paper, as shown in Figure 10.

As shown in Figure 10, when freezing progresses to 150 days, with the exception of a seepage velocity of zero, the average thickness of the entire frozen wall linearly decreases with an increase in the seepage velocity. The maximum thickness of the downstream frozen wall always exceeds the maximum thickness of the upstream and midstream frozen walls. The difference between the upstream thickness and the midstream thickness is maintained within 0.5 m. The difference between the downstream value and the upstream and midstream values range from 1.63 to 2.69 m. The maximum thickness of the downstream frozen wall initially increases with the seepage velocity and then decreases; the peak is attained when the seepage velocity is 2 m/d. The maximum thicknesses of the upstream and midstream frozen walls decrease with an increase in the seepage velocity. When the seepage velocity is less than 7 m/d, the thickness of the upstream wall is slightly greater than the thickness of the midstream wall. When the seepage velocity exceeds 7 m/d, the thickness of the midstream wall exceeds the thickness of the upstream wall.

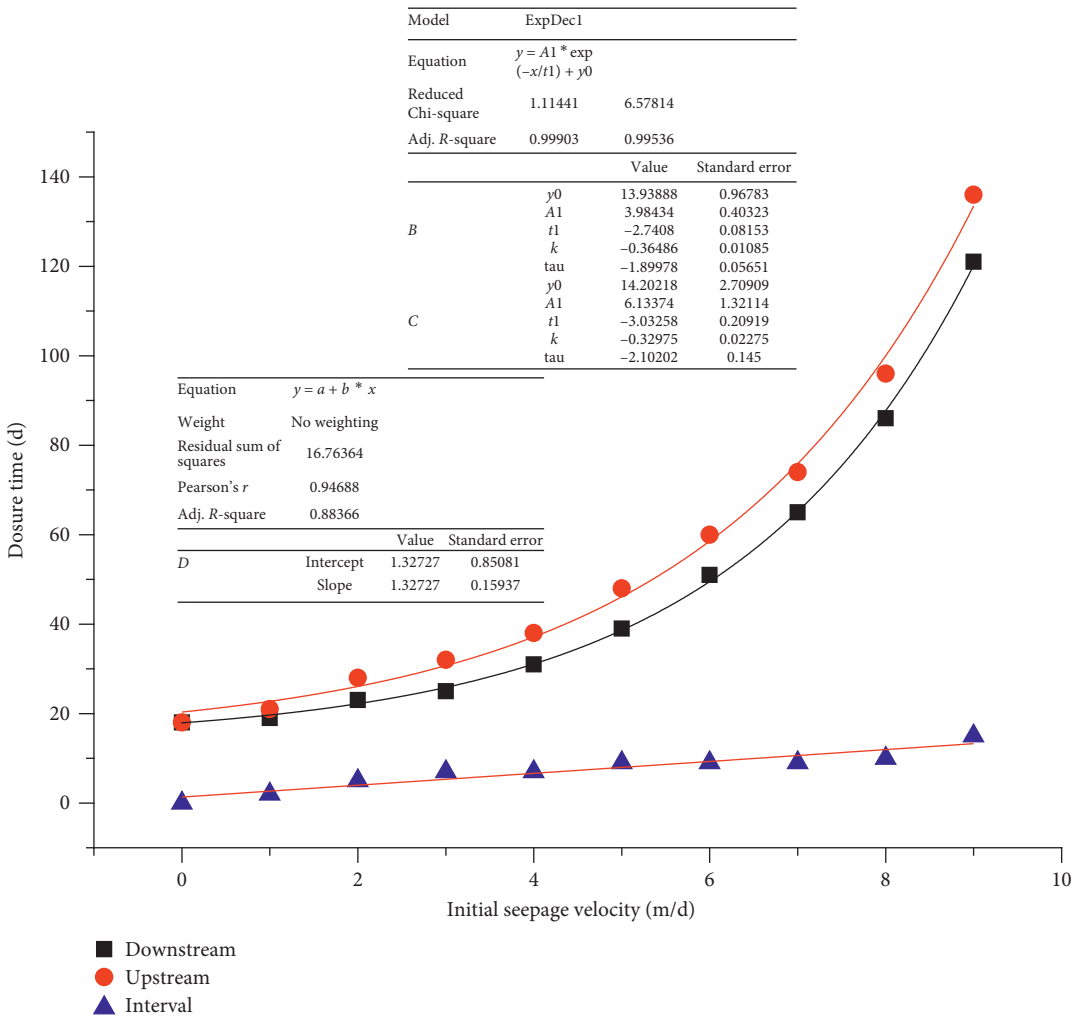

FIGURE 9: Variation curve of closure time versus initial seepage velocity.

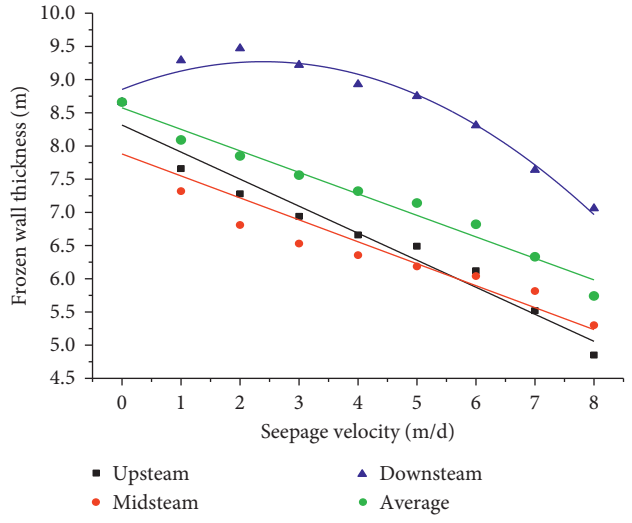

FIGURE 10: Variation of frozen wall thickness versus seepage velocity.

The cause of this phenomenon is described as follows: during the same period, the cooling energy that is removed by the seepage effect is positively related to the seepage velocity. Prior to the frozen wall closure, due to the underground water seepage effect, the temperature of the water flow gradually reduces through upstream and midstream. The disturbance of low-temperature water in the downstream area is beneficial for increasing the frozen wall thickness. However, as the seepage velocity increases, the cooling energy removed from the frozen area increases; meanwhile, the decreasing trend of low-temperature water is also limited. Therefore, the beneficial effect gradually diminishes, and the seepage velocity eventually becomes an unfavourable factor for the downstream frozen wall thickness. An increase in the seepage velocity has the following effects: prior to the frozen wall closure, the frozen wall has a thin top and a thick bottom; after the frozen wall closure, the frozen wall closure time increased and the expansion period of the freezing front in the frozen wall interior and exterior in the upstream area decreases. However, when the seepage velocity exceeds 7 m/d, offsetting the difference between the thin top and the thick bottom prior to the frozen wall closure is difficult.

Due to the seepage-temperature field coupling effect, as the seepage velocity increases, the maximum thickness of the downstream frozen wall initially increases and then decreases; however, the average thickness of the frozen wall linearly decreases. In this freezing plan, the critical seepage velocity is 7 m/d.

5. Conclusions and Suggestions

In this paper, the hydrothermal coupling process is analysed. Based on previous research, a hydrothermal full-parameter coupling equation is derived; its solution is provided via the combined programming method of MATLAB and COMSOL. First, a mine project is investigated to validate the mathematical model and solution. Second, the effect of the initial stratum seepage flow velocity on frozen wall formation is investigated and the following conclusions are obtained.

(1) During freezing, the maximum seepage velocity that the downstream hole area should resist is significantly larger than the initial stratum seepage velocity. The maximum seepage velocity decreases with an increase in the initial seepage velocity. At the end of the active freezing period, the maximum seepage velocity at the midstream peak surface is approximately two times the initial seepage velocity.

(2) Due to the seepage-temperature field coupling effect, at the lower part of the midstream area, the primary pipe closes, which is the same case for the primary and secondary pipes. After the downstream closure, the frozen area temperature rapidly decreases. The differences among the temperatures at different positions gradually decrease.

(3) As the initial stratum seepage velocity increases, the freezing temperature field inhomogeneity increases. The maximum thickness of the downstream frozen wall initially increases and then decreases. However, the average thickness of the frozen wall linearly decreases. The upstream and downstream frozen wall closure time and initial stratum seepage velocity follow a quasiexponential relation and variation of closure time interval is not conspicuous. In this freezing plan, the critical seepage velocity is 7 m/d.

Therefore, to reduce the frozen wall closure time and improve the efficiency of the total freezing construction, the recommended design principles of the freezing plan are as follows: first, the downstream area should be closed to enable the water insulation effect to reduce the outflow of cooling energy; and second, the upstream closure should be expedited to reduce the closure time of the entire frozen wall.

Data Availability

The data used to support the findings of this study are available from the corresponding author upon request.

Conflicts of Interest

The authors declare that they have no conflicts of interest.

Acknowledgments

The work presented in this paper is financially supported by the National Natural Science Foundation of China (Nos. 51804006, 51778004, 51674006, 51474004 and 51374010), National Science and Technology Major Project of China (No. 2016ZX05068-001), and Youth Science Research Foundation of Anhui University of Science and Technology (Nos. QN2017211 and QN2017222). The authors gratefully acknowledge financial support of the above-mentioned agencies.

References

[1] H. Cheng, *Theory and Technology of Freezing in Deep Alluvium*, Science and Technology Press, Beijing, China, 2016.

[2] H. Cheng and H. B. Cai, "Safety situation and thinking about deep shaft construction with freezing method in China," *Journal of Anhui University of Science and Technology Natural Science*, vol. 33, no. 2, pp. 1–6, 2013.

[3] H. Cheng and H. B. Cai, "Multi-target gray situation decision making for project determination of shaft freeing in deep alluvium," *Journal of Anhui University of Science and Technology Natural Science*, vol. 27, no. 3, pp. 22–25, 2007.

[4] Y. E. Yuxi, H. Shi, and M. Yang, "Analysis and treatment of unjoint circle of auxiliary shaft of a yili mining area," *Mining Engineering*, vol. 11, no. 6, pp. 20-21, 2013.

[5] R. L. Harlan, "Analysis of coupled heat-fluid transport in partially frozen soil," *Water Resources Research*, vol. 9, no. 5, pp. 1314–1323, 1973.

[6] Q. Li, S. Sun, and Y. Xue, "Analyses and development of a hierarchy of frozen soil models for cold region study," *Journal of Geophysical Research*, vol. 115, no. 3, pp. 1–18, 2010.

[7] Z. Liu, Y. Sun, and X. B. Yu, "Theoretical basis for modeling porous geomaterials under frost actions: a review," *Soil Science Society of America Journal*, vol. 76, no. 2, pp. 313–330, 2012.

[8] B. L. Kurylyk and K. Watanabe, "The mathematical representation of freezing and thawing processes in variably-saturated, non-deformable soils," *Advances in Water Resources*, vol. 60, pp. 160–177, 2013.

[9] M. Vitel, A. Rouabhi, M. Tijani, and F. Guérin, "Modeling heat and mass transfer during ground freezing subjected to high seepage velocities," *Computers and Geotechnics*, vol. 73, pp. 1–15, 2016.

[10] A Sres, *Theoretische und Experimentelle Untersuchungen zur künstlichen Bodenvereisung im Strömenden Grundwasser*, VDF Hochschulverlag AG, Zürich, Switzerland, 2010.

[11] P. Yang and A. R. Pi, "Study on the effects of large groundwater flow velocity on the formation of frozen wall," *Chinese Journal of Geotechnical Engineering*, vol. 23, no. 2, pp. 167–171, 2001.

[12] J. Liu, Q. Liu, D. ZHOU et al., "Influence of groundwater transverse horizontal flow velocity on the formation of artificial horizontal freezing wall," *Journal of Basic Science and Engineering*, vol. 25, no. 2, pp. 258–265, 2017.

[13] X. M. Zhou and Y. U. Lan, "The fluid flow analysis of ground freezing shaft," *Journal of China Coal Society*, vol. 26, no. 2, pp. 141–144, 2001.

[14] A. Marwan, M. M. Zhou, M. Z. Abdelrehim, and G. Meschke, "Optimization of artificial ground freezing in tunneling in the presence of seepage flow," *Computers and Geotechnics*, vol. 75, pp. 112–125, 2016.

[15] M. M. Zhou and G. Meschke, "A three-phase thermo-hydro-mechanical finite element model for freezing soils," *International Journal for Numerical and Analytical Methods in Geomechanics*, vol. 37, no. 18, pp. 3173–3193, 2013.

[16] X. Z. Xu, J. C. Wang, and L. X. Zhang, *Frozen Soil Physics*, Science Press, Beijing, China, 2010.

[17] G. Xu, *Study on Mechanical Characteristics and Multiphysical Coupling Problems of Rock at Low Temperatures*, Institute of Rock and Soil Mechanics Chinese Academy of Sciences, Wuhan, china, 2006.

[18] Y. Wang, Z. Liu, S. Lin et al., "Finte element analysis of seepage in rock based on continuum damage evolution," *Engineering Mechanics*, vol. 33, no. 11, pp. 29–37, 2016.

[19] H. B. Cai and C. X. Rong, "Non-liner finite element analysis on transient freezing temperature field based on latent heat of latent heat of phase change," *Low Temperature Architecture Technology*, vol. 31, no. 2, pp. 43–45, 2009.

Hindawi
Advances in Materials Science and Engineering
Volume 2018, Article ID 9254865, 12 pages
https://doi.org/10.1155/2018/9254865

Research Article

Entire Process Simulation of Corrosion due to the Ingress of Chloride Ions and CO_2 in Concrete

Xingji Zhu,[1] Zhaozheng Meng,[1] Yang Liu,[1] Longjun Xu,[1,2] and Zaixian Chen [1]

[1]*Department of Civil Engineering, Harbin Institute of Technology at Weihai, Weihai 264209, China*
[2]*Cooperative Innovation Center of Engineering Construction and Safety in Shandong Blue Economic Zone, Qingdao, China*

Correspondence should be addressed to Zaixian Chen; zaixian_chen@sina.com

Received 30 April 2018; Accepted 15 July 2018; Published 13 August 2018

Academic Editor: Shimin Liu

A comprehensive mathematical model which can simulate the entire corrosion process of reinforcement in concrete is proposed in this paper. The combined effect of carbonation and chloride ingress is also discussed in the mass transport module. Nonuniform corrosion distribution is employed for the study of mechanical damage in concrete. The link of ABAQUS with MATLAB is adopted for the numerical implementation of the developed model. The numerical results of an illustrative example indicate that the depassivation time of reinforcement, corrosion rate and expansion displacement, and cracking pattern of concrete all can be accurately predicted.

1. Introduction

Reinforced concrete (RC) structure is widely applied in the modern building construction area because of its advantages in structural stability. With the promotion of sustainable development strategy, great concern has been attached to the durability and longevity of reinforced concrete. Due to the alkaline environment of concrete, a spontaneous process called passivation can initiate. When the pH value ranges from 12 to 13 [1, 2], a protection oxide layer on the surface of steel reinforcement is gradually formed. This oxide layer can prevent the RC structure from corrosion. However, because concrete is a porous material, the protective layer can be damaged by the penetration of aggressive agents. In addition, through the air in pores, carbon dioxide can also diffuse in concrete. They both can reduce the service life and cause deterioration of the RC structure severely.

The main factors causing chloride-induced corrosion are the prevalent usage of deicing salt and marine moisture containing aggressive agents. And the carbonation process also appears in concrete because of the diffusion of carbon dioxide. In most cases, carbonation occurs with the chloride transfer process. According to experimental data, it was found that carbonation has obvious influence on chloride diffusion [3, 4]. Hence, the study on this combined durability is of great significance.

After the depassivation of steel reinforcement, a macrocell corrosion with a larger cathode area and smaller anode area is formed [5, 6]. The corrosion product of steel reinforcement will expand 3 to 6 times in volume [7, 8], which generates tensile stress on the inner surface of concrete. As a brittle material, the compressive stress of concrete is greater than that of tensile strength [9]. If the tensile stress of concrete is greater than the tensile strength, cracks are propagated and developed. When the cracks reach the concrete cover, more aggressive agents including oxygen, carbon dioxide, and moisture will penetrate into the RC structure, which accelerates the corrosion process [9–11].

Spalling and deterioration caused by the expansive cracks have significant damage on the mechanical performance of the RC structure. Because cracks can reduce the confinement between concrete and rebars the bond behavior of the RC structure declines drastically [12]. The carrying capacity of the RC structure is also impaired by the corrosion-induced reduction of cross-sectional area of the steel reinforcement [9, 12–15]. Therefore, the research

studies on the corrosion rate, corrosion product distribution, and cracks pattern are attached to the utmost importance. An accurate model is needed to predict the service life and durability.

Many scholars studied the corrosion process and mechanical damage in the RC structure. For simplicity, these works all assume that the corrosion products are uniformly distributed [1, 16, 17]. However, that case is only suitable for the laboratory condition, in which the external current is attached to accelerate the corrosion process [9, 13, 18, 19]. According to actual observations, it was found that most of the corrosion distribution patterns are nonuniform [15, 20]. In terms of calculation results, recent studies have verified that errors of uniform distribution cannot be neglected [21]. The service life and bearing capacity are overestimated in evenly distributed models [14, 22]. Hence, those uniform distribution models are very limited.

Additionally, numerous scholars regarded the corrosion-induced expansive displacement as the swelling displacement of the concrete layer [1, 22–27], which is applied to the mechanical part directly. However, this method is incompatible with the actual cases. Note that Young's modulus of concrete is approximately 30 GPa, while Young's modulus of rust merely varies from 60 MPa to 100 MPa which is far smaller than that of concrete. Therefore, the deformation of rust layers increases dramatically with the rise of compression stress of the concrete cover. As a consequence, the expansive displacement and displacement of concrete should be considered independently [21]. Furthermore, there are few comprehensive models depicting the whole process from corrosion initiation to cracks reaching the concrete cover. Establishing a simplified full-scale model is attached to great importance.

In this paper, a comprehensive model for the entire process of corrosion-induced concrete deterioration is proposed. After this introduction, the transport of various harmful masses and the determination of depassivation time are described in Section 2. Then, Section 3 presents the process of the electrochemical reaction and mechanical damage. Experimental verification is presented in Section 4. Numerical implementation and an illustrative example are provided in Section 5. The conclusion is given in Section 6.

2. Transport of Various Harmful Masses

2. 1. Process of Carbon Dioxide Diffusion and Carbonation. Because the diffusion process of carbon dioxide in the air is four times faster than that in water diffusion in the porous water can be neglected. Therefore, the equation depicting carbon dioxide diffusion can be drawn by

$$\frac{\partial \phi_a C_{\mathrm{CO}_2}}{\partial t} + \nabla \cdot \mathbf{J}_{\mathrm{CO}_2} = -Q_{\mathrm{C}}, \tag{1}$$

where ϕ_a is the volume fraction in the pore of the concrete; C_{CO_2} is the molar concentration of gaseous carbon dioxide in concrete; $\mathbf{J}_{\mathrm{CO}_2}$ is the flux of carbon dioxide; and Q_{C} is the depletion rate of carbon dioxide, and Q_{C} can be determined in literature [28].

Based on literature [29–31], parameters mentioned in (1) can be defined by the following equations:

$$\phi_a = \phi - \phi_{\mathrm{we}}, \tag{2}$$

$$\mathbf{J}_{\mathrm{CO}_2} = -\phi_a D^{\mathrm{car}}_{\mathrm{CO}_2} \nabla C_{\mathrm{CO}_2}, \tag{3}$$

$$D^{\mathrm{car}}_{\mathrm{CO}_2} = 1.64 \times 10^{-6} \phi^{1.8}_{\mathrm{hc}} (1-h)^{2.2}, \tag{4}$$

where ϕ is the porosity of concrete, $D^{\mathrm{car}}_{\mathrm{CO}_2}$ is the diffusion coefficient of carbon dioxide (m^2/sec), and ϕ_{hc} is the porosity of hardened concrete. More details to formulate ϕ_{hc} can be found in literature [32].

2.2. Chloride Penetration considering the Effect of Carbonation. In the combined case, we consider that there are three forms of existence of chloride in the concrete. The first form is chloride ions in the pore solution of concrete; the second is the bond chloride which is depicted by the isotherm; and the last form of existence is chlorine salt which can be turned into chloride ions through the reaction with carbon dioxide. Therefore, the total chloride content in the unit volume of concrete can be drawn by

$$C_{\mathrm{wc}} = \phi_{\mathrm{we}} C_{\mathrm{fc}} + C_{\mathrm{bc}} + C_{\mathrm{cs}}, \tag{5}$$

where C_{wc} is the whole concentration of chloride per volume of the concrete, ϕ_{we} is the volume fraction of volatile water in pore volume, C_{fc} is the concentration of free chloride ions, C_{bc} is the bound chloride, and C_{cs} is the concentration of chloride salts. Note that chloride salts can be turned into chloride ions through reaction with carbon dioxide. Consequently, with the consideration of convective term, the governing equation can be depicted by

$$\frac{\partial C_{\mathrm{wc}}}{\partial t} = \nabla \cdot D^{\mathrm{car}}_{\mathrm{fc}} \nabla \phi_{\mathrm{we}} C_{\mathrm{fc}} + \nabla \cdot D^{\mathrm{car}}_{\mathrm{h}} \phi_{\mathrm{we}} C_{\mathrm{fc}} \nabla h, \tag{6}$$

where $D^{\mathrm{car}}_{\mathrm{fc}}$ is the diffusion coefficient of free chloride ions and $D^{\mathrm{car}}_{\mathrm{h}}$ is diffusion coefficient of moisture. $D^{\mathrm{car}}_{\mathrm{h}}$ varies with the degree of carbonation.

Based on the employment of isotherm between bound chloride and chloride ions, (1) can be arranged according to chloride ions, which can be given by

$$\frac{\partial \phi_{\mathrm{we}} C_{\mathrm{fc}}}{\partial t} + \frac{\partial C_{\mathrm{bc}}}{\partial C_{\mathrm{fc}}} \frac{\partial C_{\mathrm{fc}}}{\partial t} + \frac{\partial C_{\mathrm{cs}}}{\partial t} = \nabla \cdot D^{\mathrm{car}}_{\mathrm{fc}} \nabla \phi_{\mathrm{we}} C_{\mathrm{fc}} + \nabla \cdot D^{\mathrm{car}}_{\mathrm{h}} \phi_{\mathrm{we}} C_{\mathrm{fc}} \nabla h, \tag{7}$$

which can be then expressed as

$$\frac{\partial \phi_{\mathrm{we}} C_{\mathrm{fc}}}{\partial t} + \nabla \cdot \mathbf{J}_{\mathrm{fc}} = Q_{\mathrm{rc}}, \tag{8}$$

where $\mathbf{J}_{\mathrm{fc}}$ is the flux of chloride ions; Q_{rc} is the source term which shows shifts from Friedel's salts to free chloride ions because of carbonation. Additionally, variables used in (4) can be depicted more explicitly by the following equations:

$$J_{\mathrm{fc}} = -\frac{1}{1+\left(1/\phi_{\mathrm{we}}\right)\left(\partial C_{\mathrm{bc}}/\partial C_{\mathrm{fc}}\right)} \cdot \left(D_{\mathrm{fc}}^{\mathrm{car}} \nabla \phi_{\mathrm{we}} C_{\mathrm{fc}} + \phi_{\mathrm{we}} C_{\mathrm{fc}} D_{\mathrm{h}}^{\mathrm{car}} \nabla h\right), \tag{9}$$

$$Q_{\mathrm{rc}} = -\frac{1}{1+\left(1/\phi_{\mathrm{we}}\right)\left(\partial C_{\mathrm{bc}}/\partial C_{\mathrm{fc}}\right)} \frac{\partial C_{\mathrm{cs}}}{\partial t}, \tag{10}$$

$$\frac{\partial C_{\mathrm{cs}}}{\partial t} = -\kappa_r \left(1-\alpha_c\right) C_{\mathrm{cs}}, \tag{11}$$

where κ_r is the rate of the releasing from chloride salts to chloride ions, and we regard it as the same with the rate of concrete binding which is $1 \times 10^{-5}\,\mathrm{sec}^{-1}$.

Due to the fact that carbonation has an obvious effect on porosity of concrete and pore structure, the chloride diffusion process is combined with the process of carbonation. Hence, the governing equation can be given by

$$\begin{aligned} D_{\mathrm{fc}}^{\mathrm{car}} &= D_{\mathrm{fc}} f_{\mathrm{p}}(\Omega, \delta), \\ D_{\mathrm{h}}^{\mathrm{car}} &= D_{\mathrm{h}} f_{\mathrm{p}}(\Omega, \delta), \end{aligned} \tag{12}$$

where D_{fc} and D_{h} are the initial diffusion coefficients of chloride and moisture, $D_{\mathrm{fc}}^{\mathrm{car}}$ and $D_{\mathrm{h}}^{\mathrm{car}}$ are the diffusion coefficients of chloride and moisture with the consideration of carbonation, and $f_{\mathrm{p}}(\Omega, \delta)$ is the function depicting the effect of change of pore structures due to carbonation. According to literature [33, 34], the most significant features that influence ions transfer process are Ω tortuosity and δ constrictivity, which can be determined in literature [33, 34]. Besides, function depicting the carbonation effect on chloride diffusion can be given by

$$f_{\mathrm{p}}(\Omega, \delta) = \frac{\delta}{\delta_0} \frac{\Omega_0}{\Omega}, \tag{13}$$

where Ω_0 is the initial tortuosity and δ_0 is the initial constrictivity.

2.3. Transport of Moisture. Based on sections mentioned previously, moisture has a significant impact on the diffusion process of carbon dioxide and chloride, so the study about the transfer of moisture is of great importance. The governing equation can be given by

$$\frac{\partial \phi_{\mathrm{we}}}{\partial h} \frac{\partial h}{\partial t} + \nabla \cdot \mathbf{J}_{\mathrm{h}} = I_{\mathrm{we}}, \tag{14}$$

$$I_{\mathrm{we}} = \frac{\kappa I_{\mathrm{ch}} M\left(\mathrm{H_2O}\right)}{\rho_w}, \tag{15}$$

where $\mathbf{J}_{\mathrm{h}}$ is the flux of moisture, I_{we} is the water production because of the carbonation process, and κ is the correction factor which is taken as 1 for the sake of simplicity.

2.4. Corrosion Initiation. When ignoring the impact of carbonation, the corrosion of steel reinforcement begins once chloride content reaches a certain threshold. However, the carbonation can reduce the threshold. According to literature [35, 36], the threshold varying with the carbonation degree can be given by

$$C_{\mathrm{th}}^{\mathrm{car}} = \frac{C_{\mathrm{ch,d}}}{\left[C_{\mathrm{ch,d}}\right]_0} C_{\mathrm{th}}, \tag{16}$$

where $[C_{\mathrm{ch,d}}]_0$ is the molar concentration of dissolved calcium hydroxide without considering carbonation, C_{th} is the chloride threshold without considering carbonation, and $C_{\mathrm{ch,d}}$ is the molar concentration of dissolved calcium hydroxide.

Once the pH value is lower than 11 [21], the depassivation process initiates. Hence, the pH value can be calculated based on the content of dissolved calcium hydroxide:

$$\mathrm{pH} = \begin{cases} 14 + \log\left(2 \times 10^{-3} C_{\mathrm{ch,d}}\right), & C_{\mathrm{ch,d}} \geq 1 \times 10^{-3}, \\ 8.3, & \text{otherwise.} \end{cases} \tag{17}$$

3. Mechanical Damage Process

3.1. Formula of Corrosion Rate on Steel Reinforcement. There are various models of the steel corrosion rate, most of which do not consider the change of the corrosion rate after the concrete cover is cracked. In this article, a comprehensive forecast model mentioned in literature [37] is employed. It proposes methods to determine the parameters and simplify equations. It also takes full account of the change of the corrosion rate before and after cracking of the concrete surface.

The model divides steel corrosion into two situations: high humidity (relative humidity greater than 90%) and general humidity (relative humidity less than 90%). Under high humidity conditions, the corrosion rate of reinforcement steel is controlled by the diffusion of cathode oxygen, which follows Fick's first law. As for the RC structure in marine environments, their environment conditions match high humidity conditions. Before the longitudinal cracks penetrate the concrete cover, the corrosion current density of the steel reinforcement can be expressed by

$$I_0|_{t \leq t_1} = \alpha \cdot n_c \cdot F D_{\mathrm{c0}} \frac{L_c \left[\mathrm{O_2}\right]^0}{\pi d c}, \tag{18}$$

$$D_{\mathrm{c0}} = 2.183 \cdot 10^{-9} (W/C)^{2.346} T_c^{0.423} H_w^{-3.247}, \tag{19}$$

where D_{c0} is the initial O_2 diffusion coefficient in the concrete cover in high humidity environment; α is the O_2 solubility in water, and the value is generally 0.025 – 0.028; $n_{\mathrm{c}} = 4$ is the number of electrons for the cathodic reaction unit of oxygen; $F = 96500$ C/mol is the Faraday constant, $[\mathrm{O_2}]^0$ is O_2 concentration in the external environment, and the value is 8.67 mol/m^3 in normal atmospheric conditions; d is the diameter of the steel reinforcement; c is the thickness of the concrete cover; W/C is the concrete water-cement ratio; T_c is the ambient temperature; H_w is environmental relative humidity; t_1 is the time from the corrosion process initiating to concrete surface cracking; and L_{c} is the length of oxygen permeable range on steel reinforcement.

The length range of the central rebars where oxygen is permeable can be defined as

$$L_c = \begin{cases} L_{cm} = (s + 2r), & s \le 2c, \\ L_{cm} = (2c + 2r), & s > 2c, \end{cases} \tag{20}$$

where r is the radius of steel reinforcement (m) and s is the spacing of longitudinal steel reinforcement.

The length range of the angle rebars where oxygen is permeable can be defined as

$$L_c = \begin{cases} L_{ce} = (s + 2c + 4r), & s \le 2c, \\ L_{ce} = (4c + 4r), & s > 2c, \end{cases} \tag{21}$$

After the longitudinal cracks penetrate the concrete cover, the corrosion rate is mainly controlled by macrocell corrosion due to differences in oxygen concentration [32, 38]. Hence, the corrosion rate is related to the width of longitudinal cracks. According to the experimental data [39], the corrosion current density along the longitudinal cracks is given by

$$I_0|_{t \le t_1} = (4.65w + 0.95)^{0.55} \cdot I_0|_{t \le t_1}, \tag{22}$$

where w is the width of the corrosion crack.

Literature [40] shows that the corrosion rate of steel reinforcement first decreases. Then, the corrosion rate reaches a steady state before cracking of the concrete surface. After the cracking of the concrete cover, the corrosion rate first increases rapidly and then reaches a stationary state.

In order to simplify the formula, based on the experimental results, the corrosion rate when the crack width is 0.2 mm is adopted. It is regarded as the average corrosion rate after the cracking of the concrete surface. In the analysis of rust swelling and cracking, we assume that when the crack width reaches 0.2 mm, the crack will completely penetrate through the concrete cover. When the crack width reaches 0.8 mm, the concrete cover will be completely destroyed [40].

In the general humidity environment, the corrosion rate of steel reinforcement is controlled by factors such as the O_2 diffusion rate and the concrete resistivity. For the inland RC structures, most of them are in the general humidity environment. Before the longitudinal cracks penetrate the concrete cover, the corrosion current density of the steel reinforcement is given by

$$\begin{aligned} I_0|_{t \le t_1} &= \frac{\Delta E I_a}{\Delta E + (I_a \rho_{con}/300r)}, \\ \Delta E &= 1.27 + 1.58 \times 10^{-3} T_c, \\ I_a &= \alpha \cdot n_c \cdot F \cdot D_{c1} \cdot \frac{L_c [O_2]^0}{\pi dc}, \\ D_{cl} &= 2.578 \times 10^{-9} \left(\frac{W}{C}\right)^{2.346} T_c^{0.423}, \\ \rho_{con} &= \left[k \cdot (C_{fc} - 1.8) + 100 (H_w - 1)^2 + 40\right] \\ &\quad \cdot \exp\left[3000 \left(\frac{1}{T_c + 273} - \frac{1}{298}\right)\right], \end{aligned} \tag{23}$$

where ΔE is the voltage of steel reinforcement; I_a is the standard current density; D_{cl} is the initial value of O_2 diffusion coefficient of the concrete cover before corrosion, in general humidity environment; ρ_{con} is the resistivity of concrete; k is a coefficient associated with the water-cement ratio W/C, when W/C = 0.3~0.4, $k = -11.1$, and W/C = 0.5~0.6.

When longitudinal cracks penetrate the concrete cover, the corrosion current density of the steel reinforcement can be calculated by (5). According to Faraday's law, from the initiation of corrosion to t time, the loss of corrosion of steel reinforcement can be defined as

$$\begin{aligned} m_s &= \frac{28 S_a}{F} \int_0^t I_0 \, dt, \\ S_a + S_c &= A_s = 2\pi r, \end{aligned} \tag{24}$$

where S_a is the corrosion area of the anode zone, S_c is the corrosion area of the cathode zone, and A_s is the total corrosion area. The ratio of anodic and cathodic corrosion areas can be determined as follows [41, 42]:

$$\frac{S_c}{S_a} = \begin{cases} -2.82\text{PS} + 161.9, & \text{PS} < 59, \\ 1.78 + 1.14 \exp\left[\dfrac{-(\text{PS} - 59.5)}{0.838}\right] + 0.945 \exp\left[\dfrac{-(\text{PS} - 59.2)}{10.672}\right], & 59 \le \text{PS} < 75, \\ 2, & \text{PS} \ge 75, \end{cases} \tag{25}$$

where PS is the concrete pore moisture content.

In real cases, the temperature T_c and humidity H_w vary with time, so the current density I_0 is related to the time t. In order to simplify the calculation, the mean value of temperature and humidity is taken in this paper, and the change of time is not considered. So the current density is independent of time.

3.2. Formula of Corrosion Expanding Displacement. Currently, there are mainly three models depicting corrosion distribution on the cross-sectional area, namely, the linearly decreased model [43], ellipse model [44, 45], and Gaussian model [22, 46], respectively. According to experimental data, the ellipse model and Gaussian model have relatively higher correspondence with the corrosion distribution pattern in real cases.

Exponential formula and elliptical formula depicting the corrosion distribution pattern are given in literature [47, 48]. By comparison, there are no distinct differences between experimental results and these two models. Here, given difficulties in determining variables and integral calculation of the exponential formula, the ellipse model is employed in this article.

According to the displacement distribution theory of the elliptical model, distribution of the corrosion product on cross section is shown in Figure 1. Hence, the thickness of the corrosion layer at any polar angle can be calculated by the following equations: before cracks penetrating concrete cover,

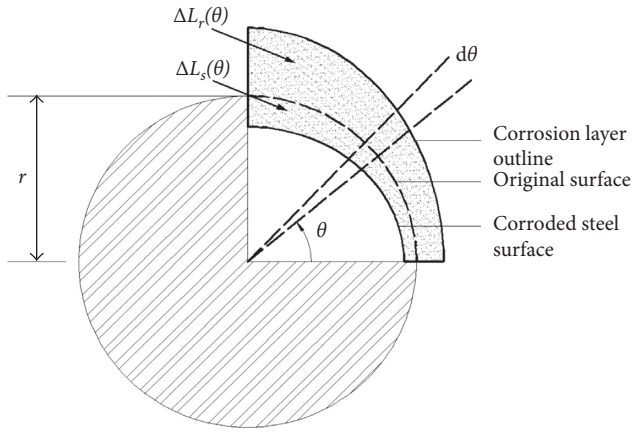

Figure 1: Oval rust expansion displacement theoretical model.

$$\Delta L_S(\theta)|_{t\le t_1} = \begin{cases} r - \dfrac{r(r-d_a)}{\sqrt{(r-d_a)^2\cos^2\theta + r^2\sin^2\theta}}, & (0 \le \theta \le \pi), \\ 0, & (\pi < \theta \le 2\pi), \end{cases} \tag{26}$$

where d_a is the maximum thickness of the corrosion layer. After cracks penetrating concrete cover,

$$\Delta L_S(\theta)|_{t\le t_1} = \begin{cases} r - \dfrac{r(r-d_a+d_b)}{\sqrt{(r-d_a+d_b)^2\cos^2\theta + r^2\sin^2\theta}}, & (0 \le \theta \le \pi), \\ d_b, & (\pi < \theta \le 2\pi), \end{cases} \tag{27}$$

where d_b is the thickness of the corrosion layer at the side far away from the cover, and it can be defined as $d_b = m \cdot d_a$ and m is a fitting parameter. Through comparison between experimental results of [42] and [49], we regard m as 0.25.

Because the diffusion rate of Fe^{2+} and Fe^{3+} is far less than that of OH^- we assume that the corrosion product all occurred at the anode area of rebars. Therefore, the thickness of the corrosion product on the original reinforcement surface can be calculated by the following equations: before cracks penetrating concrete cover,

$$\Delta L_S(\theta)|_{t\le t_1} = \begin{cases} \dfrac{r[r+(\beta-1)d_a]}{\sqrt{[r+(\beta-1)d_a]^2\cos^2\theta + r^2\sin^2\theta}} - r, & (0 \le \theta \le \pi), \\ 0, & (\pi < \theta \le 2\pi), \end{cases} \tag{28}$$

after cracks penetrating concrete cover,

$$\Delta L_S(\theta)|_{t\le t_1} = \begin{cases} \dfrac{r[r+(\beta-1)(d_a-d_b)]}{\sqrt{[r+(\beta-1)(d_a-d_b)]^2\cos^2\theta + r^2\sin^2\theta}} + (\beta-1)d_b - r, & (0 \le \theta \le \pi), \\ (\beta-1)d_b, & (\pi < \theta \le 2\pi), \end{cases} \tag{29}$$

where β is the volume expansion ratio of the corrosion product, which varies with different corrosion products. Here, due to corrosion products being regarded as $Fe(OH)_3$, we adopt 4.20 as the volume expansion ratio.

Because the only unknown parameter is d_a, the relationship between d_a and m_s can be drawn by following formulae: before cracks penetrating concrete cover,

$$\frac{m_s|_{t\le t_1}}{\rho_s} = \int_0^{\pi} \Delta L_s(\theta)|_{t\le t_1} \cdot r \cdot d\theta = \frac{\pi}{2} \cdot r \cdot d_a, \tag{30}$$

after cracks penetrating concrete cover,

$$\begin{aligned} \frac{m_s|_{t\le t_1} + m_s|_{t\le t_1}}{\rho_s} &= \int_0^{\pi} \Delta L_s(\theta)|_{t\le t_1} \cdot r \cdot d\theta \\ &\quad + \int_{\pi}^{2\pi} \Delta L_s(\theta)|_{t\le t_1} \cdot r \cdot d\theta \\ &= \left(\frac{3}{2} \cdot m + \frac{1}{2}\right) \cdot \pi \cdot r \cdot d_a, \end{aligned} \tag{31}$$

where ρ_s is the density of steel reinforcement. Substituting d_s into (13)–(16), we can get the formula depicting relationship between $\Delta L_s(\theta)$, $\Delta L_r(\theta)$, and time t.

As for the corner rebars, Zhao et al. presumed that it can be derived by deflecting the corrosion displacement model of central rebars. By experimental results comparison, when there is little difference between concrete cover thicknesses of the two directions, this model can simulate the corrosion distribution pattern of corner rebars with little errors. When the cover of the side direction is far thicker than that of the forward direction, this model tends to be irrational with lots of errors, which cannot be applied. Therefore, when corrosion occurs on the side near the concrete cover, the corrosion expansive displacement can be calculated by superimposing displacements at different angles. Then, the corrosion expansive displacement is obtained.

Compared with the radius of steel reinforcement, the corrosion layer is thinner. The elastic modulus of the corrosion layer is about 100 MPa. It is far less than that of concrete. Consequently, we simply regard corrosion displacement expansion thickness $\Delta L_r(\theta)$ as the displacement of the concrete in the radial direction. In this paper, we adopt an elliptical model to depict the corrosion distribution pattern. We discretize expansion thickness of corrosion $\Delta L_r(\theta)$ and corrosion thickness $\Delta L_s(\theta)$ along the polar angle. For each microelement $d\theta$, we can assume that it complies the formulae of the ring structure, as shown in Figure 2. In Figure 2, $u_c(\theta)$ is the radial direction displacement of concrete; $u_r(\theta)$ is the displacement of corrosion products due to pressure of concrete; and $\Delta L_r^{\text{eff}}(\theta)$ is the expansive thickness of the equivalent corrosion products on the original surface of reinforcement, which can be drawn as

$$\Delta L_r^{\text{eff}}(\theta) = \Delta L_r(\theta) - \delta_0. \tag{32}$$

According to previous studies, corrosion products can diffuse in concrete internal void and the interface between reinforcement and concrete. Hence, when corrosion thickness is less than a certain constant δ_0, there is no expansive pressure on the concrete cover. In the calculation,

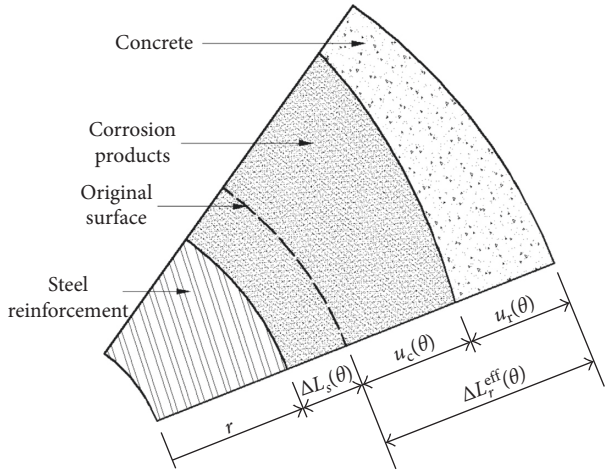

Figure 2: Rust expansion displacement relationship diagram.

we adopt δ_0 as 20 μm [50], and $\Delta L_r^{\text{eff}}(\theta)$ equals 0 when $\Delta L_r(\theta)$ is less than δ_0.

As shown in Figure 2, we can draw the relational expression between $u_r(\theta)$ and $u_c(\theta)$ as follows:

$$u_r(\theta) + u_c(\theta) = \Delta L_r^{\text{eff}}(\theta). \tag{33}$$

Formula depicting the radial direction displacement of concrete is

$$u_c(\theta) = \frac{1+\nu_c}{E_c} \cdot \frac{q(\theta) r^3}{C_d^2 - r^2} \left(1 - 2\nu_c + \frac{C_d^2}{r^2}\right), \tag{34}$$

where C_d is the thickness of the concrete cover, E_c is the elastic modulus of concrete, ν_c is the Poisson ratio of concrete, and $q(\theta)$ is the radial pressure on contact interface between concrete and corrosion.

Formula depicting radial direction displacement of corrosion can be given by

$$u_r(\theta) = \frac{q(\theta)(1+\nu_r)}{E_r} \left(\Delta L_r^{\text{eff}}(\theta) + \Delta L_s(\theta)\right), \tag{35}$$

where E_r is the elastic modulus of the corrosion product and ν_r is the Poisson ratio of corrosion.

Substituting (20) and (19) into (18), we can get a comprehensive formula about $u_c(\theta)$:

$$u_c(\theta) = \frac{\Delta L_r^{\text{eff}}(\theta)}{\left[1 + \left(\left(u_c E_c \left(C_d^2 - r^2\right) \cdot (1+\nu_r) \cdot \left(\Delta L_r^{\text{eff}}(\theta) + \Delta L_s(\theta)\right)\right) / \left(E_r r^3 \cdot (1+\nu_c) \cdot \left(1 - 2\nu_c + \left(C_d^2/r^2\right)\right)\right)\right)\right]}. \tag{36}$$

3.3. Definition of Concrete Cracking and Initial Cracks Setting. After obtaining the radial displacement of the concrete layer, the development of cracks in concrete can be predicted by the fictitious crack model in expanding finite element method (XFEM). Here, the material is supposed to be linear elastic. Once the maximum tensile stress reaches the tensile strength of concrete, f_t, cracks initiate and develop. The crack expansion is always perpendicular to the maximum tensile stress direction.

Note that there is a virtual fracture area behind the tip of the crack. In this area, the stress of the surface area is not 0, whereas the stress is a function monotonically decreasing with the crack opening displacement. This is called material softening. The softening curve of the concrete material is controlled by its fracture energy G_f. When the crack opening displacement reaches a threshold, the stress of the surface area decreases to 0. Therefore, this point is the tip of the crack in real cases, so the crack surface behind this point is called free surface.

In the XFEM model, initial cracks need to be set in advance. Then, the development of cracks can be simulated more accurately. In our model, 8 initial cracks are set uniformly along the interaction surface between the steel reinforcement and the concrete. After the beginning of calculation, 2 or 3 fastest-developed main cracks are selected, and they can develop freely. Then, under the element birth and death control, the initial cracks are closed when the changes are not obvious, for the sake of simplicity.

4. Experimental Verification

4.1. Verification of the Influence of Carbonation on the Chloride Penetration. Based on the numerical model established by the theoretical model mentioned above, the transfer process of chloride in fully carbonized concrete can be stimulated. In most cases, the chloride transfer process and carbonation alternate. This more complicated situation can also be stimulated precisely. In the alternate experiment of carbonation and chloride penetration, concrete specimens are placed in an accelerated carbonation tank and the chloride tank alternately. Hence, the transfer process of chloride ions with carbonation can be determined. Because the alternate experiment is very close to the actual use of the RC structure, we employ alternate experiment testing data for the verification.

In literature [28], the influence of carbonation on the chloride transport properties in ordinary Portland concrete and fly ash concrete was tested, respectively. Concrete specimens were immersed in 5% NaCl solution for one week at the temperature of 25°C. In the next week, they are placed in an accelerated carbonation tank. In the carbonation tank, the temperature is 25°C, and humidity is 60%, and carbon dioxide content is 10%. A 56-week circulation is adopted.

As for the coupled effect of carbonation and chloride ions, the comparison of results obtained by the experiment and numerical model is shown in Figure 3. It is obvious that carbonation accelerates the chloride ions transfer rate significantly, and the chloride ions content is increased.

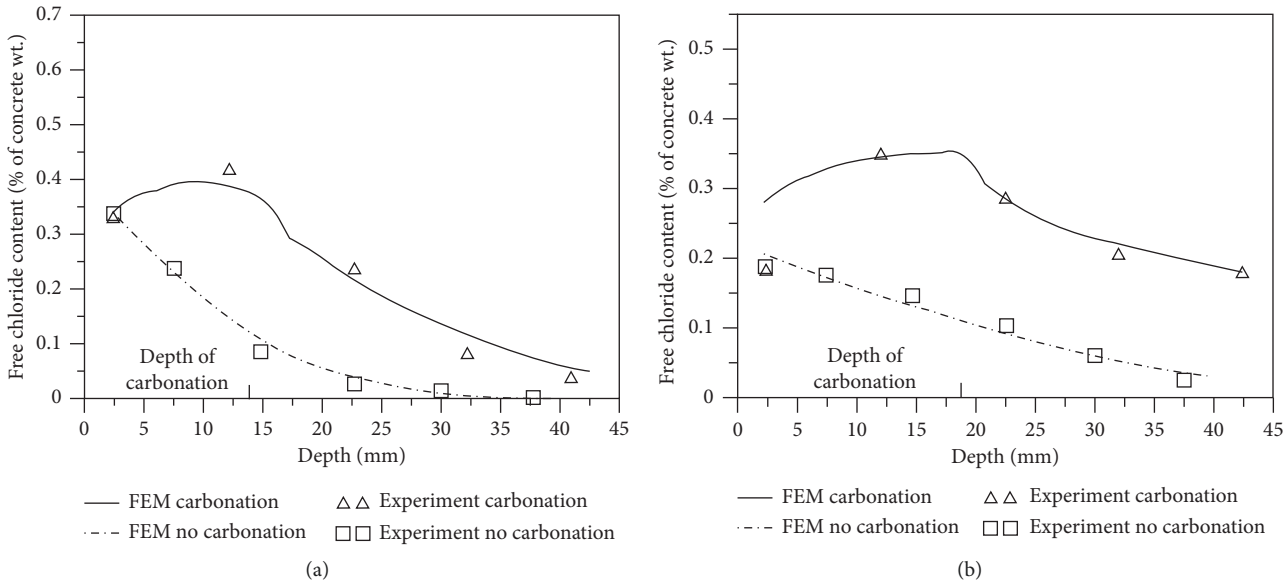

Figure 3: Concentrations of free chloride ions with respect to the depth of the specimen for (a) fly ash concrete and (b) Portland concrete.

Besides, the reaction between carbon dioxide and Friedel salt can cause the free chloride ions release effect. It can lead to an obvious jump of free chloride ions content at the edge of carbonation front (the interface between carbonized area and noncarbonized area). Because there is no enough time for the released free chloride ions to spread to two sides increasingly more free chloride ions accumulate at the reaction area. This phenomenon was precisely depicted by our numerical model. The numerical results agree well with the test results. Consequently, it shows good accuracy of the coupled mathematical model of carbonation and chloride ion penetration possesses.

4.2. Verification of the Mechanical Damage Model. Here, to determine the accuracy of the mechanical damage model, we compare the results of the numerical model and the experiment conducted in literature [51]. In the experiment, the cross section of specimens is $200 \times 200\ \text{mm}^2$. In the first case, there is a steel reinforcement of 12 mm diameter with a 20 mm concrete cover; in the second case, there is a steel reinforcement of 16 mm with a 35 mm concrete cover. The embedment length of rebars is 180 mm, while the rest part is protected by a plastic sleeve. In two cases, each longitudinal side is saturated by 1% chloride solution for 1 minute and 3 minutes, respectively. Additionally, there is a potential of +500 mV NHE to accelerate the corrosion process. As shown in Figure 4, it can be found that results derived from our proposed model agree extremely well with the experiment results.

5. Illustrative Example

5.1. Problem Description and Procedure of Numerical Implementation. Here, a steel-reinforced concrete beam is used for the parametric study. The thickness of the concrete cover is 27 mm, the diameter of rebars is 16 mm, and the space between each steel reinforcement is 135 mm. Its cross section is shown in Figure 5. There is confinement on the Y direction on the lower boundary of the beam. The left and right sides are confined on the X direction. Parameters used in the numerical example are listed in Table 1.

To determine the radial displacement variation of concrete along time order, we have to first determine the time when reaching the threshold of corrosion amount. In this paper, t_1 is regarded as the time when the cracks width reaches 0.2 mm. t_2 is regarded as the time when cracks reache 0.8 mm. From (11), it is notable that the corrosion product is in direct proportion to time, so the process to calculate t_1 (t_2) can be divided in to 5 steps:

(1) If we assume a time period t, based on the MATLAB and theoretical formulae, we can calculate the corrosion expansive displacement distribution at t moment. Then, the rust expansion displacement is discretized into 24 points along the circumferential direction of the steel bar. Each point is applied on the surface of rebars.

(2) With the application of XFEM of ABAQUS, we simulate the crack development under corrosion expansive displacement. In addition, the calculation of the crack width can be achieved. Therefore, we can determine time steps when the crack width reaches 0.2 mm and 0.8 mm, respectively.

(3) According to the linear relationship between corrosion amount and time, we can determine the corrosion expansive displacement at each time step.

(4) Based on MATLAB, the corresponding time of rust expansion displacement distribution can be deduced by the theoretical formula, which is the approximant value of t_1 (t_2).

(5) Repeating step (1)–step (4), we can get the more accurate value of t_1 and t_2.

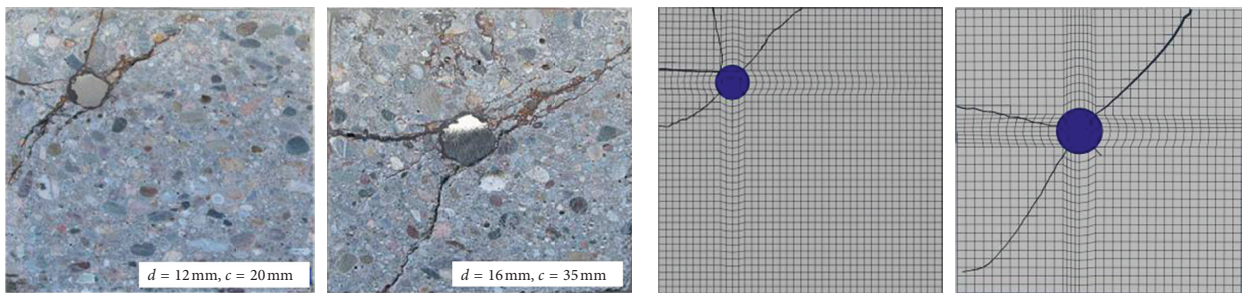

(a) (b)

Figure 4: Corrosion-induced crack pattern of concrete in (a) Ozbolt's experiment and (b) our model's simulation.

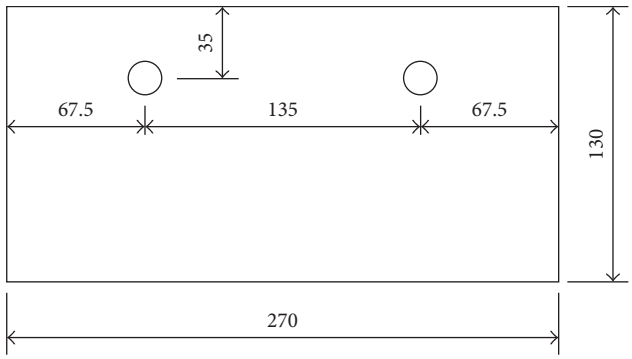

Figure 5: Cross-sectional geometry of the reinforced concrete beam (mm).

Table 1: Material parameters summary.

Parameter	Value
Elastic modulus of concrete, E_c (Pa)	3.25×10^{10}
Poisson's ratio of concrete, ν_c	0.20
Elastic modulus of corrosion products, E_r (Pa)	100×10^6
Poisson's ratio of corrosion products, ν_r	0.49
Density of steel, ρ_s (kg·m^{-3})	7800
Water-cement ratio, W/C	0.35
Environment temperature, T_c (°C)	5
Environment humidity, H_w	0.9 (0.75)
Water content of concrete, PS (%)	35
Chloride content, C_{fc} (%)	0.2
Fracture energy, (G/J·m^{-2})	140
Concrete tensile strength, f_t (N·m^{-2})	1.71×10^6

5.2. Radial Displacement Curve of Concrete under Corrosion Expansion Pressure. Figures 6 and 7 show the radial displacement of concrete $u_c(\theta)$ under corrosion expansive pressure at different time periods, when the environmental relative humidity is 90% and 75%, respectively. According to Figures 6(a) and 6(b), the corrosion before the cracking of the concrete surface mainly distributes on the half surface facing the side of the protective layer. The thickness of the corrosion layer turns smaller when it is farther from the concrete surface. Note that there is no corrosion on the half cross section which is far away from the protective layer. On the contrary, situation after cracks penetrating the concrete cover is completely different. Although less than the corrosion product on the surface close to the protective layer, corrosion appears on the surface far away from the protective layer. Additionally, under the same corrosion expansive pressure, when the structure is in high humidity, it takes less time to reach the same radial displacement of concrete. It suggests that high humidity environment contributes a lot to the corrosion process.

5.3. Crack Development under Nonuniform Corrosion Expanding Pressure. Having determined the distribution curve of radial displacement of concrete $u_c(\theta)$ along the circumferential direction of steel reinforcement, we input them as displacement load into the XFEM model of ABAQUS. Then, crack development of the concrete cover is obtained. It is more explicit and intuitional for researchers to study and analyze crack development.

Under the assumption that the environmental relative humidity is 90%, we analyze the crack development changing with time, as shown in Figure 5. Through calculation, when the corrosion expansive displacement of rebars $u_c(\theta)$ reaches what is shown in Figure 6(a) (the maximum of displacement is 0.365 mm), the surface of concrete is cracked (the crack width reaches 0.2 mm), and t_1 is 152 d. When the corrosion expansive displacement of rebars reaches Figure 6(b) (the maximum of displacement is 1.130 mm), the concrete cover is completely deteriorated (the crack width reaches 0.8 mm), and t_2 is 642 d. Development of corrosion-induced cracks is shown in Figure 8. It demonstrates that the concrete cover is cracked by corrosion-induced cracks after 5 months since the depassivation process. With the development of cracks, the concrete cover will be completely destroyed 16 months later. Consequently, as for the structure mentioned in this paper, anticorrosion methods and strengthening measures are required within 16 months when the cracks are discovered on the concrete cover.

5.4. Comparison of Crack Development under Uniform and Nonuniform Corrosion Process. Numerous studies have verified that the corrosion product distribution is nonuniform in actual cases. As mentioned previously, most researches focusing on crack development of concrete are

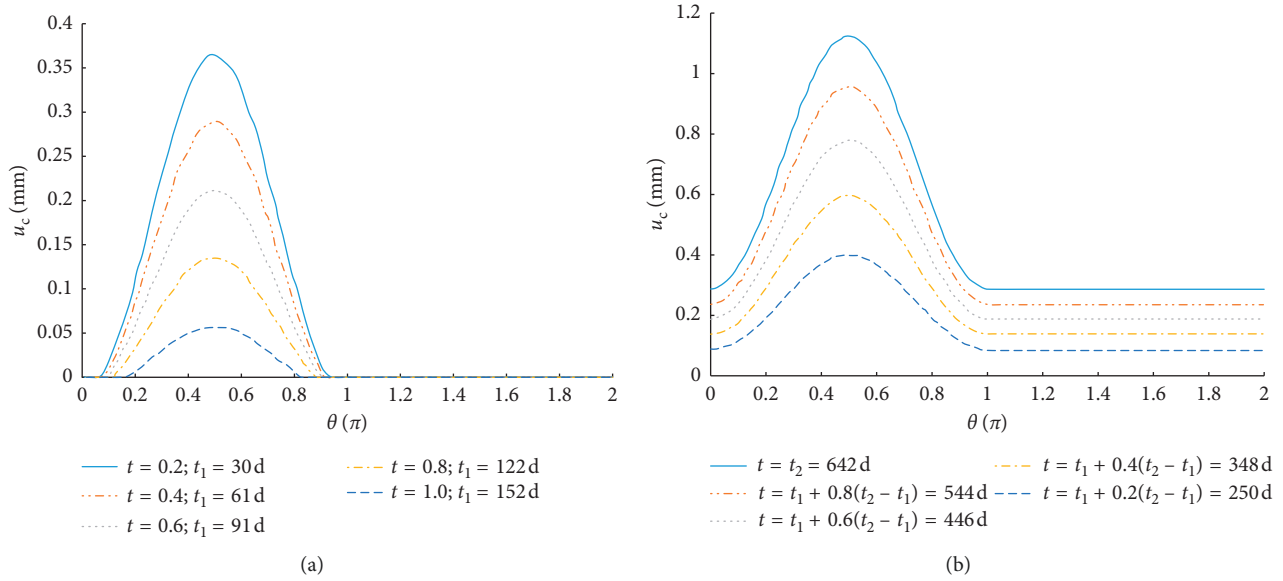

Figure 6: Distribution of concrete radial displacement $u_c(\theta)$ before (a) and after (b) cracks penetration when $H_w = 0.9$.

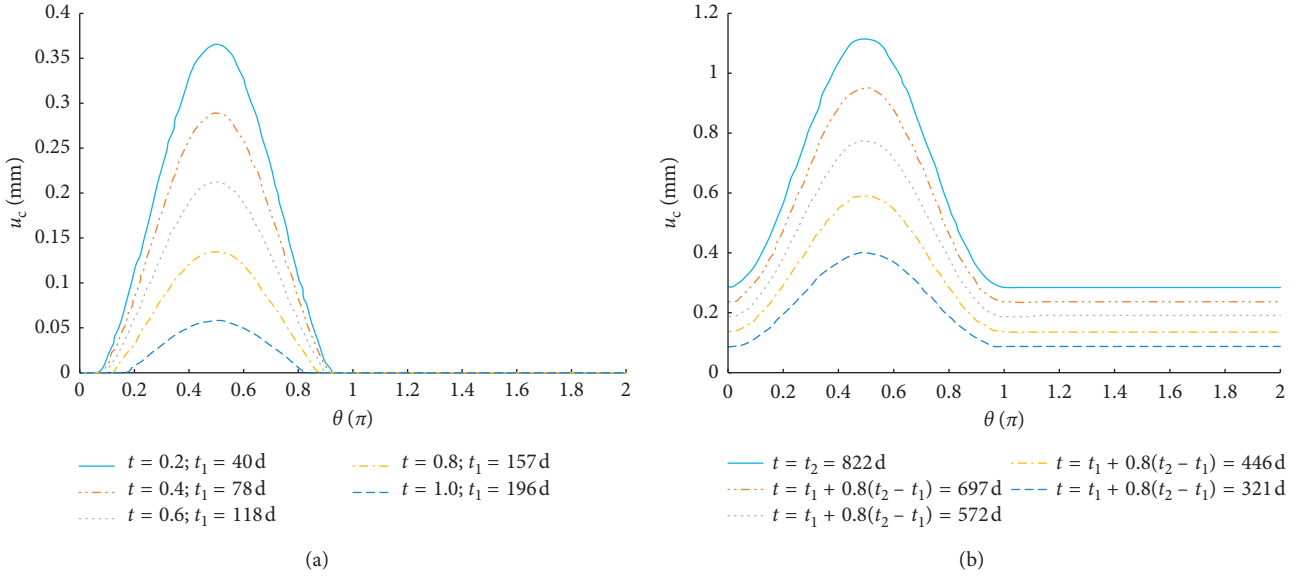

Figure 7: Distribution of concrete radial displacement $u_c(\theta)$ before (a) and after (b) cracks penetration when $H_w = 0.9$.

based on the uniform pattern. Therefore, it has been attached to the utmost significance to compare differences in crack pattern, initiation process, and cracking time. We analyze the structure shown in Figure 5 on the basis of the uniform distribution model, and the crack expanding process is shown in Figure 9.

Comparing the crack development figures of uniform corrosion distribution and nonuniform corrosion distribution, respectively, we can find distinct differences in terms of the crack pattern. The cracking process of the uniform corrosion pattern is obviously slower than that of nonuniform corrosion pattern. Under uniform distribution, it takes 19 months for cracks to penetrate the concrete cover under the uniform corrosion pattern. Then, it takes 46 months to entirely destroy the concrete layer. Therefore, if employing uniform distribution pattern in the actual cases, the load capacity and service-life of structures will be severely overestimated, which can lead to undesirable consequences.

6. Conclusion

(1) The transport of various harmful masses is described by a series of mathematical formulae, including chloride ions, carbon dioxide, and moisture. The combined effect of carbonation and chloride ingress is also studied.

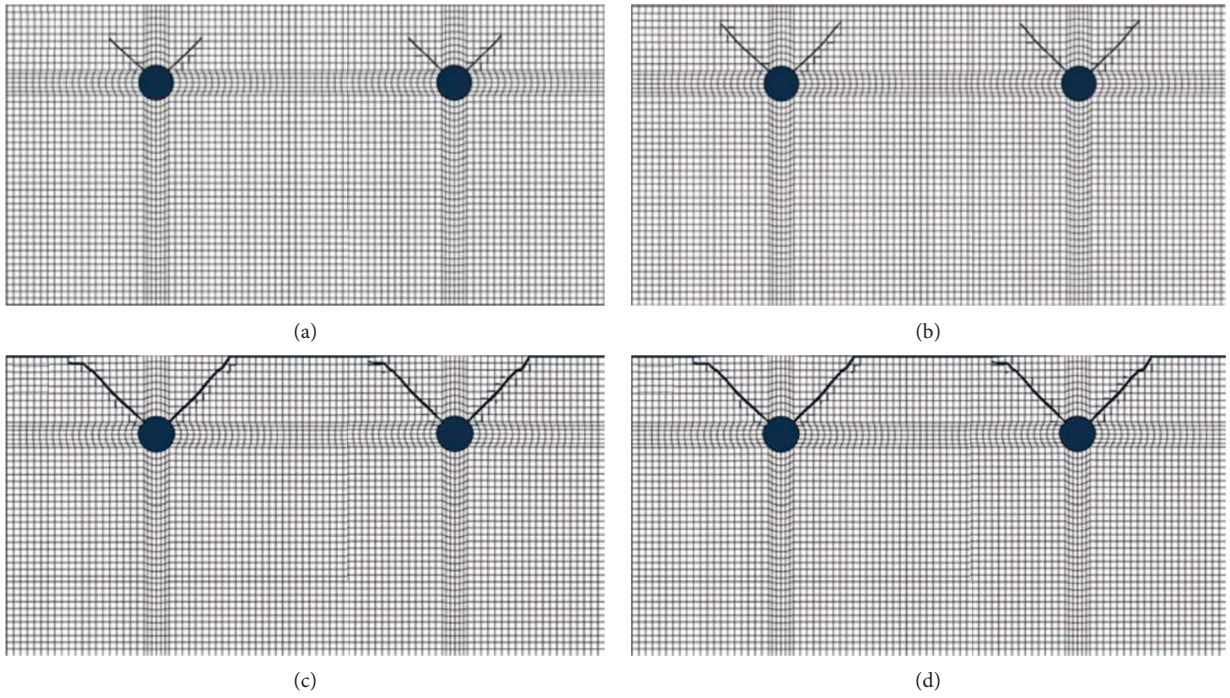

Figure 8: Concrete cover-cracking process when $t = 19$ d (a), 37 d (b), 152 d (c), and 642 d (d) under nonuniform distribution of corrosion products.

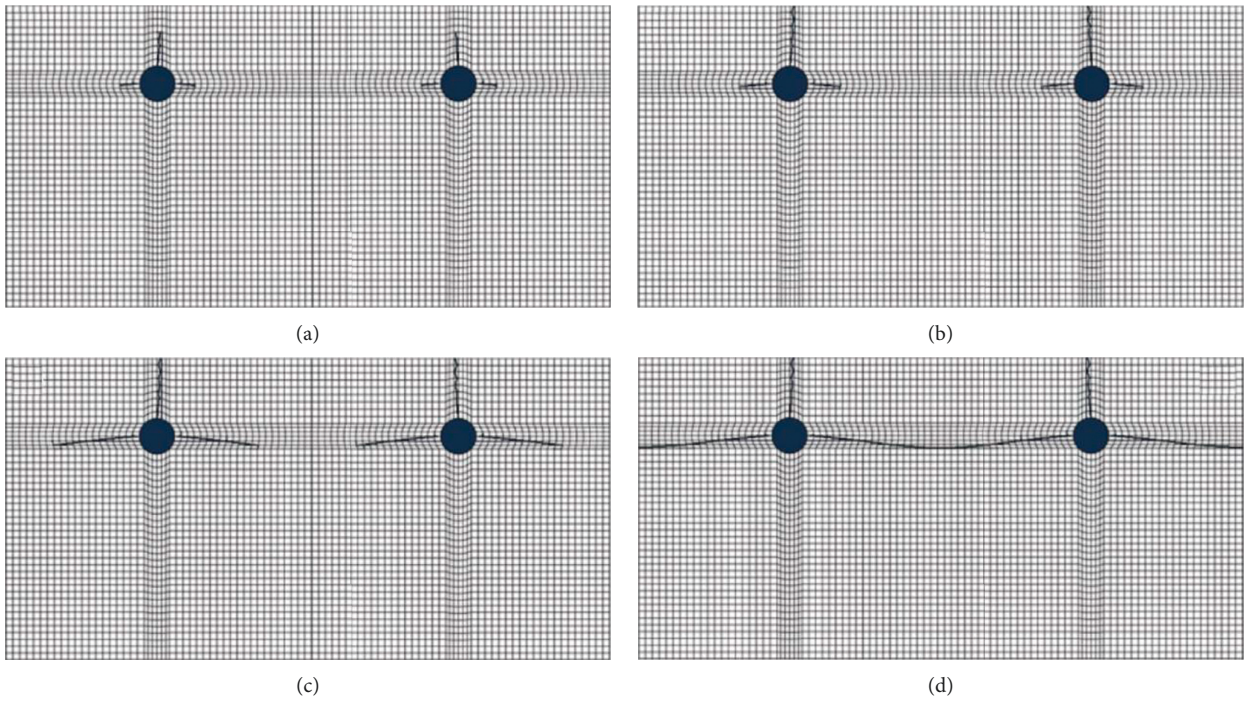

Figure 9: Concrete cover-cracking process when $t = 77$ d (a), 172 d (b), 286 d (c), and 558 d (d) under uniform distribution of corrosion products.

(2) The expansive displacement of concrete at different time periods of corrosion can be obtained directly by our proposed mathematical model.

(3) By linking ABAQUS with MATLAB, the prediction for the evolution of corrosion-induced cracking damage for the concrete cover can be numerically implemented.

(4) Various experimental data were compared with the results obtained by our model and verified its accuracy.

(5) The numerical results of an illustrative example show that there are significant differences in the crack pattern and crack development between the uniform and nonuniform corrosion. If the uniform distribution theory is used to guide actual projects, the carrying capacity of the structure will be seriously overestimated.

Data Availability

The datasets generated during and/or analyzed during the current study are available from the corresponding author on reasonable request.

Conflicts of Interest

The authors declare that they have no conflicts of interest.

Acknowledgments

This work was financially supported by the Natural Science Foundation of Shandong Province (no. ZR2018BEE044) and the National Natural Science Foundation of China (nos. 51678208 and 51678199). The authors also appreciate the support of the Major Training Program of Natural Science Research Innovation Foundation of Harbin Institute of Technology (HIT.NSRIF.201709) and the Major Program of Mutual Foundation of Weihai City with Harbin Institute of Technology (Weihai).

References

[1] S. Guzmán, J. C. Gálvez, and J. M. Sancho, "Modelling of corrosion-induced cover cracking in reinforced concrete by an embedded cohesive crack finite element," *Engineering Fracture Mechanics*, vol. 93, pp. 92–107, 2012.

[2] S. Muthulingam and B. N. Rao, "Non-uniform corrosion states of rebar in concrete under chloride environment," *Corrosion Science*, vol. 93, pp. 267–282, 2015.

[3] X. J. Zhu and G. Zi, "Probabilistic analysis of reinforcement corrosion due to the combined action of carbonation and chloride ingress in concrete," *Construction and Building Materials*, vol. 124, pp. 667–680, 2016.

[4] X. J. Zhu, G. Zi, Z. F. Cao et al., "Combined effect of carbonation and chloride ingress in concrete," *Construction and Building Materials*, vol. 110, pp. 369–380, 2016.

[5] R. J. Zhang, A. Castel, and R. François, "The corrosion pattern of reinforcement and its influence on serviceability of reinforced concrete members in chloride environment,," *Cement and Concrete Research*, vol. 39, no. 11, pp. 1077–1086, 2009.

[6] J. Ožbolt, F. Oršanić, G. Balabanić et al., "Modeling damage in concrete caused by corrosion of reinforcement: coupled 3D FE model," *International Journal of Fracture*, vol. 178, no. 1-2, pp. 233–244, 2012.

[7] H. L. Ye, N. G. Jin, C. Q. Fu et al., "Rust distribution and corrosion-induced cracking patterns of corner-located rebar in concrete cover," *Construction and Building Materials*, vol. 156, pp. 684–691, 2017.

[8] Z. P. Bažant, "Physical model for steel corrosion in concrete sea structures theory," *Journal of the Structural Division*, vol. 105, pp. 1137–1153, 1979.

[9] Y. X. Zhao, J. Yu, Y. Y. Wu et al., "Critical thickness of rust layer at inner and out surface cracking of concrete cover in reinforced concrete structures," *Corrosion Science*, vol. 59, pp. 316–323, 2012.

[10] C. Alonso, C. Andrade, J. Rodriguez et al., "Factors controlling cracking of concrete affected by reinforcement corrosion," *Materials & Structures*, vol. 31, no. 211, pp. 435–441, 1998.

[11] C. Cao, M. M. S. Cheung, and B. Y. B. Chan, "Modelling of interaction between corrosion-induced concrete cover crack and steel corrosion rate," *Corrosion Science*, vol. 69, pp. 97–109, 2013.

[12] L. Chernin and D. V. Val, "Prediction of corrosion-induced cover cracking in reinforced concrete structures," *Construction and Building Materials*, vol. 25, no. 4, pp. 1854–1869, 2011.

[13] Y. F. Ma, Z. Z. Guo, L. Wang et al., "Experimental investigation of corrosion effect on bond behavior between reinforcing bar and concrete," *Construction and Building Materials*, vol. 152, pp. 240–249, 2017.

[14] A. Dasar, H. Hamada, Y. Sagawa et al., "Deterioration progress and performance reduction of 40-year-old reinforced concrete beams in natural corrosion environments," *Construction and Building Materials*, vol. 149, pp. 690–704, 2017.

[15] W. J. Zhu, R. François, and Y. Liu, "Propagation of corrosion and corrosion patterns of bars embedded in RC beams stored in chloride environment for various periods," *Construction and Building Materials*, vol. 145, pp. 147–156, 2017.

[16] Y. X. Zhao, J. F. Dong, Y. Y. Wu et al., "Corrosion-induced concrete cracking model considering corrosion product-filled paste at the concrete/steel interface," *Construction and Building Materials*, vol. 116, pp. 273–280, 2016.

[17] O. B. Isgor and A. G. Razaqpur, "Advanced modelling of concrete deterioration due to reinforcement corrosion," *Canadian Journal of Civil Engineering*, vol. 33, no. 6, pp. 707–718, 2006.

[18] Y. X. Zhao, J. F. Dong, H. J. Ding et al., "Shape of corrosion-induced cracks in recycled aggregate concrete," *Corrosion Science*, vol. 98, pp. 310–317, 2015.

[19] R. J. Zhang, C. Arnaud, and R. François, "Concrete cover cracking with reinforcement corrosion of RC beam during chloride-induced corrosion process," *Cement and Concrete Research*, vol. 40, no. 3, pp. 415–425, 2009.

[20] X. L. Du, L. Jin, and R. B. Zhang, "Modeling the cracking of cover concrete due to non-uniform corrosion of reinforcement," *Corrosion Science*, vol. 89, pp. 189–202, 2014.

[21] X. J. Zhu and G. Zi, "A 2D mechano-chemical model for the simulation of reinforcement corrosion and concrete damage," *Construction and Building Materials*, vol. 137, pp. 330–334, 2017.

[22] Y. X. Zhao, A. R. Karimi, H. S. Wong et al., "Comparison of uniform and non-uniform corrosion induced damage in reinforced concrete based on a Gaussian description of the corrosion layer," *Corrosion Science*, vol. 53, no. 9, pp. 2803–2814, 2011.

[23] E. Chen and C. K. Y. Leung, "A coupled diffusion-mechanical model with boundary element method to predict concrete cover cracking due to steel corrosion," *Corrosion Science*, vol. 126, pp. 180–196, 2017.

[24] Y. X. Zhao, J. Yu, and W. L. Jin, "Damage analysis and cracking model of reinforced concrete structures with rebar corrosion," *Corrosion Science*, vol. 53, no. 10, pp. 3388–3397, 2011.

[25] Y. X. Zhao, J. Yu, B. Y. Hu, and W. L. Jin, "Crack shape and rust distribution in corrosion-induced cracking concrete," *Corrosion Science*, vol. 55, pp. 385–393, 2012.

[26] K. K. Tran, H. Nakamura, K. Kawamura et al., "Analysis of crack propagation due to rebar corrosion using RBSM," *Cement and Concrete Composites*, vol. 33, no. 9, pp. 906–917, 2011.

[27] B. Šavija, M. Luković, J. Pacheco et al., "Cracking of the concrete cover due to reinforcement corrosion: A two-dimensional lattice model study," *Construction and Building Materials*, vol. 44, pp. 626–638, 2013.

[28] X. D. Cheng, L. F. Sun, Z. F. Cao et al., "Cracking process analysis of concrete cover caused by non-uniform corrosion," *Journal of Chinese Society for Corrosion and Protection*, vol. 35, no. 3, pp. 257–264, 2015.

[29] V. Papadakis, C. Vayenas, and M. Fardis, "Physical and chemical characteristics affecting the durability of concrete," *ACI Materials Journal*, vol. 88, no. 2, pp. 186–196, 1991.

[30] A. Saetta and R. Vitaliani, "Experimental investigation and numerical modeling of carbonation process in reinforced concrete structures part I: theoretical formulation," *Cement and Concrete Research*, vol. 34, no. 4, pp. 571–579, 2004.

[31] A. Saetta, R. Scotta, and R. Vitaliani, "Mechanical behavior of concrete under physical-chemical attacks," *Journal of Engineering Mechanics ASCE*, vol. 124, no. 10, pp. 1100–1109, 1998.

[32] C. H. Liang, *The Introduction of Metal Corrosion*, China Machine Press, Beijing, China, 1999.

[33] T. Ishida, P. Iqbal, and H. Anh, "Modeling of chloride diffusivity coupled with non-linear binding capacity in sound and cracked concrete," *Cement and Concrete Research*, vol. 39, no. 10, pp. 913–923, 2009.

[34] K. Nakarai, T. Ishida, and K. Maekawa, "Multi-scale physicochemical modeling of soil-cementitious material interaction," *Soils and Foundations*, vol. 46, no. 5, pp. 635–664, 2006.

[35] H. Böhni, *Corrosion in Reinforced Concrete Structures*, Woodhead Publishing, Oxford, UK, 2005.

[36] L. Bertolini, B. Elsener, P. Pedeferri et al., *Corrosion of Steel in Concrete–Prevention, Diagnosis, Repair*, Wiley-VCH Verlag GmbH and Co. KGaA, Weinheim, Germany, 2013.

[37] O. Geng, *Prediction models of steel bar corrosion rate in concrete member*, Ph.D. thesis, China University of Mining and Technology, Xuzhou, China, 2008.

[38] B. M. Wei, *Metallic Corrosion Theories and Applications*, Chemical Industry Press, Beijing, China, 1984.

[39] Y. J. Mu, *Reinforcement Corrosion Dilation Effect and Forecasting Model in Concrete*, China University of Mining and Technology, Xuzhou, China, 2006.

[40] Y. X. Zhao and W. L. Jin, "Analysis on the cracking of concrete cover due to rebar corrosion," *Journal of Hydraulic Engineering*, vol. 36, no. 8, pp. 939–945, 2005.

[41] X. B. Song and X. L. Liu, "Experiment research on corrosion of reinforcement in concrete through cathode-to-anode area ratio," *ACI Structural Journal*, vol. 97, no. 2, pp. 148–155, 2000.

[42] X. B. Song, *Corrosion of steel in concrete*, Ph.D. thesis, Tsinghua University, Beijing, China, 1999.

[43] B. S. Jang and B. H. Oh, "Effects of non-uniform corrosion on the cracking and service life of reinforced concrete structures," *Cement and Concrete Research*, vol. 40, no. 9, pp. 1441–1450, 2010.

[44] X. L. Du, L. Jin, and R. B. Zhang, "Modeling the cracking of cover concrete due to non-uniform corrosion of reinforcement," *Corrosion Science*, vol. 89, pp. 189–202, 2014.

[45] Y. S. Yuan, Y. S. Ji, and Y. J. Mou, "Propagation and model of distribution for corrosion of steel bars in concrete," *China Civil Engineering Journal*, vol. 40, no. 7, pp. 5–10, 2007.

[46] Y. X. Zhao, B. Y. Hu, J. Yu, and W. L. Jin, "Non-uniform distribution of rust layer around steel bar in concrete," *Corrosion Science*, vol. 53, no. 12, pp. 4300–4308, 2011.

[47] Y. X. Zhao, B. Y. Hu, J. Yu et al., "Non-uniform distribution of rust layer around steel bar in concrete," *Corrosion Science*, vol. 53, no. 12, pp. 4300–4308, 2011.

[48] Y. S. Yuan, Y. S. Ji, and Y. J. Mu, "Propagation and model of distribution for corrosion of steel bars in concrete," *China Civil Engineering Journal*, vol. 40, no. 7, pp. 5–10, 2007.

[49] Y. S. Ji, *Correlation of reinforced concrete degradation processes in natural and artificial climate environment*, Ph.D. thesis, China University of Mining and Technology, Xuzhou, China, 2007.

[50] C. Leon and V. V. Dimitri, "Prediction of corrosion-induced cover cracking in reinforced concrete structures," *Construction and Building Materials*, vol. 25, no. 4, pp. 1854–1869, 2011.

[51] J. Ožbolt, F. Oršanić, and G. Balabanić, "Modeling pull-out resistance of corroded reinforcement in concrete: coupled three-dimensional finite element model," *Cement and Concrete Composites*, vol. 46, no. 2, pp. 41–45, 2014.